

MICROLENSING AND VARIABILITY TOWARDS M31



Chien-Hsiu Lee

MICROLENSING AND VARIABILITY TOWARDS M31

Dissertation

an der
Ludwig–Maximilians–Universität (LMU) München

Ph.D. Thesis

at the
Ludwig–Maximilians University (LMU) Munich

submitted by

Chien-Hsiu Lee

born on 11th January 1982 in Taoyuan

Munich, 1st June 2011

1st Evaluator: Prof. Dr. Ralf Bender

2nd Evaluator: Prof. Dr. Jochen Weller

Date of the oral exam: 15th July 2011

Contents

Contents	vii
List of Figures	xvi
List of Tables	xvii
Zusammenfassung	xviii
Abstract	xix
1 Introduction	1
1.1 Content of the universe	1
1.2 Searching for dark matter with microlensing	4
1.3 Microlensing basics	6
1.4 Breaking the microlensing degeneracy	8
1.5 Microlensing in the pixel-lensing regime	12
2 Finite Source Effects in Microlensing: A Precise, Easy to Implement, Fast and Numerical Stable Formalism	15
2.1 Abstract	15
2.2 Introduction	15
2.3 The finite-source microlensing equation	16
2.4 Finite source with limb darkening	19
2.5 Finite-source equation with finite lens	21
2.6 Results	23
2.7 Conclusion	24
2.8 Appendix A: Partial derivatives of the finite-source amplification for a source with uniform surface brightness	28
2.9 Appendix B: Partial derivatives of the finite-source amplification for a source with limb darkening	28
2.10 Appendix C: Partial derivatives of the finite-source and finite-lens amplification assuming a source with uniform brightness	28
3 Finite-source and finite-lens effects in astrometric microlensing	31
3.1 Abstract	31
3.2 Introduction	31

3.3	Astrometric trajectory of the lensed images	33
3.4	The Finite Source Effects	34
3.5	The Finite Lens Effects	36
3.6	The Luminous Lens effects	39
3.7	Observational Feasibility	45
3.8	Conclusion	49
4	Properties of Andromeda galaxy (M31)	51
5	The Wendelstein Calar Alto Pixellensing Project (WeCAPP): the M31 Nova catalogue	57
5.1	Abstract	57
5.2	Introduction	57
5.3	Observations and Data Reduction	59
5.4	Nova detection	60
5.5	Nova Taxonomy	68
5.5.1	S Class and the universal decline law	68
5.5.2	C Class	69
5.5.3	O Class	72
5.5.4	J Class	72
5.5.5	Other classes	74
5.6	Recurrent Novae	76
5.7	Conclusion and outlook	78
5.8	Appendix A: WeCAPP nova candidate light curves	79
5.9	Appendix B: Light curves of nova candidates from literature	102
5.10	Appendix C: Separate microlensing events from variables	121
6	First results from PAndromeda - A dedicated deep survey of M31 with Pan-STARRS	123
6.1	The PANSTARRS survey and PAndromeda	123
6.2	First season of PAndromeda data	124
6.3	Photometric stability and study of variables from PAndromeda	127
6.4	Microlensing results from PAndromeda	132
7	Summary and outlook	141
	Bibliography	153
	Acknowledgments	155
	Curriculum Vitae	157

List of Figures

1.1	Timeline of cosmic microwave background. Credit: NASA/WMAP Science Team.	1
1.2	Content of the Universe. Credit: NASA/WMAP Science Team.	2
1.3	An illustration shows the general idea of microlensing search towards Galactic Bulge.	4
1.4	PAndAS survey. Adopted from McConnachie et al. (2009)	5
1.5	A schematic view of gravitational lensing. The space-time between the source and the observer is disturbed by the gravity of the lens. The observer will see the extended source split into two arc-like images. If the source is not extended, the observer will see two points instead.	6
1.6	Configuration of microlensing.	7
1.7	Parallax effects by Earth-orbital motion in the MACHO event MACHO-LMC-5. Left panel: light curve for MACHO red (circles) and blue (crosses) filters. The dashed (solid) line indicates the best-fit model with (without) parallax effects Right panel: the trajectory of lens-source relative motion with (solid line) and without (dashed line) parallax effects, projected onto the sky in the geocentric frame. Open (filled) circles are for $t < t_0$ ($t \geq t_0$). The time difference between two consecutive circles are 5 days. $\pi_{E,old}$ is the best-fit microlens parallax from Alcock et al. (1993) under the context of heliocentric frame. $\pi_{E,new}$ is the new solution found by Gould (2004) in the geocentric scheme. Adapted from Gould (2004)	9
1.8	<i>HST</i> observation of MACHO-LMC-5. Left panel: Three-color image from the WFPC <i>V</i> -, <i>R</i> - and <i>I</i> -band observations. The source is the blue star close to the center, with the lens to be the red star indicated by the arrow. Right panel: The lens motion projected onto the sky with the best-fitted microlensing parallax. Adapted from Alcock et al. (2001)	9
1.9	Observations of OGLE-2008-BLG-290 overlaid with models of the best-fit finite-source and limb-darkening effects in <i>I</i> -band (black curve), <i>R</i> -band (red curve) and <i>V</i> -band (green curve). Adapted from Fouqué et al. (2010)	10
1.10	Centroid shifts for PSPL. Left panel: the trajectory of the plus-image (in blue), minus-image (in red), centroid of these two images (in black) and the lens (in grey) relative to the source center assuming $t_0 = 0$, $t_E = 10$ d and $u_0 = 0.5 \theta_E$. Right panel: centroid displacement for different values of u_0	11
1.11	A schematic view of the difference imaging technique in crowded field. The reference frame is constructed by good seeing images. To perfectly subtracted the background sources, the frame of interest and the reference frame are convolved to a common PSF basis. Image credit: Arno Riffeser.	12

2.1	Geometric definitions. Left: source is overlapping the lens center. Right: lens is outside the source radius.	16
2.2	Comparison of finite-source light-curve approximations. Left: moderate-amplification regime with $t_E = 10$, $u_0 = 0.1$ and $\rho_s = 0.5$. Right: high-amplification regime with $t_E = 10$, $u_0 = 0.01$ and $\rho_s = 0.05$. In <i>dashed black</i> the Paczyński light curve for a point source, in <i>solid black</i> Witt & Mao light curve, in <i>gray</i> the approximation derived by Gould (1994) and in <i>dashed white</i> Equation (2.7) with $n = 10$. The vertical lines indicate the time when $u = \rho_s$. Our formula is as good as Gould (1994) in high-amplification regime and is better in the moderate-amplification regime. . . .	19
2.3	Percentage deviation in amplification compared to Witt & Mao formalism (A_{WM}). The expression of Gould (1994) is valid for small source (<i>solid black</i>) but shows deviation $> 2.5\%$ for larger source (<i>dotted black</i>). Equation (2.7) with $n = 10$ shows a smaller deviation ($< 0.5\%$). Equation (2.7) with $n = 500$ for both source sizes are well overlapped with each other, so we show here only $\rho_s = 0.05$	20
2.4	Maximum amplification of microlensing events detected by the OGLE experiment from 2002 to 2007. Most of the events ($> 80\%$) have maximum amplification < 10 . Events with maximum amplification > 100 , which are categorized into interval 100-110 in this plot, are relatively rare ($< 4.4\%$).	20
2.5	Light-curve computation efficiency. We compare light-curve computation time of Equation (2.7) with $n = 10$ to that of Gould's formalism for various source radii ($\rho_s = 0.01, 0.1, \text{ and } 1$). The computation time for our approximation is comparable to the Gould formalism; it is about 38% faster when $u < \rho_s$ and is $> 55\%$ faster when $u > \rho_s$	20
2.6	Limb-darkening effects on the finite-source light curve in the moderate-amplification regime. In <i>dotted black</i> we show the Paczyński light curve for a point source with $t_E = 10$ and $u_0 = 0.1$. In <i>solid black</i> , we show the finite-source light curve for a uniform source with a projected source size of $\rho_s = 0.5$. In <i>dashed line</i> and <i>dash-dotted line</i> , we plot the limb-darkened finite-source light curves with $\Gamma = 0.3$ and 0.6 . Increasing Γ enhances the limb-darkening effects thus brings the finite-source light curve closer to Paczyński's formalism.	21
2.7	Image obscuration by a finite lens with radius $R_{\text{lens}} = 0.5R_E$	22
2.8	Finite-source light-curve fits for MACHO-1995-BLG-30 assuming a uniform source. Data points in R are from MACHO (<i>red</i>), CTIO, UTSO, WISE, and MJUO (<i>gray</i>) and V are from MACHO (<i>blue</i>) and UTSO (<i>green</i>). The <i>dashed line</i> shows the light curve for a point-source model. The best-fitting finite-source light-curve parameters are displayed in Table 2.1	24
2.9	Residuals of the observed light curve relative to the best-fitted point-source light curve. The <i>solid black</i> curve shows the light curve of an extended source with uniform surface brightness. The <i>solid blue</i> , <i>solid red</i> , and <i>solid green</i> curves are extended source models incorporating limb darkening in V , I and H bands with $(\Gamma_V, \Gamma_I, \Gamma_H) = (0.72, 0.44, 0.26)$. The vertical lines indicate t_0 for the best-fitted point-source (<i>solid</i>) and limb-darkened finite-source (<i>dashed</i>) model. For the light curves with the limb-darkened source we have left t_0 as a free parameter. The best-fitting value for t_0 slightly differs (see Table 2.2). This causes the asymmetric pattern of the residual relative to the Paczyński light curve.	25

2.10	Finite-source and finite-lens light-curve fits for OGLE-2003-BLG-262. Data points are in I (square), V (circle), and H (triangle). The <i>dashed line</i> shows the light curve for a point source. The <i>solid line</i> shows the light curve for an extended source with uniform surface brightness. The <i>dotted lines</i> illustrate the effects of finite lens sizes on top of finite-source size for lens sizes of $\rho_{\text{lens}} = 0.93, 0.96, 0.99, \text{ and } 1.02$	26
2.11	Fitting residual of various lens radius relative to the point-source model. Data points are in I (square), V (circle), and H (triangle). The <i>solid black line</i> shows the light curve for an extended source with uniform surface brightness. The <i>dotted lines</i> illustrate the effects of finite lens sizes on top of finite source size for lens sizes of $\rho_{\text{lens}} = 0.93, 0.96, 0.99, \text{ and } 1.02$. One sees that all these cases can be safely excluded.	26
2.12	χ^2 contour map of OGLE-2003-BLG-262. In <i>white contour</i> , levels for 1, 2, and 3σ for source and lens size fitting are shown. The <i>black triangle</i> indicates the best-fitted model with $\rho_s = 0.06056$ and $R_{\text{lens}} = 0$. This suggests that the point lens assumption is sufficient for OGLE-2003-BLG-262.	27
3.1	Centroid shifts for PSPL. Left panel: The trajectory of the plus-image (in <i>blue</i>), minus-image (in <i>red</i>), centroid of these two images (in <i>black</i>), and the lens (in <i>gray</i>) relative to the source center assuming $t_0 = 0$, $t_E = 10$ days, and $u_0 = 0.5 \theta_E$. Right panel: Centroid displacement for different values of u_0	34
3.2	Maximum values for the centroidal shift versus lens mass. For illustration, we set the lens of halo lensing towards SMC ($D_{\text{os}} = 65$ kpc) and M31 ($D_{\text{os}} = 770$ kpc) to be 15 kpc from the observer, and 1 kpc in front of the source as self-lensing. We only show the case of halo lensing for Galactic bulge ($D_{\text{os}} = 8$ kpc) assuming the lens is half way to the background source.	35
3.3	Schematic view of the lens-centered coordinates used in equation (3.10)	36
3.4	An example for centroidal shifts of a microlensing event assuming $u_0 = 0.1 \theta_E$, source radius = $0.5 \theta_E$ and lens radius = $0.5 \theta_E$. We show the trajectory of a PSPL (in <i>yellow</i>), FSPL (in <i>green</i>), PSFL (in <i>red</i>), and FSFL (in <i>blue</i>). Note that the <i>dashed red line</i> indicates the discontinuous part of the trajectory in a PSFL event.	37
3.5	Centroidal shifts decomposition and lightcurves of a microlensing event assuming $u_0 = 0.1 \theta_E$, source radius = $0.5 \theta_E$ and lens radius = $0.5 \theta_E$. We show the trajectory in the x- and y-direction (as in Fig. 3.1) of a PSPL (in <i>yellow</i>), FSPL (in <i>green</i>), PSFL (in <i>red</i>), and FSFL (in <i>blue</i>). We also show the lightcurve with the magnitude variation relative to the baseline (m_{base}). The <i>vertical dashed line</i> indicates the time when $u_0 = \rho_s$. Note that the discontinuous part of the trajectory in a PSFL event is indicated by the <i>dashed red line</i>	38
3.6	Centroidal shifts decomposition and lightcurves of a microlensing event assuming $u_0 = 0.1 \theta_E$, source radius = $0.5 \theta_E$ and lens radius = $0.5 \theta_E$. We show the trajectory in the x- and y-direction (as in Fig. 3.1) of a uniform brightness source (in <i>black</i>), a limb-darkened source with $\Gamma_S = 0.4$ (in <i>cyan</i>) and $\Gamma_S = 0.8$ (in <i>red</i>). We also show the lightcurve with the magnitude variation relative to the baseline (m_{base}). The <i>vertical dashed line</i> indicates the time when $u_0 = \rho_s$	40

- 3.7 Centroid shifts in the presence of FS and FL effects for a dark lens. We show the examples for a PSPL (in *yellow*), FSFL with a uniform surface brightness source (in *black*) and with a limb-darkened source (in *cyan*: $I_S = 0.4$ and in *red*: $I_S = 0.8$) assuming $u_0 = 0.5 \theta_E$ and with the sizes of the source and the lens varying from $0.3 \theta_E$ to $1.3 \theta_E$. The dashed lines in the plots with $\theta_S/\theta_E = 0.0$ show the discontinuity in the trajectories for the PSFL cases. The dotted line in the PSFL with $\theta_L/\theta_E = 1.3$ indicates the trajectory when the lens totally obscures both the plus- and minus-image. 41
- 3.8 Centroidal shifts decomposition and lightcurves of a microlensing event assuming $u_0 = 0.1 \theta_E$, source radius = $0.5 \theta_E$ and lens radius = $0.5 \theta_E$. We show the trajectory in the x- and y-direction (as in Fig. 3.1) of a bright lens with $\Delta m_{LS} = -2$ (in *blue*), 0 (in *gray*), 2 (in *green*) and with a dark lens (in *black*). We also show the lightcurve with the magnitude variation relative to the baseline (m_{base}). The *vertical dashed line* indicates the time when $u_0 = \rho_s$ 43
- 3.9 Centroid shifts in the presence of FS and FL effects for a luminous lens. We show the examples for a PSPL (in *yellow*), FSFL with $\Delta m_{LS} = -2$ (in *blue*), 0 (in *gray*), 2 (in *green*) and with a dark lens (in *black*) assuming $u_0 = 0.5 \theta_E$ and with the sizes of the source and the lens varying from $0.3 \theta_E$ to $1.3 \theta_E$. The dashed lines in the plots with $\theta_S/\theta_E = 0.0$ show the discontinuity in the trajectories for the PSFL cases. The dotted lines in the PSFL with $\theta_L/\theta_E = 1.3$ indicates the trajectory when the lens totally obscures both the plus- and minus-image. 44
- 3.10 First row: θ_E as a function of D_{OL} assuming the source located in the Galactic bulge ($D_{OS} = 8$ kpc), SMC ($D_{OS} = 65$ kpc), and M31 ($D_{OS} = 770$ kpc). Second and third row: θ_S/θ_E and θ_L/θ_E as a function of the lens distance assuming $M_L = 0.5 M_\odot$ 45
- 3.11 First row: Maximum centroidal shifts as a function of D_{OL} assuming the source located in the Galactic bulge ($D_{OS} = 8$ kpc), SMC ($D_{OS} = 65$ kpc), and M31 ($D_{OS} = 770$ kpc) in PSPL. Second row: Maximum deviation between the PSFL and PSPL trajectories as a function of the lens location $(1 - x)$, where $x = D_{OL}/D_{OS}$. Third row: Maximum deviation between the FSFL and PSPL trajectories. Fourth row: Maximum deviation between the FSFL and PSFL trajectories. We assume $u_0 = 0.05 \theta_E$, $t_E = 10$ days, $M_L = 0.5 M_\odot$, $R_L = 10 R_\odot$, and $R_S = 10 R_\odot$. Here we show the cases of a luminous lens with $\Delta m_{LS} = 2$ (in *dashed*), 0 (in *dotted*), -2 (in *dash-dotted*), and a dark lens (in *solid*). 47
- 3.12 Astrometric trajectory of the SMC microlensing event MACHO-97-SMC-1 with $t_E = 123.5$ days and $u_0 = 0.426824 \theta_E$. We show the case when the lens is located in the Galactic halo (upper panels) and in SMC (lower panels). We assume the lens is $1 M_\odot$ and the size of the lens and the source are assumed to be 1, 5, and $10 R_\odot$, respectively. The color convention is the same as Fig. 3.4. We calculate the theoretical trajectory within a time interval of $t_0 \pm 1000$ days. We then simulate the measurements of *SIM*, with a sampling rate of every 90 days spanning for $t_0 \pm 1$ year and $30 \mu\text{as}$ error in both x and y direction. The dashed square in the halo lensing cases outlines the dimension showed in the self-lensing regime. 48
- 4.1 A schematic view of M31 as seen from an observer on Earth. 51

- 4.2 M31 surface brightness (SFB) profile derived from SDSS g -band data by [Tempel et al. \(2011\)](#). The black solid line is the SFB measured from the SDSS data. They also generate a model for SFB (red solid line) and give the individual components contribute to the SFB (dashed line). Upper panel shows the SFB along the major axis of M31, while the lower panel is the SFB along the minor axis. 53
- 4.3 Number density (N) of the bulge stars (*left*) and the disk stars (*right*) with the absolute magnitude \mathcal{M}_R brighter than 0 mag in units of stars per arcsec². The contours demonstrate the value of $d^2N/(dx dy)|_{\mathcal{M}_R \leq 0} = \int_{-\infty}^0 \int_0^{\infty} \tilde{\Phi}(\mathcal{M}_R) n_S(x, y, D_{OS}) dD_{OS} d\mathcal{M}_R$ with the interval listed above the figure. It is obtained from the number density and luminosity functions of the bulge and disk of M31. The dashed contour indicates $\log_{10}N = 1$ and implies that even giant stars in the center of M31 are not resolvable for most of the ground-based observatories. The $17'.2 \times 17'.2$ field of view of the WeCAPP campaign is outlined by a box. Adopted from [Riffeser et al. \(2006\)](#). 54
- 4.4 Upper panel: SDSS i' -band image without correction of extinction. Lower panel: SDSS i' -band image dereddened with extinction map by [Montalto et al. \(2009\)](#). The colorbar indicates the logarithmic intensity levels in the units of Jansky. The resolution of the images is $6''/\text{pixel}$. Adapted from [Montalto et al. \(2009\)](#). 55
- 4.5 Upper panel: SDSS g' -band image before photometric alignment for the different drift scan runs. Lower panel: SDSS g' -band image after photometric alignment for the different drift scan runs. 56
- 5.1 Fraction of good quality data points in t averaged over the survey area. The definition of good quality is given in the text. The vertical grey zones indicate the time when M31 is not observable from the location of the telescopes during May and June). 0% indicates we have no observations during the night. 60
- 5.2 Fraction of good quality data points in (x, y) averaged over time t . The definition of good quality is given in the text. The low fraction in the central part is caused by the high noise of M31 itself. 62
- 5.3 Distribution of the WeCAPP nova candidates. The overlaying image is a three-color-combined image using the observations obtained from Calar Alto observatories in V , R and I -band. The image has a size of $17'.2 \times 17'.2$ 63
- 5.4 S Class novae with free t_0 . The single offsets are -15.04 for N08, -3.59 for N30, -2.81 for N31, 2.84 for N37, -18.02 for N39, -0.88 for N42, -9.89 for N68, -8.06 for N72, -11.81 for N79 and 1.02 for N82, 5.14 for N83, -13.66 for N84 and 5.37 for N90 respectively. Note that for most of the data points the error bars are smaller than the symbol of the data points. Here we only show the decline part of the light curve. Full light curves can be found in the appendix. 69
- 5.5 S Class novae with fixed t_0 . The single offsets are -8.84 for N22, 15.17 for N26, 12.44 for N33, -6.44 for N34, 4.97 for N40, -10.40 for N45, 2.53 for N48, 10.92 for N50, -13.97 for N52, 8.05 for N59, -0.22 for N65, -1.84 for N71, 16.24 for N75, 6.70 for N85, -11.06 for N87 and -5.14 for N88 respectively. Here we only show the decline part of the light curve. Full light curves can be found in the appendix. 70

5.6	C Class novae. The offsets applied to the magnitudes are -15.07 for N07, -11.88 for N10, -8.26 for N12, -17.71 for N13, -11.58 for N14, -13.79 for N15, -9.16 for N32, -19.19 for N53, -19.15 for N62 and -13.04 for N67 respectively. Here we only show the decline part of the light curve. Full light curves can be found in the appendix.	73
5.7	O Class novae. The offset is -15.77 for N11 and -17.61 for N28 respectively. Here we only show the decline part of the light curve. Full light curves can be found in the appendix.	74
5.8	J Class nova. The single offsets are -16.99 for N27. Here we only show the decline part of the light curve. Full light curves can be found in the appendix.	75
5.9	J-class peak intervals for nova N27, using <i>R</i> -band data.	76
5.10	Position of the recurrent nova candidates. The larger circle in the center indicates the 1".0 radius for our selection criteria. The position of potential recurrent nova candidates are marked by the smaller circles.	77
5.11	Recurrent nova candidates light curves. The single offsets are -11.76 for N02, -15.76 for N19, -18.86 for N29 and -9.86 for N83 respectively. Here we only show the decline part of the light curve. Full light curves can be found in the appendix.	78
5.12	Light curves of WeCAPP nova N01-N04.	79
5.13	Light curves of WeCAPP nova N05-N08.	80
5.14	Light curves of WeCAPP nova N09-N12.	81
5.15	Light curves of WeCAPP nova N13-N16.	82
5.16	Light curves of WeCAPP nova N17-N20.	83
5.17	Light curves of WeCAPP nova N21-N24.	84
5.18	Light curves of WeCAPP nova N25-N28.	85
5.19	Light curves of WeCAPP nova N29-N32.	86
5.20	Light curves of WeCAPP nova N33-N36.	87
5.21	Light curves of WeCAPP nova N37-N40.	88
5.22	Light curves of WeCAPP nova N41-N44.	89
5.23	Light curves of WeCAPP nova N45-N48.	90
5.24	Light curves of WeCAPP nova N49-N52.	91
5.25	Light curves of WeCAPP nova N53-N56.	92
5.26	Light curves of WeCAPP nova N57-N60.	93
5.27	Light curves of WeCAPP nova N61-N64.	94
5.28	Light curves of WeCAPP nova N65-N68.	95
5.29	Light curves of WeCAPP nova N69-N72.	96
5.30	Light curves of WeCAPP nova N73-N76.	97
5.31	Light curves of WeCAPP nova N77-N80.	98
5.32	Light curves of WeCAPP nova N81-N84.	99
5.33	Light curves of WeCAPP nova N85-N88.	100
5.34	Light curves of WeCAPP nova N89 and N90.	101
5.35	The S/N and χ used to filter out microlensing candidates (black) from the 22646 pixel light curves with good PSF fitting (green) obtained in the WeCAPP campaign. The blue points are the novae from the WeCAPP catalogue. The red points show the variables presented in Fliri et al. (2006) . The magenta points indicate the light curves fulfilling the S/N and χ criteria mentioned in the main text. The black points are the microlensing candidates which pass further criteria.	121

5.36	The t_{FWHM} and χ used to filter out microlensing candidates (black) from the 22646 pixel light curves with good PSF fitting (green) obtained in the WeCAPP campaign. The blue points are the novae from the WeCAPP catalogue. The red points show the variables presented in Fliri <i>et al.</i> (2006) . The magenta points indicate the light curves fulfilling the t_{FWHM} and χ criteria mentioned in the main text. The black points are the microlensing candidates which pass further criteria.	122
6.1	The Giga Pixel Camera (GPC) and its 60 Orthogonal Transfer Arrays (OTAs). Each OTA is composed of 8×8 CCDs and has 584×591 pixels per CCD. The field of view of GPC is ~ 7 degree ² . The entire Andromeda galaxy, M32 and NGC 205 can be imaged with one pointing (as shown in the figure).	124
6.2	The Andromeda galaxy observed by PS1. The color image is combined by g' , r' and i' images taken during the commissioning run in 2007.	125
6.3	Accumulated number of images observed by PAndromeda in r' - and i' -band.	125
6.4	PAndromeda observation cadence. The histogram shows the number of visits (0, 1 or 2 times per night) on M31. The black line indicates the lunar phase (1 for full moon and 0 for dark night). The red line shows the distance of the M31 center from the moon as a function of observing date.	126
6.5	Point-Spread Function (PSF) distribution of the first season of PAndromeda in the bulge (upper panel) and disk (lower panel) field. The PSF distributions of the r' (i') data are shown in the blue (red). The dashed vertical lines indicate the promised PSF ($0''.8$) of PS1.	128
6.6	Photometric accuracy (rms) as a function of the magnitude of stars from images taken by PAndromeda. The rms is derived from the light curves of each stars. The R -band magnitude is obtained by comparing the flux of stars in the PAndromeda data to the USNO-A2 catalog (Since at that time when this figure was made the absolute flux calibration in the static sky image of the PAndromeda data was not precisely known).	129
6.7	Delta Cepheid light curves from PAndromeda data. Upper panel: magnitude as a function of the PAndromeda observing date. Lower panel: magnitude as a function of the pulsation phase. The magnitude is obtained by comparing the r' -band flux from the stars in PAndromeda to the R -band catalog in USNO-A2. Here we focus on the variation in the magnitude rather than the absolute magnitude of the Delta Cepheid.	130
6.8	Light curve of the nova M31N-2010-10a from PAndromeda r' -band data. The vertical axis is the difference flux (relative to the mean flux of the PSF standard).	131
6.9	Position of the six microlensing event candidates detected in the central region of M31 from PAndromeda.	133
6.10	Light curves of the microlensing event PAnd 1 detected in the bulge of M31 from PAndromeda. Upper (lower) panel shows the light curve in r' (i'). In the figure there are also the name of the event (PAnd 1), the coordinates α (RA) and δ (Dec) at the epoch of J2000, the distance to the center of M31 (Δ_{M31}) in arcminutes. The best-fit light curves and parameters are shown in red, which are the time at maximum magnification (t_0), the event timescale (t_{FWHM}) in units of a day, the equivalent magnitude at maximum magnification (F_{eff}) in each filter, the normalized $\chi_n := \sqrt{\chi_n^2}$ in each filter and the color (R-I) of the event.	134

6.11	Light curves of the microlensing event PAnd 2 detected in the bulge of M31 from PAndromeda.	135
6.12	Light curves of the microlensing event PAnd 3 detected in the bulge of M31 from PAndromeda.	136
6.13	Light curves of the microlensing event PAnd 4 detected in the bulge of M31 from PAndromeda.	137
6.14	Light curves of the microlensing event PAnd 5 detected in the bulge of M31 from PAndromeda.	138
6.15	Light curves of the microlensing event PAnd 6 detected in the bulge of M31 from PAndromeda.	139

List of Tables

1.1	Dark matter candidates	3
1.2	Baryon budget from Fukugita & Peebles (2004)	3
2.1	Light-curve parameters for MACHO-1995-BLG-30	23
2.2	Light-curve parameters for OGLE-2003-BLG-262.	24
3.1	$D_{\text{OL}}(D_{\text{OS}} - D_{\text{OL}})/D_{\text{OS}}$ for several astrophysical objects.	46
5.1	Principal M31 classical nova surveys	59
5.2	Detection criteria for nova candidates	61
5.3	WeCAPP nova catalogue	64
5.4	WeCAPP nova catalogue. This table continues Table. 5.3.	65
5.5	WeCAPP nova catalogue. This table continues Table. 5.3.	66
5.6	WeCAPP nova catalogue. This table continues Table. 5.3.	67
5.7	Power-law decline fitting for s-class nova.	71
5.8	Recurrent Nova Candidates	77
6.1	PAndromeda integration time in r' - and i' -band.	124

Zusammenfassung

Das Standardmodell der Kosmologie besagt, dass sich das Universum nur zu 4% aus Baryonen zusammensetzt. Die übrigen 24% beziehungsweise 72% bestehen aus dunkler Materie und dunkler Energie. Die Existenz dunkler Materie wird durch die flachen Rotationskurven von Spiralgalaxien demonstriert, wobei jedoch ihre Natur unklar bleibt. Es werden hauptsächlich zwei Arten von dunkler Materie diskutiert, schwach wechselwirkende massive Teilchen (WIMPs) und massive kompakte Haloobjekte (MACHOs). Es war Paczynski (1986), der als erster vorschlug, Microlensing zur Detektion von MACHOs in unserer Galaxie zu nutzen. Seine Berechnungen zeigen, dass die Wahrscheinlichkeit ein Microlensing-Ereignis in Richtung des Bulges der Milchstraße zu beobachten, 1:1000000 beträgt. Paczynskis wegweisende Publikation führte zu zahlreichen Beobachtungen dichter Himmelsregionen wie dem Galaktischen Bulge oder den Magellanschen Wolken, und es folgten Berichte über tausende Ereignisse, die in den meisten Fällen Selbst-Lensing (ein Stern wird von einem Stern und nicht von einem MACHO gelinst) als Ursache haben. Allerdings kann aus der Mikrolinsenlichtkurve in der Paczynski Näherung (eine Punklinse linst eine Punktquelle) als einziger physikalischer Parameter nur die Ereignisdauer direkt aus diesen Beobachtungen ermittelt werden. Die Ereignisdauer setzt sich in einer entarteten Weise aus der Masse, der Entfernung und der Geschwindigkeit des MACHOs zusammen. Daher liefert sie nur eine Wahrscheinlichkeitsverteilung für diese physikalischen Größen. Das Aufheben dieser Entartung erfordert die zusätzliche Berücksichtigung von Microlensing-Effekten höherer Ordnung, wie zum Beispiel die Berücksichtigung der endlichen Quellenausdehnung im Vergleich zur Punktquelle-Punklinse-Betrachtung. In den ersten Teilen dieser Dissertation wird ein exakter analytischer Formalismus für ausgedehnte Quellen entwickelt, der sehr einfach für Lichtkurven-Fitting-Routinen implementiert werden kann. Dieser Formalismus ermöglicht es, die Auswirkungen ausgedehnter Quellen photometrisch und astrometrisch zu untersuchen. Der entwickelte Algorithmus wurde erfolgreich bei einem, von Fouque et al. (2010) analysierten, OGLE-2008-BLG-290-Ereignis angewandt.

Neben den Magellanschen Wolken stellt M31 ein weiteres ideales Ziel für MACHO-Suchen dar, da mehrere Sichtlinien in Richtung von M31 möglich sind. Dies ermöglicht eine bessere Unterscheidung zwischen Selbst-Lensing (Sterne linsen Sterne in M31) und Halo-Lensing (MACHOs im Halo der Milchstraße oder von M31 linsen Sterne in M31). Die extragalaktische Gruppe an der USM hat Microlensing-Ereignisse in Richtung von M31 über viele Jahre untersucht. Ich war an der letzten Phase des Wendelstein Calar Alto Pixellensing Projektes (WeCAPP) beteiligt, bei dem der Bulge von M31 kontinuierlich von 1997 bis 2008 mit 1-Meter-Klasse-Teleskopen von München und Spanien aus beobachtet wurde. Die stärkste Kontamination von Kurzzeitskalen-Microlensing-Ereignissen wird durch Novae verursacht. Daher wurde eine gründliche Untersuchung der Novae im WeCAPP-Datensatz durchgeführt, um eine obere Grenze für das χ^2 des Microlensing-Lichtkurven-Fittings zu ermitteln und zuverlässig zwischen MACHOs und Novae unterscheiden zu können. In diesem Zusammenhang wurden 90 Novae detektiert, die zum gegenwärtigen Zeitpunkt den grössten Satz an CCD-basierender Nova-Lichtkurven in Richtung von M31 darstellen.

Desweiteren bin ich stark in das fortlaufende PAndromeda-Projekt eingebunden, einer intensiven Überwachung von M31 mit dem 1.8-Meter PanSTARRS-Teleskop auf dem Haleakala in Hawaii. Ziel ist die Bestimmung des Anteils der MACHOs im Halo der Milchstraße und M31. Zum Zeitpunkt der Verfassung dieser Dissertation ist eine Beobachtungskampagne (fünf Monate) abgeschlossen. Als vorläufiger Test wurde ein Teilfeld des Bulges von M31 auf die Stabilität der Datenqualität als Funktion der Zeit untersucht. Die Analyse zeigt, dass die Datenqualität für MACHO-Detektionen geeignet ist. Es wurden sogar sechs Microlensing-Ereignisse in diesem Subfeld detektiert. Zur Zeit erfolgt die Analyse des vollständigen PAndromeda-Datensatzes.

Abstract

According to the standard model of cosmology, only 4% of our universe are composed of baryons. The rest of our universe are in the form of dark matter (24%) and dark energy (72%). The existence of dark matter is revealed e.g. by the flat rotation curves of spiral galaxies but its nature remains unknown. Two classes of cold dark matter candidates are mostly considered: weakly interacting massive particles (WIMPs) and massive compact halo objects (MACHOs). Paczynski (1986) first proposed to use microlensing as a probe to detect the MACHOs in our Galaxy. His calculation shows that the chance of observing microlensing effects towards the stars in the Galactic bulge is 1 : 1,000,000. Triggered by Paczynski's seminal paper, numerous experiments have monitored crowded fields such as the Galactic bulge and the Magellanic clouds and have reported thousands of events mostly caused by self-lensing. However, the only physical parameter that one can retrieve is the event timescale. This is a degenerate combination of the mass, the distance, and the velocity of the MACHOs, and one can only obtain the probability distribution of these physical properties through a statistical study with large amount of events. To break this degeneracy for individual events, we require higher order effects from the microlensing, such as the finite-source effects relative to the point-source point-lens cases. In the first parts of this thesis I have developed an exact and analytical formula for the extended sources, which can be easily implemented for light-curve fitting routines. With these formula, I am able to study the finite-source effects photometrically and astrometrically. We have successfully applied my algorithm in the OGLE-2008-BLG-290 event analyzed by Fouque et al. (2010).

Besides the Magellanic clouds, M31 is another ideal target for MACHO searches because we can have various lines of sight towards M31. This enables us to better distinguish between self-lensing (stars lens stars in M31) and halo lensing (MACHOs in the Galactic or M31's halo lens stars in M31). The Extragalactic group at USM has studied microlensing towards M31 for many years. I have participated in the very last phase of Wendelstein Calar Alto Pixellensing Project (WeCAPP), which continuously monitored the bulge of M31 from 1997 till 2008 with one-meter class telescopes in Munich and Spain. The most severe contamination of the short time-scale microlensing events in M31 comes from novae. Thus we carried out a thorough study of the novae in the WeCAPP data set and obtained an upper limit of the χ^2 for microlensing light-curve fitting to securely separate MACHO from novae. We also detected 90 novae and presented the largest amount of CCD based novae light curves towards M31 up-to-date.

I am also strongly involved in the ongoing PAndromeda project, a dedicated deep survey of M31 using the 1.8-meter PanSTARRS telescope located at Haleakala in Hawaii. The aim of PAndromeda is to constrain the fraction of MACHOs in the halo of the Milky Way and M31. During the time when this thesis is written, PAndromeda has just finished its first observing season (five months). As a preliminary test, I used a sub-field from the bulge of M31 and investigated the stability of the data quality as a function of time. The study showed that the data is sufficient for MACHO detections. Indeed, we have discovered six microlensing events in this sub-field. A science paper for these six events is in preparation. Currently we are analyzing the full amount of the PAndromeda data.

Chapter 1

Introduction

1.1 Content of the universe

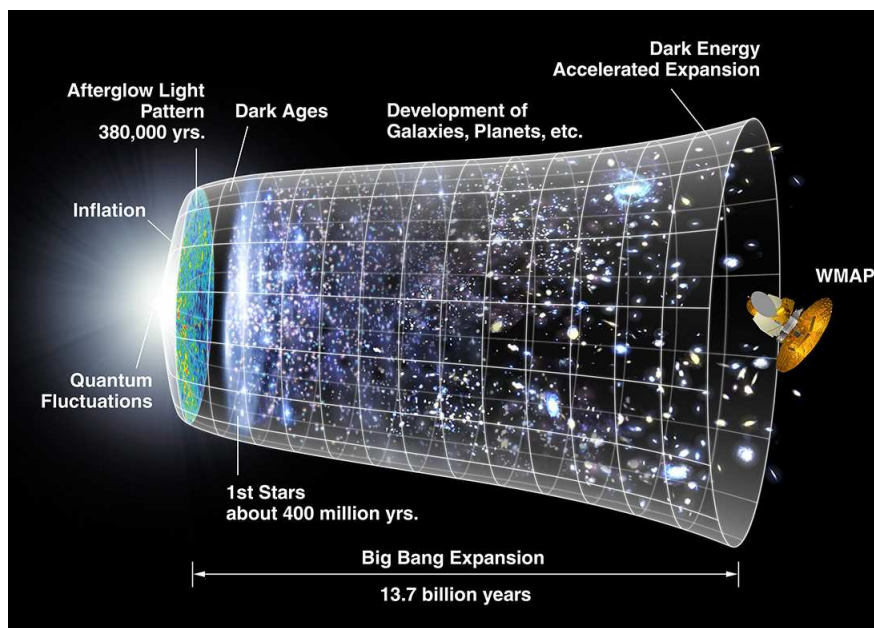


Figure 1.1: Timeline of cosmic microwave background. Credit: NASA/WMAP Science Team.

The current study of cosmology indicates our universe started from a big bang about 13.7 billion years ago. Based on the Big Bang theory, our universe is very hot at birth and cools down as it expands. The Big Bang theory predicts the remnant heat from the early epochs of the universe, dubbed as cosmic microwave background radiation (CMB), to be around 2.725 K and permeates our universe nowadays (Peebles, 1993). This has been observed by Penzias & Wilson (1965) and thus verified the Big Bang theory. The tiny fluctuation in the CMB sheds light on the structure formation in the early universe and helps constrain the parameters of Big Bang theory, which gives us information on the density and composition of the universe. Observations from the Wilkinson Microwave Anisotropy Probe (WMAP) show that our universe is composed of three components: The vast majority belongs

to the regime of dark energy, leaving only one quarter of the universe to be dark matter and atoms (see. Fig. 1.4). Surprisingly, the most well-known and thoroughly studied part of the universe, i.e. the atoms, only contribute to 4% of the universe and this suggests that we have very little understanding of our universe!

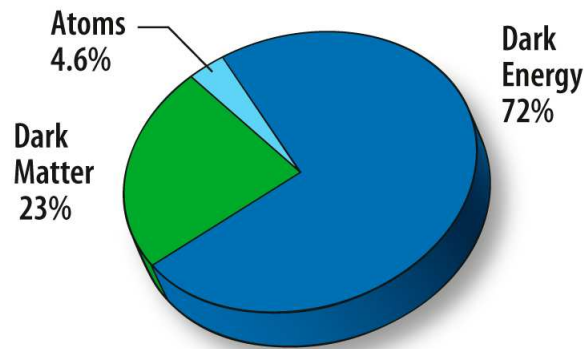


Figure 1.2: Content of the Universe. Credit: NASA/WMAP Science Team.

Observational evidences, based on the distant supernovae from the Supernova Cosmology Project (Perlmutter *et al.*, 1999) and High- z Supernova Search (Riess *et al.*, 1998), show that the universe is expanding at an accelerated rate. Therefore, we require an expelling force to counteract the gravitational force. One can achieve a force that is counter-acting the gravitation by introducing a fluid in the energy momentum tensor which has an equation of state $w = P/\rho$, where w is negative. The nature of this fluid and its exact equation of state (redshift evolution) is not known. The energy density represented by the fluid is called dark energy (Frieman *et al.*, 2008).

The term dark matter was first proposed by Zwicky (1937). He applied the virial theorem to estimate the mass of the Coma galaxy cluster and found that the estimated mass of the galaxy cluster exceeds the mass from luminous matter in the galaxy cluster. To explain these discrepancies, he suggested that most of the mass of galaxy clusters resides in the form of unseen dark matter.

Another evidence of dark matter comes from the rotation curve of spiral galaxies (Rubin *et al.*, 1980). If most of the mass is concentrated in the center of the galaxy, as traced by the surface brightness of the galaxy, we would expect the stars and gases in the galaxy to follow the Keplerian dynamics and the rotation speed would decrease inversely proportional to the square root of the distance. However, the rotation curve remains flat even at very large distances from the galaxy center and indicates there is dark matter permeating the entire galaxy and is substantially extended relative to the visible part of the galaxy.

There are two proposed candidate classes for dark matter. The first one is massive compact halo object (MACHO), which is either a stellar remnant (e.g. a neutron star or a stellar black hole (BH) or a brown dwarf that does not have enough mass to ignite hydrogen burning in the core. Previous microlensing surveys towards LMC conclude that MACHOs can contribute up to 20% of the mass of Galactic halo (Alcock *et al.* 2000). Alternatively MACHOs could also consist of primordial BHs that were built before Big Bang Nucleosynthesis (BBN) and do not enter the baryon budget afterwards. This implies that there is no limit on the amount of primordial BHs from BBN.

The second class of dark matter candidate is a non-baryonic particle beyond the standard model. It can be sub-classified into hot dark matter, which has relativistic speed and cold dark matter which moves

slower. The hot dark matter has too large energy and can hardly clump for the formation of structure in the early universe, thus is ruled out by the current cosmology model. The possible cold dark matter candidates are weak interaction massive particle (WIMP) or super-symmetry particles such as axion. However, none of them have been detected by the current experiments. A list of the dark matter candidates is shown in Table 1.1.

Table 1.1: Dark matter candidates

Massive compact halo object (MACHO)
Brown dwarf
White dwarf
Neutron star
Primordial black holes
Hot dark matter
Neutrino
Cold dark matter
Axion
WIMP - neutralino
WIMPZILLA
Soliton

The last and most well-known component of the cosmic pie are the baryons. Fukugita & Peebles (2004) constrained the mass budget of baryons with the results of different experiments (see Table 1.2). In their inventory, about 90% of the baryons are not well understood and could be hidden in the warm intergalactic plasma outside galaxies and clusters of galaxies.

Table 1.2: Baryon budget from Fukugita & Peebles (2004)

Main-sequence stars: spheroids and bulges	0.0015 ± 0.0004
Main-sequence stars: disks and irregulars	0.00055 ± 0.00014
White dwarfs	0.00036 ± 0.00008
Neutron stars	0.00005 ± 0.00002
Black holes	0.00007 ± 0.00002
Substellar objects	0.00014 ± 0.00007
H I + He I	0.00062 ± 0.00010
Molecular gas	0.00016 ± 0.00006
Intracluster plasma	0.0018 ± 0.0007
Total known	0.00525 ± 0.00083
Total baryons from BBN	0.045 ± 0.003

Regarding the baryonic and non-baryonic dark matter, an interesting question to ask is, what is the composition of the galactic halo. Since dark matter hardly emits light, the best way to detect dark matter would be gravitational lensing. In the past decades, numerous microlensing survey have been

conducted and search for MACHOs as dark matter candidates towards the Galactic bulge, Large and Small Magellanic Clouds and especially M31.

1.2 Searching for dark matter with microlensing

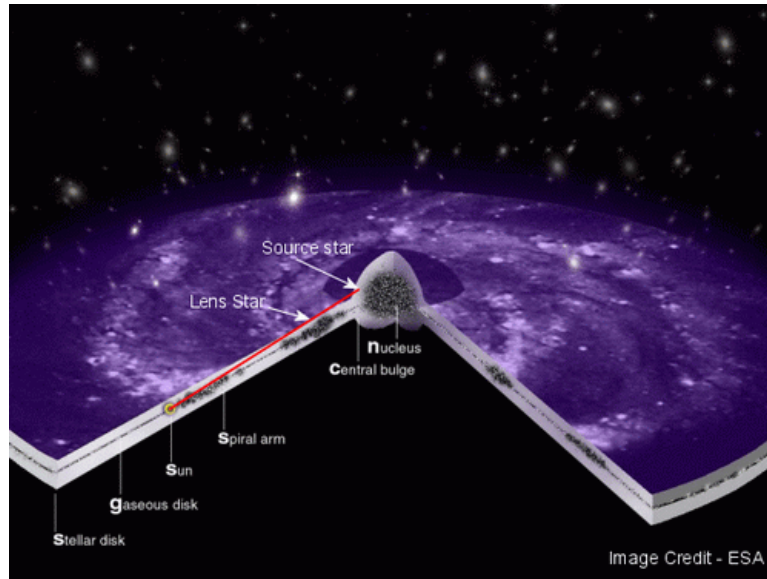


Figure 1.3: An illustration shows the general idea of microlensing search towards Galactic Bulge.

Although Einstein has already derived the equation for lensing by a point mass back to 1936 (the calculation has been done even prior then the publication of the general theory of relativity, see [Renn *et al.* \(1997\)](#)), he regarded the phenomenon as ‘no hope of observing’ ([Einstein, 1936](#)) due to the small chance to form such lens-source alignments along a line-of-sight. The gravitational lensing of a distant QSO was first observed by [Walsh *et al.* \(1979\)](#). A few years later, the giant arcs around galaxy clusters were discovered by [Lynds & Petrosian \(1986\)](#); [Soucail *et al.* \(1987\)](#) and were interpreted as strong lensing signature by [Paczynski \(1987\)](#). These discoveries all together demonstrated the feasibility of observing gravitational lensing. It is until the emergence of modern CCDs that led [Paczynski \(1986\)](#) to the proposal of using microlensing as an elegant way to probe massive compact halo object as dark matter. In his seminal paper, Paczynski calculated the probability of a microlensing event with amplification $A = 1.34$ at any time to be 1 out of 1 million stars. Thus it is possible to catch such events in crowded stellar fields. Motivated by the insight of Paczynski, numerous experiments were triggered to exhaustively monitor crowded fields such as Galactic Bulge, Magellanic Clouds, and M31. The very first events were detected in 1993 ([Alcock *et al.*, 1993](#); [Aubourg *et al.*, 1993](#); [Udalski *et al.*, 1993](#)).

M31 has been proposed as a target of microlensing by several authors ([Crofts, 1992](#); [Baillon *et al.*, 1993](#); [Jetzer, 1994](#)). M31 is suitable for a microlensing search because it is possible to cover the entire M31 halo with a few pointings (at least for present day, large mosaic cameras). One can probe various lines of sights and distinguish halo lensing (either from M31 or Milky Way) from self-lensing (lensing by disk and bulge stars within M31) in the inner part of M31. Self-lensing contamination is severe

in Magellanic Clouds and can dramatically change the interpretation of the MACHO content in the Milky Way halo (Alcock *et al.*, 2000; Tisserand *et al.*, 2007). Besides, observations of tidal streams in the halo of M31 show that M31 had a close encounter with M33 and has accreted material from M33 and cannibalized neighboring dwarf galaxies (Ibata *et al.*, 2001; McConnachie *et al.*, 2009). Thus it is possible that MACHOs (stellar remnants and brown dwarfs) from the tidal stream contribute to the total MACHO signal and place a lower limit also in the outskirts of M31.

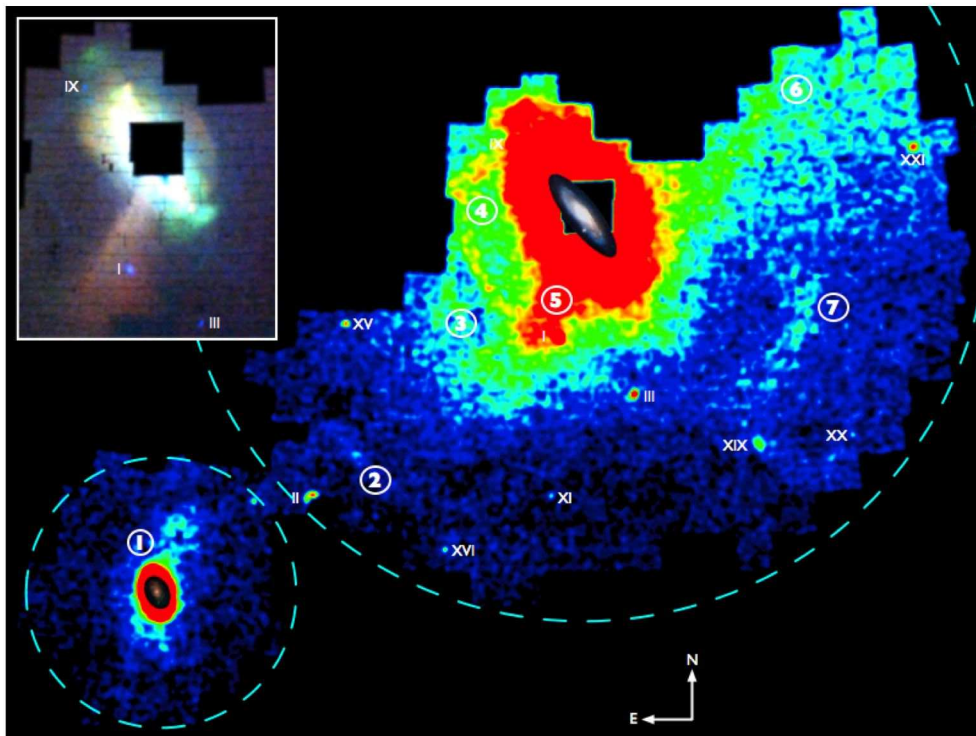


Figure 1.4: PAndAS survey. Adopted from McConnachie *et al.* (2009).

Microlensing events towards M31 are different from those in the Galactic bulge and Magellanic clouds because the stars can not be resolved in M31. Such crowded field microlensing is called pixel-lensing because many sources ($\gg 100$ stars with $M_R < 0$ mag in the center of M31, see Riffeser *et al.* (2006)) contribute to the flux of one pixel. In the pixel-lensing regime, the measurable parameters of the microlensing event differ from the classical regime. That is, one measures the full-width-half-maxima time scale (t_{FWHM}) and excess flux (ΔF) of the event instead of the canonical Einstein time scale and impact parameter (Gould, 1996). Thanks to the difference imaging algorithm (DIA) proposed by Alard & Lupton (1998), t_{FWHM} and ΔF can be quantified with very high precision.

1.3 Microlensing basics

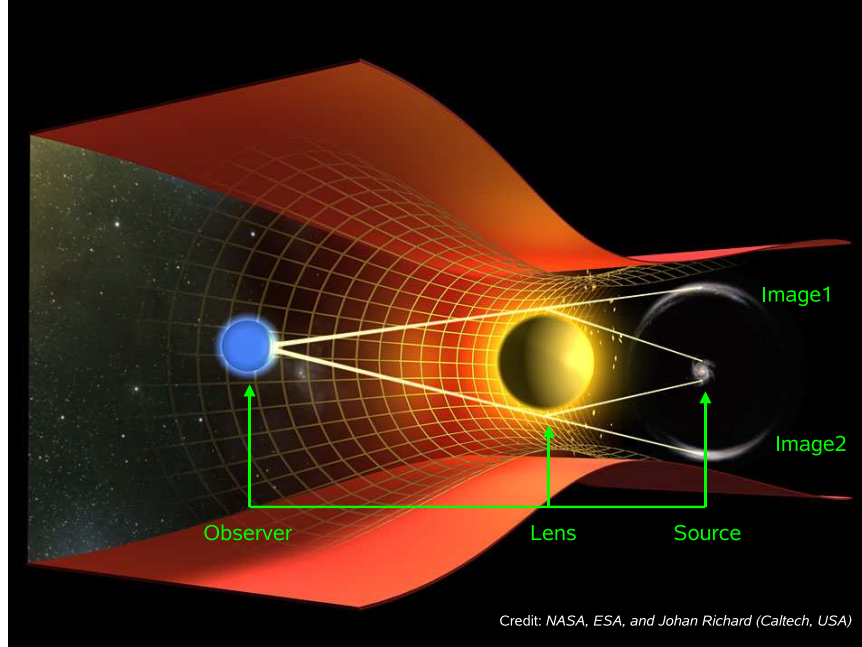


Figure 1.5: A schematic view of gravitational lensing. The space-time between the source and the observer is disturbed by the gravity of the lens. The observer will see the extended source split into two arc-like images. If the source is not extended, the observer will see two points instead.

The underlying physics of gravitational lensing is Einstein’s general theory of relativity. When a mass (*e.g.* brown dwarf, black hole) passes between the observer and the background source (*e.g.* star, quasar), the mass induces space-time curvature and thus serves as a ‘gravitational’ lens. The light rays from the background source are bent and, instead of observing the original source, the observer sees two separate distorted images (if the source is extended) projected onto the source plane (assuming a single, point-like mass, see Fig. 1.5). The position of the images on the source plane can be derived from the lens equation¹. Let us take a look at Fig. 1.6. In the triangle OIS, $\overline{IS} = \alpha D_{LS} = (\theta_I - \theta_S) D_{OS}$, where $D_{OS} = D_{OL} + D_{LS}$ is the distance between the observer and the background source², and the light bending angle

$$\alpha = \frac{4GM}{c^2 D_{OL} \theta_I} \quad (1.1)$$

can be calculated from Einstein’s general theory of relativity (Schneider *et al.*, 2006). Thus one can

¹ Here we assume the thin lens approximation is satisfied, where all the action of deflection is considered to take place at a single distance (Wambsganss, 1998), which requires: (1) The relative velocities of lens, source and observer are small compared to the velocity of light and (2) small Newtonian potential $|\Phi| \ll c^2$. These two assumptions are justified in all astronomical cases of interest.

² In order to derive the microlensing equations, angles are related to length scales using Euclidean geometry. These equations are still valid in an expanding universe if the distances are interpreted as angular diameter distances (Schneider *et al.*, 2006).

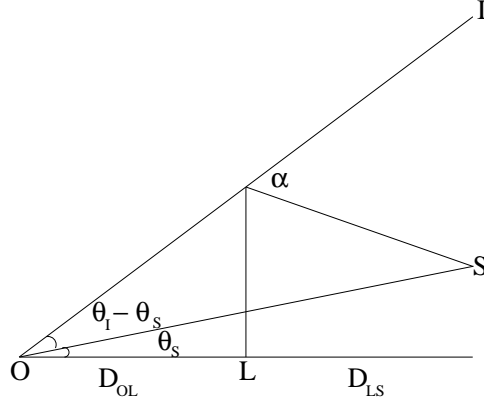


Figure 1.6: Configuration of microlensing.

derive the lens equation

$$\theta_I (\theta_I - \theta_S) = \frac{4GM}{c^2} \frac{D_{LS}}{D_{OL} D_{OS}} \equiv \theta_E^2. \quad (1.2)$$

When the observer, lens and source are so well aligned that the lens overlaps with the source in the line-of-sight direction, the two distorted images connect together and form a ring, the so called ‘Einstein ring’. The angular Einstein ring radius can be expressed as

$$\theta_E = \sqrt{\frac{4GM}{c^2} \left(\frac{1}{D_{OL}} - \frac{1}{D_{OS}} \right)} = 0.902 \text{mas} \left(\frac{M}{M_\odot} \right)^{1/2} \left(\frac{10 \text{ kpc}}{D_{OL}} \right)^{1/2} \left(1 - \frac{D_{OL}}{D_{OS}} \right)^{1/2} \quad (1.3)$$

in case of a point mass and a point source. Microlensing bears the name of ‘micro’ because such events were first observed towards distant quasars, and the size of the Einstein ring is in the scale of micro-arcsecond.

If we normalize the length scale to θ_E and define

$$u \equiv \theta_S / \theta_E, \quad (1.4)$$

the root of the lens equation (equation 1.2) provides us with the position of the distorted images,

$$u_{\pm} = (u \pm \sqrt{u^2 + 4})/2, \quad (1.5)$$

where $u_{\pm} = \theta_{I_{\pm}} / \theta_E$. Due to the conservation of surface brightness (Schneider *et al.*, 1992), the amplification of the background source is simply the ratio between the area of the images to the area of the source. So the amplification of the distorted images and the total amplification can be calculated by³

$$A_{\pm} = \left| \frac{u_{\pm}}{u} \frac{du_{\pm}}{du} \right|, \quad A = A_+ + A_- = \frac{u^2 + 2}{u\sqrt{u^2 + 4}} \underset{u \ll 1}{\approx} \frac{1}{u}, \quad (1.6)$$

and yet it is only a function of u . This is the beauty of microlensing because one can calculate the light curve merely by the relative lens and source position projected onto the sky.

³ This holds for a ‘small’ source of negligible extent and is often referred as point-source approximation (Schneider *et al.*, 2006).

If we assume the relative lens-source motion to be rectilinear, u can be decomposed into components parallel and perpendicular to the direction of the relative lens-source motion. u and A can thus be calculated as

$$A(t) = \frac{u(t)^2 + 2}{u(t)\sqrt{u(t)^2 + 4}}, \quad u(t) = \sqrt{\left(\frac{t-t_0}{t_E}\right)^2 + u_0^2}, \quad (1.7)$$

where t_0 and u_0 are the time and impact parameter at the closest-approach. t_E is the Einstein timescale, which is defined as the time required for the lens to traverse the Einstein radius

$$t_E = \frac{\theta_E}{\mu_{\text{rel}}} = 0.214 \text{yr} \left(\frac{M}{M_\odot}\right)^{1/2} \left(\frac{D_{\text{OL}}}{10 \text{kpc}}\right)^{1/2} \left(1 - \frac{D_{\text{OL}}}{D_{\text{OS}}}\right)^{1/2} \left(\frac{200 \text{km/s}}{V_{\text{rel}}}\right). \quad (1.8)$$

1.4 Breaking the microlensing degeneracy

Since the first discovery of microlensing events in 1993 (Alcock *et al.*, 1993; Aubourg *et al.*, 1993; Udalski *et al.*, 1993), thousands of events have been reported. However, the only parameter one can retrieve from the light curve is the event timescale t_E . The Einstein timescale is unfortunately a degenerated parameter consisted of the lens mass, lens distance, and the relative lens-source velocity μ_{rel} . Thus it is impossible to characterize the lens and the source of a single event through light curve measurement - if not provided with further information, and the properties of the lens can only be revealed through bulk statistic studies.

Gould (1992) points out that, in order to break the microlensing degeneracy, one requires the measurements of both the angular Einstein radius θ_E and the microlens parallax

$$\pi_E := \frac{AU}{\tilde{r}_E} \quad (1.9)$$

where \tilde{r}_E is the Einstein radius projected on the observer plane. The mass of the lens can be determined without ambiguity (Gould, 2000):

$$M = \frac{\theta_E}{\kappa \pi_E}, \quad \kappa := \frac{4GM}{c^2 AU} \approx 8.14 \text{mas } M_\odot^{-1}. \quad (1.10)$$

The microlens parallax can be derived from, for example, the Earth-orbital parallax caused by the orbital motion of Earth around the Sun. This will result in parabolic lens-source trajectory instead of the rectilinear motion during the time of closest-approach in the geocentric observation (see Fig. 1.7). The information of microlens parallax can be obtained by fitting the tiny asymmetry in the light curve. The Einstein radius can also be obtained by several methods. The first one is applicable when both the lens and the source are stellar objects, that is, to take a snapshot with very high precision astrometry long after the event. From the time span Δt and the separation between the lens and the source $\Delta \theta$, one can easily calculate the relative lens-source velocity μ_{rel} . Combined with the Einstein timescale t_E obtained from the light curve, one can thus derive the Einstein radius by $\theta_E = t_E \times \mu_{\text{rel}}$. So far there are only two such cases, MACHO-LMC-5 (Alcock *et al.*, 2001) and MACHO-95-BLG-37 (Kozłowski *et al.*, 2007), because this method requires the lens-source relative velocity to be very large and both the lens and the source must be luminous enough for detection (see Fig. 1.8). For the case of MACHO-LMC-5, the parallax effects can be inferred with tiny asymmetry in the light curve,

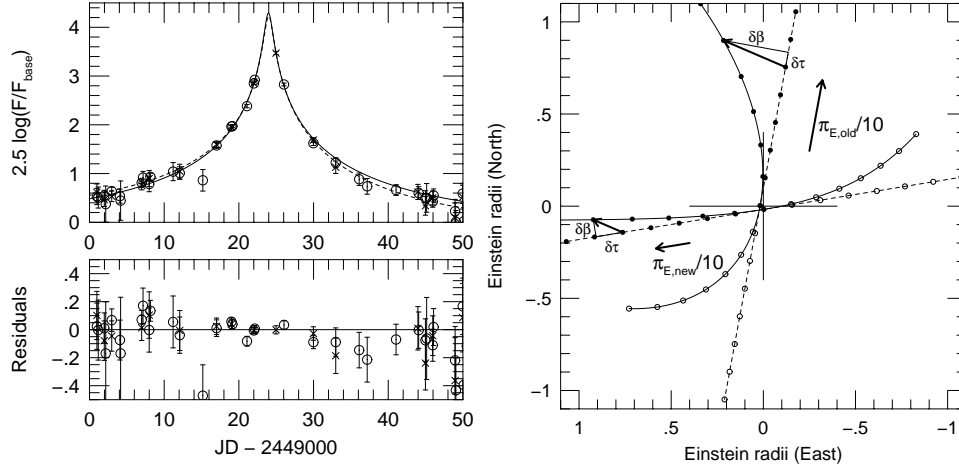


Figure 1.7: Parallax effects by Earth-orbital motion in the MACHO event MACHO-LMC-5. Left panel: light curve for MACHO red (circles) and blue (crosses) filters. The dashed (solid) line indicates the best-fit model with (without) parallax effects. Right panel: the trajectory of lens-source relative motion with (solid line) and without (dashed line) parallax effects, projected onto the sky in the geocentric frame. Open (filled) circles are for $t < t_0$ ($t \geq t_0$). The time difference between two consecutive circles are 5 days. $\pi_{E,\text{old}}$ is the best-fit microlens parallax from [Alcock *et al.* \(1993\)](#) under the context of heliocentric frame. $\pi_{E,\text{new}}$ is the new solution found by [Gould \(2004\)](#) in the geocentric scheme. Adapted from [Gould \(2004\)](#)

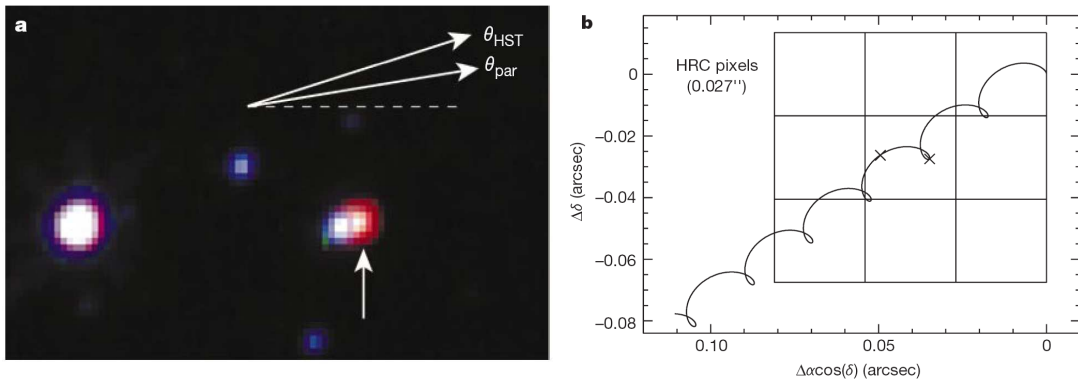


Figure 1.8: *HST* observation of MACHO-LMC-5. Left panel: Three-color image from the WFPC V-, R- and I-band observations. The source is the blue star close to the center, with the lens to be the red star indicated by the arrow. Right panel: The lens motion projected onto the sky with the best-fitted microlensing parallax. Adapted from [Alcock *et al.* \(2001\)](#).

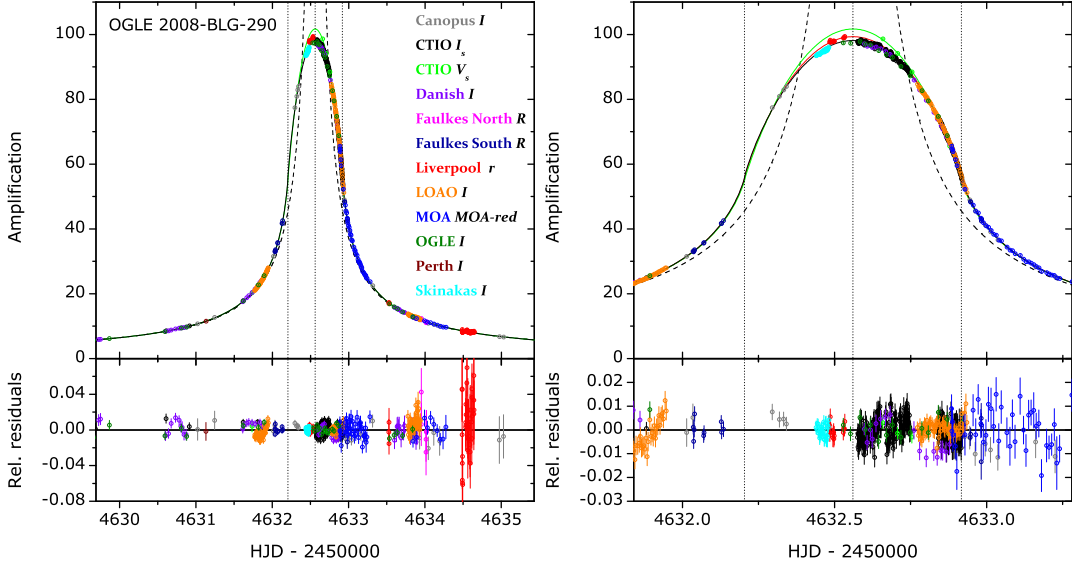


Figure 1.9: Observations of OGLE-2008-BLG-290 overlaid with models of the best-fit finite-source and limb-darkening effects in I -band (black curve), R -band (red curve) and V -band (green curve). Adapted from Fouqué *et al.* (2010).

which sheds light on the properties of the lens, such as its mass and location (Alcock *et al.*, 2001; Gould, 2004; Drake *et al.*, 2004; Gould *et al.*, 2004).

The second method is through the finite-source (FS) effects (e.g. Albrow *et al.*, 2000). When the lens transits the surface of the source during the course of microlensing, the point-source approximation in equation (1.6) is no longer valid. One has to integrate equation (1.6) over the surface of the source by

$$A_{\text{FS}}(u|\rho_s) = \frac{\int_0^{2\pi} \int_0^{\rho_s} A \left[\sqrt{(u + r \cos \theta)^2 + (r \sin \theta)^2} \right] r dr d\theta}{\int_0^{2\pi} \int_0^{\rho_s} r dr d\theta}, \quad (1.11)$$

where $\rho_s = \theta_*/\theta_E$ is the angular source radius in units of θ_E . When the lens is perfectly aligned with the source ($u = 0$), the amplification is reduced to $\sqrt{\rho_s^2 + 4}/\rho_s$, in comparison with the infinite amplification in the point-source regime. One thus can retrieve the source size in units of the Einstein radius by fitting the light curve with one more parameter (the source size ρ_s). Furthermore, if one has multi-band observations, it is also possible to fit the limb-darkening parameters (see Fig. 1.9) in different bandpasses using, for example, the linear limb-darkening law

$$S(r/\rho_s) = \bar{S} [1 - \Gamma_S (1 - 1.5 \sqrt{1 - r^2/\rho_s^2})], \quad (1.12)$$

where r is the distance to the source center. Γ_S is the wavelength-dependent limb-darkening coefficient. \bar{S} is the mean surface brightness of the source. Equation (1.11) then becomes

$$A_{\text{FS}}(u|\rho_s) = \frac{1}{\pi \rho_s^2 \bar{S}} \int_0^{2\pi} \int_0^{\rho_s} A(u) S(r/\rho_s) r dr d\theta. \quad (1.13)$$

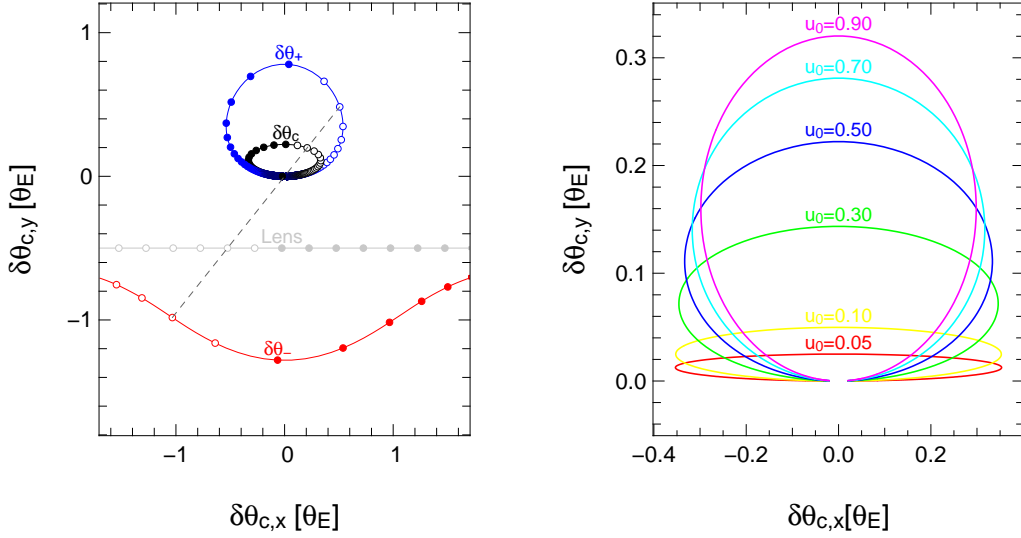


Figure 1.10: Centroid shifts for PSPL. Left panel: the trajectory of the plus-image (in blue), minus-image (in red), centroid of these two images (in black) and the lens (in grey) relative to the source center assuming $t_0 = 0$, $t_E = 10$ d and $u_0 = 0.5 \theta_E$. Right panel: centroid displacement for different values of u_0 .

Finite-source microlensing thus serves as a powerful method to probe the surface-brightness profile of distant stars. As long as one gets the source size in terms of the Einstein radius, one can thus infer the Einstein radius by comparing ρ_s to the actual source size derived from the empirical surface brightness – color relation. For example, [Kervella *et al.* \(2004\)](#) proposed the following relation for angular diameter for either dwarf stars with spectral types between A0 and M2 or subgiants in the range of A0 to K0:

$$\log(2\theta_*) = 0.0755(V - K) + 0.5170 - 0.2K, \quad (1.14)$$

where V is in Johnson system and K with $\lambda = 2.0 - 2.4 \mu\text{m}$.

However, the typical value of θ_E is in the order of 0.5 mas while the θ_* is $\sim 0.5 \mu\text{as}$, so one will need events with $A > 1000$. The chance for the lens to transit the source is very slim and only a handful of such events have been observed so far.

The third method is through astrometric microlensing ([Hosokawa *et al.*, 1993](#); [Hog *et al.*, 1995](#); [Witt & Mao, 1994](#); [Miyamoto & Yoshii, 1995](#)). The idea is that, although the state-of-art observatories are not able to resolved the two microlensed images, it is possible to measure the astrometric centroid of the plus- and minus-image relative to the source,

$$\delta\theta_c = \frac{A_+\theta_+ + A_-\theta_-}{A_+ + A_-} - u = \frac{u}{u^2 + 2} \quad (1.15)$$

with maximum deviation $\sim 0.35 \theta_E$ occurs at $u = \sqrt{2}$. It has been shown ([Walker, 1995](#)) that the astrometric centroid relative to the source will trace out an ellipse, and the size of of the ellipse gives the scale of the Einstein radius (see Fig. 1.10). This implies that one can determine the Einstein radius for virtually every single event if the astrometric signal is large enough to be observed. For

example, a source in the Galactic bulge lensed by an object of $0.5 M_{\odot}$ on the half way has $\theta_E \sim 0.7$ mas, which is an order of 2 larger than the accuracy of up-coming *Space Interferometry Mission* (*SIM*, Allen *et al.*, 1997). However, the astrometric signal for self-lensing events towards Magellanic Clouds and M31 is beyond the detection limit of *SIM*.

1.5 Microlensing in the pixel-lensing regime

When the sources of the microlensing events are in crowded fields or can not be resolved at all (such that many stars contribute to one pixel of the detector), it is referred to the pixel-lensing regime. In the pixel-lensing regime the transient event can be detected with the difference imaging technique advocated by Alard & Lupton (1998). The idea is to convolve the PSF of the frame of interest and the reference frame to a common basis so that varying objects can be revealed after the subtraction of the reference frame (see Fig. 1.11). In the pixel-lensing regime, the observables are the full-width-

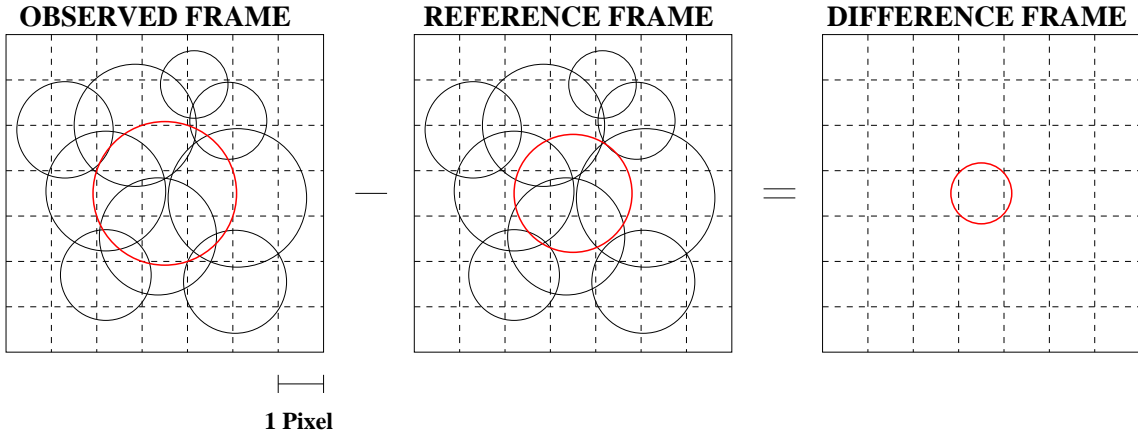


Figure 1.11: A schematic view of the difference imaging technique in crowded field. The reference frame is constructed by good seeing images. To perfectly subtracted the background sources, the frame of interest and the reference frame are convolved to a common PSF basis. Image credit: Arno Riffeser.

half-maximum timescale of the event (t_{FWHM}) and the flux excess above the background (Δ_F). These two quantities are related to the canonical microlensing parameters as following: The event timescale t_{FWHM} of a light curve is defined by

$$A\left(\frac{t_{\text{FWHM}}}{2}\right) - 1 := \frac{A_0 - 1}{2} \quad (1.16)$$

where A_0 is the maximum amplification of the light curve. After some iteration, t_{FWHM} can be expressed as a combination of the Einstein timescale and a function of A_0 ,

$$t_{\text{FWHM}} = t_E Y(A_0) \quad , \quad (1.17)$$

where

$$Y(A_0) = 2\sqrt{u\left(\frac{A_0+1}{2}\right)^2 - u(A_0)^2} = \sqrt{8} \frac{[(A_0+1)^{3/2} - A_0(A_0+3)^{1/2}]^{1/2}}{[(A_0-1)(A_0+1)(A_0+3)]^{1/4}} \quad . \quad (1.18)$$

u is the lens-source separation projected onto the sky as introduced before in equation (1.4) and can be expressed as a function of A from equation (1.6). Since the pixel-lensing events are often only detectable if $A_0 \gg 1$, Gould (1996) derived an approximation form of equation (1.7) assuming high magnification:

$$\Delta_F^{\text{Gould}}(t) \approx F_{\text{eff}} \left[\frac{(t-t_0)^2}{t_{\text{eff}}^2} + 1 \right]^{-1/2}, \quad (1.19)$$

where $F_{\text{eff}} := \frac{F_0}{u_0}$ and $t_{\text{eff}} := u_0 t_E$. While equation 1.19 is useful in filtering out high magnification events, it fails for the moderately amplified events. Riffeser *et al.* (2006) thus suggested to use

$$\Delta_F(t) \approx F_{\text{eff}} \left[\frac{12(t-t_0)^2}{t_{\text{FWHM}}^2} + 1 \right]^{-1/2}, \quad (1.20)$$

which provides a good description for both high and moderate magnification.

If the events are monitored with two filters⁴, the color \mathcal{C} of the source can be derived which sheds light on the identity of the source. These observables are essential ingredients to predict the microlensing event rate towards a given line-of-sight. A detailed description of how the observables are related to the microlensing event rate is shown in Chapter 4.

⁴ This is often the case to confirm the events from their achromaticity.

Chapter 2

Finite Source Effects in Microlensing: A Precise, Easy to Implement, Fast and Numerical Stable Formalism

This chapter has been published in [Lee *et al.* \(2009\)](#).

2.1 Abstract

The goal of this paper is to provide a numerically fast and stable description for the microlensing amplification of an extended source (either uniform or limb-darkened) that holds in any amplification regime. We show that our method of evaluating the amplification can be implemented into a light-curve fitting routine using the Levenberg-Marquardt algorithm. We compare the accuracy and computation times to previous methods that either work in the high-amplification regime only, or require special treatments due to the singularity of elliptic integrals.

In addition, we also provide the equations including finite lens effects in microlensing light curves. We apply our methods to the MACHO-1995-BLG-30 and the OGLE-2003-BLG-262 events and obtain results consistent to former studies. We derive an upper limit for the OGLE-2003-BLG-262 event lens size.

We conclude that our method allows to simultaneously search for point-source and finite-source microlensing events in future large area microlensing surveys in a fast manner.

2.2 Introduction

In large area microlensing surveys, one has to search for microlensing signatures in billions of variable sources. This is straightforward to do and computationally inexpensive in the point-source approximation. One either fits a Paczyński light curve ([Paczynski, 1986](#)), or, if appropriate, the Gould high-amplification approximation for point sources ([Gould, 1996](#)). One major disadvantage of these point-source light curves is the infinite amplification for a lens exactly in front of the point source.

[Gould \(1994\)](#) extended Paczyński's light curve to finite sources which also avoids infinite amplifications. His equation describes the amplification as the two-dimensional integration of the Paczyński amplification over the circular source, assumed to have constant surface brightness.

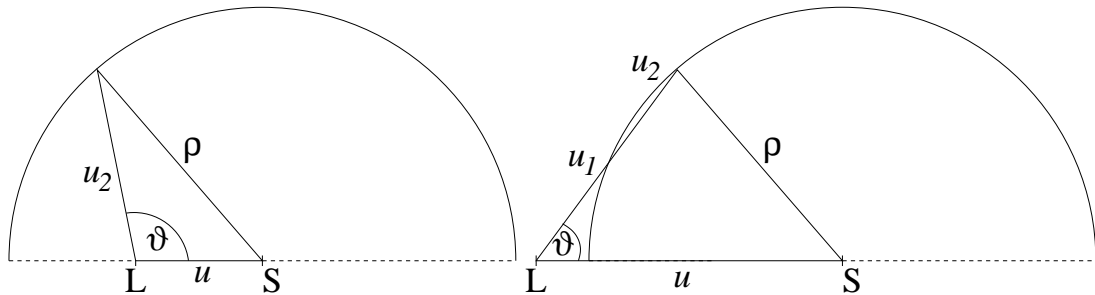


Figure 2.1: Geometric definitions. Left: source is overlapping the lens center. Right: lens is outside the source radius.

Using the limiting form of Paczynski light curve under high amplification, Gould is able to factor out the two-dimensional integral into point source amplification times a much simpler integral. Meanwhile, [Witt & Mao \(1994\)](#) obtained the finite source amplification directly from the lens equation by comparing the area of the source and its lensed images. However, one needs to take care of the singular points for the elliptic integrals of the first and the third kind when using their formula.

In this paper we adopt the same strategy as [Gould \(1994\)](#), because in this way more general surface-brightness profiles for the sources (e.g. limb-darkened ones) can be taken into account straightforwardly. For the cases of a uniform disk we will also compare our results with [Witt & Mao \(1994\)](#).

The technical issue of the integration in the Gould extended source formalism can be carried out in several different ways. The two straightforward ones are to use polar coordinates and to choose the coordinate center either (1) at the source center or (2) at the lens center. [Gould \(1994\)](#) took the first choice. [Riffeser et al. \(2006\)](#) have shown for the very special case where the lens is positioned along the line of sight to the source that the integration can be solved very easily if the second option is chosen.

This leads us to choose the lens center as the coordinate center in general to benefit from the more simple integrand. We will show (in Section 2.3) that in this way the amplification of a uniform circular source is reduced to a one-dimensional integral and can be computed numerically fast and stable by using the composite Simpson’s rule. A limb-darkened source is treated in Section 2.4. The two-dimensional integral can be solved numerically again in a fast and stable fashion, and light-curve fits for limb-darkened profiles can be obtained with the Levenberg-Marquardt algorithm (see [Press, 2002](#)) with less than 100 steps. We also allow for finite lens sizes in Section 2.5. As a test example, we apply our fitting methods to a MACHO ([Alcock et al., 1992](#)) event and an OGLE (The Optical Gravitational Lensing Experiment; [Udalski et al., 1992](#)) event in Section 2.6. We conclude in Section 2.7.

2.3 The finite-source microlensing equation

We first introduce our notation. Let R_E be the Einstein radius of a point mass lens, and b be the impact parameter of a point source. Then one can write the amplification of the point source by the point mass lens as a function of the dimensionless impact parameter $u := b/R_E \equiv \theta/\theta_E$ as

$$A_{\text{ps}}(u) = \frac{u^2 + 2}{u\sqrt{u^2 + 4}} \tag{2.1}$$

(Paczynski, 1986).

If the source is extended one can obtain the lensed flux and the total amplification by integrating $A(u)$ over the source area, weighted by the surface-brightness profile of the source. We now derive the amplification for a circular source¹ with radius ρ_s ($\rho_s \equiv \frac{R_* D_{OL}}{R_E D_{OS}}$ is the projected source size in units of the Einstein radius R_E and R_* is the physical source size). The situation is sketched in Figure 2.1. There are two cases: either the center of the lens L (projected along the line of sight) is within the extended source centered at S (the left side of Figure 2.1) or the lens is outside the extended source (the right side of Figure 2.1), i.e., either $u \leq \rho_s$ or $u > \rho_s$. One obtains the amplification of the extended uniform source by integrating the point-source amplification over the source area $\mathcal{A}_{\text{source}}$:

$$A^*(u; \rho_s) = \frac{\int_{\mathcal{A}_{\text{source}}} A_{\text{ps}} d\mathcal{A}}{\int_{\mathcal{A}_{\text{source}}} d\mathcal{A}} = \frac{1}{\pi \rho_s^2} \int_{\mathcal{A}_{\text{source}}} A_{\text{ps}} d\mathcal{A}. \quad (2.2)$$

Using polar coordinates centered on the lens, one can write

$$A^*(u; \rho_s) = \frac{2}{\pi \rho_s^2} \int_0^{\pi} \int_{u_1(\vartheta)}^{u_2(\vartheta)} A_{\text{ps}}(\tilde{u}) \tilde{u} d\tilde{u} d\vartheta. \quad (2.3)$$

The integration boundaries u_1 and u_2 are

$$u_1(\vartheta) = \begin{cases} 0 & , u \leq \rho_s \\ u \cos \vartheta - \sqrt{\rho_s^2 - u^2 \sin^2 \vartheta} & , u > \rho_s \wedge \vartheta \leq \arcsin(\rho_s/u) \\ 0 & , u > \rho_s \wedge \vartheta > \arcsin(\rho_s/u) \end{cases}, \quad (2.4)$$

$$u_2(\vartheta) = \begin{cases} u \cos \vartheta + \sqrt{\rho_s^2 - u^2 \sin^2 \vartheta} & , u \leq \rho_s \\ u \cos \vartheta + \sqrt{\rho_s^2 - u^2 \sin^2 \vartheta} & , u > \rho_s \wedge \vartheta \leq \arcsin(\rho_s/u) \\ 0 & , u > \rho_s \wedge \vartheta > \arcsin(\rho_s/u) \end{cases}, \quad (2.5)$$

and so the amplification becomes

$$A^*(u; \rho_s) = \frac{1}{\pi \rho_s^2} \int_0^{\pi} \left[u_2(\vartheta) \sqrt{u_2(\vartheta)^2 + 4} - u_1(\vartheta) \sqrt{u_1(\vartheta)^2 + 4} \right] d\vartheta, \quad (2.6)$$

which can be approximated numerically using the composite Simpson's rule with n (an even number) grids:

$$A^*(u; \rho_s) \approx \begin{cases} \frac{1}{\pi \rho_s^2} \frac{\pi}{2n} \left[\frac{(u+\rho_s) \sqrt{(u+\rho_s)^2 + 4} - (u-\rho_s) \sqrt{(u-\rho_s)^2 + 4}}{3} + \frac{2}{3} \sum_{k=1}^{n-1} f\left(\frac{2k\pi}{2n}\right) + \frac{4}{3} \sum_{k=1}^n f\left(\frac{(2k-1)\pi}{2n}\right) \right] & , u \leq \rho_s \\ \frac{1}{\pi \rho_s^2} \frac{\arcsin(\rho_s/u)}{n} \left[\frac{(u+\rho_s) \sqrt{(u+\rho_s)^2 + 4} - (u-\rho_s) \sqrt{(u-\rho_s)^2 + 4}}{3} + \frac{2}{3} \sum_{k=1}^{n/2-1} f\left(\frac{2k \arcsin(\rho_s/u)}{n}\right) + \frac{4}{3} \sum_{k=1}^{n/2} f\left(\frac{(2k-1) \arcsin(\rho_s/u)}{n}\right) \right] & , u > \rho_s \end{cases}, \quad (2.7)$$

¹ The reader is referred to Heyrovsky & Loeb (1997) for a more general case of elliptical source.

where $f(\vartheta) = [u_2(\vartheta)\sqrt{u_2(\vartheta)^2 + 4} - u_1(\vartheta)\sqrt{u_1(\vartheta)^2 + 4}]$. The upper limit of ϑ changes from $\frac{\pi}{2}$ to π when the lens crosses the edge of the source from outside to inside, thus we set a grid of $2n$ for $u \leq \rho_s$ in order to have the same step size on both sides.

Gould (1994) argued that the finite-source effects are prominent only when the lens is very close to the source center ($u \ll 1$), and thus one can approximate Equation (2.1) by

$$A_{\text{PS}}(u) = \frac{u^2+2}{u\sqrt{u^2+4}} \approx u^{-1} \quad , u \ll 1 \quad , \quad (2.8)$$

and the finite-source light curve can be obtained by solving elliptic integrals (see also Yoo *et al.*, 2004; Cassan *et al.*, 2006)

$$A_{\text{Gould}}^*(u; \rho_s) \simeq A_{\text{PS}}(u) \frac{4u}{\pi\rho_s} E\left(\vartheta_{\text{max}}, \frac{u}{\rho_s}\right) \quad , \quad (2.9)$$

where $E(\phi, k)$ is the elliptic integral of the second kind and ϑ_{max} is defined as

$$\vartheta_{\text{max}} = \begin{cases} \frac{\pi}{2} & , u \leq \rho_s \\ \arcsin(\rho_s/u) & , u > \rho_s \end{cases} \quad . \quad (2.10)$$

We now compare our method for $A^*(u; \rho_s)$ with previous ones, i.e. with Paczynski (1986), Gould (1994) and Witt & Mao (1994), and illustrate these comparisons in Figures 2.2 and 2.3.

Equation (2.9) and (2.10) allow a fast computation of finite-source light curves in the Gould approximation, which however is accurate only for a high-amplification event. This is shown in Figure 2.2, where for high amplifications (right panel) the Gould finite-source approximation (*gray*) is very close to the Witt & Mao (1994) light curve (displayed in *solid black*), but fairly off when the lens transits the source for low amplifications (left panel).

Our formalism from Equation (2.6) and that of Witt & Mao (1994) both provide the exact light curves for uniform extended sources. In the Witt & Mao formalism one has to evaluate an elliptic integral which shows singularity when the impact parameter u is similar to the source size ρ_s . Witt & Mao therefore derived a separate solution for the case of $u = \rho_s$. This method is difficult to implement into numerical fitting routines in general, and particular cumbersome for those fast numerical fitting routines, where the partial derivatives have to be provided.

We therefore suggest to start from our exact formalism given in Equation (2.6) and estimate values for the integral using Equation (2.7) with $n = 10$. The comparison with results from higher values for $n = 500$ or the comparison with the Witt & Mao (1994) formalism – see the *gray* and *dash-dotted curves* in Figure 2.3 – shows that Equation (2.7) (with $n = 10$) provides a precise numerical estimate for the integral already. Another advantage of our formalism is that one can obtain the derivatives of Equation (2.6) with respect to source radius ρ_s and u in a straightforward manner (see Appendix A). This enables us to use fitting routines as, e.g., the Levenberg-Marquardt algorithm (see Press, 2002) which converge in this case in less than 100 iterations.

The approximation by Gould (1994) with $A_{\text{PS}}(u)$ evaluated according to Equation (2.1) is actually valid for all u provided that $\rho_s \ll 1$, so it deviates from Equation (2.6) for larger source size. In fact, more than 80% (2548 out of 3153) of the microlensing events detected from the OGLE experiment²

² <http://ogle.astrouw.edu.pl/ogle3/ews/ews.html>

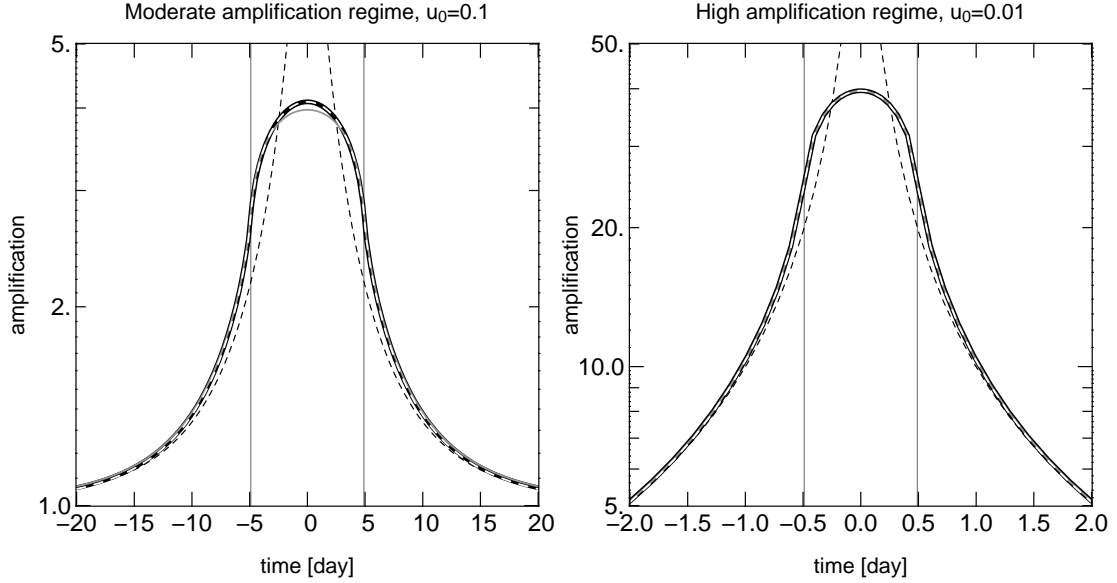


Figure 2.2: Comparison of finite-source light-curve approximations. Left: moderate-amplification regime with $t_E = 10$, $u_0 = 0.1$ and $\rho_s = 0.5$. Right: high-amplification regime with $t_E = 10$, $u_0 = 0.01$ and $\rho_s = 0.05$. In *dashed black* the Paczyński light curve for a point source, in *solid black* Witt & Mao light curve, in *gray* the approximation derived by Gould (1994) and in *dashed white* Equation (2.7) with $n = 10$. The vertical lines indicate the time when $u = \rho_s$. Our formula is as good as Gould (1994) in high-amplification regime and is better in the moderate-amplification regime.

(Udalski, 2003) have maximum amplification < 10 (see Figure 2.4). This highlights the necessity of a fast fitting routine for the moderate-amplification regime. We then compare the light-curve computation time of Equation (2.7) to Gould’s formalism (see Figure 2.5). With $n = 10$, Equation (2.7) is about 38% faster than Gould’s formalism when $u \leq \rho_s$ and is $> 55\%$ faster when $u > \rho_s$. Therefore, our $n = 10$ approximation turns out to be a practical fast fitting routine for both moderate- and high-amplification regimes.

2.4 Finite source with limb darkening

The next step towards a more precise microlensing light curve for extended sources is to account for limb darkening. Since the darkening is increasing towards the edges of the source, the limb darkening brings finite-source light curves closer to the Paczyński light curve which can be considered as the most extreme limb-darkening model with a delta function.

We use the one-parameter linear limb-darkening profile from Yoo *et al.* (2004) for the surface brightness of the source,

$$S(r/R_*, \Gamma) = \bar{S} \left[1 - \Gamma \left(1 - \frac{3}{2} \sqrt{1 - \left(\frac{r}{R_*} \right)^2} \right) \right], \quad (2.11)$$

where r is the distance to the source center.

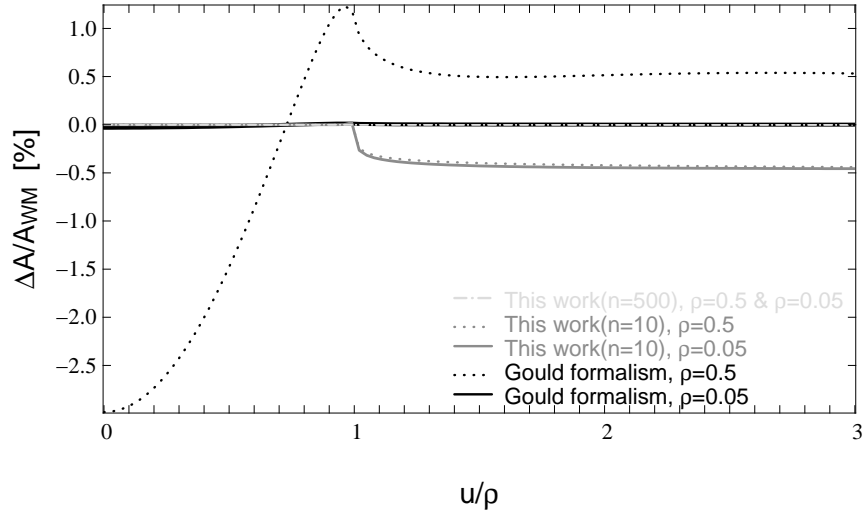


Figure 2.3: Percentage deviation in amplification compared to Witt & Mao formalism (A_{WM}). The expression of Gould (1994) is valid for small source (solid black) but shows deviation $> 2.5\%$ for larger source (dotted black). Equation (2.7) with $n = 10$ shows a smaller deviation ($< 0.5\%$). Equation (2.7) with $n = 500$ for both source sizes are well overlapped with each other, so we show here only $\rho_s = 0.05$.

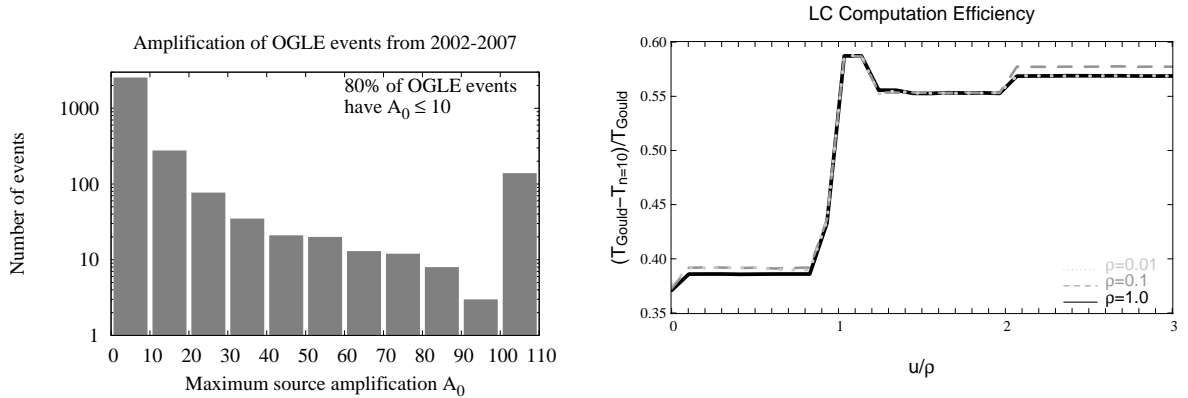


Figure 2.4: Maximum amplification of microlensing events detected by the OGLE experiment from 2002 to 2007. Most of the events ($> 80\%$) have maximum amplification < 10 . Events with maximum amplification > 100 , which are categorized into interval 100-110 in this plot, are relatively rare ($< 4.4\%$).

Figure 2.5: Light-curve computation efficiency. We compare light-curve computation time of Equation (2.7) with $n = 10$ to that of Gould's formalism for various source radii ($\rho_s = 0.01, 0.1,$ and 1). The computation time for our approximation is comparable to the Gould formalism; it is about 38% faster when $u < \rho_s$ and is $> 55\%$ faster when $u > \rho_s$.

Γ is the limb-darkening coefficient, and depends on the wavelength range used for the observations.

\bar{S} is the mean surface brightness of the source and defined as

$$\int_0^{2\pi} \int_0^{R_*} S(\tilde{r}/R_*, \Gamma) \tilde{r} d\tilde{r} d\vartheta = \pi R_*^2 \bar{S}. \quad (2.12)$$

We implemented the limb-darkening effects in our finite-source light curve as follows:

$$\begin{aligned} A_{\text{LD}}^*(u; \rho_s) &= \frac{2}{\pi \rho_s^2 \bar{S}} \int_0^{\pi} \int_{u_1(\vartheta)}^{u_2(\vartheta)} A_{\text{PS}}(\tilde{u}) S(r/R_*, \Gamma) \tilde{u} d\tilde{u} d\vartheta \\ &= \frac{2}{\pi \rho_s^2} \int_0^{\pi} \int_{u_1(\vartheta)}^{u_2(\vartheta)} \frac{\tilde{u}^2 + 2}{\sqrt{\tilde{u}^2 + 4}} \left[1 - \Gamma \left(1 - \frac{3}{2} \sqrt{1 - \frac{\tilde{u}^2 - 2\tilde{u}\tilde{u} \cos \vartheta + \tilde{u}^2}{\rho_s^2}} \right) \right] d\tilde{u} d\vartheta. \end{aligned} \quad (2.13)$$

Equation (2.13) is still a double integral over \tilde{u} and ϑ . But even here the divergent part cancels, and the function is numerically stable and can be evaluated using a small grid. The limb-darkening effects under moderate-amplification regime is shown in Figure 2.6.

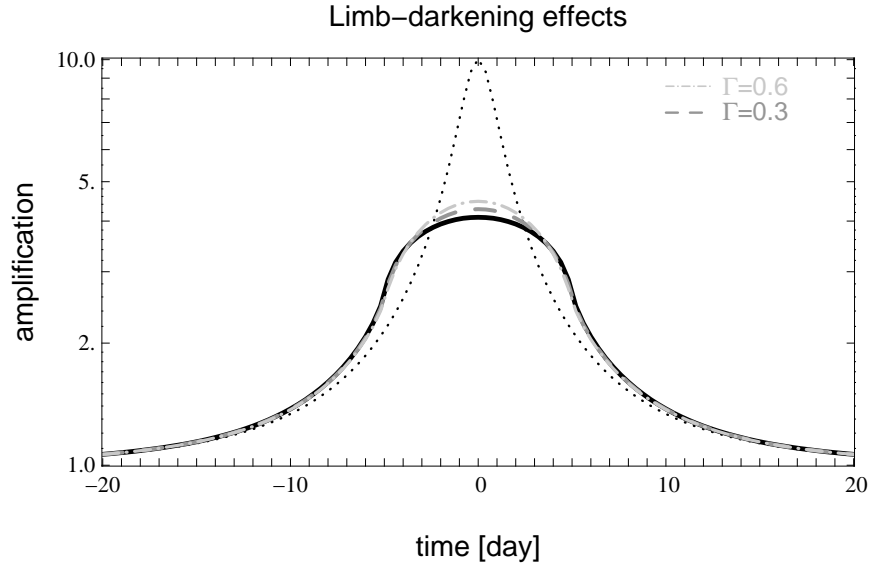


Figure 2.6: Limb-darkening effects on the finite-source light curve in the moderate-amplification regime. In *dotted black* we show the Paczyński light curve for a point source with $t_E = 10$ and $u_0 = 0.1$. In *solid black*, we show the finite-source light curve for a uniform source with a projected source size of $\rho_s = 0.5$. In *dashed line* and *dash-dotted line*, we plot the limb-darkened finite-source light curves with $\Gamma = 0.3$ and 0.6 . Increasing Γ enhances the limb-darkening effects thus brings the finite-source light curve closer to Paczyński's formalism.

2.5 Finite-source equation with finite lens

Given a finite-size lens, one can always find a time interval when the lens obscures the inner (and the outer, depending on the lens size) lensed image in the early rising stage and in the final declining stage of the light curve. In the following, we investigate how large this effect is depending on the lens size.

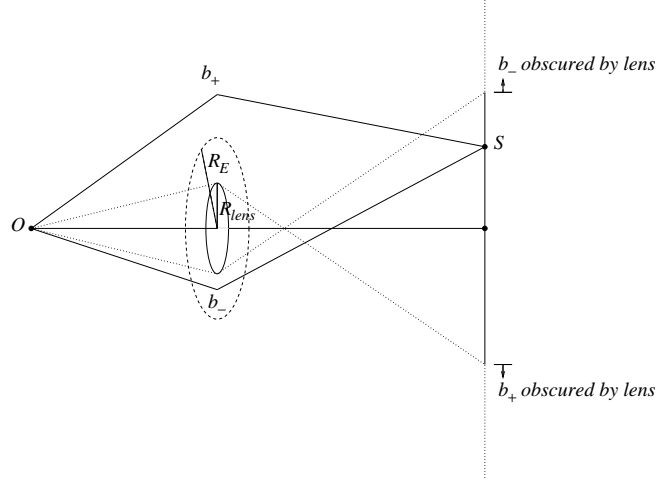


Figure 2.7: Image obscuration by a finite lens with radius $R_{lens} = 0.5R_E$.

Agol (2002) derived the lens-modified amplification by calculating how much area is unobscured by the lens in the image plane. One has to solve for the image position by inverting the lens equation and one has to evaluate the image area from the image boundary using Stokes' theorem. Depending on the source and lens radii, there are 7 different cases for the inner image and 6 cases for the outer image to be considered if one follows the derivation of Agol.

Here we show that the finite lens amplification of a finite source again can be much more easily evaluated if one uses the polar coordinates \tilde{u} and ϑ again. First, we consider a lens with physical radius R_{lens} transiting the surface of the source. The light emitted at a given point from the source follows the lens equation

$$\frac{b}{R_E} = \frac{b_{\pm}}{R_E} - \frac{R_E}{b_{\pm}}, \quad (2.14)$$

which gives the position of the two images in the lens plane (recall $u := \frac{b}{R_E}$)

$$\frac{b_{\pm}}{R_E} = \frac{u \pm \sqrt{u^2 + 4}}{2} \quad (2.15)$$

with amplifications

$$A_{\pm}(u) = \frac{u^2 + 2}{2u\sqrt{u^2 + 4}} \pm \frac{1}{2} \quad (2.16)$$

Here, $\frac{b_+}{R_E}$ denotes the outer image, and $\frac{b_-}{R_E}$ denotes the inner image in units of the Einstein radius. The sum of $A_+(u)$ and $A_-(u)$ gives the Paczyński light curve.

An image is unobscured if $-\frac{b_-}{R_E} > \rho_{lens}$ or $\frac{b_+}{R_E} > \rho_{lens}$ holds, where $\rho_{lens} \equiv \frac{R_{lens}}{R_E}$ is the lens radius in units of the Einstein radius. Following this criterion and Figure 2.7, there exists an upper limit for $\frac{b_-}{R_E} < -\rho_{lens}$ and a lower limit for $\frac{b_+}{R_E} > \rho_{lens}$ to be unobscured by the lens. Therefore, we only need to

consider these two limitations when integrating the amplification in Equation (2.3):

$$\begin{aligned}
A_{\text{FL}}^*(u; \rho_s) &= \frac{2}{\pi \rho_s^2} \int_0^\pi \int_{u_1(\vartheta)}^{u_2(\vartheta)} \left[A_+(\tilde{u}) \Theta \left(\frac{b_+}{R_E} - \rho_{\text{lens}} \right) + A_-(\tilde{u}) \Theta \left(-\frac{b_-}{R_E} - \rho_{\text{lens}} \right) \right] \tilde{u} d\tilde{u} d\vartheta \\
&= \frac{1}{\pi \rho_s^2} \int_0^\pi \left[\left(\frac{\tilde{u}}{2} \sqrt{\tilde{u}^2 + 4} + \frac{\tilde{u}^2}{2} \right) \Big|_{\max[u_1(\vartheta), \rho_{\text{lens}} - \frac{1}{\rho_{\text{lens}}]}]}^{u_2(\vartheta)} + \left(\frac{\tilde{u}}{2} \sqrt{\tilde{u}^2 + 4} - \frac{\tilde{u}^2}{2} \right) \Big|_{u_1(\vartheta)}^{\min[u_2(\vartheta), -\rho_{\text{lens}} + \frac{1}{\rho_{\text{lens}}]}]} \right] d\vartheta,
\end{aligned} \tag{2.17}$$

where $\Theta(x)$ defines the Heaviside step function.

Combining Equation (2.13) and Equation (2.17) fully considers a limb-darkened source and a finite lens:

$$A_{\text{LD\&FL}}^*(u; \rho_s) = \frac{2}{\pi \rho_s^2} \int_0^\pi \int_{u_1(\vartheta)}^{u_2(\vartheta)} \left[A_+(\tilde{u}) \Theta \left(\frac{b_+}{R_E} - \rho_{\text{lens}} \right) + A_-(\tilde{u}) \Theta \left(-\frac{b_-}{R_E} - \rho_{\text{lens}} \right) \right] S(r/R_*, \Gamma) \tilde{u} d\tilde{u} d\vartheta. \tag{2.18}$$

2.6 Results

When we implemented the finite-source fitting using the Levenberg-Marquardt algorithm, we recognized that a good set of initial values is needed to bring the algorithm to convergence. Fitting a Paczyński light curve to derive these initial values for the finite-source fitting leads to very good results. The algorithm is stable and for an initial value of $\rho_s = 0.1$ it converges within 100 iterations. [Alcock *et al.* \(1997a\)](#) were able to measure a microlensing light curve with finite-source effects in MACHO-1995-BLG-30. We extracted the data points from their paper and applied our finite-source fitting algorithms to them. Fitting Equation (2.7) with $n = 10$ to the data yields a perfect agreement (see Table 2.1 and Figure 2.8) with the parameters given in Table 2 of [Alcock *et al.* \(1997a\)](#):

Table 2.1: Light-curve parameters for MACHO-1995-BLG-30

Fit	$A_{\text{PS}}(u)$ (this work)	$A^*(u; \rho_s)$ (this work)	Alcock <i>et al.</i> (1997a) , Table 2 ^a
t_0	1321.260 ± 0.002	1321.235 ± 0.002	1321.2(1)
t_E	34.41 ± 0.02	34.25 ± 0.02	33.68(1)
u_0	0.04133 ± 0.00004	0.05569 ± 0.00006	0.05579(1)
ρ_s	–	0.0722 ± 0.0001	0.07335(1)

a. The reported uncertainties in the final significant digit(s) of [Alcock *et al.* \(1997a\)](#) are the maximum extent of the surface in parameter space which has a χ^2 greater than the best-fit value by 1.

[Alcock *et al.* \(1997a\)](#) then obtained the limb darkening coefficients of MACHO-1995-BLG-30 utilizing spectroscopic information. However, [Heyrovský \(2003\)](#) argued that the surface-brightness profile of this event can not be fully recovered due to its intrinsic complex variability. Therefore, we tested our limb-darkening fitting routine to another limb-darkened finite-source event OGLE-2003-BLG-262. Our results are shown in Table 2.2, Figure 2.9 and Figure 2.10 in comparison with [Yoo *et al.* \(2004\)](#).

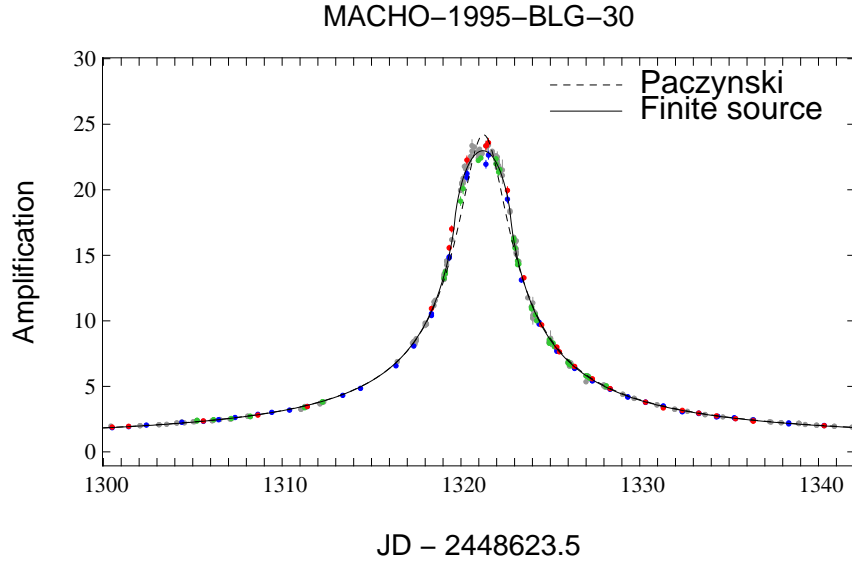


Figure 2.8: Finite-source light-curve fits for MACHO-1995-BLG-30 assuming a uniform source. Data points in R are from MACHO (red), CTIO, UTSO, WISE, and MJUO (gray) and V are from MACHO (blue) and UTSO (green). The dashed line shows the light curve for a point-source model. The best-fitting finite-source light-curve parameters are displayed in Table 2.1

Table 2.2: Light-curve parameters for OGLE-2003-BLG-262.

Fit	$A_{\text{ps}}(u)$	$A^*(u; \rho_s)$	$A_{\text{LD}}^*(u; \rho_s)$
t_0	2839.852 ± 0.001	2839.838 ± 0.001	2839.8361 ± 0.001
t_E	12.83 ± 0.01	12.61 ± 0.01	12.559 ± 0.016
u_0	0.02877 ± 0.00008	0.0365 ± 0.0002	0.0361 ± 0.0002
ρ_s	–	0.0581 ± 0.0002	0.0598 ± 0.0002

Note. We fixed the limb-darkening coefficients at $(\Gamma_V, \Gamma_I, \Gamma_H) = (0.72, 0.44, 0.26)$

Finally, we choose several lens sizes for the configuration of OGLE-2003-BLG-262 to investigate the influence of the finite lens effects on the microlensing light curve in Figure 2.10. The light curve is strongly altered only if the lens size is comparable to or larger than the Einstein radius.

When the lens size is smaller than $0.93R_E$, it only partially covers the outer image and the finite lens effects can be observed only at the very beginning of the rising and near the end of the declining stage of the lensing event. Therefore, we fitted various lens sizes up to $\rho_{\text{lens}} = 1.1R_E$ using the full OGLE I -band data set. However, no improvement in χ^2 has been found by introducing lens sizes as an extra parameter in the finite-source model (see Figure 2.12). This implies that the lens size effect is negligible for OGLE-2003-BLG-262.

2.7 Conclusion

We have demonstrated that finite-source effects can be more conveniently evaluated in the lens-centered polar coordinate system. The uniform source case can be reduced to a one-dimensional

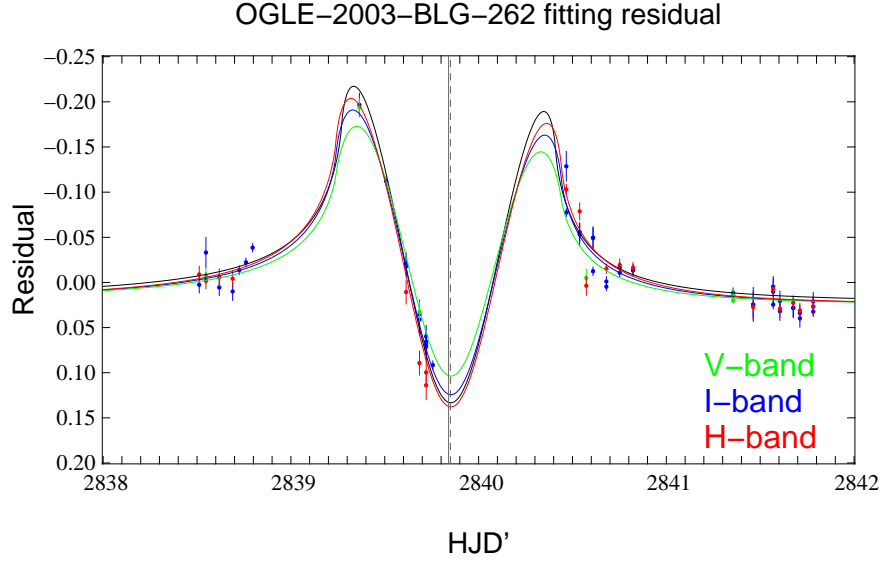


Figure 2.9: Residuals of the observed light curve relative to the best-fitted point-source light curve. The *solid black* curve shows the light curve of an extended source with uniform surface brightness. The *solid blue*, *solid red*, and *solid green* curves are extended source models incorporating limb darkening in V , I and H bands with $(\Gamma_V, \Gamma_I, \Gamma_H) = (0.72, 0.44, 0.26)$. The vertical lines indicate t_0 for the best-fitted point-source (*solid*) and limb-darkened finite-source (*dashed*) model. For the light curves with the limb-darkened source we have left t_0 as a free parameter. The best-fitting value for t_0 slightly differs (see Table 2.2). This causes the asymmetric pattern of the residual relative to the Paczyński light curve.

integral, which can be solved in a fast and numerically stable manner. The previously available formalisms were either comparably fast but held only in the high-amplification regime (the Gould finite-source approximation) or held in any amplification regime but involved an integral which has singularity and is slower to solve (the Witt & Mao approach). We also showed that the vast majority of the OGLE-lensing events have maximum amplifications smaller than 10, and therefore cannot be precisely described in the high-amplification, finite-source approximation of Gould. Our formalism allows a fast and simultaneous search for microlensing events with extended or pointlike sources in any amplification regime.

We also presented the limb-darkening effects and finite lens size effects in our formalism. We showed for the case of OGLE-2003-BLG-262 how one can constrain the source size and obtain upper limits for the lens size.

The Appendix provides the partial derivatives of the amplification for a uniform surface brightness source (Appendix A), a limb-darkened source (Appendix B), and a uniform surface brightness source with a finite lens (Appendix C), which are required in, e.g., the Levenberg-Marquardt algorithm to obtain microlensing light-curve fits.

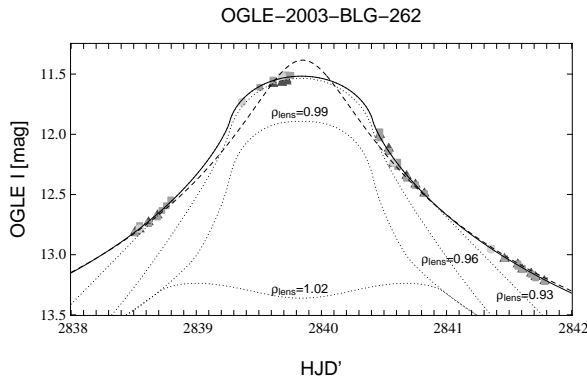


Figure 2.10: Finite-source and finite-lens light-curve fits for OGLE-2003-BLG-262. Data points are in I (square), V (circle), and H (triangle). The *dashed line* shows the light curve for a point source. The *solid line* shows the light curve for an extended source with uniform surface brightness. The *dotted lines* illustrate the effects of finite lens sizes on top of finite-source size for lens sizes of $\rho_{\text{lens}} = 0.93, 0.96, 0.99,$ and 1.02 .

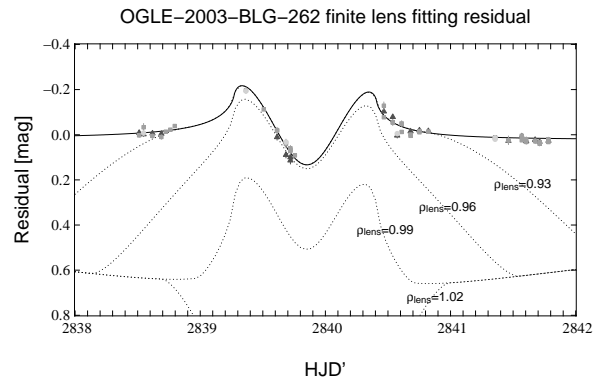


Figure 2.11: Fitting residual of various lens radius relative to the point-source model. Data points are in I (square), V (circle), and H (triangle). The *solid black line* shows the light curve for an extended source with uniform surface brightness. The *dotted lines* illustrate the effects of finite lens sizes on top of finite source size for lens sizes of $\rho_{\text{lens}} = 0.93, 0.96, 0.99,$ and 1.02 . One sees that all these cases can be safely excluded.

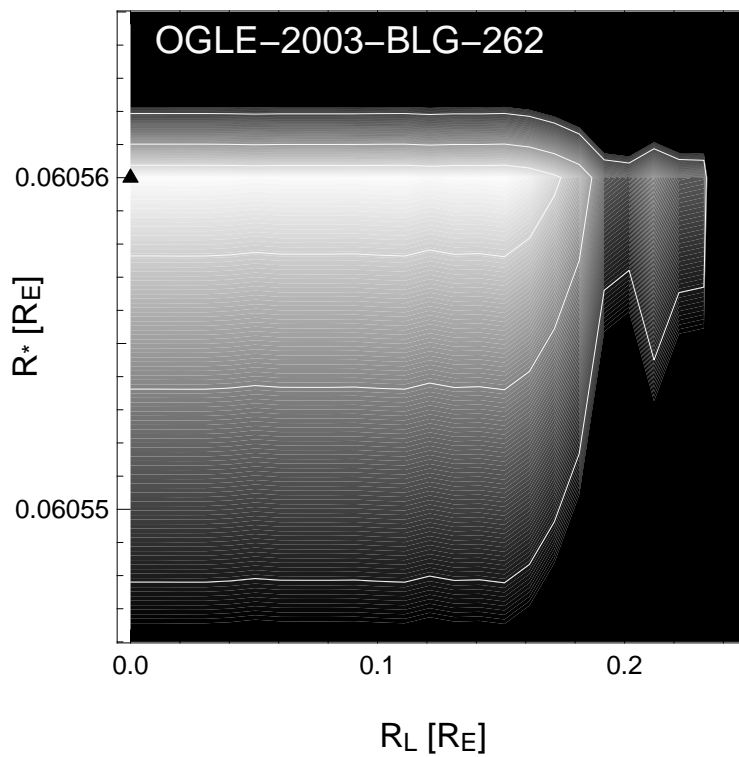


Figure 2.12: χ^2 contour map of OGLE-2003-BLG-262. In *white contour*, levels for 1, 2, and 3σ for source and lens size fitting are shown. The *black triangle* indicates the best-fitted model with $\rho_s = 0.06056$ and $R_{\text{lens}} = 0$. This suggests that the point lens assumption is sufficient for OGLE-2003-BLG-262.

2.8 Appendix A: Partial derivatives of the finite-source amplification for a source with uniform surface brightness

$$\begin{aligned}\frac{\partial A^*}{\partial u}(u, \rho_s) &= \frac{2}{\pi \rho_s^2} \int_0^\pi \left\{ \frac{u_2^2+2}{\sqrt{u_2^2+4}} \left[\cos \vartheta - \frac{u \sin^2 \vartheta}{\sqrt{\rho_s^2 - u^2 \sin^2 \vartheta}} \right] - \frac{u_1^2+2}{\sqrt{u_1^2+4}} \left[\cos \vartheta + \frac{u \sin^2 \vartheta}{\sqrt{\rho_s^2 - u^2 \sin^2 \vartheta}} \right] \right\} d\vartheta \\ \frac{\partial A^*}{\partial \rho_s}(u, \rho_s) &= \frac{2}{\pi \rho_s} \int_0^\pi \left[\frac{u_2^2+2}{\sqrt{u_2^2+4} \sqrt{\rho_s^2 - u^2 \sin^2 \vartheta}} - \frac{u_1^2+2}{\sqrt{u_1^2+4} \sqrt{\rho_s^2 - u^2 \sin^2 \vartheta}} \right] d\vartheta - 2 \frac{A^*(u, \rho_s)}{\rho_s}.\end{aligned}\quad (2.19)$$

2.9 Appendix B: Partial derivatives of the finite-source amplification for a source with limb darkening

$$\begin{aligned}\frac{\partial A^*(u, \rho_s, \Gamma_\lambda)}{\partial u} &= \frac{2}{\pi \rho_s^2} \int_0^\pi \left[\frac{\partial u_2}{\partial u} \frac{u_2^2+2}{\sqrt{u_2^2+4}} \frac{S_\lambda}{S_\lambda} - \frac{\partial u_1}{\partial u} \frac{u_1^2+2}{\sqrt{u_1^2+4}} \frac{S_\lambda}{S_\lambda} \right] d\vartheta + \frac{2}{\pi \rho_s^2} \int_0^\pi \int_{u_1}^{u_2} \frac{\tilde{u}^2+2}{\sqrt{\tilde{u}^2+4}} \frac{\partial}{\partial u} \left(\frac{S_\lambda}{S_\lambda} \right) d\tilde{u} d\vartheta \\ \frac{\partial A^*(u, \rho_s, \Gamma_\lambda)}{\partial \rho_s} &= \frac{2}{\pi \rho_s^2} \int_0^\pi \left[\frac{\partial u_2}{\partial \rho_s} \frac{u_2^2+2}{\sqrt{u_2^2+4}} \frac{S_\lambda}{S_\lambda} - \frac{\partial u_1}{\partial \rho_s} \frac{u_1^2+2}{\sqrt{u_1^2+4}} \frac{S_\lambda}{S_\lambda} \right] d\vartheta + \frac{2}{\pi \rho_s^2} \int_0^\pi \int_{u_1}^{u_2} \frac{\tilde{u}^2+2}{\sqrt{\tilde{u}^2+4}} \frac{\partial}{\partial \rho_s} \left(\frac{S_\lambda}{S_\lambda} \right) d\tilde{u} d\vartheta - 2 \frac{A^*(u, \rho_s, \Gamma_\lambda)}{\rho_s} \\ \frac{\partial A^*(u, \rho_s, \Gamma_\lambda)}{\partial \Gamma_\lambda} &= \frac{2}{\pi \rho_s^2} \int_0^\pi \int_{u_1}^{u_2} \frac{\tilde{u}^2+2}{\sqrt{\tilde{u}^2+4}} \frac{\partial}{\partial \Gamma_\lambda} \left(\frac{S_\lambda}{S_\lambda} \right) d\tilde{u} d\vartheta\end{aligned}\quad (2.20)$$

with $\frac{\partial u_1}{\partial u} = \cos \vartheta + u \sin^2 \vartheta / \sqrt{\rho_s^2 - u^2 \sin^2 \vartheta}$, $\frac{\partial u_2}{\partial u} = \cos \vartheta - u \sin^2 \vartheta / \sqrt{\rho_s^2 - u^2 \sin^2 \vartheta}$,
 $\frac{\partial u_1}{\partial \rho_s} = -\rho_s / \sqrt{\rho_s^2 - u^2 \sin^2 \vartheta}$, $\frac{\partial u_2}{\partial \rho_s} = \rho_s / \sqrt{\rho_s^2 - u^2 \sin^2 \vartheta}$, $\frac{\partial}{\partial u} \left(\frac{S_\lambda}{S_\lambda} \right) = -\frac{3}{4} \Gamma_\lambda (-2\tilde{u} \cos \vartheta + 2u) / \left(\rho_s^2 \sqrt{1 - \frac{\tilde{u}^2 - 2\tilde{u} \cos \vartheta + u^2}{\rho_s^2}} \right)$,
 $\frac{\partial}{\partial \rho_s} \left(\frac{S_\lambda}{S_\lambda} \right) = \frac{3}{2} \Gamma_\lambda (\tilde{u}^2 - 2\tilde{u} \cos \vartheta + u^2) / \left(\rho_s^3 \sqrt{1 - \frac{\tilde{u}^2 - 2\tilde{u} \cos \vartheta + u^2}{\rho_s^2}} \right)$,
 $\frac{\partial}{\partial \Gamma_\lambda} \left(\frac{S_\lambda}{S_\lambda} \right) = -1 + \frac{3}{2} \sqrt{1 - \frac{\tilde{u}^2 - 2\tilde{u} \cos \vartheta + u^2}{\rho_s^2}}$ when u_1 and u_2 are not equal to zero.

2.10 Appendix C: Partial derivatives of the finite-source and finite-lens amplification assuming a source with uniform brightness

$$\begin{aligned}\frac{\partial A^*}{\partial u}(u, \rho_s, \rho_{\text{lens}}) &= \frac{1}{\pi \rho_s^2} \int_0^\pi \frac{\partial u_2}{\partial u} \left[(A_{\text{PS}}(u_2)+1) \Theta \left(u_2 - \rho_{\text{lens}} + \frac{1}{\rho_{\text{lens}}} \right) + (A_{\text{PS}}(u_2)-1) \Theta \left(-u_2 - \rho_{\text{lens}} + \frac{1}{\rho_{\text{lens}}} \right) \right] u_2 d\vartheta \\ &\quad - \frac{1}{\pi \rho_s^2} \int_0^\pi \frac{\partial u_1}{\partial u} \left[(A_{\text{PS}}(u_1)+1) \Theta \left(u_1 - \rho_{\text{lens}} + \frac{1}{\rho_{\text{lens}}} \right) + (A_{\text{PS}}(u_1)-1) \Theta \left(-u_1 - \rho_{\text{lens}} + \frac{1}{\rho_{\text{lens}}} \right) \right] u_1 d\vartheta \\ \frac{\partial A^*}{\partial \rho_s}(u, \rho_s, \rho_{\text{lens}}) &= \frac{1}{\pi \rho_s^2} \int_0^\pi \frac{\partial u_2}{\partial \rho_s} \left[(A_{\text{PS}}(u_2)+1) \Theta \left(u_2 - \rho_{\text{lens}} + \frac{1}{\rho_{\text{lens}}} \right) + (A_{\text{PS}}(u_2)-1) \Theta \left(-u_2 - \rho_{\text{lens}} + \frac{1}{\rho_{\text{lens}}} \right) \right] u_2 d\vartheta \\ &\quad - \frac{1}{\pi \rho_s^2} \int_0^\pi \frac{\partial u_1}{\partial \rho_s} \left[(A_{\text{PS}}(u_1)+1) \Theta \left(u_1 - \rho_{\text{lens}} + \frac{1}{\rho_{\text{lens}}} \right) + (A_{\text{PS}}(u_1)-1) \Theta \left(-u_1 - \rho_{\text{lens}} + \frac{1}{\rho_{\text{lens}}} \right) \right] u_1 d\vartheta \\ &\quad - 2 \frac{A^*(u, \rho_s, \rho_{\text{lens}})}{\rho_s} \\ \frac{\partial A^*}{\partial \rho_{\text{lens}}}(u, \rho_s, \rho_{\text{lens}}) &= \frac{1}{\pi \rho_s^2} \int_0^\pi \int_{u_1}^{u_2} (A_{\text{PS}}(\tilde{u})+1) \delta \left(\tilde{u} - \rho_{\text{lens}} + \frac{1}{\rho_{\text{lens}}} \right) \frac{\partial \left(\tilde{u} - \rho_{\text{lens}} + \frac{1}{\rho_{\text{lens}}} \right)}{\partial \rho_{\text{lens}}} \tilde{u} d\tilde{u} d\vartheta \\ &\quad + \frac{1}{\pi \rho_s^2} \int_0^\pi \int_{u_1}^{u_2} (A_{\text{PS}}(\tilde{u})-1) \delta \left(-\tilde{u} - \rho_{\text{lens}} + \frac{1}{\rho_{\text{lens}}} \right) \frac{\partial \left(-\tilde{u} - \rho_{\text{lens}} + \frac{1}{\rho_{\text{lens}}} \right)}{\partial \rho_{\text{lens}}} \tilde{u} d\tilde{u} d\vartheta.\end{aligned}\quad (2.21)$$

The derivatives can be obtained numerically by utilizing the same approach as shown in Equation (2.7). We also find that for $u > \rho_s$, substituting integration variable ϑ with $v \equiv \frac{u}{\rho_s} \sin \vartheta$ gives a numerically more stable estimations of the derivatives for a uniform brightness source:

$$\begin{aligned} \frac{\partial A^*}{\partial u}(u, \rho_s) &= \frac{u}{\pi \rho_s} \int_0^1 \frac{1}{U^3} \left[\frac{(u^2 - \rho_s^2)(U + \Omega) - 4\Omega}{\sqrt{(U + \Omega)^2 + 4}} - \frac{(u^2 - \rho_s^2)(U - \Omega) + 4\Omega}{\sqrt{(U - \Omega)^2 + 4}} \right] dv \\ \frac{\partial A^*}{\partial \rho_s}(u, \rho_s) &= \frac{1}{\pi \rho_s^2} \int_0^1 \frac{1}{U^3} \left[-\frac{u^2(u^2 - \rho_s^2)(U + \Omega) - 4(\Omega v^2 \rho_s^2 - U^3)}{\sqrt{(U + \Omega)^2 + 4}} + \frac{u^2(u^2 - \rho_s^2)(U - \Omega) + 4(\Omega v^2 \rho_s^2 + U^3)}{\sqrt{(U - \Omega)^2 + 4}} \right] dv \end{aligned} \quad (2.22)$$

with $U = \sqrt{u^2 - v^2 \rho_s^2}$ and $\Omega = \rho_s \sqrt{1 - v^2}$.

Chapter 3

Finite-source and finite-lens effects in astrometric microlensing

This chapter has been published in [Lee *et al.* \(2010\)](#).

3.1 Abstract

The aim of this paper is to study the astrometric trajectory of microlensing events with an extended lens and/or source. We consider not only a dark lens but also a luminous lens as well. We find that the discontinuous finite-lens trajectories in [Takahashi \(2003\)](#) will become continuous in the finite-source regime. The point lens (source) approximation alone gives an under (over)-estimation of the astrometric signal when the size of the lens and source are not negligible. While the finiteness of the source is revealed when the lens transits the surface of the source, the finite-lens signal is most prominent when the lens is very close to the source. Astrometric microlensing towards the Galactic bulge, SMC, and M31 are discussed, which indicate that the finite-lens effect is beyond the detection limit of current instruments. Nevertheless, it is possible to distinguish between self- and halo lensing through a (non)detection of the astrometric ellipse. We also consider the case where the lens is luminous itself, as has been observed where a lensing event was followed up with the *Hubble Space Telescope*. We show that the astrometric signal will be reduced in a luminous-lens scenario. The physical properties of the event, such as the lens-source flux ratio, the size of the lens and source nevertheless can be derived by fitting the astrometric trajectory.

3.2 Introduction

Most of the microlensing events detected to date are through photometric monitoring of the source flux. In this case, the information on the physical identity of the lens is reduced, because the only quantity one can retrieve from the lightcurve is the Einstein timescale t_E . t_E is defined by the time required for the source to transit the angular Einstein radius θ_E of the lens ([Gould, 2000](#)):

$$t_E = \frac{\theta_E}{|\mu_{rel}|}, \quad \theta_E = \sqrt{k M_L \pi_{rel}}, \quad k \equiv \frac{4G}{c^2 \text{AU}} \approx 8.14 \frac{\text{mas}}{M_\odot}, \quad (3.1)$$

where μ_{rel} is the relative lens-source proper motion, M_L is the mass of the lens, $\pi_{rel} := \text{AU}/(D_{OL}^{-1} - D_{OS}^{-1})$ is the relative lens-source parallax, D_{OL} and D_{OS} are distance to the lens and the source from the observer, respectively. Equation (3.1) shows that the mass, distance, and velocity of the lens are degenerated into t_E .

To better constrain the lens properties, Hog *et al.* (1995), Walker (1995), and Miyamoto & Yoshii (1995) thus suggested to use astrometric microlensing. That is, to measure the centroid displacement of the two images during the course of microlensing. Former studies have shown that the trajectory of the centroid displacement will trace out an ellipse, and the size of the ellipse is proportional to the angular Einstein radius. Therefore, one can determine θ_E through the observation of such astrometric ellipses and constrain the relative lens-source proper motion. Gould (1992) has shown that if one can further measure the microlens parallax $\pi_E = \sqrt{\frac{\pi_{rel}}{kM_L}}$ from the lightcurve distortion induced by the orbital motion of the Earth, the lens mass M_L and the relative lens-source parallax π_{rel} can be determined without ambiguity:

$$M_L = \frac{\theta_E}{k\pi_E}, \quad \pi_{rel} = \pi_E \theta_E. \quad (3.2)$$

The location of the lens can be derived as well if the distance to the source is well-known, which is often the case towards the Galactic bulge and Magellanic Clouds.

The typical value of the astrometric microlensing signal for a source in the Galactic bulge and a $0.5 M_\odot$ lens located half way to the source is of order of 0.1 mas, which is much larger than the astrometric accuracy of upcoming space missions such as *SIM* (*Space Interferometry Mission*, Allen *et al.*, 1997), *GAIA* (*Global Astrometric Interferometer for Astrophysics*, Lindegren *et al.*, 1994) and ground-based instruments, e.g. *PRIMA* (*Phase Referenced Imaging and Micro-arcsecond Astrometry*, Quirrenbach *et al.*, 1998). *GAIA* will survey the whole sky with sources brighter than 20 magnitudes in *V* band. It is expected to reach an astrometric accuracy of $30 \mu\text{as}$ ($150 \mu\text{as}$) with $V < 12$ ($V < 16$) for a single measurement (Belokurov & Evans, 2002) and an estimated detection of ≈ 1000 events (Dominik & Sahu, 2000). Unlike *GAIA*, which only scans the sky with a pre-determined pattern, *SIM* can point to selectable targets and thus tracks the ongoing microlensing event upon request. The expected accuracy of *SIM* is $5 \mu\text{as}$ ($20 \mu\text{as}$) for $V < 12$ ($V < 16$) with one hour integration time (Goullioud *et al.*, 2008). While *SIM* and *GAIA* are scheduled to launch in the next few years, *PRIMA* has already been installed on the VLT Interferometer and aims at achieving $10 \mu\text{as}$ accuracy level in 30 minutes integration time provided a reference star within 10 arcsec and a 200 m baseline (Delplancke, 2008).

In addition to the standard point-source point-lens (PSPL) microlensing, single lens events revealing an extended source signal have also been observed photometrically (e.g. Alcock *et al.*, 1997a; Yoo *et al.*, 2004; Jiang *et al.*, 2004; Cassan *et al.*, 2006; Batista *et al.*, 2009; Yee *et al.*, 2009; Zub *et al.*, 2011). Mao & Witt (1998) thus derived the astrometric trajectory of finite-source events with a point-lens (FSPL). On the other hand, Takahashi (2003) studied the centroid displacement of finite-lens effects but assuming a point-source (PSFL). Furthermore, Agol (2002) and Lee *et al.* (2009) have investigated the combination of finite-source and finite-lens effects (FSFL) photometrically, but left aside the astrometric aspect. Since the FSFL lightcurve deviates from either the PSFL or FSPL, as shown by Agol (2002), we are motivated to study the astrometric behavior when both finite-source and finite-lens effects are relevant. There are events where both the source and the lens are resolved by the *Hubble Space Telescope* (*HST*). This implies that the lens can also be a star and implies a luminous lens scenario rather than a dark lens (Alcock *et al.*, 2001; Kozłowski *et al.*, 2007),

which is also the case for self-lensing. We thus consider the light contribution from the lens star and study the astrometric behavior by allowing for a luminous lens.

Our paper is organized as following: in § 3.3 we introduce the theory of astrometric microlensing. We take into account the FS effects either with a uniform surface brightness source or with a more general surface brightness profile in § 3.4. We further include a dark lens with finite size in § 3.5. One might expect not only shadowing but also light contribution from the lens as well. Therefore, we allow for a luminous lens in § 3.6. The aforementioned properties of the microlensing system can be estimated by fitting the formula in § 3.6. A discussion of possible events with sources located in the Galactic bulge, SMC and M31 is presented in § 3.7 followed by a summary in § 3.8.

3.3 Astrometric trajectory of the lensed images

Let φ_s and φ_L be the angular position of the source and lens, then one can derive the position (θ) and the amplification (A) of the two lensed images in the lens plane through the dimensionless impact parameter $u := (\varphi_s - \varphi_L)/\theta_E$ (see *e.g.* Hosokawa *et al.*, 1993; Hog *et al.*, 1995; Walker, 1995; Miyamoto & Yoshii, 1995):

$$\theta_{\pm} = \frac{1}{2} \left[u \pm \sqrt{u^2 + 4} \right] \hat{u}, \quad A_{\pm} = \frac{1}{2} \left[\frac{u^2 + 2}{u\sqrt{u^2 + 4}} \pm 1 \right], \quad (3.3)$$

where $u = |u|$ and $\hat{u} = u/u$. Note that θ_{\pm} and \hat{u} are vectors while A_{\pm} are scalars. The centroid of the images can be calculated by weighting the position of the two images with their amplification:

$$\theta_{c,\text{PSPL}} = \frac{A_+ \theta_+ + A_- \theta_-}{A_+ + A_-} = \frac{1}{2} \left[\frac{u(u^2 + 4)}{u^2 + 2} + u \right] \hat{u} \quad (3.4)$$

and the centroidal shift relative to the source is:

$$\delta\theta_{c,\text{PSPL}} = \theta_c - u = \frac{u}{u^2 + 2} \hat{u}. \quad (3.5)$$

If we neglect the parallax effects, the relative motion between the lens and source can be approximated by rectilinear motion so that

$$u(t) = \sqrt{\tau^2 + u_0^2}, \quad \tau = \frac{t - t_0}{t_E}, \quad (3.6)$$

where u_0 is the closest approach at t_0 .

The centroidal shift can then be decomposed into components parallel to μ_{rel} , $\delta\theta_{c,\text{PSPL},x}$, and perpendicular to μ_{rel} , $\delta\theta_{c,\text{PSPL},y}$ (see Fig. 3.1). One further finds that the centroidal shift actually traces out an ellipse (Walker, 1995)

$$\left(\frac{\delta\theta_{c,\text{PSPL},x}}{a} \right)^2 + \left(\frac{\delta\theta_{c,\text{PSPL},y} - b}{b} \right)^2 = 1, \quad (3.7)$$

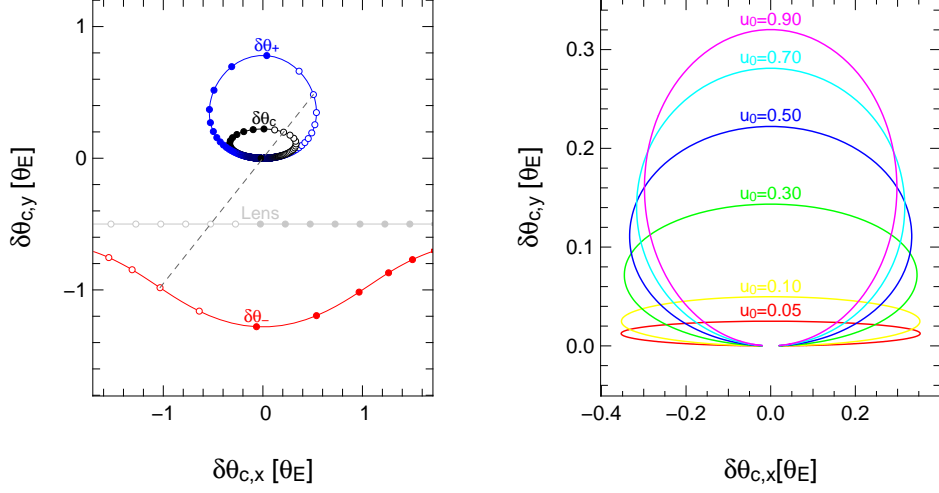


Figure 3.1: Centroid shifts for PSPL. Left panel: The trajectory of the plus-image (in blue), minus-image (in red), centroid of these two images (in black), and the lens (in gray) relative to the source center assuming $t_0 = 0$, $t_E = 10$ days, and $u_0 = 0.5 \theta_E$. Right panel: Centroid displacement for different values of u_0 .

where a and b are the semi-major and semi-minor axis of the ellipse respectively,

$$a = \frac{1}{2} \frac{1}{\sqrt{u_0^2 + 2}}, \quad b = \frac{1}{2} \frac{u_0}{u_0^2 + 2}. \quad (3.8)$$

The trajectory of centroidal shift with different values of u_0 is shown in Fig. 3.1.

Taking the derivative of Eq. (3.5), one finds that the maximum centroidal shift occurs when $u = \sqrt{2}$ and has an absolute value of $\frac{\sqrt{2}}{2+2} = \frac{1}{2\sqrt{2}} \approx 0.3536$, *i.e.* about one-third of the angular Einstein radius. For a source located in the Galactic bulge with a lens of $0.5 M_\odot$ located half way to the source, the angular Einstein radius is $712 \mu\text{as}$, which is one (two) magnitudes larger than the planned astrometric accuracy of the *GAIA (SIM)* mission even after taking one-third of its value. The maximum values for the centroidal shifts with halo and self-lensing towards SMC and M31 are shown in Fig. 3.2.

3.4 The Finite Source Effects

For an extended source, the centroid of the two images is obtained by a two-dimensional integral of the image position weighted by its amplification over the surface of the source (Walker, 1995; Mao & Witt, 1998):

$$\delta\theta_{c,\text{FSPL}} = \frac{\int_0^{2\pi} \int_0^{\rho_s} [A_+ \theta_+ + A_- \theta_-] S\left(\frac{r}{\rho_s}\right) r dr d\phi}{\int_0^{2\pi} \int_0^{\rho_s} [A_+ + A_-] S\left(\frac{r}{\rho_s}\right) r dr d\phi} - u \quad (3.9)$$

where $S\left(\frac{r}{\rho_s}\right)$ is the source surface-brightness profile, $\rho_s := \frac{\theta_s}{\theta_E}$ is the source radius in units of the angular Einstein ring radius and r is the distance to the source center.

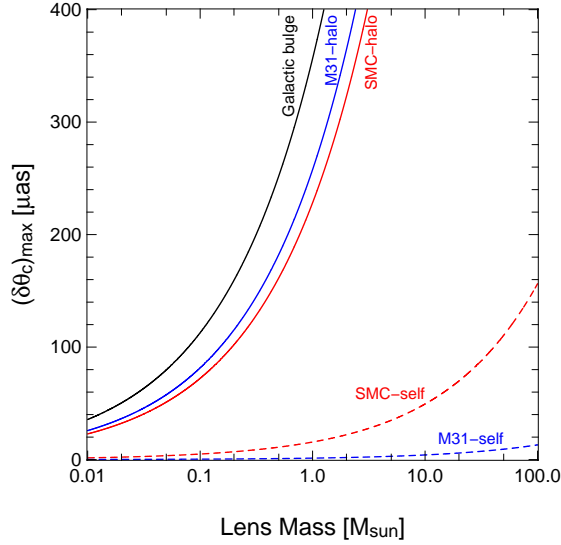


Figure 3.2: Maximum values for the centroidal shift versus lens mass. For illustration, we set the lens of halo lensing towards SMC ($D_{\text{OS}} = 65$ kpc) and M31 ($D_{\text{OS}} = 770$ kpc) to be 15 kpc from the observer, and 1 kpc in front of the source as self-lensing. We only show the case of halo lensing for Galactic bulge ($D_{\text{OS}} = 8$ kpc) assuming the lens is half way to the background source.

For a source with uniform surface brightness (*i.e.* $S(\frac{r}{\rho_s})$ is constant all over the surface of the source), the integration over the source surface can be reduced into a one-dimensional integral following the lens-centered coordinates approach of [Lee *et al.* \(2009\)](#). One thus derives the values for $\delta\theta_{c,\text{FSPL},x}$ and $\delta\theta_{c,\text{FSPL},y}$

$$\begin{aligned}\delta\theta_{c,\text{FSPL},x} &= \frac{\int_0^{2\pi} \left[\frac{1}{3}(\tilde{u}^2+1)\sqrt{\tilde{u}^2+4} \right]_{\tilde{u}=u_1}^{u_2} \cos(\vartheta+\alpha) d\vartheta}{\int_0^{2\pi} \left[\frac{1}{2}\tilde{u}\sqrt{\tilde{u}^2+4} \right]_{\tilde{u}=u_1}^{u_2} d\vartheta} - \tau, \\ \delta\theta_{c,\text{FSPL},y} &= \frac{\int_0^{2\pi} \left[\frac{1}{3}(\tilde{u}^2+1)\sqrt{\tilde{u}^2+4} \right]_{\tilde{u}=u_1}^{u_2} \sin(\vartheta+\alpha) d\vartheta}{\int_0^{2\pi} \left[\frac{1}{2}\tilde{u}\sqrt{\tilde{u}^2+4} \right]_{\tilde{u}=u_1}^{u_2} d\vartheta} - u_0,\end{aligned}\tag{3.10}$$

where the integration boundaries u_1 and u_2 are

$$\begin{aligned}u_1 &= \begin{cases} 0 & u \leq \rho_s \\ u \cos \vartheta - \sqrt{\rho_s^2 - u^2 \sin^2 \vartheta} & u > \rho_s \wedge \vartheta \leq \sin^{-1}\left(\frac{\rho_s}{u}\right) \\ 0 & u > \rho_s \wedge \vartheta > \sin^{-1}\left(\frac{\rho_s}{u}\right) \end{cases} \\ u_2 &= \begin{cases} u \cos \vartheta + \sqrt{\rho_s^2 - u^2 \sin^2 \vartheta} & u \leq \rho_s \\ u \cos \vartheta + \sqrt{\rho_s^2 - u^2 \sin^2 \vartheta} & u > \rho_s \wedge \vartheta \leq \sin^{-1}\left(\frac{\rho_s}{u}\right) \\ 0 & u > \rho_s \wedge \vartheta > \sin^{-1}\left(\frac{\rho_s}{u}\right) \end{cases}\end{aligned}\tag{3.11}$$

and $\alpha = \tan^{-1}\left(\frac{u_0}{\tau}\right)$. The relative lens-source configuration and the parameters used in Eq. (3.10)-(3.11) are sketched in Fig. 3.3.

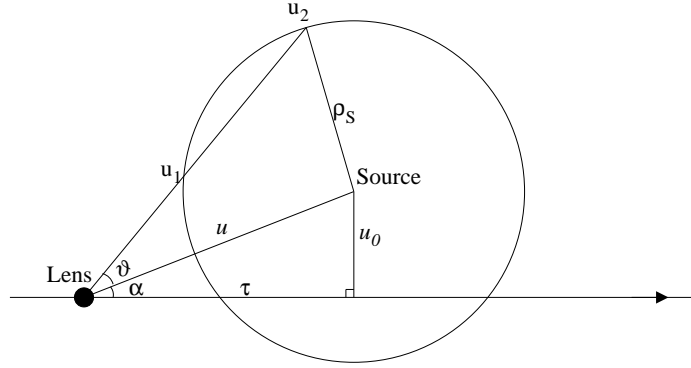


Figure 3.3: Schematic view of the lens-centered coordinates used in equation (3.10)

An example for a FS centroidal shift is shown in Fig. 3.4 along with the lightcurve in Fig. 3.5. The FS effect drives the centroidal shift towards the source center for small u , and the trajectory becomes clover-leaf like when u_0 is smaller than the source radius (see Fig. 3.7).

We also show the centroidal shifts of a limb-darkened source with an one parameter linear limb-darkening profile (Yoo *et al.*, 2004), that is

$$s\left(\frac{r}{\rho_s}\right) = \bar{s} \left[1 - I_S \left(1 - \frac{3}{2} \sqrt{1 - \left(\frac{r}{\rho_s}\right)^2} \right) \right], \quad (3.12)$$

where r is the distance to the source center. I_S is the wavelength-dependent limb-darkening coefficient. \bar{s} is the mean surface brightness of the source. When $I_S = 0$, Eq. (3.12) gives us a source with uniform brightness. The trajectory of the centroidal shift by the limb-darkened sources shows only small difference from that of the uniform brightness source, as shown in Fig. 3.6 and Fig. 3.7.

3.5 The Finite Lens Effects

For simplicity, we begin with the case of PSFL. The light from the plus-image will be obscured by the lens if its distance to the lens is smaller than the lens radius. That is, the plus-image vanishes when $\theta_+ = |\theta_+| < \rho_L$ ($\rho_L := \frac{\theta_L}{\theta_E}$). Similarly, the minus-image vanishes when $\theta_- = |\theta_-| < \rho_L$. Therefore, the centroidal shift taking into account the lens size is (Takahashi, 2003)

$$\delta\theta_{c,\text{PSFL}} = \frac{A_+ \theta_+ \Theta(\theta_+ - \rho_L) + A_- \theta_- \Theta(\theta_- - \rho_L)}{A_+ \Theta(\theta_+ - \rho_L) + A_- \Theta(\theta_- - \rho_L)} - u, \quad (3.13)$$

where $\Theta(x)$ is the Heaviside step function. An example for a PSFL centroidal shift is shown in Fig. 3.4 along with the lightcurve in Fig. 3.5. The trajectory is composed of two discontinuous parts: it follows the plus-image trajectory at larger u and returns to the PSPL centroidal trajectory at smaller u . This can be explained as following: When the FL effects sets in, the lens first obscures the minus-image because it is always inside the Einstein ring and has smaller distance to the lens

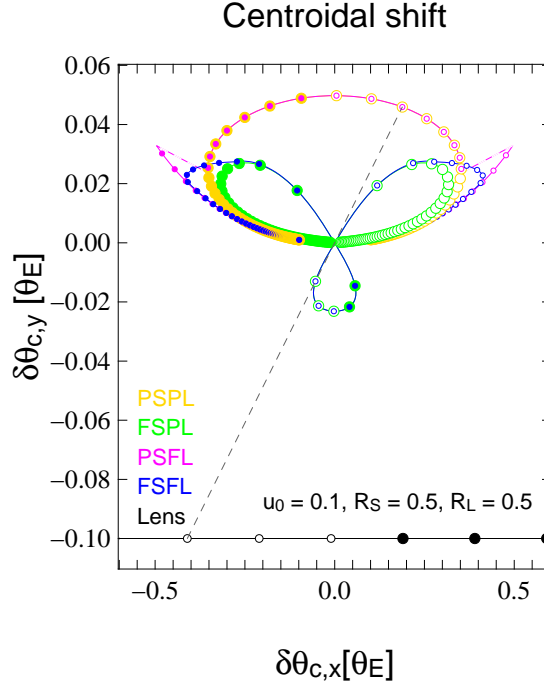


Figure 3.4: An example for centroidal shifts of a microlensing event assuming $u_0 = 0.1 \theta_E$, source radius = $0.5 \theta_E$ and lens radius = $0.5 \theta_E$. We show the trajectory of a PSPL (in yellow), FSPL (in green), PSFL (in red), and FSFL (in blue). Note that the dashed red line indicates the discontinuous part of the trajectory in a PSFL event.

compared to the plus-image (which is always outside the Einstein ring). In addition, the value of θ_- becomes larger for smaller u , as we can see from Fig. 3.1, which brings the trajectory back to the PSPL centroidal trajectory at smaller u for smaller ρ_L . As a consequence, when the size of the lens increases, the trajectory tends to be more plus-image-like until the lens size becomes so large that it completely obscures the light even from the plus-image.

Combining Eq. (3.9) and (3.13), we are able to fully consider the FSFL effects,

$$\delta\theta_{c,FSFL} = \frac{\int_0^{2\pi} \int_0^{\rho_S} [A_+ \theta_+ \Theta(\theta_+ - \rho_L) + A_- \theta_- \Theta(\theta_- - \rho_L)] S\left(\frac{r}{\rho_S}\right) r dr d\phi}{\int_0^{2\pi} \int_0^{\rho_S} [A_+ \Theta(\theta_+ - \rho_L) + A_- \Theta(\theta_- - \rho_L)] S\left(\frac{r}{\rho_S}\right) r dr d\phi} - u. \quad (3.14)$$

The result is again shown in Fig. 3.4 along with the lightcurve. The trajectory first follows the PSFL trajectory at larger u , but, instead of a discontinuous jump, the FS effects is now bending the trajectory towards the FSPL trajectory until it fully becomes the FSPL trajectory at small u .

To illustrate the importance of simultaneously including the finiteness of both the lens and the source, we compare $\delta\theta_{c,x}$ and $\delta\theta_{c,y}$ for the cases of PSPL, FSPL, PSFL, and FSFL in Fig. 3.5. When the size of the lens and the source are both negligible, it is clear that one would overestimate $\delta\theta_c$ by adopting the PS approximation. On the other hand, taking the PL assumption would underestimate the value of $\delta\theta_c$. Another important point is that in the FSFL scenario, one can not determine the lens size by

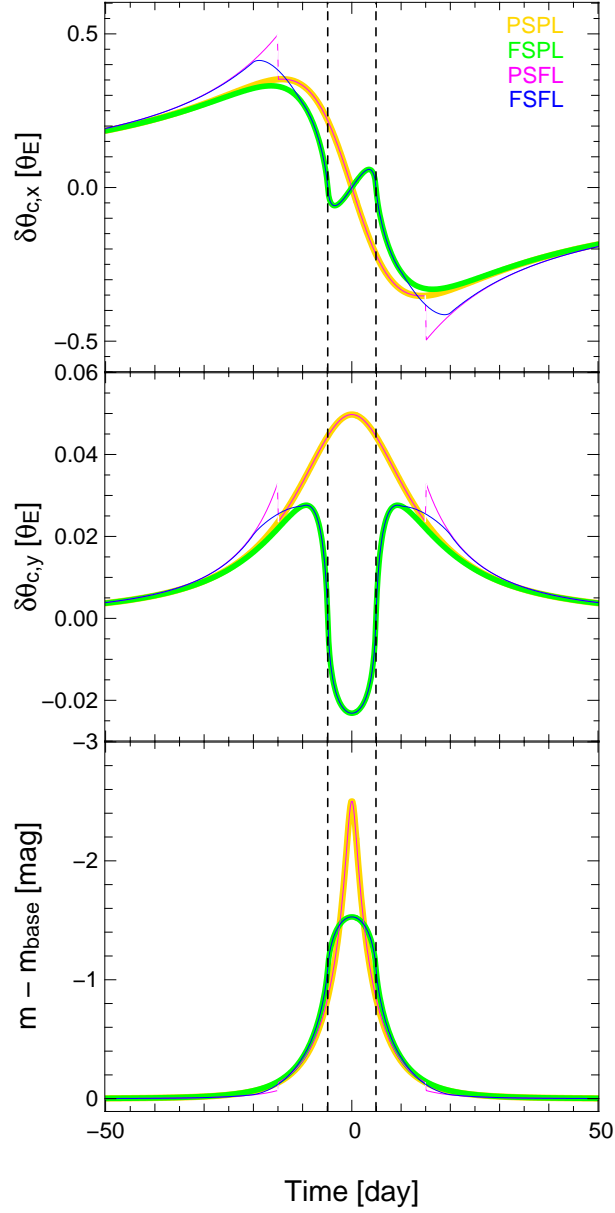


Figure 3.5: Centroidal shifts decomposition and lightcurves of a microlensing event assuming $u_0 = 0.1 \theta_E$, source radius = $0.5 \theta_E$ and lens radius = $0.5 \theta_E$. We show the trajectory in the x- and y-direction (as in Fig. 3.1) of a PSPL (in yellow), FSPL (in green), PSFL (in red), and FSFL (in blue). We also show the lightcurve with the magnitude variation relative to the baseline (m_{base}). The vertical dashed line indicates the time when $u_0 = \rho_s$. Note that the discontinuous part of the trajectory in a PSFL event is indicated by the dashed red line.

measuring the discontinuities in the trajectory presented by [Takahashi \(2003\)](#) because the FS effect makes the trajectory continuous. One thus needs to use Equation (3.14) for deriving both ρ_L and ρ_S . We also show how the limb-darkening changes the centroidal shift on top of a FSFL event (see Fig. 3.6) assuming different values of the limb-darkening coefficient I_S . In general, the limb-darkening only slightly modifies the astrometric trajectory. The FS effects and the limb-darkening are most prominent when the lens transits the surface of the source, as indicated in Fig. 3.5 and Fig. 3.6.

By fitting the centroidal shifts and/or the lightcurve as presented in Fig. 3.5 and Fig. 3.6, one is able to constrain the value of ρ_S , ρ_L , and the limb-darkening coefficient I_S . Events exhibiting FS effects have been detected photometrically (e.g. [Alcock et al., 1997a](#); [Yoo et al., 2004](#); [Jiang et al., 2004](#); [Cassan et al., 2006](#); [Batista et al., 2009](#); [Yee et al., 2009](#); [Zub et al., 2011](#)), and the information of ρ_S and I_S has been retrieved by fitting the lightcurve. Although it is hard to tell the difference between the FS and PS lightcurve by eye-inspection, including the FS effects actually dramatically reduces the χ^2 value for the best-fitted parameters. One can further fit the limb-darkening coefficient in different wavelength on top of the FS effects if multi-wavelength observation are available. Practically, the limb-darkening is relevant when one wants to simultaneously fit photometric observations from different bands. However, one can not measure the value of θ_E directly from the lightcurve and thus the information of the actual source size is unknown. [Albrow et al. \(2000\)](#) suggested to deal with this problem in the other way around. That is, given the color information of the source by photometric observation, one can apply the relation between the color and the surface brightness to obtain the actual source size if the stellar type of the source is known from the spectroscopic observation. Then the value of θ_E can be calculated by $\theta_E := \frac{\theta_S}{\rho_S}$. Constraints on the lens mass and distance are also possible given the information of microlens parallax π_E . However, inferring θ_E photometrically from the source size is achievable only if the FS effect can be seen in the lightcurve, which is the case only when the lens transits the surface of the source, as discussed by [Gould \(1994\)](#).

The advantage of astrometric microlensing is that the size of the astrometric signal is proportional to the value of θ_E . This means one can potentially measure θ_E for every single event even if the FS effects in the lightcurve are not prominent. Given the information of θ_E , the actual size of the lens and the source are ρ_S and ρ_L multiplied by θ_E . It is also possible to compare the source size derived from the astrometric microlensing and from the color to surface brightness relation.

We show the FSFL effects for a source of a uniform and a limb-darkend surface brightness profile with different source and lens sizes in Fig. 3.7 to illustrate how the combination of FS and FL influence the centroidal trajectory. The upper row of Fig. 3.7 gives the cases of PL approximation, which are comparable to the results of [Mao & Witt \(1998\)](#). The left column of Fig. 3.7 shows the cases of PS approximation comparable to the results by [Takahashi \(2003\)](#).

3.6 The Luminous Lens effects

There are microlensing systems where both the source and the lens are resolved by *HST* ([Alcock et al., 2001](#); [Kozłowski et al., 2007](#)). This indicates that the lens might be a luminous foreground star and thus perturbs the light-centroid during the course of microlensing.

Let us now consider the case where the light contribution from the lens is not negligible and start with the simple PSPL case. When the source is lensed by a point luminous lens (PSPLL), the centroid becomes the sum of the position multiplied by the flux of the two images and the lens over the total

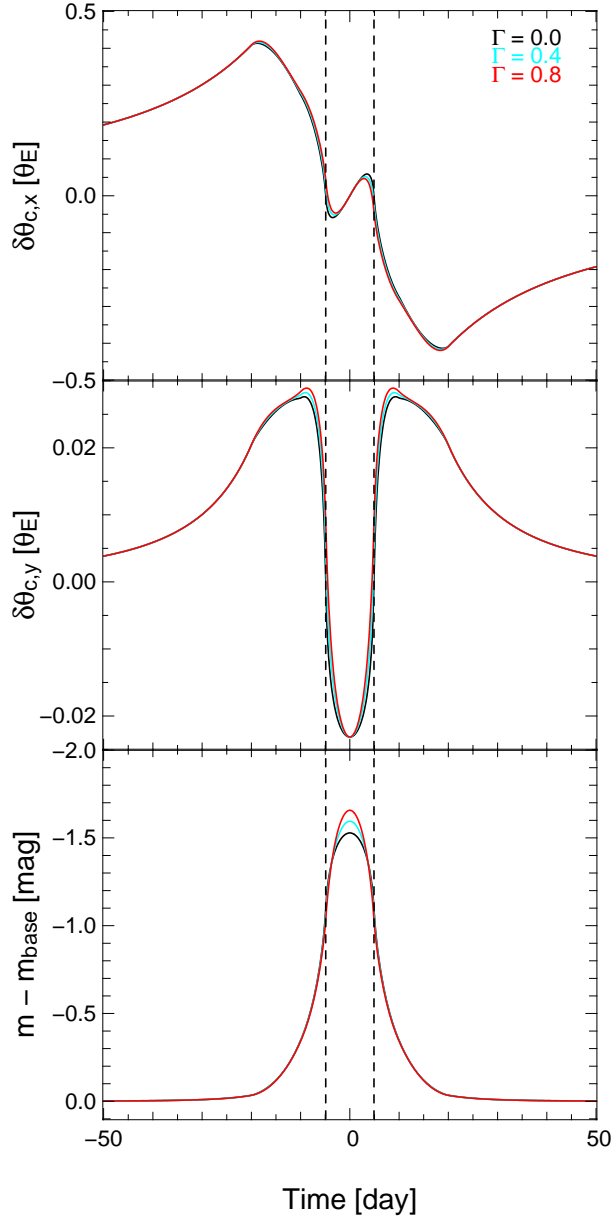


Figure 3.6: Centroidal shifts decomposition and lightcurves of a microlensing event assuming $u_0 = 0.1 \theta_E$, source radius = $0.5 \theta_E$ and lens radius = $0.5 \theta_E$. We show the trajectory in the x- and y-direction (as in Fig. 3.1) of a uniform brightness source (in *black*), a limb-darkened source with $I_S = 0.4$ (in *cyan*) and $I_S = 0.8$ (in *red*). We also show the lightcurve with the magnitude variation relative to the baseline (m_{base}). The *vertical dashed line* indicates the time when $u_0 = \rho_S$.

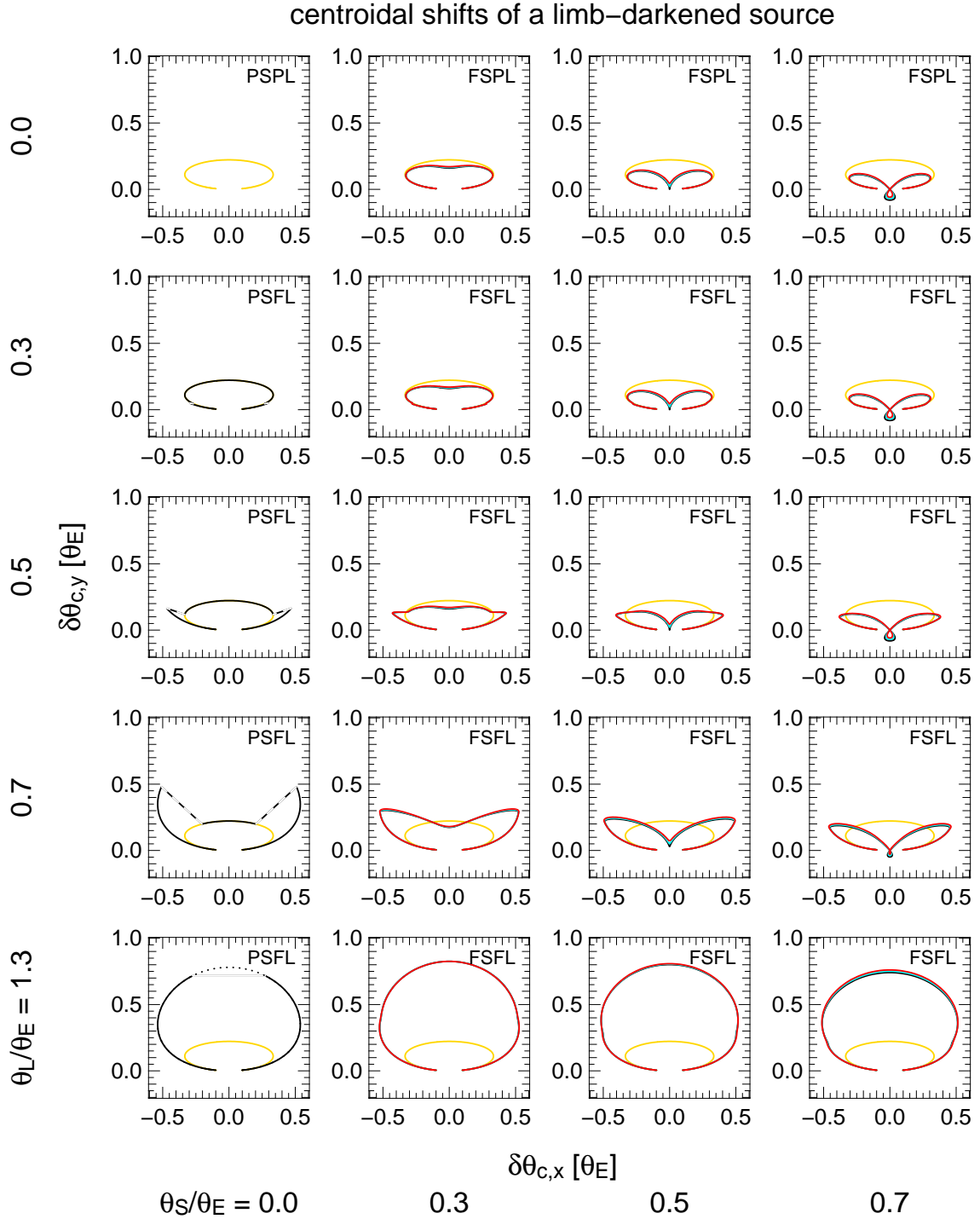


Figure 3.7: Centroid shifts in the presence of FS and FL effects for a dark lens. We show the examples for a PSFL (in yellow), FSFL with a uniform surface brightness source (in black) and with a limb-darkened source (in cyan: $\Gamma_S = 0.4$ and in red: $\Gamma_S = 0.8$) assuming $u_0 = 0.5 \theta_E$ and with the sizes of the source and the lens varying from $0.3 \theta_E$ to $1.3 \theta_E$. The dashed lines in the plots with $\theta_S/\theta_E = 0.0$ show the discontinuity in the trajectories for the PSFL cases. The dotted line in the PSFL with $\theta_L/\theta_E = 1.3$ indicates the trajectory when the lens totally obscures both the plus- and minus-image.

one. Furthermore, the reference point for the centroid shift is no longer the source center, but the flux center between the un-lensed source and the lens instead (Boden *et al.*, 1998; Jeong *et al.*, 1999; Dominik & Sahu, 2000):

$$\delta\theta_{c,\text{PSPLL}} = \frac{A_+\theta_+ + A_-\theta_- + f_{\text{LS}}\theta_L}{A_+ + A_- + f_{\text{LS}}} - \frac{u}{1 + f_{\text{LS}}}, \quad (3.15)$$

where $f_{\text{LS}} = \frac{f_L}{f_S}$ is the flux ratio between the lens and source and θ_L is the position of the lens on the lens plane. Here the $f_{\text{LS}}\theta_L$ term vanishes benefiting from the advantage of the lens-centered coordinates. For the case of FSFL, one just needs to modify the first part of Eq. (3.15) by putting in the FL criteria of Eq. (3.13) and performing the integration over the source surface as Eq. (3.10) for a uniform brightness source or Eq. (3.9) for a more general source brightness profile, that is,

$$\delta\theta_{c,\text{FSFLL}} = \frac{\int_0^{2\pi} \int_0^{\rho_S} [A_+\theta_+\Theta(\theta_+ - \rho_L) + A_-\theta_-\Theta(\theta_- - \rho_L)] S\left(\frac{r}{\rho_S}\right) r dr d\phi + f_{\text{LS}}\theta_L}{\int_0^{2\pi} \int_0^{\rho_S} [A_+\Theta(\theta_+ - \rho_L) + A_-\Theta(\theta_- - \rho_L)] S\left(\frac{r}{\rho_S}\right) r dr d\phi + f_{\text{LS}}} - \frac{u}{1 + f_{\text{LS}}}. \quad (3.16)$$

Here we illustrate the influence of the luminous lens effects on the centroidal shifts (and lightcurve) on top of a FSFL event in Fig. 3.8. Since the limb-darkening only slightly modifies the trajectory as shown in Fig. 3.6, we demonstrate the luminous lens effects in the FSFL regime assuming a uniform brightness source in Fig. 3.8. We show the luminous lens effects with various values for an apparent magnitude difference between the lens and source

$$\Delta m_{\text{LS}} = m_L - m_S = -2.5 \log_{10}(f_{\text{LS}}). \quad (3.17)$$

For illustrational purpose, we show the luminous lens effects on top of the FSFL for different sizes of the lens and the source in Fig. 3.9. When the lens is getting brighter, the trajectory becomes smaller and rounder. The signal of centroidal shift is thus reduced for a source blended by a luminous lens. The case of a PSPL events with luminous lens in Fig. 3.9 (upper-left corner) is comparable to the results of Jeong *et al.* (1999). Note that for the PSFL when $\rho_L = 1.3$ (lower-left corner), the trajectory vanishes when $\rho_L > \theta_+$ for the dark lens case (*black dotted line*), but follows the trajectory of the lens for luminous lens cases.

Since Eq. (3.16) gives us the full consideration of the FSFL effects with the brightness of the source and lens (note that we only need to consider the flux ratio between the lens and the source, so the limb-darkening effects of the lens does not need to be taken into account), one is able to derive the information of ρ_S , I_S , ρ_L , and f_{LS} by fitting the centroidal shifts. In principle one can fit both the centroidal shifts and the lightcurve, to utilize both the astrometric and photometric information and thus to have a better constrain on the events parameters in Eq. (3.16). Once the aforementioned parameters are all well determined, we can use the value of θ_E to derive both the size of the lens and the source. We can also derive the mass of the lens as shown in Eq. (3.2) given the information of the microlens parallax π_E . The distance to the lens is also available if the distance to the source is well-known, *e.g.* if the source is located in the Galactic bulge or Magellanic Clouds, which is often the case for the current microlensing surveys. In these cases, we are able to estimate the physical parameters of the whole microlensing systems.

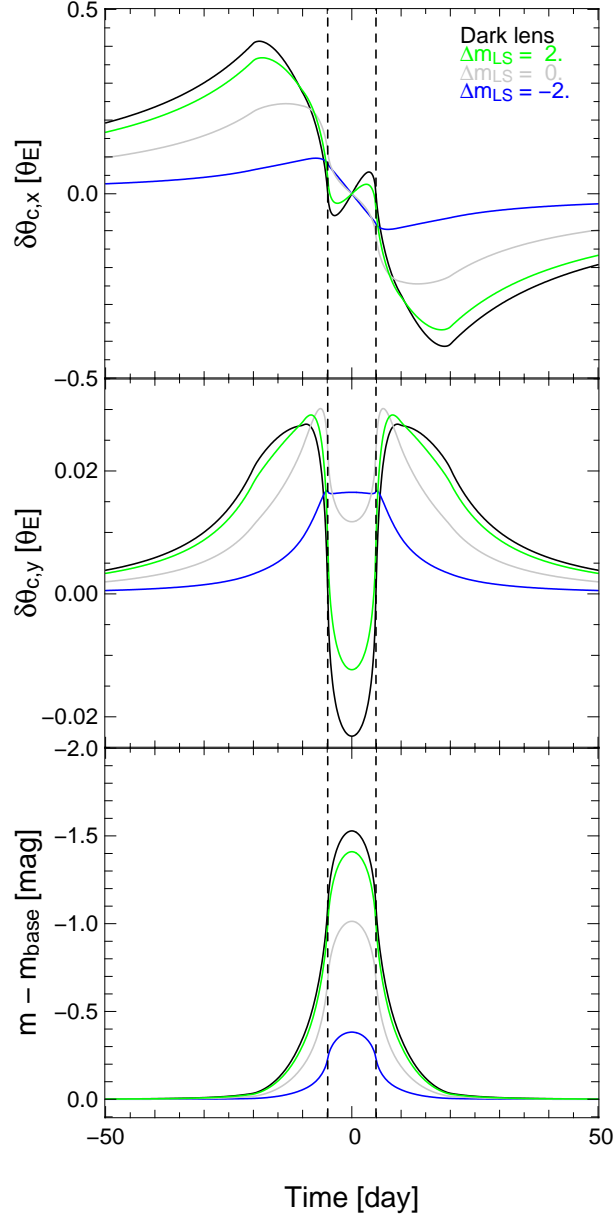


Figure 3.8: Centroidal shifts decomposition and lightcurves of a microlensing event assuming $u_0 = 0.1 \theta_E$, source radius = $0.5 \theta_E$ and lens radius = $0.5 \theta_E$. We show the trajectory in the x- and y-direction (as in Fig. 3.1) of a bright lens with $\Delta m_{LS} = -2$ (in blue), 0 (in gray), 2 (in green) and with a dark lens (in black). We also show the lightcurve with the magnitude variation relative to the baseline (m_{base}). The vertical dashed line indicates the time when $u_0 = \rho_s$.

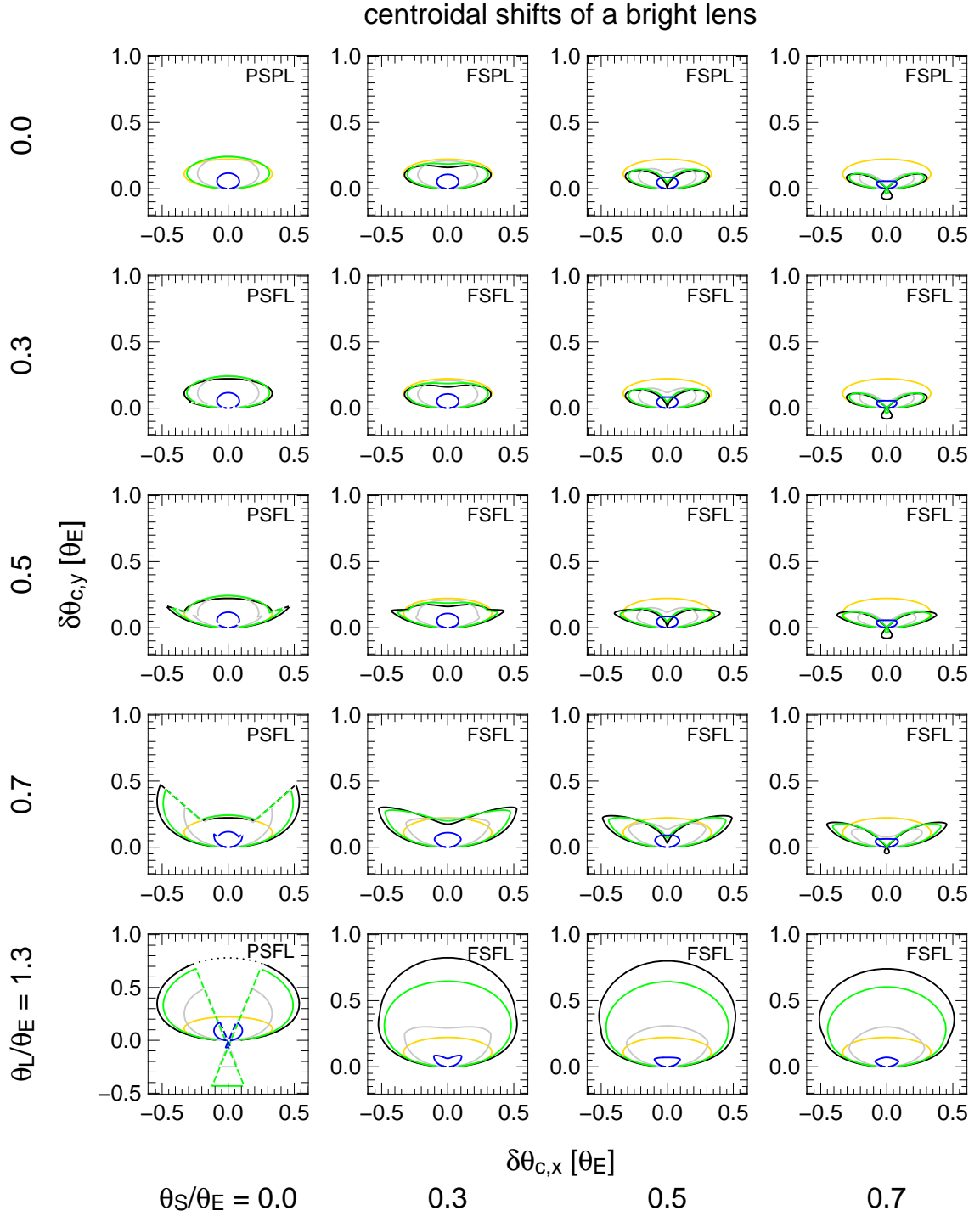


Figure 3.9: Centroidal shifts in the presence of FS and FL effects for a luminous lens. We show the examples for a PSPL (in yellow), FSFL with $\Delta m_{LS} = -2$ (in blue), 0 (in gray), 2 (in green) and with a dark lens (in black) assuming $u_0 = 0.5 \theta_E$ and with the sizes of the source and the lens varying from $0.3 \theta_E$ to $1.3 \theta_E$. The dashed lines in the plots with $\theta_S/\theta_E = 0.0$ show the discontinuity in the trajectories for the PSFL cases. The dotted lines in the PSFL with $\theta_L/\theta_E = 1.3$ indicates the trajectory when the lens totally obscures both the plus- and minus-image.

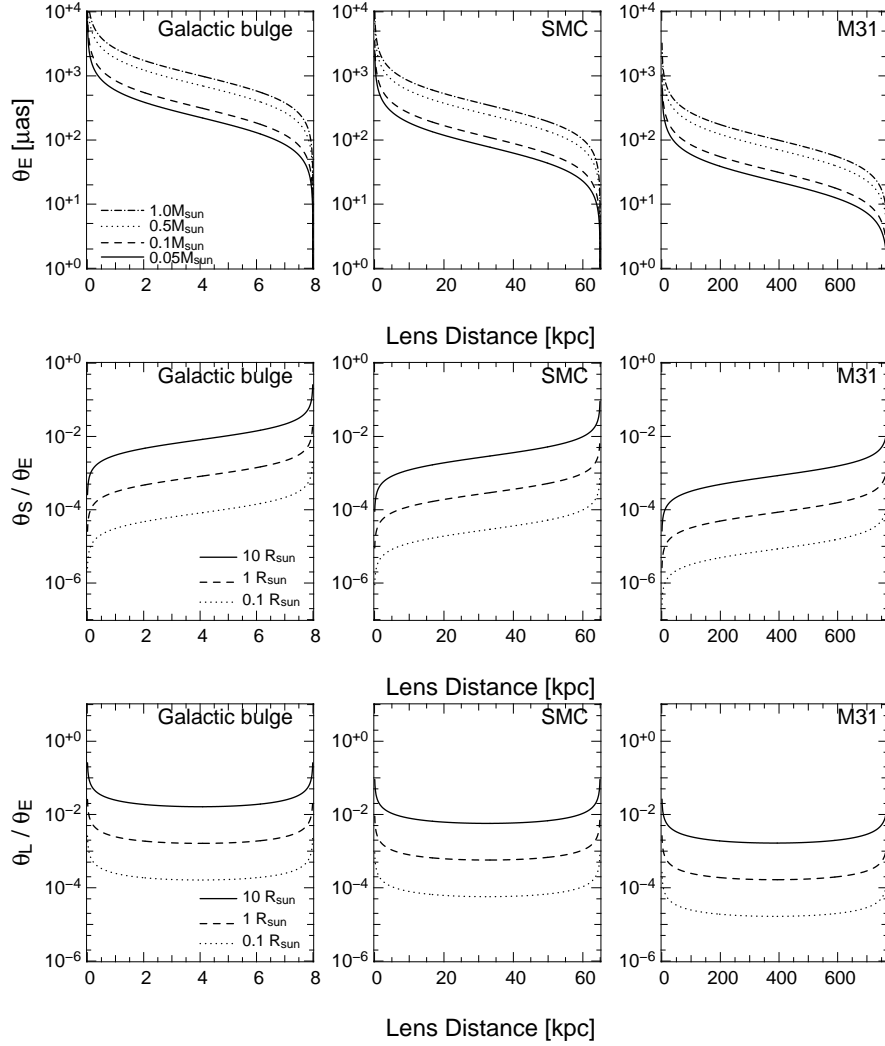


Figure 3.10: First row: θ_E as a function of D_{OL} assuming the source located in the Galactic bulge ($D_{OS} = 8$ kpc), SMC ($D_{OS} = 65$ kpc), and M31 ($D_{OS} = 770$ kpc). Second and third row: θ_S/θ_E and θ_L/θ_E as a function of the lens distance assuming $M_L = 0.5M_\odot$.

3.7 Observational Feasibility

In this section we consider the astrometric events towards the Galactic bulge, SMC and M31 assuming $D_{OS} = 8, 65,$ and 770 kpc, respectively. We substitute $D_{OL}/D_{OS} = x$ into Eq. (3.1), which then becomes

$$\theta_E = \sqrt{\frac{4GM_L}{c^2 D_{OS}} \left(\frac{1}{x} - 1 \right)} \quad . \quad (3.18)$$

Therefore, θ_E is smaller for a source located at larger distance and is smaller for larger lens distance given the same source location (see upper panels in Fig. 3.10).

Table 3.1: $D_{\text{OL}}(D_{\text{OS}} - D_{\text{OL}})/D_{\text{OS}}$ for several astrophysical objects.

Name	Radius (R_{\odot})	Mass (M_{\odot})	$\frac{D_{\text{OL}}}{D_{\text{OS}}}(D_{\text{OS}} - D_{\text{OL}})$
Sun	1.	1.	551 AU
Jupiter	0.1	0.001	5.5×10^3 AU
Earth	0.009	3×10^{-6}	1.5×10^4 AU
Brown dwarf	0.1	0.05	110 AU
White dwarf	0.009	1.	0.045 AU
Neutron star	2.8×10^{-5}	1.4	3.1×10^{-7} AU
Black hole	4.2×10^{-5}	10.	9.9×10^{-8} AU
Test case	10.	0.5	1.1×10^5 AU

Equation (3.18) also implies that the halo lensing events have larger Einstein radii than self-lensing events for a given lens mass. For instance, halo lensing events towards SMC with $D_{\text{OL}} = 15$ kpc and $M_{\text{L}} = 1 M_{\odot}$ mass will induce an astrometric signal with $\theta_{\text{E}} = 645 \mu\text{as}$, which is one order of magnitude larger than for self-lensing events ($44 \mu\text{as}$ at $D_{\text{OL}} = 64$ kpc). Thus we are able to distinguish halo and self-lensing events by the size of the astrometric ellipse.

The FS effects play an important role when $u_0 \leq \rho_{\text{S}}$, which is often the case when $u_0 \ll 1$ (Gould, 1994). However, such a configuration leads to a smaller centroidal shift (as shown in Fig. 3.1) and is thus very challenging to distinguish between the PSPL and FSPL trajectories observationally.

FL effects are prominent when ρ_{L} is close to and larger than unity (as shown in Fig. 3.7). We thus calculate ρ_{L} by dividing the angular lens radius θ_{L} by θ_{E} (see the lower panel in Fig. 3.10). Because θ_{L} is proportional to $1/x$ while θ_{E} is a function of $\sqrt{1/x-1}$, ρ_{L} is actually a function of $(x(1-x))^{-1/2}$. We would expect to see the FL effects when the lens is located either close to the observer ($x \approx 0$) or to the source ($x \approx 1$). By equating θ_{L} to θ_{E} , we have

$$\frac{D_{\text{OL}}}{D_{\text{OS}}}(D_{\text{OS}} - D_{\text{OL}}) = \frac{R_{\text{L}}^2 c^2}{4GM_{\text{L}}}. \quad (3.19)$$

The left-hand side of this equation gives us the information on the location of the lens to have prominent FL effects (Agol, 2002). If the lens is very close to the observer such that $D_{\text{OL}} \ll D_{\text{OS}}$, Eq. (3.19) gives us an upper limit of D_{OL} so that for lenses beyond this value, the FL effect is not prominent. On the other hand, if the lens is very close to the source so that $D_{\text{OL}} \approx D_{\text{OS}}$, then Eq. (3.19) actually gives us a maximum separation between the lens and the source in order to have non-negligible FL effects. The value of $D_{\text{OL}}(D_{\text{OS}} - D_{\text{OL}})/D_{\text{OS}}$ for several astrophysical objects are given in Table 3.1.

We then calculate the maximum centroid deviation versus lens distance for the cases of PSPL, PSFL, FSPL, and FSFL assuming that a source of $10 R_{\odot}$ is amplified by a lens of $0.5 M_{\odot}$ and $10 R_{\odot}$ with the minimum lens-source separation projected onto the sky to be $0.05 \theta_{\text{E}}$. Because there are only small differences between PSPL, PSFL, FSPL, and FSFL, we only show the case of PSPL in Fig. 3.11. To see how much the FL trajectory deviates from that of PL and the influence from FS, we further calculate the maximum difference between the PSPL, PSFL, and FSFL trajectories at a given time. The result is shown in Fig. 3.11 for a lens with $\Delta m_{\text{LS}} = 2, 0, -2$ and a dark lens. The FSFL only shows small difference to that of PSFL and PSPL. The difference is less than $10 \mu\text{as}$ for the case of Galactic bulge, and even smaller than $1 \mu\text{as}$ for the more distant source in the SMC and M31. This is because the FL effect is important only when the lens is extremely close to the observer or the source and the

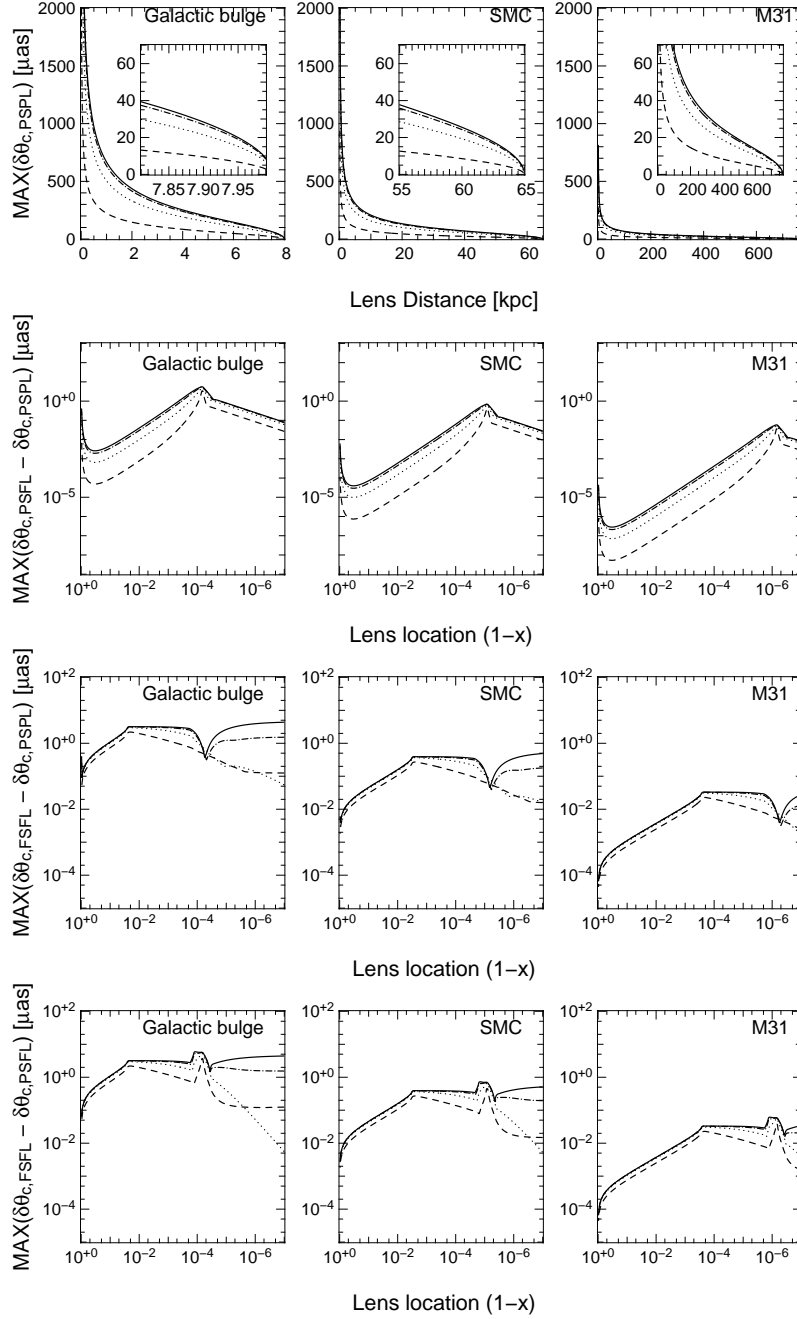


Figure 3.11: First row: Maximum centroidal shifts as a function of D_{OL} assuming the source located in the Galactic bulge ($D_{\text{OS}} = 8$ kpc), SMC ($D_{\text{OS}} = 65$ kpc), and M31 ($D_{\text{OS}} = 770$ kpc) in PSPL. Second row: Maximum deviation between the PSFL and PSPL trajectories as a function of the lens location $(1-x)$, where $x = D_{\text{OL}}/D_{\text{OS}}$. Third row: Maximum deviation between the FSFL and PSPL trajectories. Fourth row: Maximum deviation between the FSFL and PSFL trajectories. We assume $u_0 = 0.05 \theta_E$, $t_E = 10$ days, $M_L = 0.5 M_\odot$, $R_L = 10 R_\odot$, and $R_S = 10 R_\odot$. Here we show the cases of a luminous lens with $\Delta m_{\text{LS}} = 2$ (in dashed), 0 (in dotted), -2 (in dash-dotted), and a dark lens (in solid).

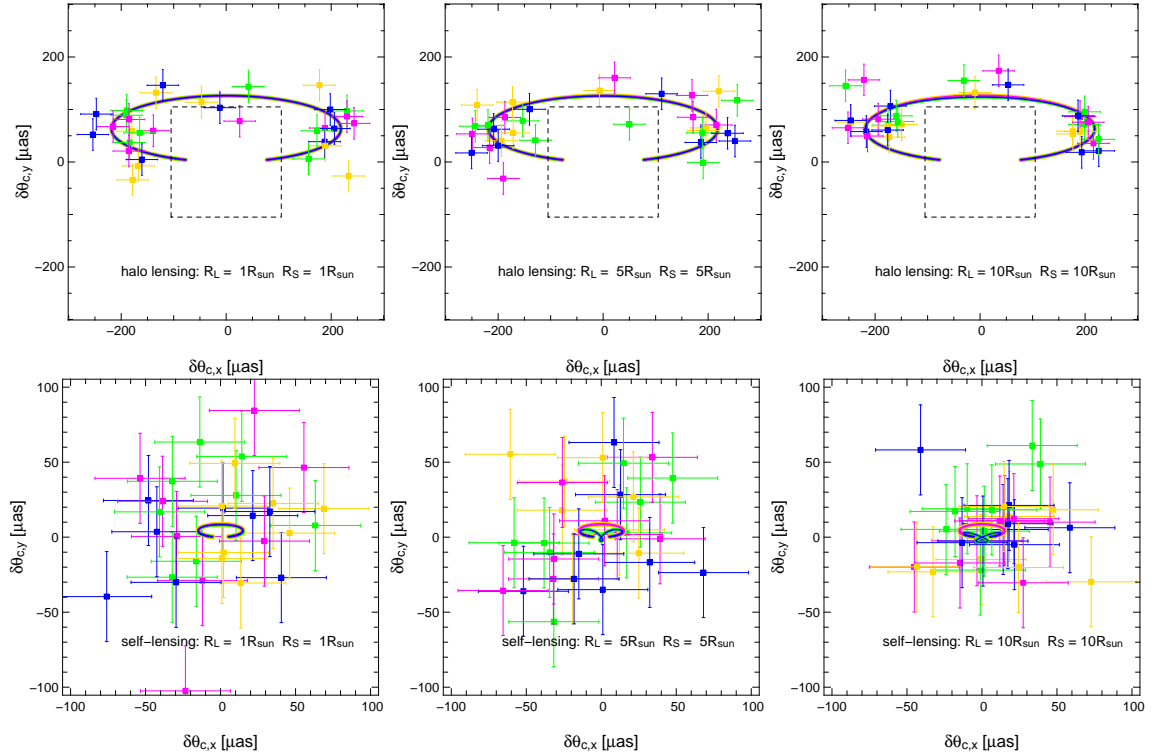


Figure 3.12: Astrometric trajectory of the SMC microlensing event MACHO-97-SMC-1 with $t_E = 123.5$ days and $u_0 = 0.426824 \theta_E$. We show the case when the lens is located in the Galactic halo (upper panels) and in SMC (lower panels). We assume the lens is $1 M_\odot$ and the size of the lens and the source are assumed to be 1, 5, and $10 R_\odot$, respectively. The color convention is the same as Fig. 3.4. We calculate the theoretical trajectory within a time interval of $t_0 \pm 1000$ days. We then simulate the measurements of *SIM*, with a sampling rate of every 90 days spanning for $t_0 \pm 1$ year and $30 \mu\text{as}$ error in both x and y direction. The dashed square in the halo lensing cases outlines the dimension showed in the self-lensing regime.

major difference between FSFL and PSPL or PSFL comes from the finiteness of the source. Since u_0 is larger than ρ_s for most of the time, the FS effect only slightly changes the astrometric trajectory. Even when the lens is extremely close to the source (see Fig. 3.11), the already reduced θ_E makes the difference so small that it is hardly observable.

In order to test if the astrometric signal is observable towards SMC, we simulate the astrometric trajectory of MACHO-97-SMC-1 (Alcock *et al.*, 1997b). This event has baseline magnitude $V = 17.7$, so it will take *SIM* ~ 3 hours to reach $30 \mu\text{as}$ accuracy (Goullioud *et al.*, 2008). We thus simulate observations by *SIM* assuming the measurement errors to be Gaussian distribution with $\sigma = 30 \mu\text{as}$. We put the lens at a distance of 15 kpc and 64 kpc corresponding to the halo and self-lensing scenario towards SMC. We then assign a putative finite-size of 1, 5, and $10 R_\odot$ to the lens and the source. The mass of the lens is set to be $1 M_\odot$. From Fig. 3.12 we can see that if the lens is in the Galactic halo, we are able to detect the astrometric signal because of the very large θ_E . However, the finite-size of the source and the lens is not revealed in such a close lens. On the other hand, the FS and FL effects are prominent in the self-lensing regime due to the small θ_E . But the astrometric trajectory is too small

to be constrained by current instruments, not to mention to disentangle between the PSPL and FSPL or PSFL. Nevertheless, it is still possible to use the (non)detection of the astrometric ellipse to infer if the lens is in the Galactic halo or it is a self-lensing event towards SMC.

We also considered the possibility to detect the astrometric trajectory from ground-based instruments such as *PRIMA* for VLTI. *PRIMA* can determine the astrometry to $10 \mu\text{as}$ level in 30 minutes provided a reference star within 10 arcsec and a 200 m baseline (ATs mode). The goal of *PRIMA* is to perform astrometric measurement for a target as faint as 18 (15) mag with UTs (ATs) provided a 13 (10) mag reference star in *K* band (Delplancke, 2008). There is a bright star ($K = 10.28$) in the vicinity of MACHO-97-SMC-1 (separated at 30.4 arcsec), so theoretically it would be possible to obtain $30 \mu\text{as}$ accuracy in astrometric measurements within one hour with the UTs (130 m baseline). However, for the two stars separated by 20 arcsec, there is already 90% reduction in the interferometric fringe visibility. Thus it would be very challenging to conduct such measurement. It would be very difficult to routinely measure the astrometry towards SMC/LMC with *PRIMA* because most of the single lens events in the Magellanic Clouds (14 out of 15, except MACHO-97-SMC-1) have sources fainter than 19 mag in *V* (1 in Alcock *et al.*, 1997b; 12 in Alcock *et al.*, 2000; 1 in Tisserand *et al.*, 2007, which is the same as Alcock *et al.*, 1997b, and 2 in Wyrzykowski *et al.*, 2009).

To perform astrometric measurements for microlensing events towards M31 is beyond the limit of both *PRIMA* and *SIM* since the sources in M31 are too faint (see *e.g.* Riffeser *et al.*, in preparation, and reference therein).

3.8 Conclusion

We have studied the astrometric aspects of microlensing by simultaneously including the FS and FL effects. Our results show that the astrometric signal is under- or over-estimated by assuming PL or PS, respectively. While the FS effect is prominent when the lens transits the surface of the source, the FL effect is revealed when the lens is very close to the source, which would be in the self-lensing regime. In the context of the self-lensing scenario, where a background star is lensed by a foreground star, the light contribution from the lens is in general not negligible. We thus consider the luminous lens scenario, which attenuates the signal of the centroidal displacement. Astrometric trajectories with a source located in the Galactic bulge, SMC, and M31 are discussed, which show that θ_E of halo lensing events is at least one order of magnitude larger than that of self-lensing in SMC and M31. Our results also indicate that the finiteness of the lens is more likely to be revealed in the self-lensing scenario towards distant source located in Magellanic Clouds or M31, although it is very difficult to distinguish between PL and FL with current instruments.

Chapter 4

Properties of Andromeda galaxy (M31)

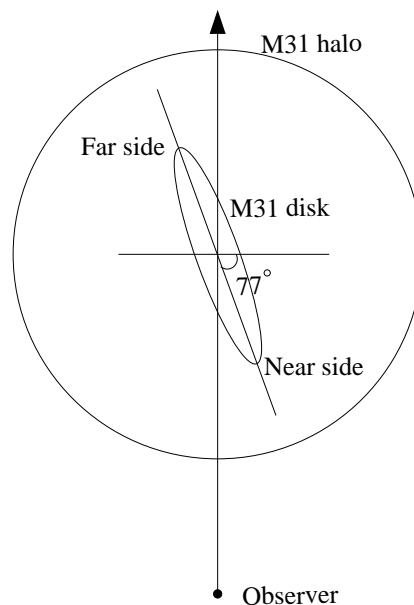


Figure 4.1: A schematic view of M31 as seen from an observer on Earth.

The Andromeda galaxy (M31), a SA(s)b type spiral galaxy (de Vaucouleurs *et al.*, 1991) at a distance of 770 kpc (Madore & Freedman, 1991), is the twin galaxy of our Milky Way. Because of its proximity and similarity to our Galaxy, M31 is a good candidate for microlensing experiments to explore the halo content of spiral galaxies. The M31 disk is inclined by about 77 degrees (Walterbos & Kennicutt, 1987) along the line of sight. The line of sight to stars in the far side of the disk therefore passes through a higher line-of-sight projected dark matter halo density (see Fig. 4.1). If part of this dark matter is composed of MACHOs, microlensing will be more likely towards the far side of the disk. In fact, it has first been noted by Crotts (1992) that the detection of an asymmetry of the microlensing event rate between the far and near side is one signature for a MACHO-halo component. To quantitatively interpret the microlensing events towards M31, we require the understanding of properties of M31, e.g. surface brightness profile (see Fig. 4.2), extinction, stellar population, etc.. The dependencies of the event rate on these quantities can be seen in the equation derived by Riffeser *et al.* (2006).

This equation describes the contribution to the total event rate in terms of event location (x,y) on the plane of sky, in terms of t_{FWHM} of the event, the $(r-i)$ color \mathcal{C} of the event and flux excess Δ_F at light curve maximum.

$$\begin{aligned} \frac{d^5 \Gamma(x,y,t_{\text{FWHM}},\Delta_F,\mathcal{C})}{dx dy dt_{\text{FWHM}} d\Delta_F d\mathcal{C}} &= \sum_s \sum_l \frac{2}{t_{\text{FWHM}}^3} \int_0^\infty \xi(M) \int_{-\infty}^{+\infty} p_{\text{cmd}}(\mathcal{M},\mathcal{C}) \int_0^\infty n_s(x,y,D_{\text{OS}}) \\ &\times \left[\frac{\Psi}{F_0} \int_0^{D_{\text{ol}}^*} \rho(x,y,D_{\text{ol}}) R_E^3 p_{v_t}(v_t) dD_{\text{ol}} + \Omega^* \rho(x,y,D_{\text{ol}}^*) R_E^{*3} \int_0^{u_0^*} p_{v_t}(v_t^*) \Upsilon^{*2} du_0 \right] dD_{\text{OS}} d\mathcal{M} dM. \end{aligned} \quad (4.1)$$

The sums over s and l extend over all source and lens components of M31 (bulge and disk stars can serve as sources to be lensed and as lenses, the unknown halo MACHO component acts as lenses only). On the right hand side of this equation is the stellar and MACHO mass function $\xi(M)$ (which itself is normalized to $\int \xi(M) M dM = 1$; see Binney & Tremaine (1987), p. 747). If the event rates are well measured and detection efficiencies are known, and if the remaining quantities on the right hand side are known, $\xi(M)$ can be determined in particular for the bulge stars and for the halo MACHO component. The remaining quantities are defined by the M31 model under consideration and they are: i) $p_{\text{cmd}}(\mathcal{M},\mathcal{C})$, the color-magnitude relations of stars; ii) $n(x,y,D_{\text{OS}})$, the line-of-sight spatial density of sources at position (x,y) on the plane of sky and at a distance D_{OS} . This can be constrained by the observed light of the stellar population (see Fig. 4.3). iii) $\rho(x,y,D_{\text{OL}})$, the mass density of lenses at position (x,y) on the sky and at a distance D_{OL} . This depends on the dynamical model under consideration; iv) the Einstein radius R_E (as defined in Chapter 1) is a combination of the mass of the lens and the relative distance between the observer, lens and source; v) $p_{v_t}(v_t)$, the transversal projected lens-source velocity probability at velocity v_t . Equation (4.1) includes events under point-source and finite-source regimes simultaneously. In the bracket of equation (4.1), the first term deals with point-source events, i.e. when $u_0 > \rho_s \approx R_* D_{\text{OL}} (2R_E D_{\text{OS}})$ (see equations. [65] and [66] in Riffeser *et al.* (2006)). In this equation ρ_s is the size of the source star in units of the Einstein radius. The second term takes into account the extended nature of the source. We use [67] in Riffeser *et al.* (2006) when $u_0 < \rho_s$. For clarity, functions related to the finiteness of the source ($R_*(\mathcal{M},\mathcal{C})$) are marked with “*”.

Equation (4.1) contains the following functions:

$$\begin{aligned} u_0 &= \left[2A_0(A_0^2 - 1)^{-1/2} - 2 \right]^{1/2} \\ \Upsilon(\Delta_F/F_0 + 1) &= \Upsilon(A_0) = 2\sqrt{u \left(\frac{A_0+1}{2} \right)^2 - u(A_0)^2} = \sqrt{8 \frac{[(A_0+1)^{3/2} - A_0(A_0+3)]^{1/2}}{[(A_0-1)(A_0+1)(A_0+3)]^{1/4}}}; \\ \Psi(\Delta_F/F_0 + 1) &= \left| \frac{du_0}{dA_0} \right| \Upsilon^2(A_0) = 4\sqrt{2} \frac{[A_0 + (A_0^2 - 1)^{1/2}]^{1/2} [(A_0+1)^{3/2} - A_0(A_0+3)]^{1/2}}{(A_0^2 - 1)^{7/4} (A_0+3)^{1/2}}; \\ D_{\text{ol}}^*(R_*, D_{\text{OS}}, M, \Delta_F, F_0) &= D_{\text{OS}} \left(1 + \frac{\Delta_F(2F_0 + \Delta_F)}{C D_{\text{OS}}} \right)^{-1} \quad \text{with } C := \frac{16F_0^2 GM}{c^2 R_*^2}; \\ u_0^*(R_*, D_{\text{OL}}, D_{\text{OS}}, M) &= \left\{ 2 \left[1 + \left(\frac{R_* D_{\text{OL}}}{2R_E D_{\text{OS}}} \right)^2 \right]^{1/2} - 2 \right\}^{1/2}, \text{ with}; \\ \Omega^*(\Delta_F, D_{\text{OS}}, F_0, M, R_*) &= \left| \frac{dD_{\text{ol}}^*(\Delta_F)}{d\Delta_F} \right| = 2C D_{\text{OS}}^2 (F_0 + \Delta_F) [C D_{\text{OS}} + \Delta_F (2F_0 + \Delta_F)]^{-2}; \\ \Upsilon^*(u_0, R_*, D_{\text{OL}}, D_{\text{OS}}, M) &= 2\sqrt{\frac{2(A_0^*+1)}{\sqrt{(A_0^*-1)(A_0^*+3)}} - 2 - u_0^2} \quad \text{with } A_0^* = \sqrt{1 + \left(\frac{2R_E D_{\text{OS}}}{R_* D_{\text{OL}}} \right)^2}; \\ v_t(D_{\text{OL}}, D_{\text{OS}}, M, t_{\text{FWHM}}, \Delta_F, F_0) &= \frac{R_E}{t_{\text{FWHM}}} \Upsilon^*; \\ v_t^*(u_0, D_{\text{OL}}, D_{\text{OS}}, M, t_{\text{FWHM}}, R_*) &= \frac{R_E}{t_{\text{FWHM}}} \Upsilon^{*2}; \end{aligned}$$

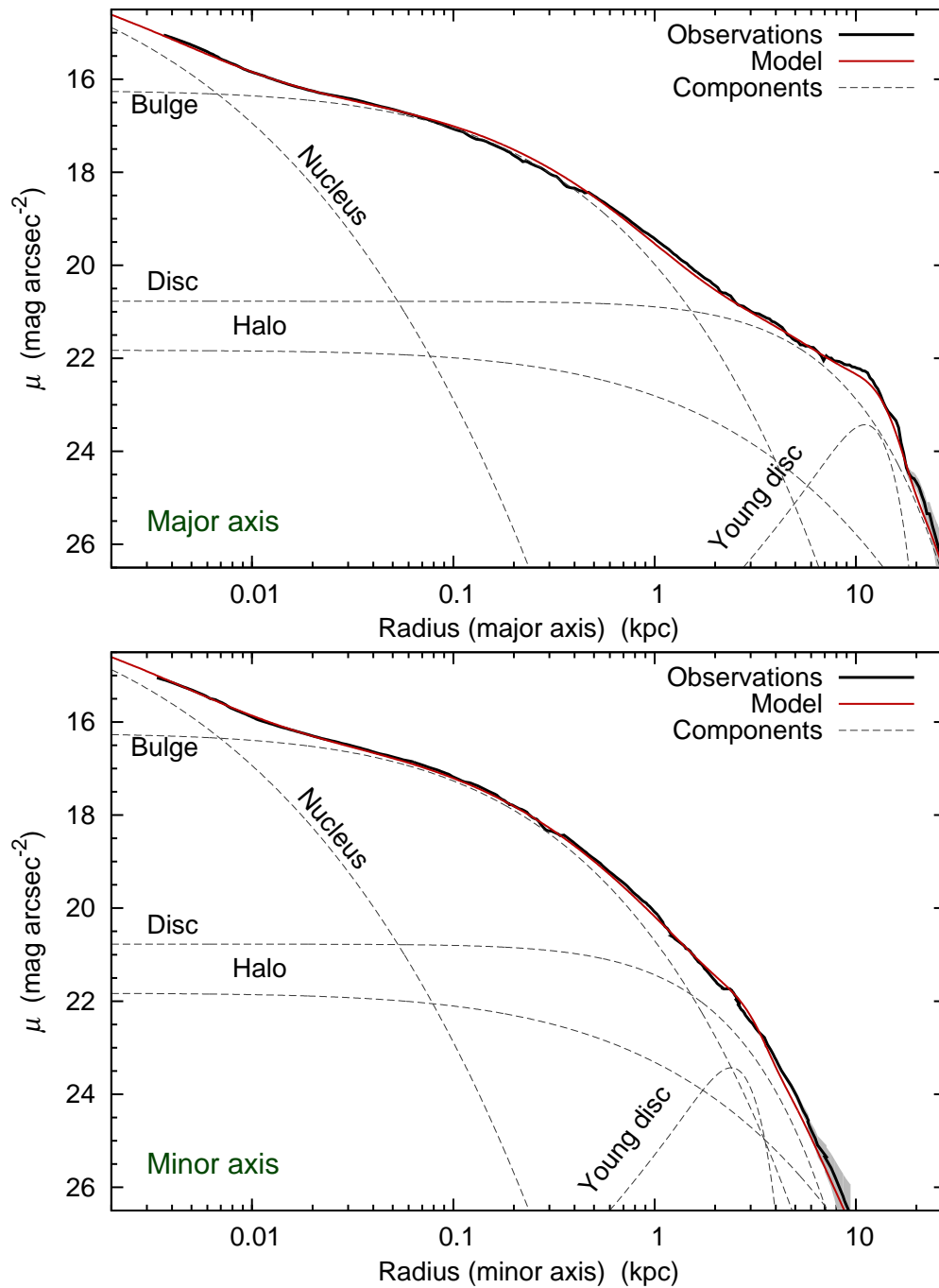


Figure 4.2: M31 surface brightness (SFB) profile derived from SDSS g -band data by [Tempel *et al.* \(2011\)](#). The black solid line is the SFB measured from the SDSS data. They also generate a model for SFB (red solid line) and give the individual components contribute to the SFB (dashed line). Upper panel shows the SFB along the major axis of M31, while the lower panel is the SFB along the minor axis.

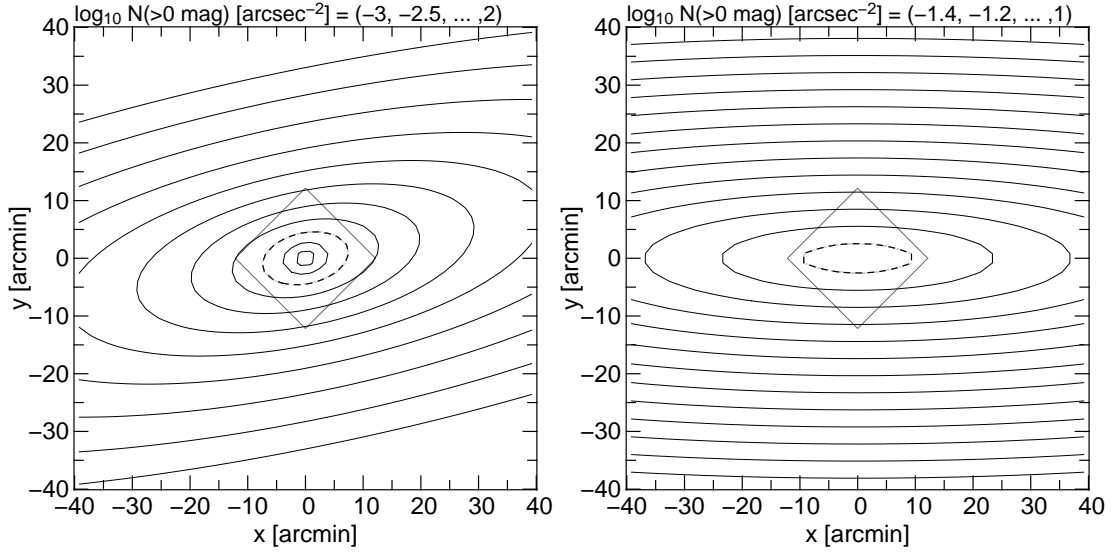


Figure 4.3: Number density (N) of the bulge stars (*left*) and the disk stars (*right*) with the absolute magnitude \mathcal{M}_R brighter than 0 mag in units of stars per arcsec^2 . The contours demonstrate the value of $d^2N/(dx dy)|_{\mathcal{M}_R \leq 0} = \int_{-\infty}^0 \int_0^{\infty} \tilde{\Phi}(\mathcal{M}_R) n_S(x, y, D_{\text{os}}) dD_{\text{os}} d\mathcal{M}_R$ with the interval listed above the figure. It is obtained from the number density and luminosity functions of the bulge and disk of M31. The dashed contour indicates $\log_{10}N = 1$ and implies that even giant stars in the center of M31 are not resolvable for most of the ground-based observatories. The $17'.2 \times 17'.2$ field of view of the WeCAPP campaign is outlined by a box. Adopted from [Riffeser et al. \(2006\)](#).

All ingredients - dynamical model, stellar population model and dust extinction - have been known to some degree for M31 already ([Kent \(1989\)](#); [McElroy \(1983\)](#); [Hodge & Lee \(1988\)](#); [Xu & Helou \(1996\)](#)). To improve these models we have taken and analyzed spectra of the M31 bulge within our group. The work led by R. P. Saglia ([Saglia et al., 2010](#)) has shown that the M31 bulge is a factor of 2 more massive than previously estimated. It is old (> 12 Gyr) and it is of solar metallicity and slightly α -element overabundant ($[\alpha/\text{Fe}] \sim 0.2$). The very same data will be taken as well to derive a improved M31 dynamical model.

The equation (4.1) demonstrates that for a quantitative microlensing analysis the density and velocity distribution of stars and dark matter test particles (MACHOs) have to be known, and that also the stellar population content (color-magnitude diagram of source stars, size of source stars) has to be known. This is also the case for extinction by dust, because it makes the number of stars that produce the observed combined stellar luminosity larger than estimated without extinction, but it also dimms a microlensing event.

Finally, our group has also analyzed Spitzer, GALEX and SDSS M31 data to constrain the dust properties and derive extinction maps along the M31 line of sight. The result of this work led by M. Montalto ([Montalto et al., 2009](#)) are:

- The mean intensity of the radiation, which is typically below two times the value in the solar neighborhood.
- Although the dust mass M_{dust} is only weakly constrained by the infrared spectrum due to a lack

of submillimeter observations, we derive a lower limit of $M_{\text{dust}} \leq 1.1 \times 10^7 M_{\odot}$ with a best-fit model value of $7.6 \times 10^7 M_{\odot}$.

- In 83% of the regions analyzed across the 10 kpc ring, the dust absorbs more than 50% of the energy at $\lambda > 4000 \text{ \AA}$ and it appears to be mainly heated by populations a few Gyr old.
- The attenuation varies radially and reaches a maximum near 10 kpc. It decreases more rapidly as a function of the radius in the inner regions of M31 than in the outer region;
- An attenuation map of M31 has been produced and applied to SDSS i -band image (see Fig. 4.4).

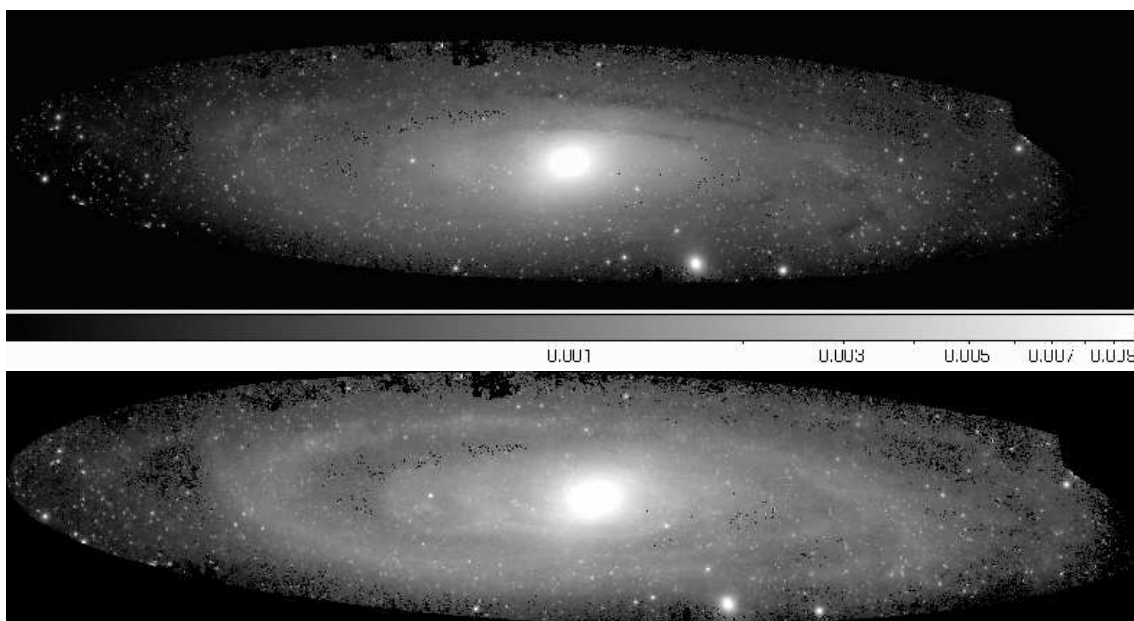


Figure 4.4: Upper panel: SDSS i' -band image without correction of extinction. Lower panel: SDSS i' -band image dereddened with extinction map by [Montalto *et al.* \(2009\)](#). The colorbar indicates the logarithmic intensity levels in the units of Jansky. The resolution of the images is $6''/\text{pixel}$. Adapted from [Montalto *et al.* \(2009\)](#).

My main contribution to this work was to recalibrate public SDSS M31 data photometrically. The images from SDSS are obtained in two scans, each containing six columns of CCDs, giving a total number of 12 scanlines parallel to the major axis of M31. We use the 55 arcsec overlapping area among the scanlines and bring all the images to the same photometric basis for further analysis.

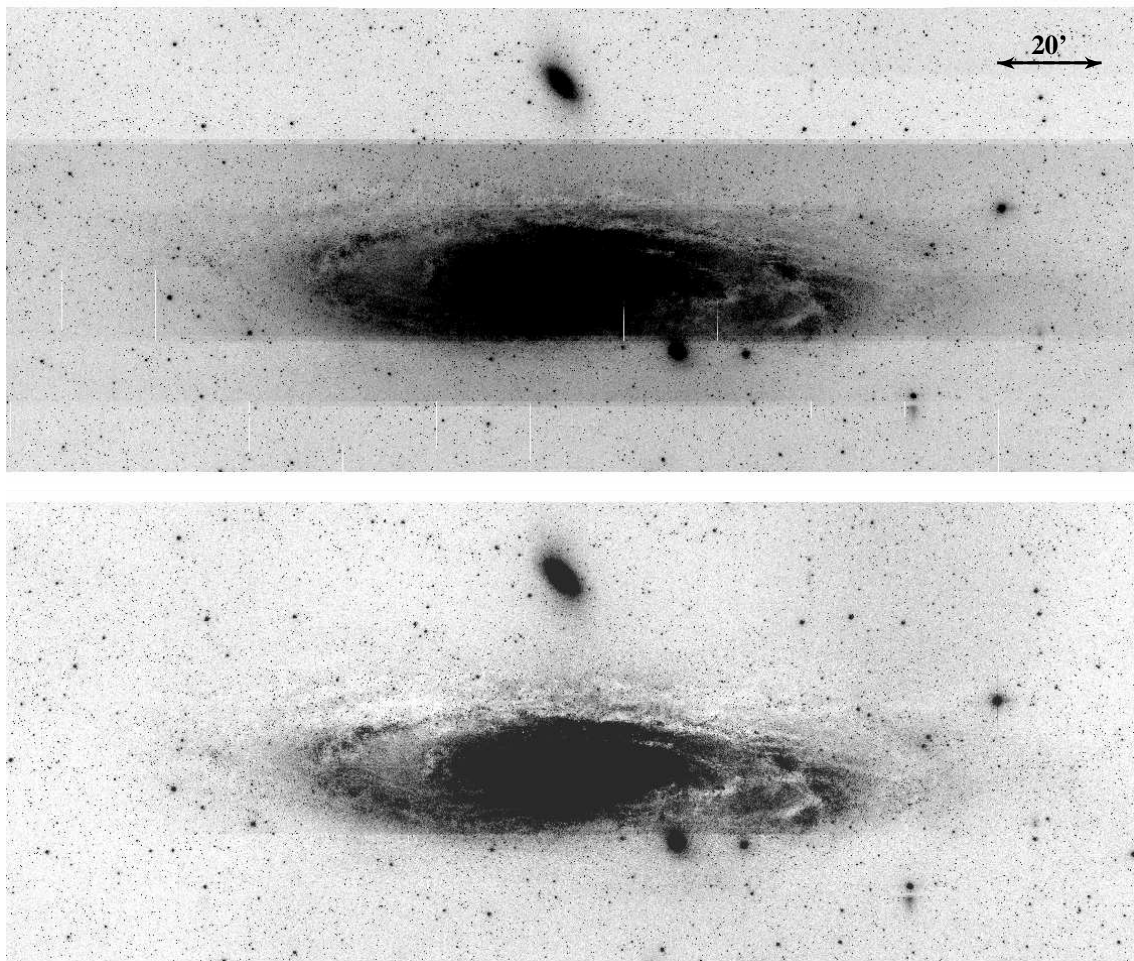


Figure 4.5: Upper panel: SDSS g' -band image before photometric alignment for the different drift scan runs. Lower panel: SDSS g' -band image after photometric alignment for the different drift scan runs.

Chapter 5

The Wendelstein Calar Alto Pixellensing Project (WeCAPP): the M31 Nova catalogue

This chapter, except appendix C, has been submitted to A&A ([Lee *et al.*, 2011 submitted](#)).

5.1 Abstract

We present light curves from the novae detected in the long-term, M31 monitoring WeCAPP project. The goal of WeCAPP is to constrain the compact dark matter fraction of the M31 halo with microlensing observations. As a by product we have detected 90 novae benefiting from the high cadence and highly sensitive difference imaging technique required for pixellensing. We thus can now present the largest CCD and optical filters based nova light curve sample up-to-date towards M31. We also obtained thorough coverage of the light curve before and after the eruption thanks to the long-term monitoring. We apply the nova taxonomy proposed by Strobe *et al.* (2010) to our nova candidates and found 29 S-class novae, 10 C-class novae, 2 O-class novae and 1 J-class nova. We have investigated the universal decline law advocated by Hachichu and Kato (2006) on the S-class novae. In addition, we correlated our catalogue with the literature and found 4 potential recurrent novae. Part of our catalogue has been used to search for optical counter-parts of the super soft X-ray sources detected in M31 (Pietsch *et al.* 2005). Optical surveys like WeCAPP, and coordinated with multi-wavelength observation, will continue to shed light on the underlying physical mechanism of novae in the future.

5.2 Introduction

Classical novae span a subclass of cataclysmic variables, consisting of a white dwarf which interacts with a late-type companion star. The companion loses its mass through Roche lobe overflow, forming an accretion disk around the white dwarf. The mass transfer from the companion induces thermonuclear runaway (TNR) onto the surface of the white dwarf, which leads to the nova eruption. Novae are important in several aspects. First of all, they have the potential to serve as standard candles of extra-galactic distance indication. This is due to the relation between the maximum luminosity of the light curve and the rate of decline. [Hubble \(1929\)](#) first noticed that brighter novae are prone

to steeper decline. The empirical ‘Maximum Magnitude versus Rate of Decline’ (MMRD) relation was further investigated by Zwicky (1936) and studied quantitatively by McLaughlin (1945) and Arp (1956). The theoretical foundation for MMRD relation is laid down by Shara (1981) and further revised by Livio (1992).

Novae do also shed light on the underlying stellar population of the environment. For example, della Valle & Livio (1995) point out that fast novae ($t_2 < 12$ days) are related to stars belonging to Population I with relatively massive white dwarfs, while slow novae are associated to Population II stars and have less massive white dwarfs.

In addition, novae play a role in the galactic abundances. Novae have been considered as major sources of galactic ^{13}C , ^{15}N and ^{17}O , and minor contributors to ^7Li , ^9F and ^{26}Al . However, novae hardly contribute to the overall galactic metallicity compared to supernovae or AGB stars, because only 10^{-4} to $10^{-5}M_{\odot}$ are ejected per nova outburst (José & Hernanz, 2007).

Recurrent novae are also regarded as possible supernovae progenitor candidates (see e.g. Schaefer, 2010, and reference therein.). The fundamental question is whether recurrent novae accumulate enough mass onto the central white dwarf envelope and turn into supernovae progenitors even after several novae explosions.

Last but not the least, novae are main contributors to the class of super soft X-ray sources (SSS). Pietsch *et al.* (2005) searched for X-ray counterparts of the optical novae in M31, and found that novae are major sources of soft X-ray emission. The SSS phase can provide us with information on the white dwarf mass, the ejected and burned mass in the outburst (e.g. Pietsch, 2010).

Due to the interstellar extinction in the Galactic disk, we can only observe a small fraction of the Galactic novae that erupt each year (Shafter, 1997). Thus, we need to take into account rather large (and likely uncertain) corrections for incompleteness when determining the spatial distribution or estimation of the Galactic nova rate. In such case, M31 is an ideal target for a novae survey because novae are still bright enough to be observed ($m_R < 20$ mag) and it is possible to cover the entire M31 galaxy within several pointings.

Novae monitoring campaigns towards M31 can be dated back to the pioneering work done by Hubble in 1920s (Hubble, 1929).

A list of all the campaigns with published novae in M31 that we are aware of is shown in Table 5.2, with most of the data compiled by Shafter & Irby (2001) and Darnley *et al.* (2004).

Despite the extensive search towards M31, most of previous studies have only sparse observations and thus make the analysis of nova light curve rather difficult. Our WeCAPP project is dedicated to monitoring M31 with upto daily sampling for a duration of 11 years. The use of two filters (R and I -band) for the novae observations partly compensates for not having used an $\text{H}\alpha$ filter as it was done in previous studies. Instead of observing the $\text{H}\alpha$ strength we least can measure the color evolution of the novae.

This paper is organized as following. In Sec. 5.3 we describe the observations and data reduction. In Sec. 5.4 we present our novae detection algorithm. In Sec. 5.5 we categorize our nova candidates according to the classification scheme of Strope *et al.* (2010). We apply the power-law decline proposed by Hachisu & Kato (2006) to fit the smooth class light curves in Sec. 5.5.1. Novae showing cusp, oscillation or jitter features in their light curves are presented in Sec. 5.5.2 - Sec. 5.5.4. We then correlate our nova candidates with literature to search for recurrent novae in Sec. 5.6 and end the paper with the conclusions in Sec. 5.7. All the light curves in our catalogue are presented in the Appendix.

Table 5.1: Principal M31 classical nova surveys

Author(s)/Project	Epoch	Filter(s)	Detector	Novae	#/yr	Reference(s)
Hubble	1909–1927	B	Plates	85	~ 30	Hubble (1929)
Arp	1953–1954	B	Plates	30	24 ± 4	Arp (1956)
Rosino <i>et al.</i>	1955–1986	B	Plates	142	-	Rosino (1964, 1973) Rosino <i>et al.</i> (1989)
Ciardullo <i>et al.</i>	1982–1986	B, H α	CCD	40	-	Ciardullo <i>et al.</i> (1987, 1990)
Sharov & Alksins	1969–1989	B	Plates	21	-	Sharov & Alksnis (1991)
Tomaney & Shafter	1987–1989	H α	CCD	9	-	Tomaney & Shafter (1992)
Shafter & Irby	1990–1997	H α	CCD	72	37^{+12}_{-8}	Shafter & Irby (2001)
Rector <i>et al.</i>	1995–1999	H α	CCD	44	-	Rector <i>et al.</i> (1999b)
AGAPE	1994–1996	<i>R, I</i>	CCD	12	-	Ansari <i>et al.</i> (2004)
POINT-AGAPE	1999–2002	<i>r', i', g'</i>	CCD	20	65^{+16}_{-15}	Darnley <i>et al.</i> (2006)
NMS	2001–2002	<i>R, I</i>	CCD	2	-	Joshi <i>et al.</i> (2004)
WeCAPP	1997–2008	<i>R, I</i>	CCD	90	-	This work

5.3 Observations and Data Reduction

The WeCAPP project (Riffeser *et al.*, 2001) was a dedicated survey to search for microlensing events towards our neighboring galaxy M31. We continuously monitored the bulge of M31 (when it was visible, when the weather was cooperative and when there was an observer) between September 1997 and March 2008 using the 0.8 m telescope of the Wendelstein Observatory located in the Bavarian Alps. The data was taken optimally on a daily basis in both *R* and *I* filters with a field of view of $8'.3 \times 8'.3$. From June 1999 to February 2002 we further extended our observations with the 1.23 m ($17'.2 \times 17'.2$ FOV) telescope of the Calar Alto Observatory in Spain.

The data volume and quality of the four pointings (F1, F2, F3, F4) drastically differs during the 11 seasons.

A detailed overview of the data is given in Riffeser *et al.* (in prep.).

To quantify a realistic time sampling of the survey we define “good quality data points” as data points with PSF fluxes with an error below $0.4 \times 10^{-5} \text{ Jy}$. In Fig. 5.1 we show for every night the fractional area of pixels with errors below this limit. 0% indicates we have no observations during the night.

Fig. 5.2 shows the spatial variation of the fraction of all data with flux errors below the flux error limit averaged over 11 seasons. It demonstrates that we expect most of our novae in field F1 and fewer in the fields F2, F3, and F4. The field F1 was observed much more frequently than the other one because it is the subfield with highest lensing probability.

The data was then reduced by our customized pipeline MUPIPE (see Gössl & Riffeser, 2002), which performs CCD reduction, position alignment, photometric alignment, frame stacking and difference imaging following the algorithm of Alard & Lupton (1998).

After the difference imaging, we perform PSF photometry on each pixel as follows. First, we extracted the PSF from several isolated, bright and unsaturated reference stars. Then we fit this PSF to all variable sources. Finally, we integrate the count rates over the area of the PSF to determine the flux of the source.

The results of the project are presented in Riffeser *et al.* (2003, 2008) and partially contributed to Calchi Novati *et al.* (2010). In addition to the original microlensing targets, the intensive observations

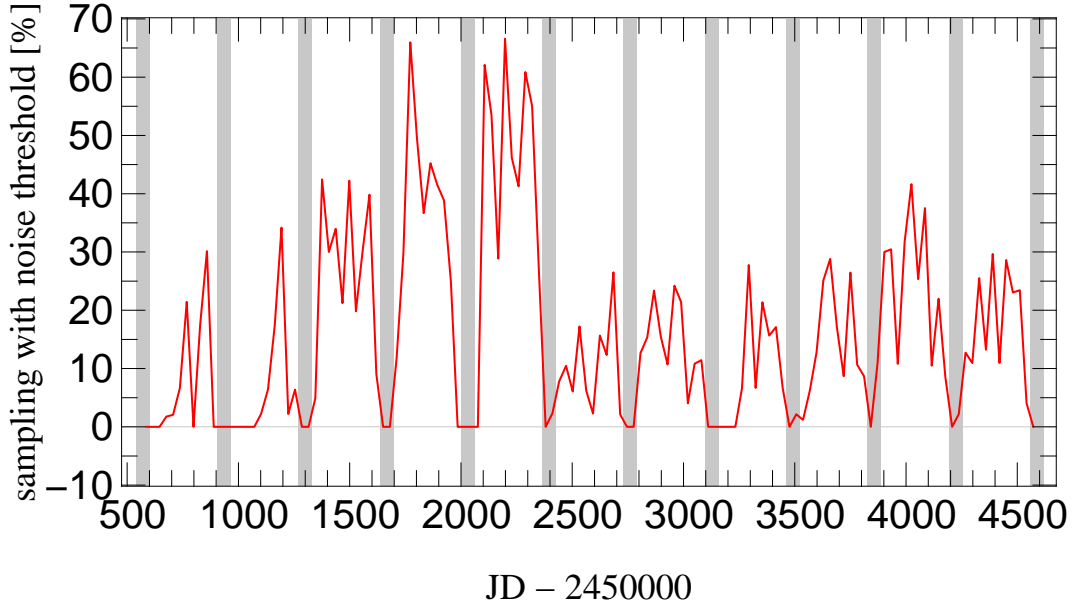


Figure 5.1: Fraction of good quality data points in t averaged over the survey area. The definition of good quality is given in the text. The vertical grey zones indicate the time when M31 is not observable from the location of the telescopes during May and June). 0% indicates we have no observations during the night.

in two bands also yields more than 20,000 variables in the bulge of M31 (Fliri *et al.*, 2006) and the nova candidates presented in this paper.

5.4 Nova detection

To establish an automatic detection for nova candidates, we apply the following criteria for candidates selection based on the measured R -band PSF flux (as mentioned in Section 5.3):

- The significance for variability must be 10σ relative to the baseline and the measured flux excess of the variable source must be a local maximum around neighbouring pixels at a given time step. Note that σ throughout this paper refers to the errors of the individual PSF flux excess measurements.
- The variable source must have a measured flux excess larger than 4×10^{-5} Jy in R -band (corresponding to $m_R = -2.5 \log(\frac{4 \times 10^{-5} \text{ Jy}}{F_{\text{Vega},R}}) \sim 19.7$ mag, with $F_{\text{Vega},R} = 3060$ Jy being the flux of Vega in the R -band) and the first measurement after the measured maximum flux excess must have a flux excess $> 2 \times 10^{-5}$ Jy.
- To use the eruptive nature of novae, we define the strength s of the outburst:

$$s = \frac{\Delta F_{\text{max}}/\sigma_{\text{max}}^2 + \Delta F_{\text{max}+1}/\sigma_{\text{max}+1}^2}{1/\sigma_{\text{max}}^2 + 1/\sigma_{\text{max}+1}^2} \quad (5.1)$$

where ΔF_{\max} is the measured maximum flux excess relative to the reference image and $\Delta F_{\max+1}$ is the first measurement after the measured maximum flux excess. The σ_{\max} and $\sigma_{\max+1}$ are the errors in the measurements of the flux excess. We require $s > 4.6 \times 10^{-5}$ Jy nova detection.

- To avoid false contamination from periodically varying sources, we define the asymmetry a between positive and negative outliers in the light curve relative to the baseline:

$$a = \frac{\text{Number of data points with } \Delta F > 5\sigma}{\text{Number of data points with } \Delta F < -5\sigma} - 1. \quad (5.2)$$

This quantity a is useful in filtering out normal variable sources, which have $a \sim 0$, while the eruptive nature of novae lead to $a \gg 1$. We empirically require a to be larger than 4.7 to be suitable for nova detection.

- We then apply a special mask to filter false detections around bright stars, especially spikes.
- After the masking, we apply a group algorithm to find multiple pixel detections connecting to the same nova candidate in different time steps.
- In the last step, we inspect the difference images and light curves by eye to make sure that no image artefact escapes our detection and is misinterpreted as a nova.

We combine the criteria 1-4 into one single step. The detections filtered out by each steps are shown in Table. 5.2.

Table 5.2: Detection criteria for nova candidates

Criterion	Number
Full light curves	4043256
Local flux maximum & $s > 4.6 \times 10^{-5}$ Jy & $a > 4.7$	1005
Masking of bright stars	156
Grouping	105
Inspection by eye	90

Among the nova candidates, 24 are discovered by WeCAPP project for the first time, while 5 of them are known but were not officially published and can be found on the CBAT¹ or Extragalactic Novae² webpages. The rest of the nova candidates are published and can be found in the literature, see e.g. Pietsch *et al.* (2007); Pietsch (2010)³. The positions and light curves of these 90 novae can be found in Table 5.3 and in the Appendix.

¹ M31 (Apparent) Novae Page, http://www.cfa.harvard.edu/iau/CBAT_M31.html

² www.rochesterastronomy.org/novae.html

³ An up-to-date online-version of the catalog can be found at <http://www.mpe.mpg.de/~m31novae/opt/m31/index.php>

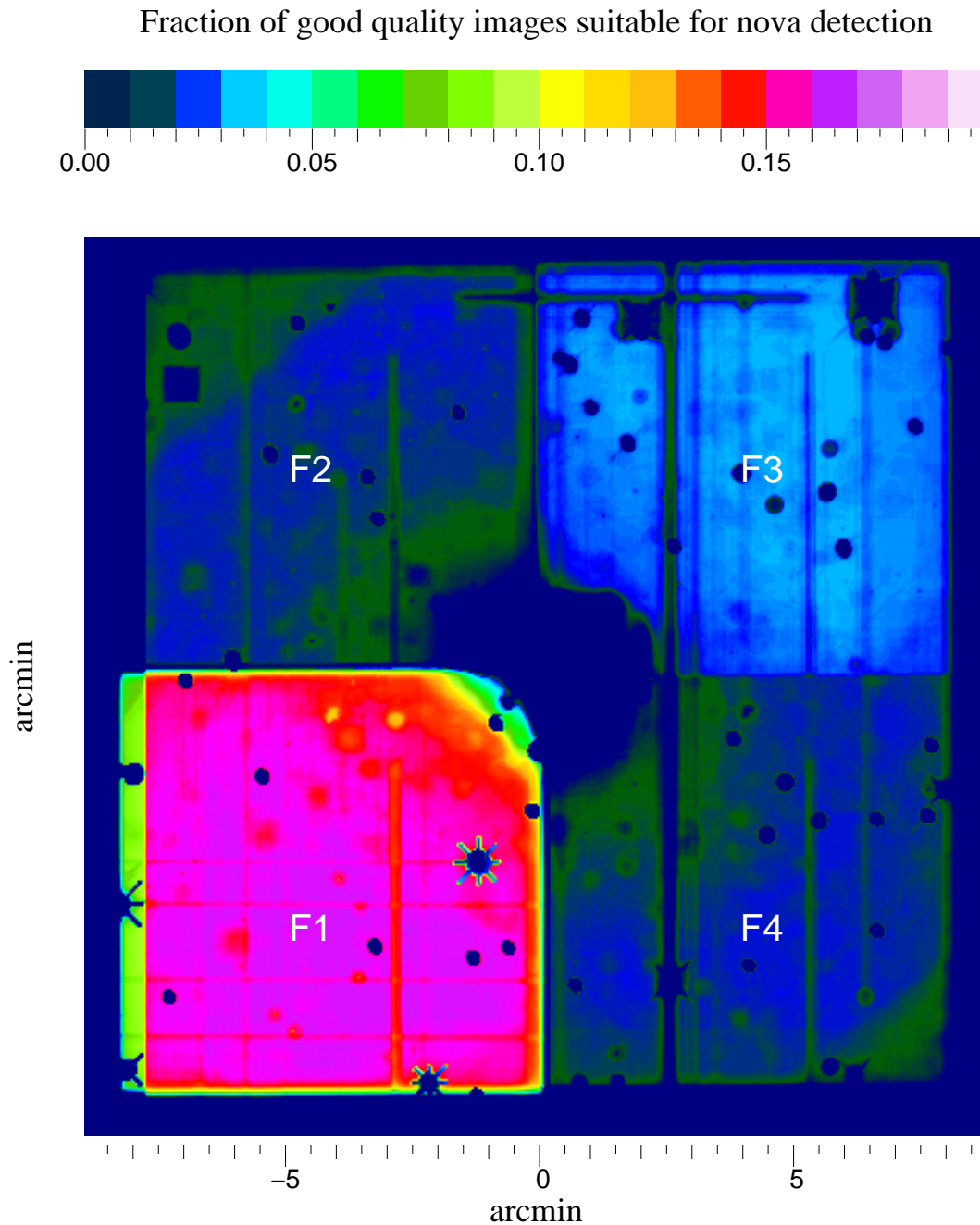


Figure 5.2: Fraction of good quality data points in (x,y) averaged over time t . The definition of good quality is given in the text. The low fraction in the central part is caused by the high noise of M31 itself.

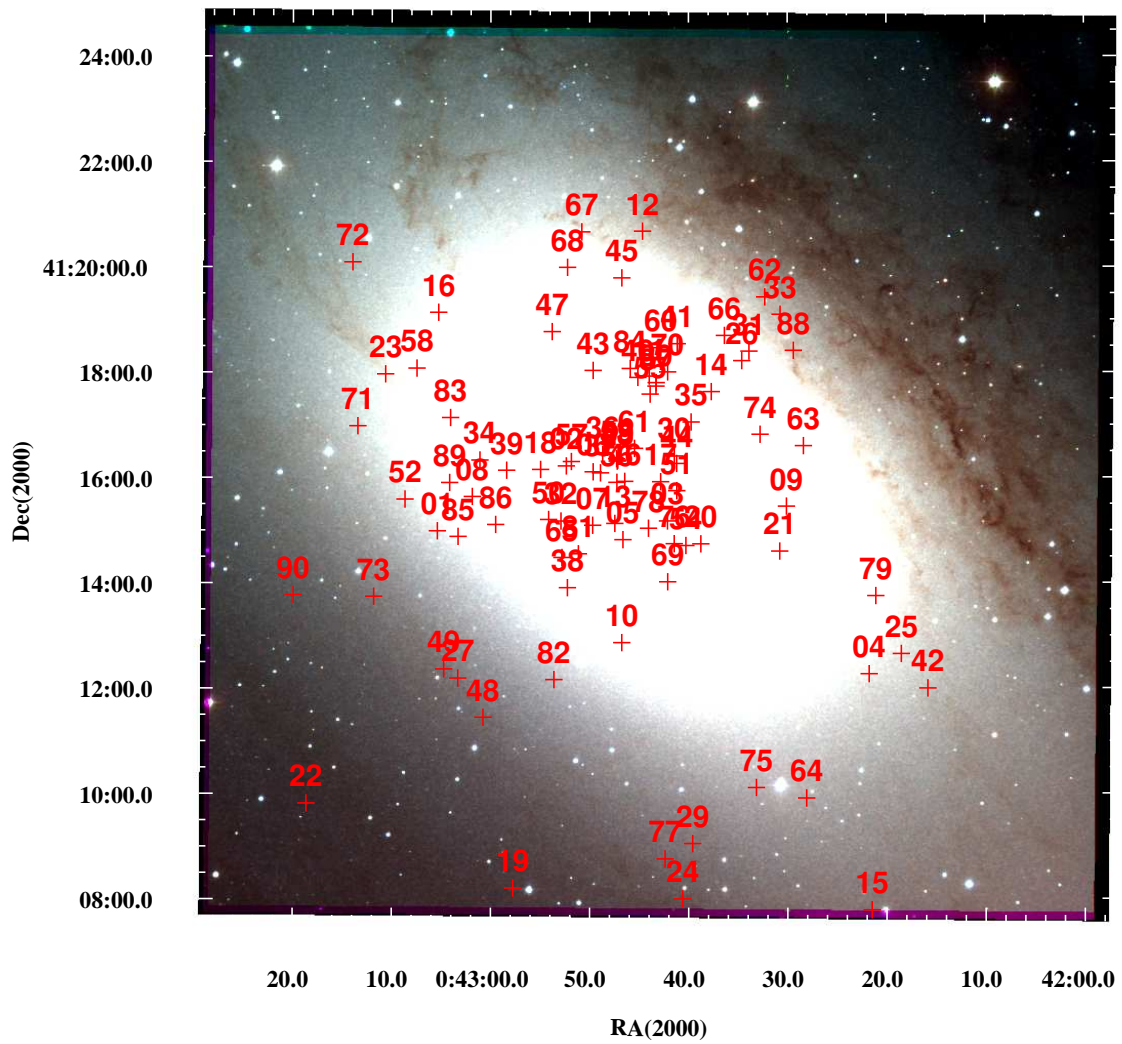


Figure 5.3: Distribution of the WeCAPP nova candidates. The overlaying image is a three-color-combined image using the observations obtained from Calar Alto observatories in V , R and I -band. The image has a size of $17'.2 \times 17'.2$.

Table 5.3: WeCAPP nova catalogue

Name	RA(2000)	Dec(2000)	t_{\max}	Δt_{\max}	Class	CBAT naming	Discovery (and light curve) reference(s)	X-ray obs.	Spec. obs.
N01	00:43:05.37	41:14:59.2	745.52	29.01	Unclassified	1997-10e	1997-14 in Shafter & Irby (2001)		
N02	00:42:52.35	41:16:13.2	750.45	33.95	Unclassified	1997-10f	1997-10 in Shafter & Irby (2001)		
N03	00:42:42.13	41:15:10.4	753.55	37.05	Unclassified	1997-11a	1997-07 in Shafter & Irby (2001)	P07 H10A,H10B	
N04	00:42:21.76	41:12:16.2	753.55	37.05	Unclassified	1997-10c	1997-02 in Shafter & Irby (2001)		
N05	00:42:46.64	41:14:49.2	1109.48	243.19	Unclassified	1998-09d	IAUC 7015, Sharov et al. (2000)		Fe II, S11
N06	00:42:49.65	41:16:06.5	1251.30	2.00	Unclassified	1999-02a			
N07	00:42:49.69	41:15:05.6	1359.55	0.93	Cusp	1999-06a	IAUC 7218, PAV-78668 in An et al. (2004)		Fe II, S11
N08	00:43:01.85	41:15:38.4	1372.62	1.01	Smooth	1999-06b	Rector et al. (1999a)		
N09	00:42:30.11	41:15:27.3	1719.62	553.15	Unclassified	2000-06a			
N10	00:42:46.75	41:12:51.9	1726.63	1.00	Cusp	2000-08b	Pietsch et al. (2007)		
N11	00:42:43.97	41:17:55.5	1754.64	18.01	Oscillation	2000-07a	PACN-00-01 in Darnley et al. (2004)	P05,P07 O06	
N12	00:42:44.65	41:20:40.6	1755.65	1.02	Cusp	2000-07b	PACN-00-03 in Darnley et al. (2004)		
N13	00:42:47.45	41:15:07.8	1763.66	1.02	Cusp	2000-08a	Pietsch et al. (2007)	P05,P07	
N14	00:42:37.70	41:17:37.8	1766.64	1.00	Cusp	2000-08d	PACN-00-04 in Darnley et al. (2004)		
N15	00:42:21.49	41:07:47.3	1932.34	1.04	Cusp	2001-01a		H10A,H10B	
N16	00:43:05.26	41:19:08.2	1948.34	4.02	Unclassified	2001-01b			
N17	00:42:42.82	41:15:55.2	1940.33	6.04	Unclassified	2001-01c			
N18	00:42:54.95	41:16:09.2	1948.34	4.02	Unclassified	2001-02a			
N19	00:42:57.75	41:08:12.3	2097.56	124.25	Unclassified	2001-07b			
N20	00:42:38.76	41:14:44.4	2097.56	124.25	Unclassified	2001-07c			
N21	00:42:30.79	41:14:36.1	2130.63	3.00	Unclassified	2001-07d	IAUC 7674, PACN-01-01 in Darnley et al. (2004)		
N22	00:43:18.62	41:09:49.0	2094.56	121.25	Smooth	2001-07a	PAV-74935 in An et al. (2004)	P05,P07	
N23	00:43:10.62	41:17:58.0	2163.65	28.02	Unclassified	2001-08b	PACN-01-03 in Darnley et al. (2004)		
N24	00:42:40.60	41:07:59.9	2163.65	28.02	Unclassified	2001-08c	PACN-01-04 in Darnley et al. (2004)		
N25	00:42:18.52	41:12:39.3	2163.65	28.02	Unclassified	2001-08a	IAUC 7684, PACN-01-02 in Darnley et al. (2004)		

Table 5.4: WeCAPP nova catalogue. This table continues Table. 5.3.

Name	RA(2000)	Dec(2000)	t_{\max}	Δt_{\max}	Class	CBAT naming	Discovery (and light curve) reference(s)	X-ray obs.	Spec. obs.
N26	00:42:34.62	41:18:13.0	2151.60	0.99	Smooth	2001-08d	IAUC 7709, PAC-26277 in An et al. (2004)	P05,P07	
N27	00:43:03.31	41:12:11.5	2190.48	1.90	Jitter	2001-10a	IAUC 7729, PACN-01-06 in Darnley et al. (2004) NMS2 in Joshi et al. (2004)	P07 H10A,H10B	Fe II, S11
N28	00:42:47.21	41:16:18.7	2197.32	0.98	Oscillation	2001-10c			
N29	00:42:39.59	41:09:02.9	2299.32	2.99	Unclassified	2001-12b			
N30	00:42:41.44	41:16:24.6	2266.30	0.92	Smooth	2001-12a	IAUC 7794		Fe II, S11
N31	00:42:33.89	41:18:24.0	2282.31	6.02	Smooth	2002-01b	IAUC 7794, PAV-26285 in An et al. (2004)	P05,P07	He/N, S11
N32	00:42:52.89	41:15:10.4	2283.30	0.99	Cusp	2002-01a	IAUC 7794, PAV-79136 in An et al. (2004)		
N33	00:42:30.74	41:19:05.9	2325.38	4.02	Smooth	2002-02a			
N34	00:43:01.08	41:16:19.9	2476.54	13.00	Smooth	2002-07a	IAUC 7937, IAUC 7938		
N35	00:42:39.74	41:17:03.3	2521.57	38.01	Doubtful	2002-07b			
N36	00:42:48.66	41:16:26.3	2573.63	26.07	Doubtful	2002-08b			
N37	00:42:48.90	41:16:05.3	2661.25	6.82	Smooth	2003-01b			
N38	00:42:52.24	41:13:54.5	2797.53	91.24	Doubtful	2003-01c	IAUC 8155		
N39	00:42:58.38	41:16:08.3	2797.53	91.24	Smooth	2003-06a	IAUC 8155		
N40	00:42:45.12	41:17:54.0	2820.50	21.94	Unclassified	2003-06c	IAUC 8165		
N41	00:42:41.14	41:18:32.4	2832.56	12.05	Unclassified	2003-06d	IAUC 8165		
N42	00:42:15.85	41:11:59.9	2834.44	5.96	Smooth	2003-07b	IAUC 8165, N3 in Šimon et al. (2005)		
N43	00:42:49.64	41:18:02.0	2867.53	6.11	Doubtful	2003-08a	IAUC 8210		
N44	00:42:41.20	41:16:16.0	2925.46	16.95	Unclassified	2003-08c	IAUC 8226	H10B	
N45	00:42:46.74	41:19:47.4	2931.30	22.96	Smooth	2003-09b	IAUC 8222, N5 in Šimon et al. (2005)		
N46	00:42:46.45	41:15:55.6	2925.42	26.88	Unclassified	2003-10a			
N47	00:42:53.78	41:18:46.2	2949.54	8.12	Unclassified	2003-11a	IAUC 8248	P07 H10A	
N48	00:43:00.76	41:11:26.9	2978.22	6.86	Smooth	2003-11b	IAUC 8253	P07 H10A	
N49	00:43:04.73	41:12:21.9	2992.32	7.02	Unclassified	2003-12a	IAUC 8262, N8 in Šimon et al. (2005)	P07	
N50	00:42:54.14	41:15:12.2	2994.32	2.00	Smooth	2003-12b	IAUC 8262	P07	

Table 5.5: WeCAPP nova catalogue. This table continues Table. 5.3.

Name	RA(2000)	Dec(2000)	t_{\max}	Δt_{\max}	Class	CBAT naming	Discovery (and light curve) reference(s)	X-ray obs.	Spec. obs.
N51	00:42:41.18	41:15:45.0	3006.24	52.88	Unclassified	2004-01b		P07 H10B	
N52	00:43:08.65	41:15:35.3	3039.29	38.95	Smooth	2004-01a	N9 in Šimon <i>et al.</i> (2005)	P07	
N53	00:42:47.28	41:16:21.4	3039.29	52.81	Cusp	2004-02a		P07	
N54	00:42:40.28	41:14:42.5	3254.44	193.14	Unclassified	2004-09a	IAUC 8404	P07	Fe II, S11
N55	00:42:43.90	41:17:35.0	3319.60	9.30	Doubtful	2004-07a	Pietsch <i>et al.</i> (2007)	P07	
N56	00:42:47.24	41:15:54.5	3291.45	7.92	Unclassified	2004-10b	Pietsch <i>et al.</i> (2007)	P07	
N57	00:42:51.84	41:16:18.2	3291.37	7.84	Unclassified	2004-10a	ATEL 346	P07	
N58	00:43:07.46	41:18:04.6	3319.49	15.13	Unclassified	2004-11b	Pietsch <i>et al.</i> (2007)	P07 H10A	He/N, S11
N59	00:42:47.17	41:16:19.8	3319.49	15.13	Smooth	2004-11f	CBAT	P07	
N60	00:42:42.81	41:18:27.8	3319.60	9.30	Unclassified	2004-11a	Pietsch <i>et al.</i> (2007)	P07	Fe II, S11
N61	00:42:45.47	41:16:33.2	3348.42	28.93	Unclassified	2004-11d	Pietsch <i>et al.</i> (2007)	P07	
N62	00:42:32.29	41:19:25.7	3346.36	25.92	Cusp	2004-11c	CBAT	P07	
N63	00:42:28.39	41:16:36.1	3382.36	4.09	Unclassified	2005-01a	Pietsch <i>et al.</i> (2007)	P07	Fe II, S11
N64	00:42:28.10	41:09:54.7	3381.36	21.03	Unclassified	2004-12a	ATEL 379	P07	
N65	00:42:52.79	41:14:28.8	3426.28	17.92	Smooth	2005-02a	ATEL 421	P07 H10A,H10B	
N66	00:42:36.37	41:18:41.8	3427.38	1.03	Doubtful	2005-02b			
N67	00:42:50.80	41:20:39.8	3592.47	100.43	Cusp	2005-07a	Pietsch <i>et al.</i> (2007)	H10A	Fe II, S11
N68	00:42:52.25	41:19:59.4	3635.37	15.94	Smooth	2005-09a	CBAT	H10A	Fe II, ATEL 850
N69	00:42:42.11	41:14:01.1	3635.59	9.30	Unclassified	2005-09d		H10A	
N70	00:42:42.12	41:18:00.3	3661.54	1.17	Unclassified	2005-10b	ATEL 651	H10A	
N71	00:43:13.42	41:16:58.9	3863.57	50.27	Smooth	2006-04a	ATEL 805	H10A,H10C	
N72	00:43:13.93	41:20:05.5	3863.57	50.27	Smooth	2006-05a		H10A	
N73	00:43:11.81	41:13:44.7	3880.53	2.98	Unclassified	2006-06a		H10A	Fe II, ATEL 850
N74	00:42:32.77	41:16:49.1	3867.57	54.27	Unclassified	2006-06b	ATEL 829	H10A,H10B	
N75	00:42:33.17	41:10:06.8	3984.41	3.89	Smooth	2006-09a	Calchi Novati <i>et al.</i> (2007)	H10A	

Table 5.6: WeCAPP nova catalogue. This table continues Table. 5.3.

Name	RA(2000)	Dec(2000)	t_{\max}	Δt_{\max}	Class	CBAT naming	Discovery (and light curve) reference(s)	X-ray obs.	Spec. obs.
N76	00:42:41.45	41:14:44.5	4000.42	8.92	Unclassified	2006-09b	ATEL 884	H10A	
N77	00:42:42.39	41:08:45.6	3999.40	4.98	Unclassified	2006-09c	ATEL 887, <i>Shafter et al. (2011a)</i>	H10A,H10B	Fe II, S11
N78	00:42:44.05	41:15:02.1	4096.47	1.09	Unclassified	2006-11b [†]			
N79	00:42:21.08	41:13:45.4	4095.38	5.02	Smooth	2006-12a		H10A,H10B	Fe II, S11
N80	00:42:43.22	41:17:48.4	4095.52	5.08	Unclassified	2006-12c	ATEL 973	H10A,H10B	
N81	00:42:51.15	41:14:33.5	4122.43	6.14	Unclassified	2007-01a	CBAT	H10A,H10B	
N82	00:42:53.61	41:12:09.9	4166.30	13.03	Smooth	2007-03a	CBAT	H10A,H10B	
N83	00:43:04.05	41:17:08.3	4296.48	24.96	Smooth	2007-07a	ATEL 1131	H10B	
N84	00:42:45.91	41:18:04.4	4297.50	1.01	Smooth	2007-07b	ATEL 1139	H10B	Fe II, ATEL 1186
N85	00:43:03.29	41:14:53.0	4307.48	9.02	Smooth	2007-07c	ATEL 1146	H10B	Hybrid or He/N, ATEL 1186
N86	00:42:59.49	41:15:06.6	4337.45	2.95	Unclassified	2007-07d	ATEL 1162	H10B	
N87	00:42:43.30	41:17:44.1	4314.55	15.01	Smooth	2007-07e	ATEL 1156	H10B	Fe II, ATEL 1186
N88	00:42:29.39	41:18:24.8	4356.49	16.92	Smooth	2007-08c	IAUC 7664, ATEL 1198	H10B	
N89	00:43:04.18	41:15:54.1	4425.30	14.81	Unclassified	2007-11c	ATEL 1275	H10B	Fe II, S11
N90	00:43:19.98	41:13:46.3	4444.61	18.35	Smooth	2007-12b		ATEL 1360,1647 B09	He/N, S11

We show the position and the time of maximum flux (expressed in JD-2450000) of the nova candidates in columns 2, 3 and 4. The uncertainty of the position is smaller than $0''.1$ (see Riffeser et al., in prep.). The uncertainty in the time of maximum flux Δt_{\max} in column 5 is derived from the time difference between t_{\max} and the last measurement before t_{\max} . The light curve classification is shown in column 6, with 'unclassified' indicates those novae we are not able to classify and 'doubtful' indicates the novae are more similar to other variables than novae. In column 7 we give the corresponding CBAT nomenclature. Column 8 list the references for discovery (and light curves) in optical. The spectroscopic and X-ray observations are shown in column 9 and 10. The 24 novae without discovery references are newly discovered by WeCAPP.

[†] We also detected M31N-2006-12d on the same position, which is possibly rebrightening of M31N-2006-11b given the short time difference.

References: P05:*Pietsch et al. (2005)*, P07:*Pietsch et al. (2007)*, O06:*Orio (2006)*, B09:*Bode et al. (2009)*, H10A:*Henze et al. (2010a)*, H10B:*Henze et al. (2010b)*, H10C:*Henze et al. (2010c)*, S11:*Shafter et al. (2011b)*

5.5 Nova Taxonomy

Although all novae slightly differ, it is possible to group novae by their light-curve or spectroscopic properties. One of the commonly used methods to characterize novae is the ‘speed class’ proposed by [Payne-Gaposchkin \(1964\)](#), who categorized novae according to their light-curve evolution and described the decline time-scale by the time needed to drop by 2 magnitudes below the maximum (t_2). [Williams \(1992\)](#) did a thorough study of the spectroscopic properties of the novae, and categorized novae into Fe (galactic thick disk novae) or He (galactic disk novae) group according to the most prominent features in their spectra. [Della Valle & Livio \(1998\)](#) further established the connection between the speed class and spectroscopic classification. They found that fast novae are mainly related to the He novae, while the slow novae tend to show Fe II features in their spectra.

The physical explanation behind is that He novae are from the galactic disk and prone to have massive white dwarfs, thus having fast and steep decline. On the other hand, the Fe II novae originate from the less massive population II stars in the galactic thick disk, and hence have a slow decline.

The speed class is not enough to fully account for the differences between novae. [Strope *et al.* \(2010\)](#) gathered 93 galactic novae from the American Association of Variable Star Observers (AAVSO) and made a thorough study using the complete coverage of their light curves.

They suggested to classify the novae according to their distinct features during their decline, such as the plateau, the cusp by the secondary brightening and the dip by the dust.

In this section we classify our nova candidates (if possible) following the taxonomy proposed by [Strope *et al.* \(2010\)](#). Readers are referred to Table 3 and Figure 2 in [Strope *et al.* \(2010\)](#) for the definition and exemplary light curves for different nova classes. Note that the classification scheme of [Strope *et al.* \(2010\)](#) is based on the V -band magnitude, while we are using R -band and might be affected by the strong $H\alpha$ emission. We thus check our I -band light curve, which does not affected by the strong $H\alpha$ emission, and identify the apparent features in the nova classification scheme of [Strope *et al.* \(2010\)](#) in both R and I -band.

5.5.1 S Class and the universal decline law

The S-class novae have smooth light curves following the universal power-law decline ($F \propto t^{-1.75}$) due to free-free emission expanding shell as proposed by [Hachisu & Kato \(2006\)](#). In principle, the classification scheme of [Strope *et al.* \(2010\)](#) is based on the fact that all the light curves originate from the S-class. The S-class is indeed consistent to the vast majority of our nova candidates. To verify the universal decline law, we thus fit our candidate light curves with a 4-parameter formula:

$$\Delta F = f_b + f_0 \times (t - t_0)^\alpha, \quad (5.3)$$

where f_b is the baseline level and will be different from zero in cases where the nova candidate flux is present in the reference frame used in difference imaging or there is a variable close to it (see e.g. the light curve of WeCAPP-N10 in the appendix). f_0 gives the proportional factor between the flux and time, t_0 is the onset of nova outburst and α is the index of the power-law decline. After the first iteration, we found that some candidates have unreasonable t_0 long before the nova eruption. For such events, we use a 5-parameter formula

$$\Delta F = f_b + f_0 \times (t - t_0)^\alpha, \quad t_0 \equiv t_{-1} + \delta^2 \quad (5.4)$$

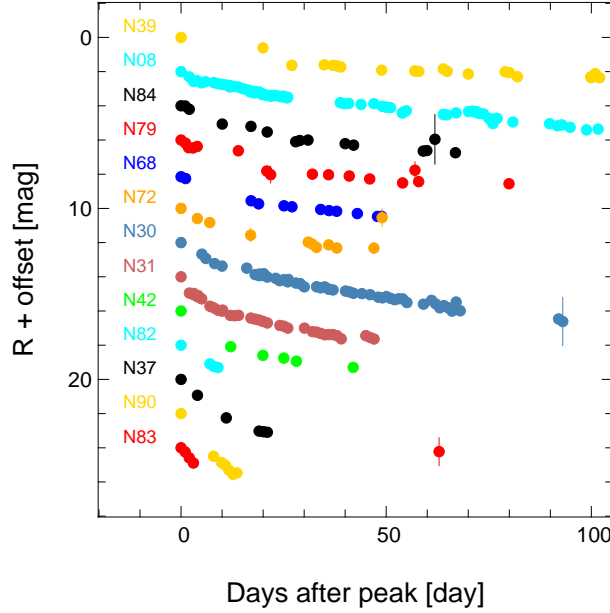


Figure 5.4: S Class novae with free t_0 . The single offsets are -15.04 for N08, -3.59 for N30, -2.81 for N31, 2.84 for N37, -18.02 for N39, -0.88 for N42, -9.89 for N68, -8.06 for N72, -11.81 for N79 and 1.02 for N82, 5.14 for N83, -13.66 for N84 and 5.37 for N90 respectively. Note that for most of the data points the error bars are smaller than the symbol of the data points. Here we only show the decline part of the light curve. Full light curves can be found in the appendix.

with t_{-1} fixed at the last data point in the baseline just before the eruption to avoid unreasonable t_0 . The best-fit parameters for equations (5.3) and (5.4) are given in Table 5.5.1.

For the S-class nova, we first tried to fit the power-law decline for all the nova candidates. A candidate is classified as S-class nova only when the fitting routine finds a solution for either equation 5.3 or equation 5.4. N01, N09, N17, N24, N41, N49, N54, N58 and N77 are not attributed to S-class because the fitting routine failed to find a solution.

Our best-fit value of α from Table 5.5.1 for free t_0 solely and combined with fixed t_0 are -1.51 and -1.32, respectively. The power-law index for a free t_0 is close to the value given by Hachisu & Kato (2006), while the value of α from a combination of both free and fixed t_0 deviates from -1.75, which indicates that we might have missed the true eruption date for some of the novae. Note that we constrain the value of power-law index α from the R -band images, which are contaminated by the $H\alpha$ emission line and might differ from the universal power-law index from Hachisu & Kato (2006).

5.5.2 C Class

The light curves of C-class novae have cusp shape, which first follow a power-law decline, then rise steeply to a second maximum and finally have a sharp drop. The characteristic C-class light curve has a secondary maximum emerging between 1 to 8 months after the primary peak (Strope *et al.*, 2010). Kato *et al.* (2009) found that C-class light curve can be well-fitted by an exponential component superimposed on the smooth decline. They further proposed that the cusps can originate from a secondary ejection and the break-out into the optically thick nova winds. Hachisu & Kato (2009) also

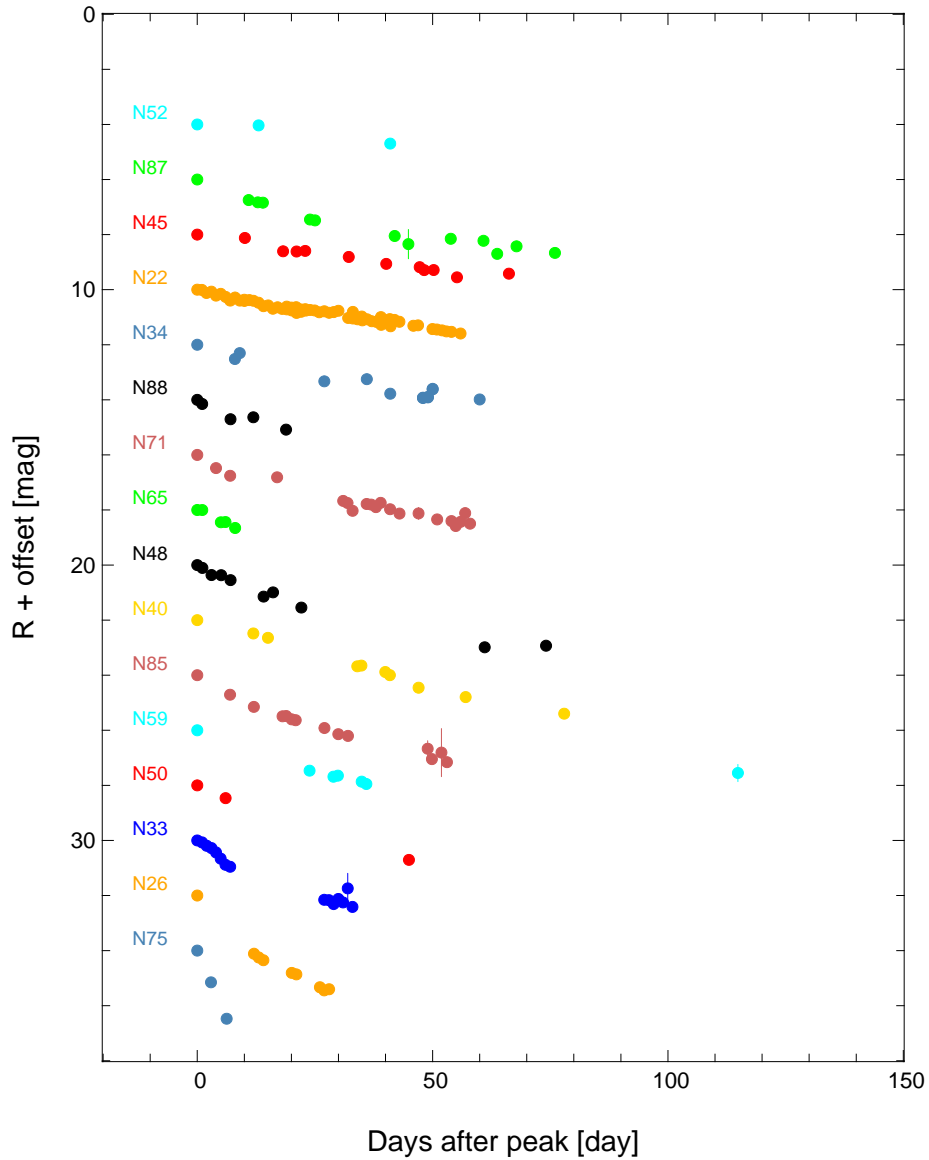


Figure 5.5: S Class novae with fixed t_0 . The single offsets are -8.84 for N22, 15.17 for N26, 12.44 for N33, -6.44 for N34, 4.97 for N40, -10.40 for N45, 2.53 for N48, 10.92 for N50, -13.97 for N52, 8.05 for N59, -0.22 for N65, -1.84 for N71, 16.24 for N75, 6.70 for N85, -11.06 for N87 and -5.14 for N88 respectively. Here we only show the decline part of the light curve. Full light curves can be found in the appendix.

Free t_0		
Name	$t_0(\text{JD}-2450000)$	α
N08	1337.9 ± 0.5	-2.07 ± 0.02
N30	2257.3 ± 0.1	-1.55 ± 0.01
N31	2277.9 ± 0.2	-1.29 ± 0.02
N37	2647.4 ± 1.4	-3.44 ± 0.28
N39	2776.6 ± 1.1	-1.31 ± 0.04
N42	2831.0 ± 0.2	-1.21 ± 0.03
N68	3627.7 ± 0.6	-1.08 ± 0.05
N72	3845.5 ± 2.4	-2.04 ± 0.16
N79	4088.9 ± 0.4	-0.89 ± 0.03
N82	4155.1 ± 1.6	-2.06 ± 0.23
N83	4288.2 ± 2.1	-2.55 ± 0.51
N84	4289.8 ± 0.9	-1.05 ± 0.08
N90	4437.3 ± 1.5	-3.20 ± 0.44

Fixed t_0		
Name	$t_0(\text{JD}-2450000)$	α
N22	1964.3	-4.35 ± 0.17
N26	2145.5	-1.92 ± 0.04
N33	2321.4	-1.22 ± 0.02
N34	2447.5	-1.70 ± 0.06
N40	2798.6	-1.67 ± 0.03
N45	2908.3	-0.97 ± 0.03
N48	2971.4	-0.92 ± 0.01
N50	2985.3	-1.37 ± 0.04
N52	3003.3	-1.43 ± 0.03
N59	3304.4	-1.63 ± 0.32
N65	3408.4	-1.44 ± 0.10
N71	3813.3	-2.92 ± 0.22
N75	3980.5	-2.28 ± 0.15
N85	4298.5	-1.16 ± 0.05
N87	4299.5	-1.22 ± 0.11
N88	4339.6	-1.48 ± 0.40

Table 5.7: Power-law decline fitting for s-class nova.

connect the formation of the cusp shape to the input of the magnetic energy from rotating white dwarf. In addition, the sharp drop before the light curve returns to the power-law decline is attributed to the sudden formation of dust as proposed by Lynch *et al.* (2008). We have found in total 10 candidates showing cusp features in our WeCAPP catalog and show their light curves in Fig. 5.6.

5.5.3 O Class

The O-class light curve follows the S-class light curve, but with the exception that at a given time interval the light curve shows quasi-sinusoidal self-similar oscillations during the course of decline. It has been shown that the white dwarf of the O-class novae is both highly magnetic and massive (Strope *et al.*, 2010). However, these can not be the only effect leading to oscillation because the nova V1500 Cyg in Strope *et al.* (2010) which fulfills these requirements but does not show oscillation. There have been many proposals for the mechanism of oscillation, but none of them have been compared to and verified by observation (see Section 4 in Strope *et al.*, 2010). The oscillation starts generally around 3 mag below the peak, which indicates that we might have missed the peak in our nova candidates N11 and N28, where the light curves are shown in Fig. 5.7 and in the appendix. In Fig. 5.7 we show the two O-class candidates discovered during our observation campaign.

5.5.4 J Class

The characteristics of J-class novae are the jitters on top of the smooth decline. These jitters are symmetric and sharp-topped flares superposed on the base of S-class light curve, which is the major difference from the O-class novae, while the latter bears oscillations up and down the smooth decline. The jitter usually has variations with amplitude larger than half of a magnitude. Jitters do not occur in the late tail of the light curve and most of them occur within 3 mag below the peak. Strope *et al.* (2010) further propose for two subclasses according to the emergence of the jitters: one subclass has jitters only near the peak, while the other has jitters spread all over the light curve roughly until the nova is 3 mag dimmer than the peak. Among our candidates we found one evident J-class light curve, which belongs to the second subclass of Strope *et al.* (2010) and is shown in Fig. 5.8.

It has been reported that there is a gradual increase of the time intervals between two successive jitters (Bianchini *et al.*, 1992; Csák *et al.*, 2005; Pejcha, 2009; Tanaka *et al.*, 2011), while Strope *et al.* (2010), using the same data set as Pejcha (2009), found no distinctive trend. We thus tried to search for such trend in our nova candidate N27 and performed a fitting with the following equation:

$$\log(t_J - t_{J-1}) = a \log(t_J - t_{max}) + b, \quad (5.5)$$

where t_J is the time of the J -th jitter.

The jitters used in the fitting are indicated by the vertical marks in Fig. 5.8. The time intervals between the successive jitters are shown in 5.9. Our best-fitted value is $a = 0.64 \pm 0.09$ and $b = 0.11 \pm 0.16$. The slope is smaller than the values of DK Lac ($a = 0.88$) and V4745 Sgr ($a = 0.79$) derived by Pejcha (2009) and $a = 0.79$ for the 6 novae presented by Tanaka *et al.* (2011). With only one J-class nova candidate in our catalog, we can not tell if this is a difference between the nova in M31 and Galactic novae, or it is simply a variation among individual novae.

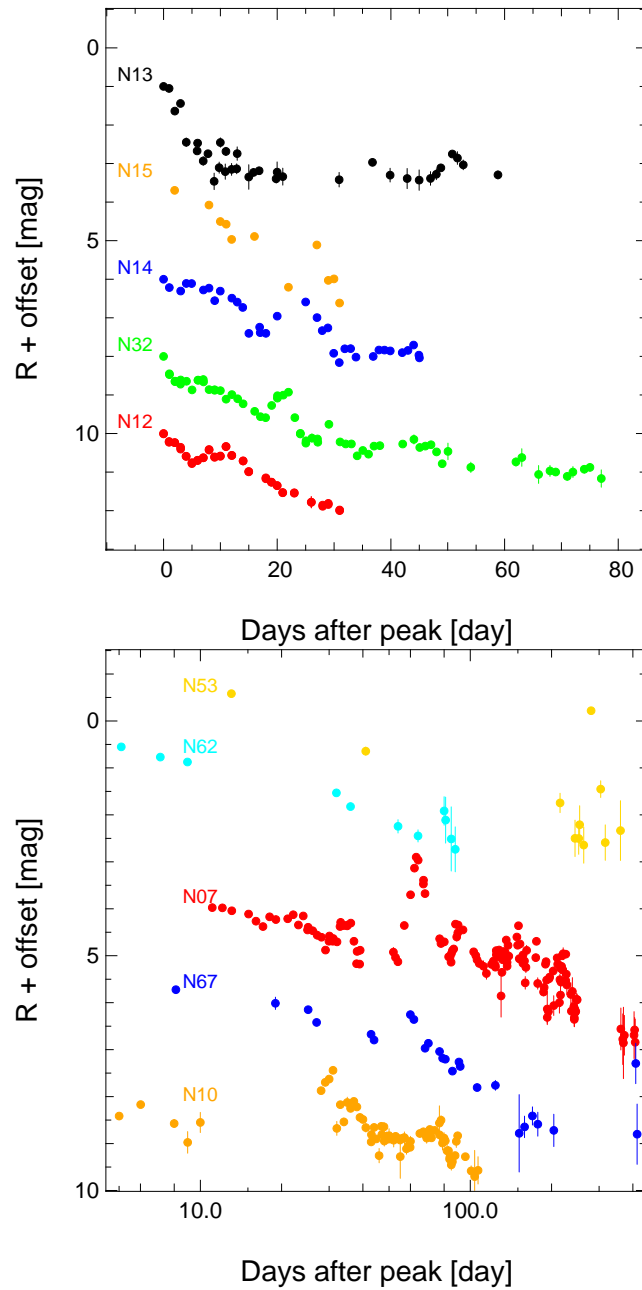


Figure 5.6: C Class novae. The offsets applied to the magnitudes are -15.07 for N07, -11.88 for N10, -8.26 for N12, -17.71 for N13, -11.58 for N14, -13.79 for N15, -9.16 for N32, -19.19 for N53, -19.15 for N62 and -13.04 for N67 respectively. Here we only show the decline part of the light curve. Full light curves can be found in the appendix.

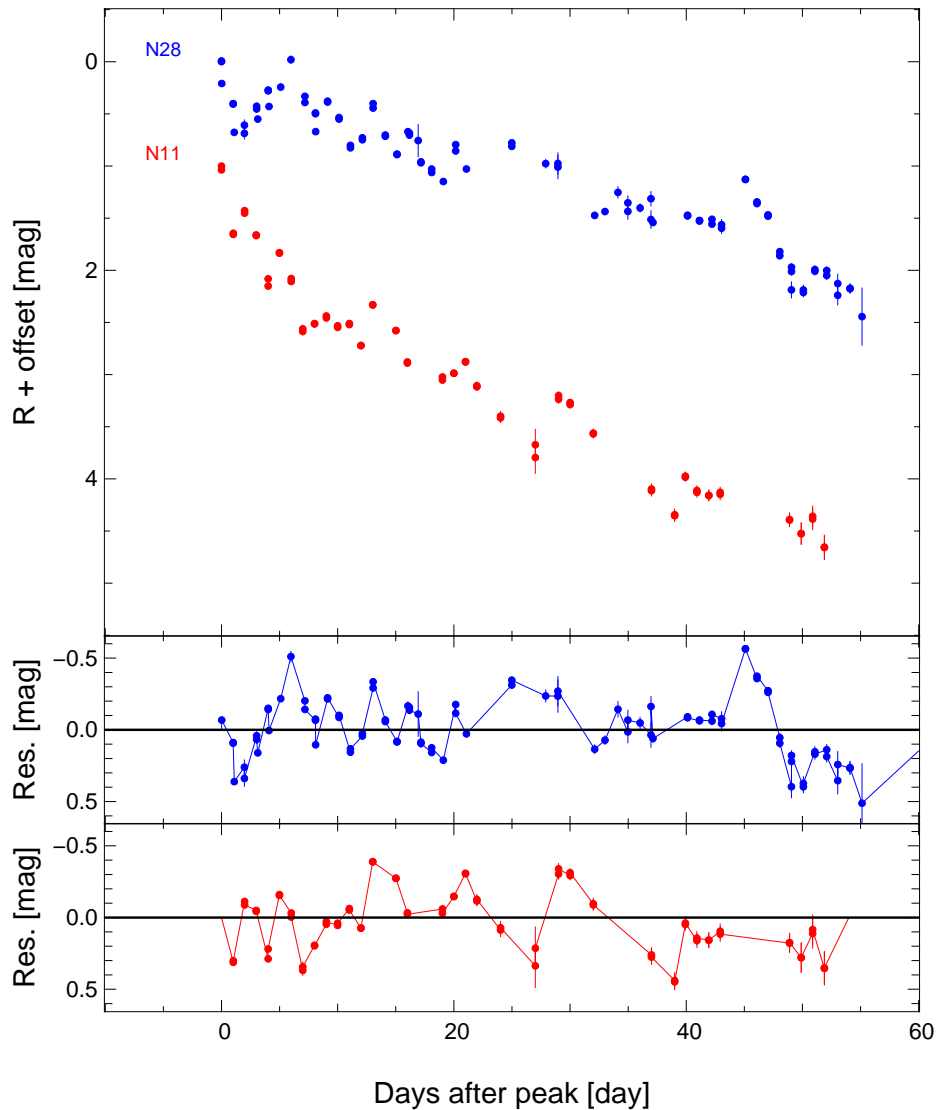


Figure 5.7: O Class novae. The offset is -15.77 for N11 and -17.61 for N28 respectively. Here we only show the decline part of the light curve. Full light curves can be found in the appendix.

5.5.5 Other classes

Besides the above-mentioned classes, there remains three more classes in the taxonomy of *Strope et al. (2010)*:

- Flat topped (F) class which has an extended interval at the peak with near constant brightness.
- Dust dip (D) class where the decline is interrupted by another very steep decline and followed by the recovery to just below the original decline.
- Plateau (P) class that the smooth decline is interrupted by a long-lasting and nearly flat interval, succeeded by the return to the original decline.

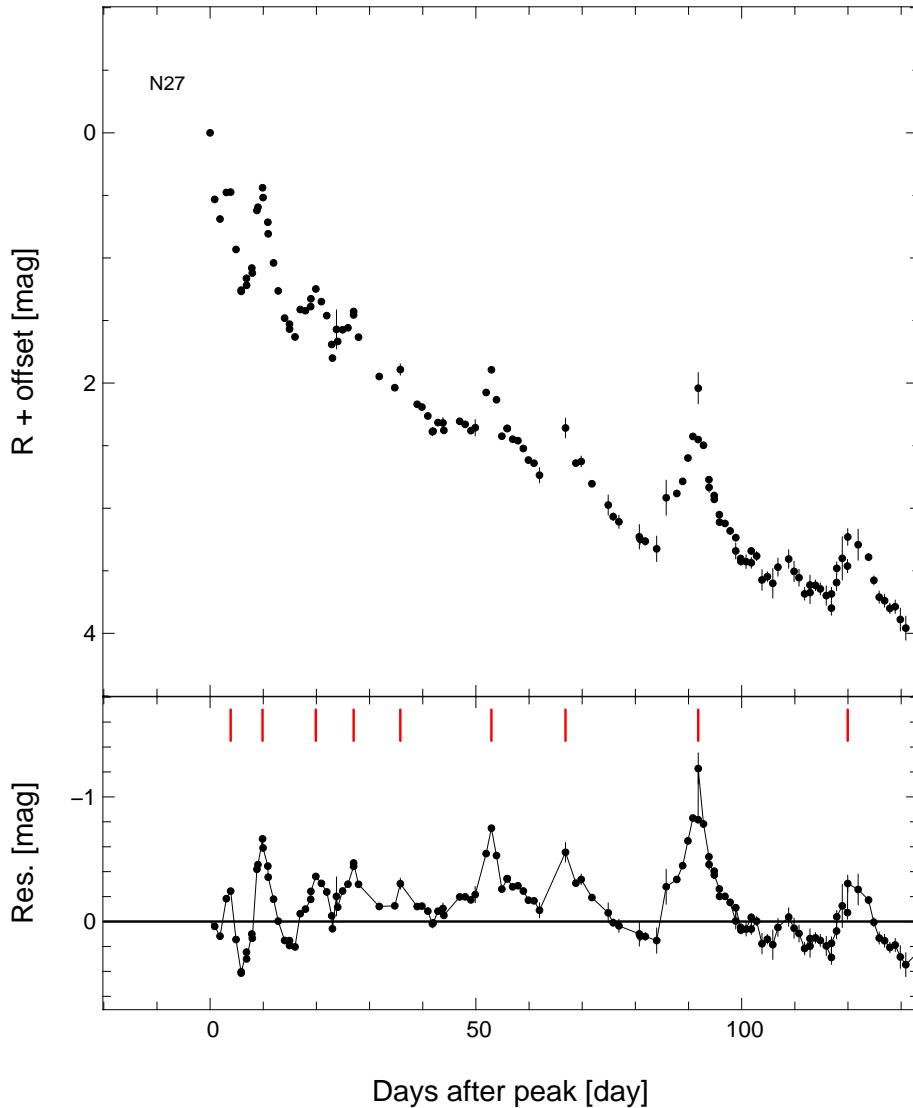


Figure 5.8: J Class nova. The single offsets are -16.99 for N27. Here we only show the decline part of the light curve. Full light curves can be found in the appendix.

Among our candidates, however, we do not find evident light curves belonging to these classes. This could be partially attributed to the set-up of our observation campaign. For example, the dust dip for the extreme shallow dips in [Strope *et al.* \(2010\)](#) occur more than 1 month after the peak, with the dip to be about 6 mag dimmer than the light curve maximum. Such magnitude variation can hardly be observed in M31, because it is too faint to be discerned. This implies that we might misclassified the D-class novae into other classes. The non-detection of the P-class novae can be explained by the filter system we used. [Hachisu & Kato \(2006\)](#) pointed out that the true plateau from the continuum radiation is best observed in the *y*-band filter. Since we are using the *R* and *I*-filter, it is possible that the plateau phase does not exist in the *R* and *I*-bands due to the influence of the emission lines during the course of decline.

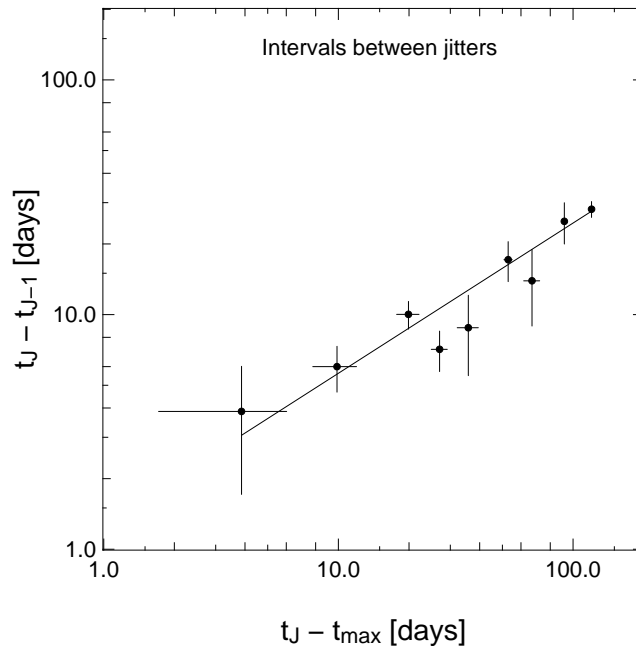


Figure 5.9: J-class peak intervals for nova N27, using *R*-band data.

To summarize, we have classified 42 nova candidates and find 69% to be S-class, 24% to be C-class, 5% to be O-class and 2% to be J-class, while [Strope *et al.* \(2010\)](#) find 38% to be S-class, 1% to be C-class, 4% to be O-class and 16% to be J-class in their sample.

5.6 Recurrent Novae

Recurrent novae are potential supernovae progenitors ([Schaefer, 2010](#)). We compare the position of our nova candidates with the catalog by [Pietsch *et al.* \(2007\)](#); [Pietsch \(2010\)](#). We have found 4 recurrent novae candidates by selecting novae in the literature which are located within 1 arcsec to our nova candidates (see Table 5.8 and Fig. 5.10). Among the potential recurrent nova candidates N19 has 3 outbursts in 12 years, which would be an unprecedented short period. As pointed out by [Henze *et al.* \(2009\)](#), the outburst appears earlier in UV and $H\alpha$ than in *R*-band does not fit very well to the nova scheme. They thus suggest an alternative scheme, that this event could be a dwarf nova in the Milky Way.

To test how likely an uncorrelated nova is falling into the 1 arcsec area, we perform a test by using the upper-right quarter of our pointing F1, which has the highest M31 light contribution from the bulge and contains 42 novae. The ratio of the area occupied by the $1''.0$ circle of these 42 novae to the total area of this quarter (300×300 arcsec²), implies the chance of an uncorrelated nova to coincide with an existing nova is low (1.5 : 1000).

Note that we use stricter selection criteria to search for recurrent novae, thus we have less candidates than presented by [Pietsch *et al.* \(2007\)](#); [Pietsch \(2010\)](#).

[Hachisu & Kato \(2006\)](#) suggested that recurrent novae all bear the plateau light curve. However, in our light curve we did not detect evident plateaus. The main reason is we do not have comprehensive

Table 5.8: Recurrent Nova Candidates

WeCAPP ID	RA	DEC	NAME	RA	DEC	Dist.
N02(1997-10f)	00:42:52.35	41:16:13.2	2008-08b	00:42:52.38	41:16:12.9	0".54
N19(2001-07b)	00:42:57.75	41:08:12.3	1963-09c	00:42:57.73	41:08:12.4	0".32
N19(2001-07b)	00:42:57.75	41:08:12.3	1968-09a	00:42:57.71	41:08:11.9	0".72
N19(2001-07b)	00:42:57.75	41:08:12.3	2010-10e	00:42:57.76	41:08:12.3	0".15
N29(2001-12b)	00:42:39.59	41:09:02.9	1997-11k	00:42:39.59	41:09:02.9	0".00
N29(2001-12b)	00:42:39.59	41:09:02.9	2009-11b	00:42:39.61	41:09:03.2	0".42
N83(2007-07a)	00:43:04.05	41:17:08.3	1990-10a	00:43:04.05	41:17:07.5	0".80

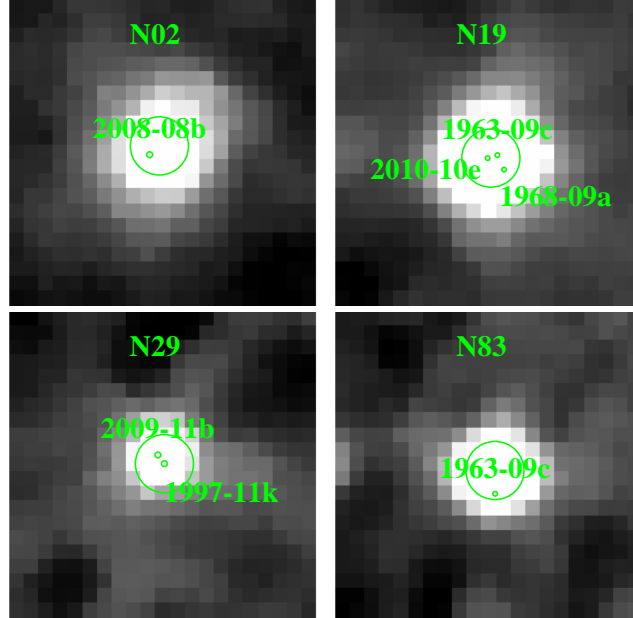


Figure 5.10: Position of the recurrent nova candidates. The larger circle in the center indicates the 1".0 radius for our selection criteria. The position of potential recurrent nova candidates are marked by the smaller circles.

coverage of the light curves. Despite of the lack of highly sampled observation, it would be hard to find such plateaus because the light curves in R or I are contaminated by the bright emission lines. Hachisu *et al.* (2008) thus advocate observations in Strömgren y -band since it is designed to cut the strong emission lines in the wide V bandpass filter and can follow the continuum flux more accurately. However, the y -filter is narrow and requires longer exposure time, so we use the I -filter instead of the y -filter for the confirmation of microlensing event from achromaticity when the WeCAPP was initiated.

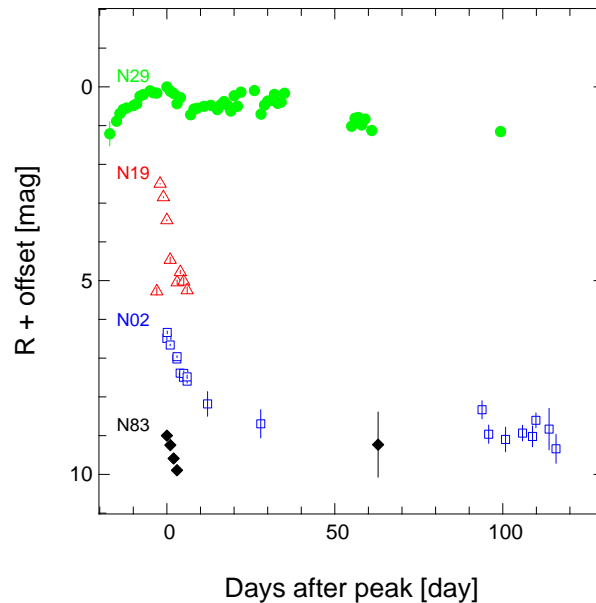


Figure 5.11: Recurrent nova candidates light curves. The single offsets are -11.76 for N02, -15.76 for N19, -18.86 for N29 and -9.86 for N83 respectively. Here we only show the decline part of the light curve. Full light curves can be found in the appendix.

5.7 Conclusion and outlook

We have presented the position, out-burst time and the maximum brightness of the 90 nova candidates discovered during the time span of the WeCAPP project. Light-curve classifications under the taxonomic scheme of [Strope et al. \(2010\)](#) have been shown and the full *R* and *I*-band light curves of each individual nova during the outburst are also presented in the Appendix.

We provide the full light curve data of the novae on request, as well as the postage stamps of the reduced, stacked, or difference-imaging frames.

Part of this catalogue has been used to find the X-ray counter-part by [Pietsch et al. \(2005, 2007\)](#) and showed that super soft X-ray sources (SSS) in M31 are mostly constituted by the novae during eruption. The turn on and turn off of the SSS phase provide us the information of the ejected and accreted mass onto the surface of the white dwarf.

Besides the X-ray monitoring campaign, there is also a survey of M31 novae in infrared using *Spitzer Space Telescope* ([Shafter et al., 2011a](#)), which indicates a correlation between the dust formation timescales and the nova speed class. Such studies would not be possible without the speed class determined by the optical observations. Ground-based optical surveys, such as PTF ([Law et al., 2009; Rau et al., 2009](#)), PanSTARRS ([Kaiser et al., 2002](#)) and LSST ([Tyson, 2002](#)), will continue to play an important role in the regime of multi-wavelength novae observation and help us to gain insight of the underlying physical mechanism of novae.

5.8 Appendix A: WeCAPP nova candidate light curves

Nova light curves and postage stamps (*R*-band in upper row and *I*-band in lower row) for all the candidates. The numbers on the right of the light curves are the corresponding *R* and *I*-band magnitudes. The red square in the postage stamps indicates the postage stamp at that time when the nova reaches flux maximum.

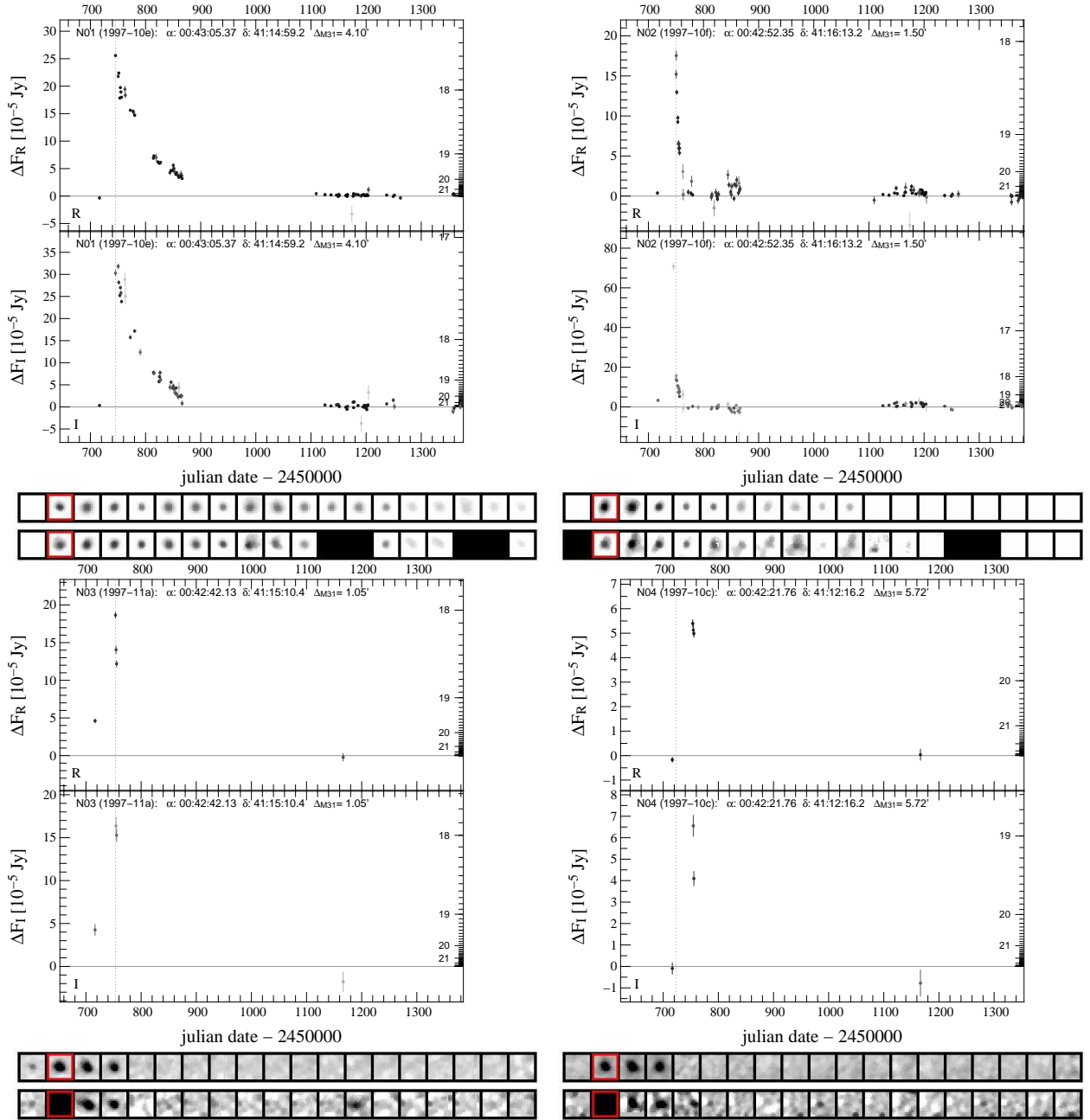


Figure 5.12: Light curves of WeCAPP nova N01-N04.

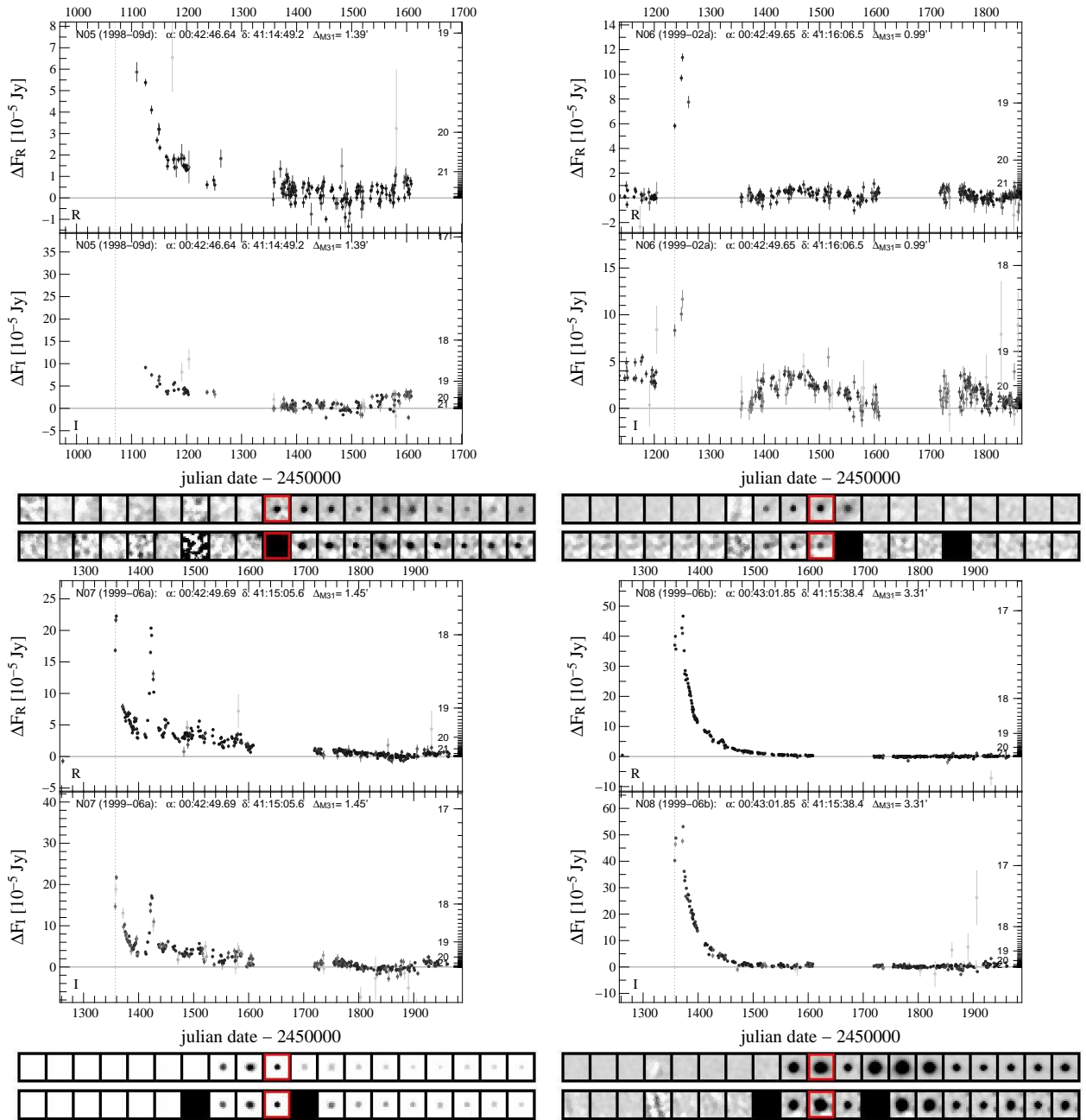


Figure 5.13: Light curves of WeCAPP nova N05-N08.

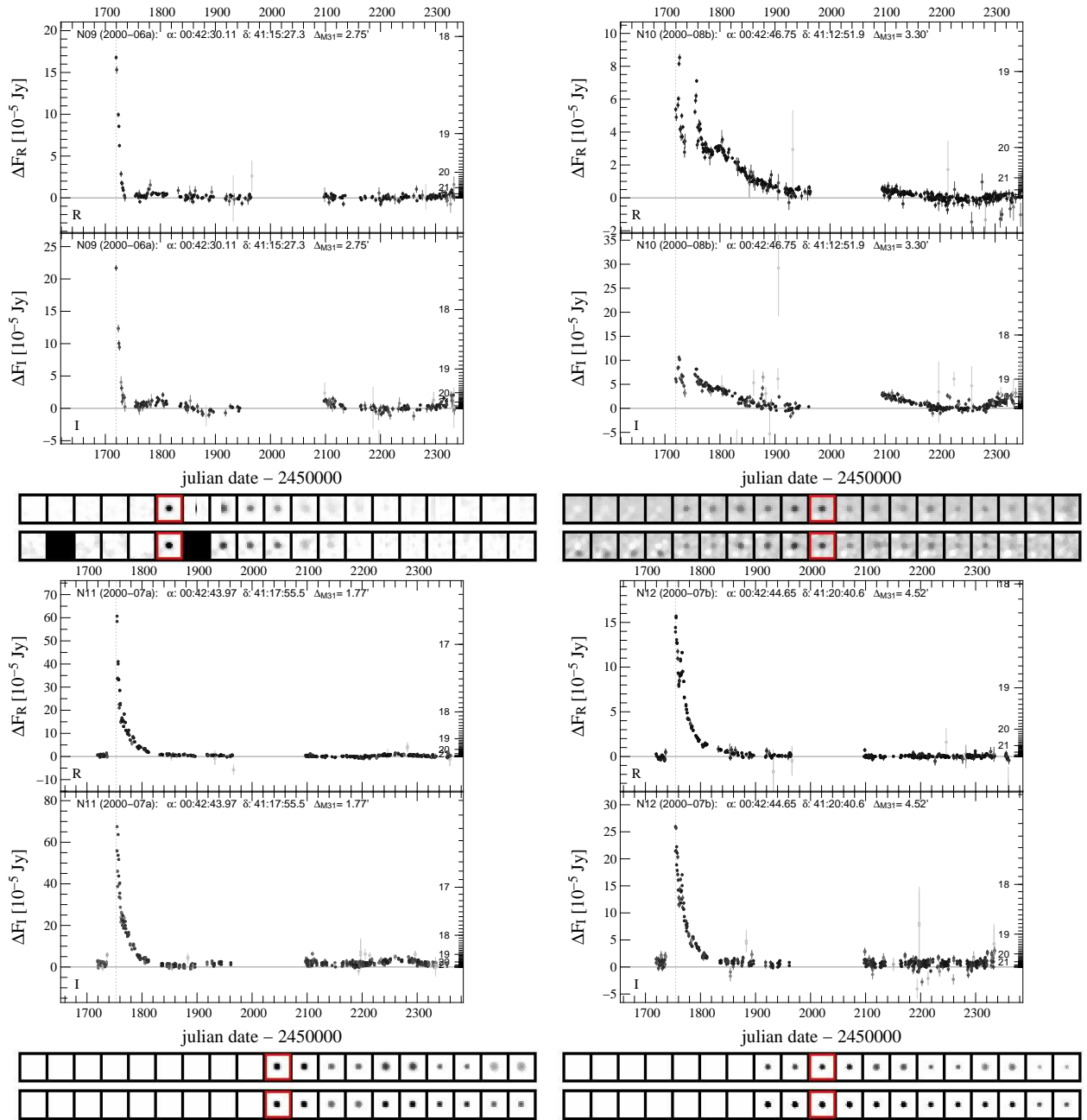


Figure 5.14: Light curves of WeCAPP nova N09-N12.

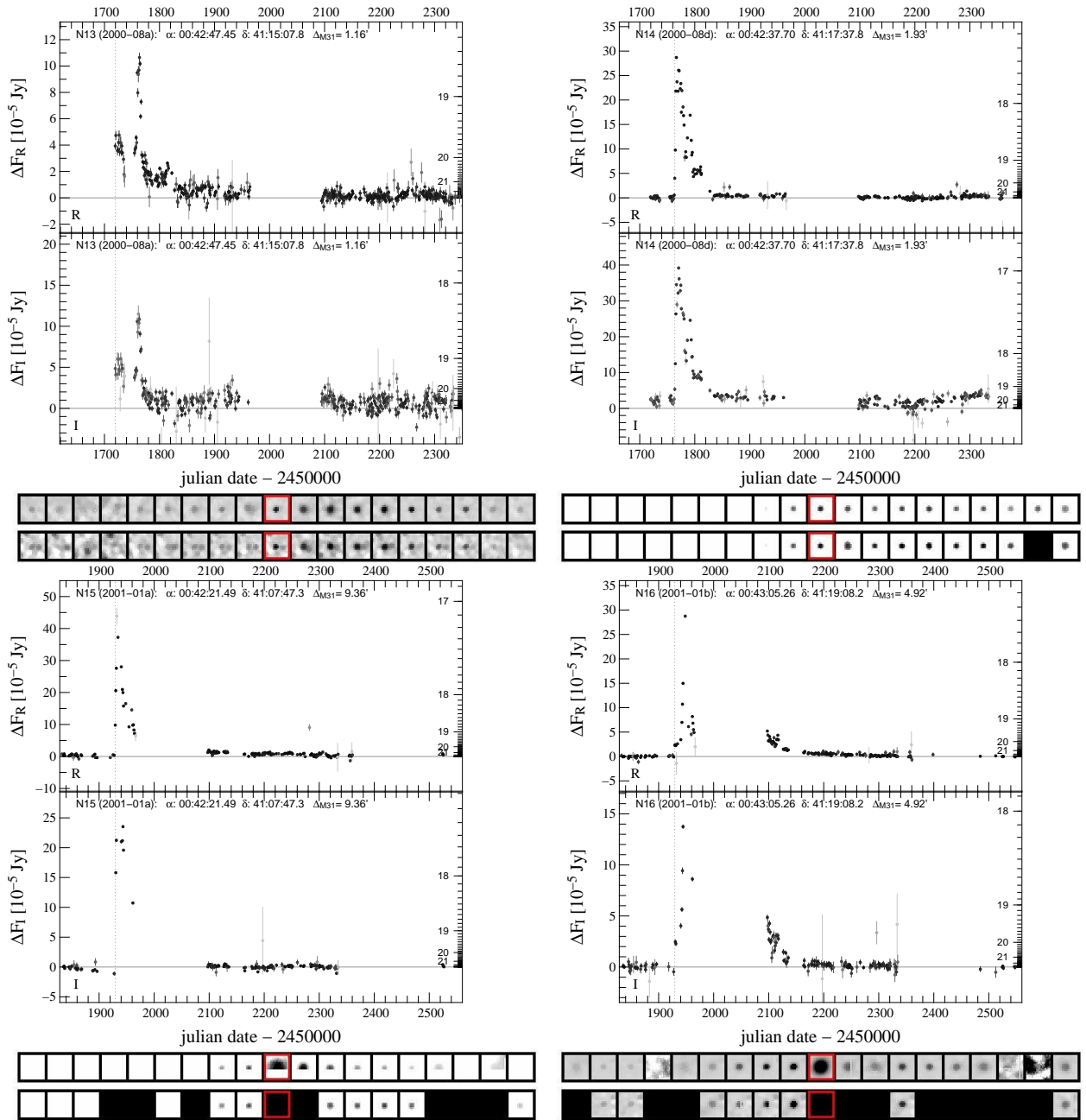


Figure 5.15: Light curves of WeCAPP nova N13-N16.

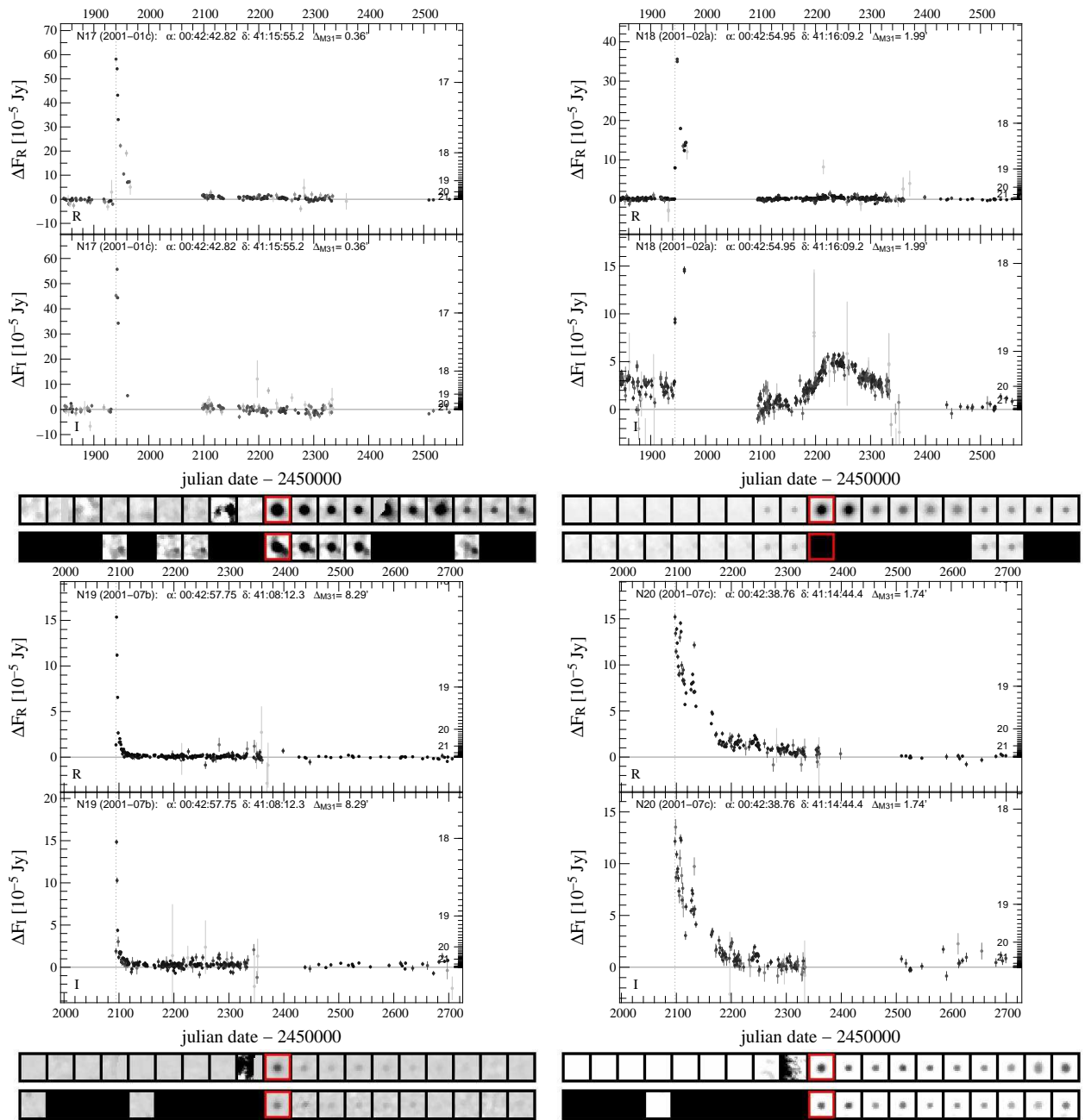


Figure 5.16: Light curves of WeCAPP nova N17-N20.

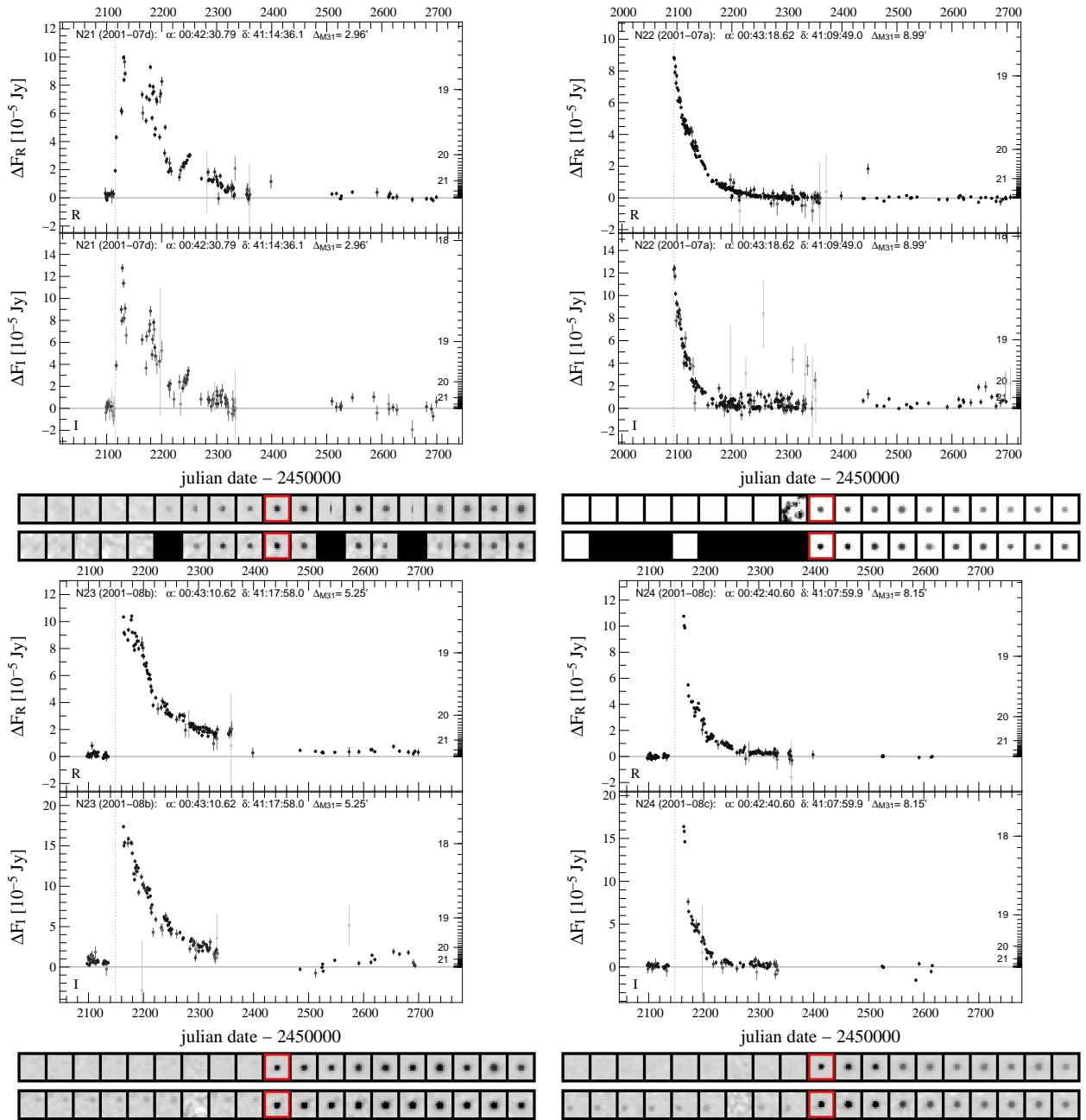


Figure 5.17: Light curves of WeCAPP nova N21-N24.

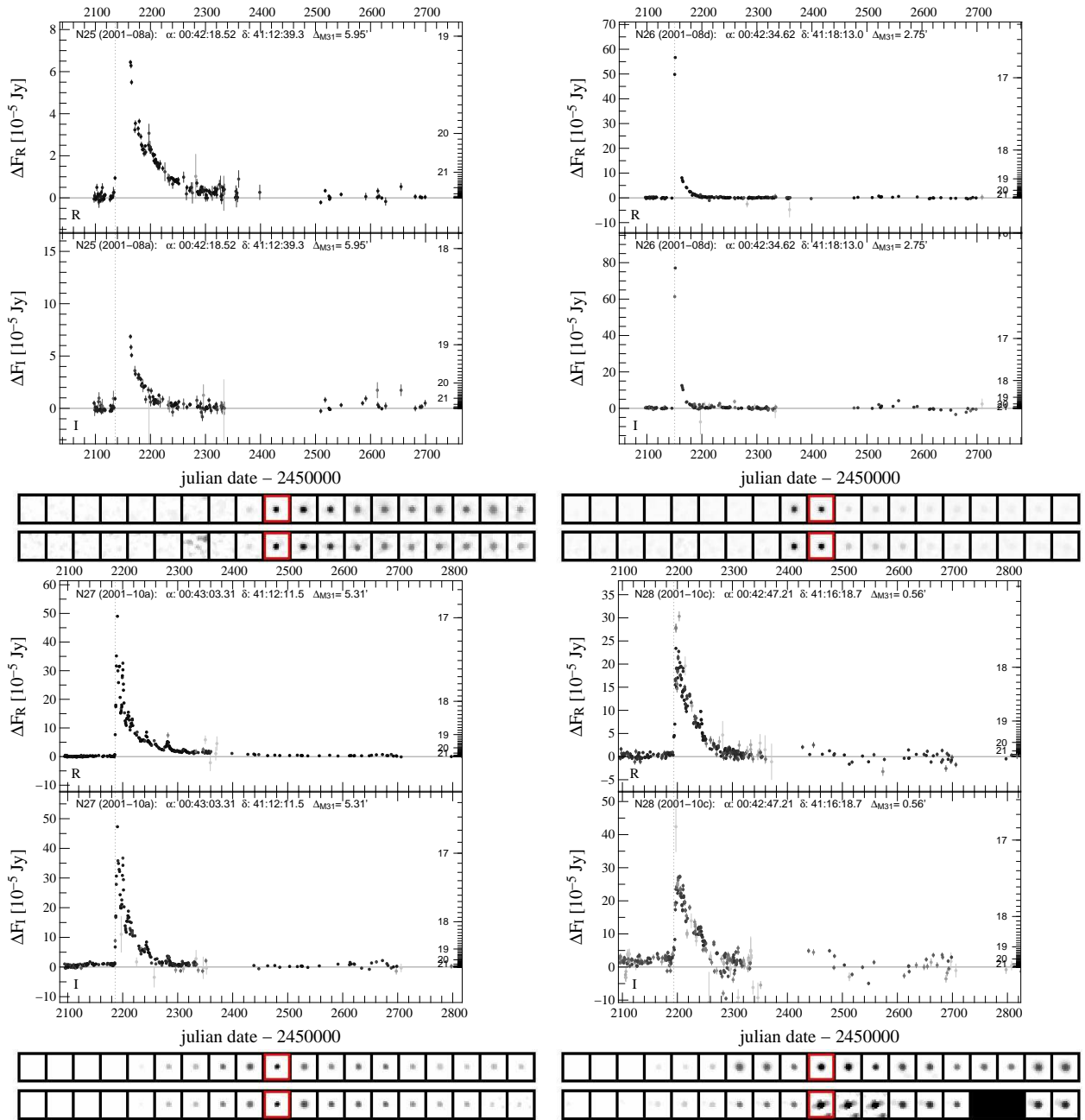


Figure 5.18: Light curves of WeCAPP nova N25-N28.

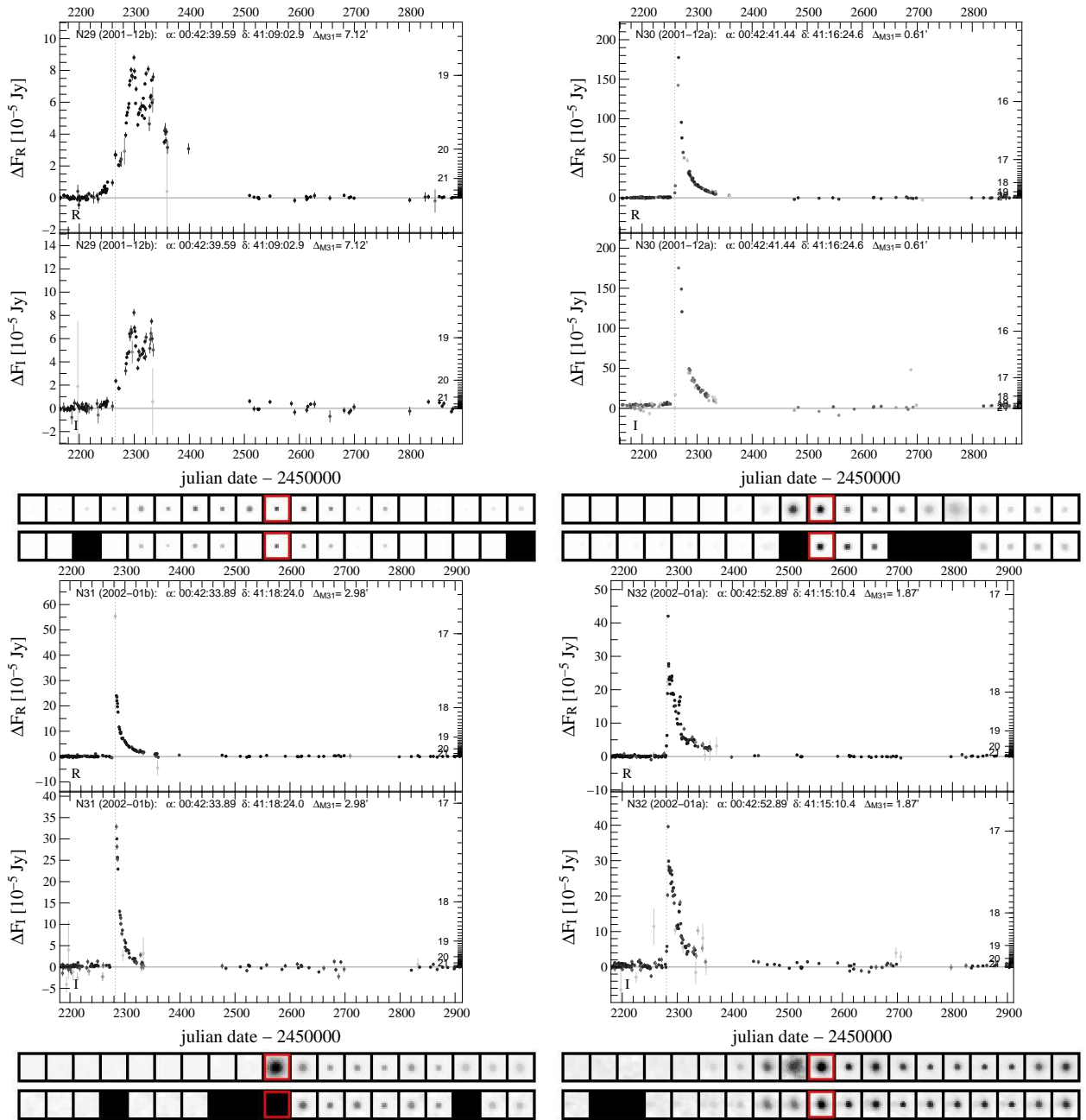


Figure 5.19: Light curves of WeCAPP nova N29-N32.

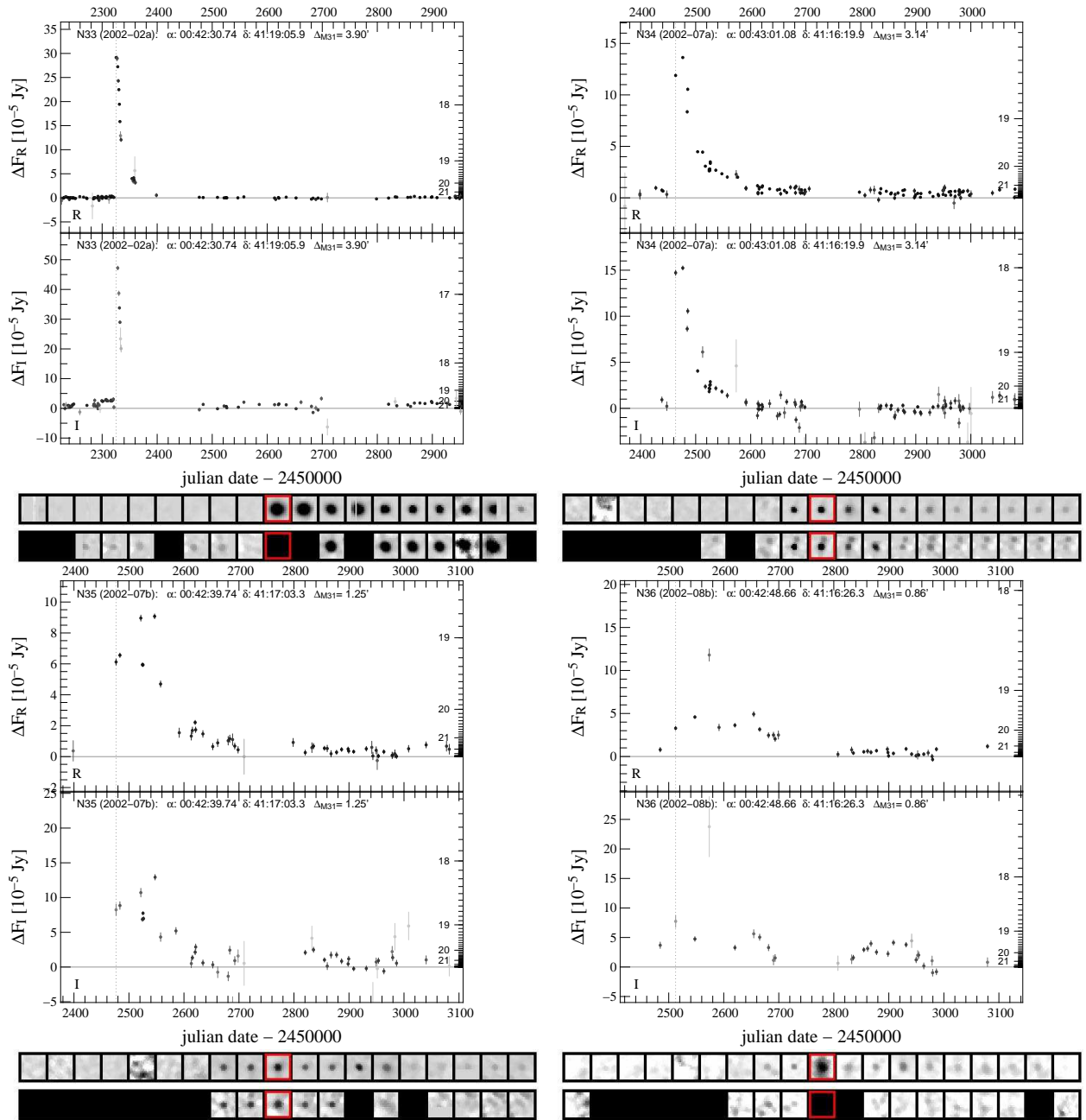


Figure 5.20: Light curves of WeCAPP nova N33-N36.

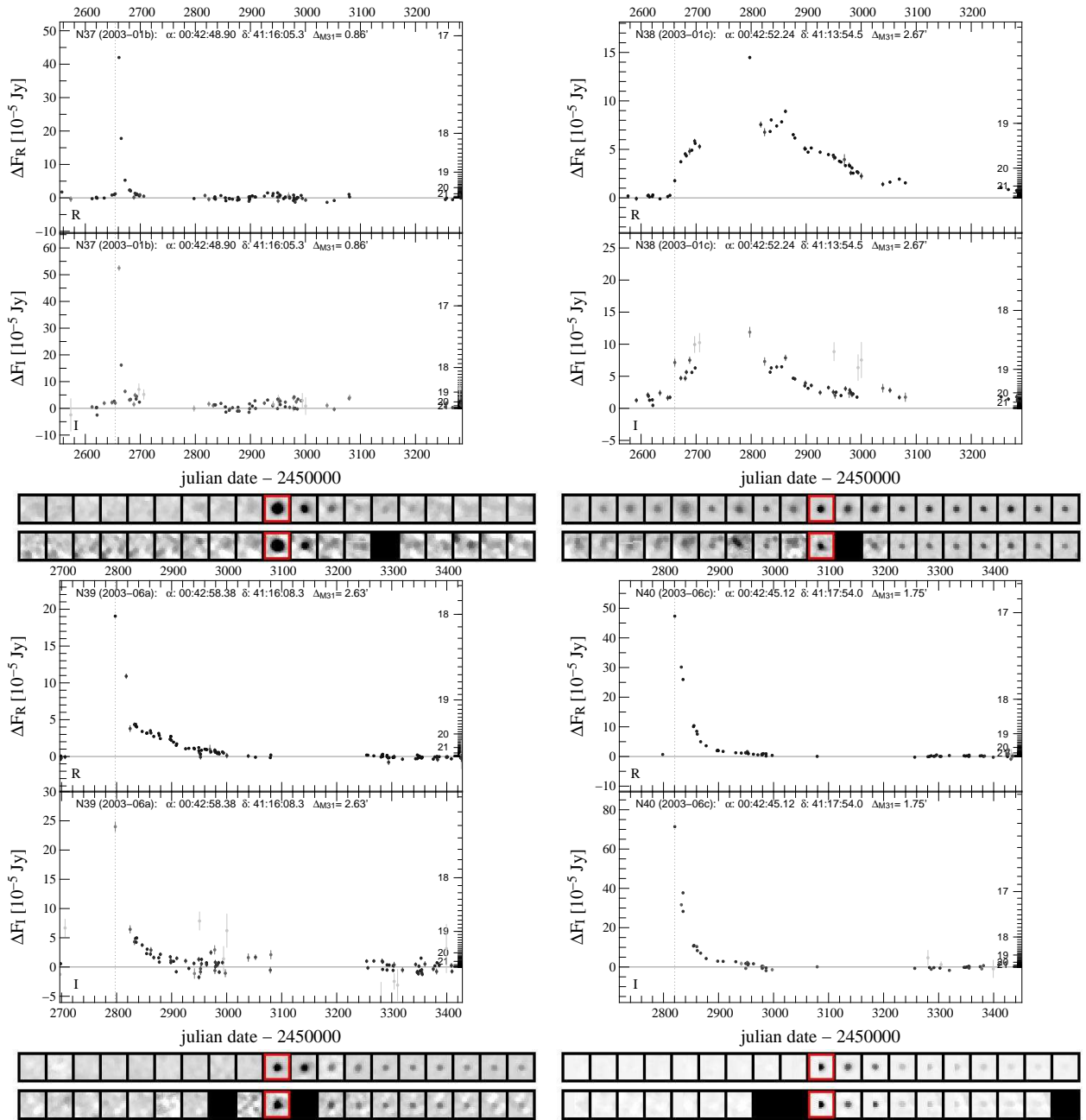


Figure 5.21: Light curves of WeCAPP nova N37-N40.

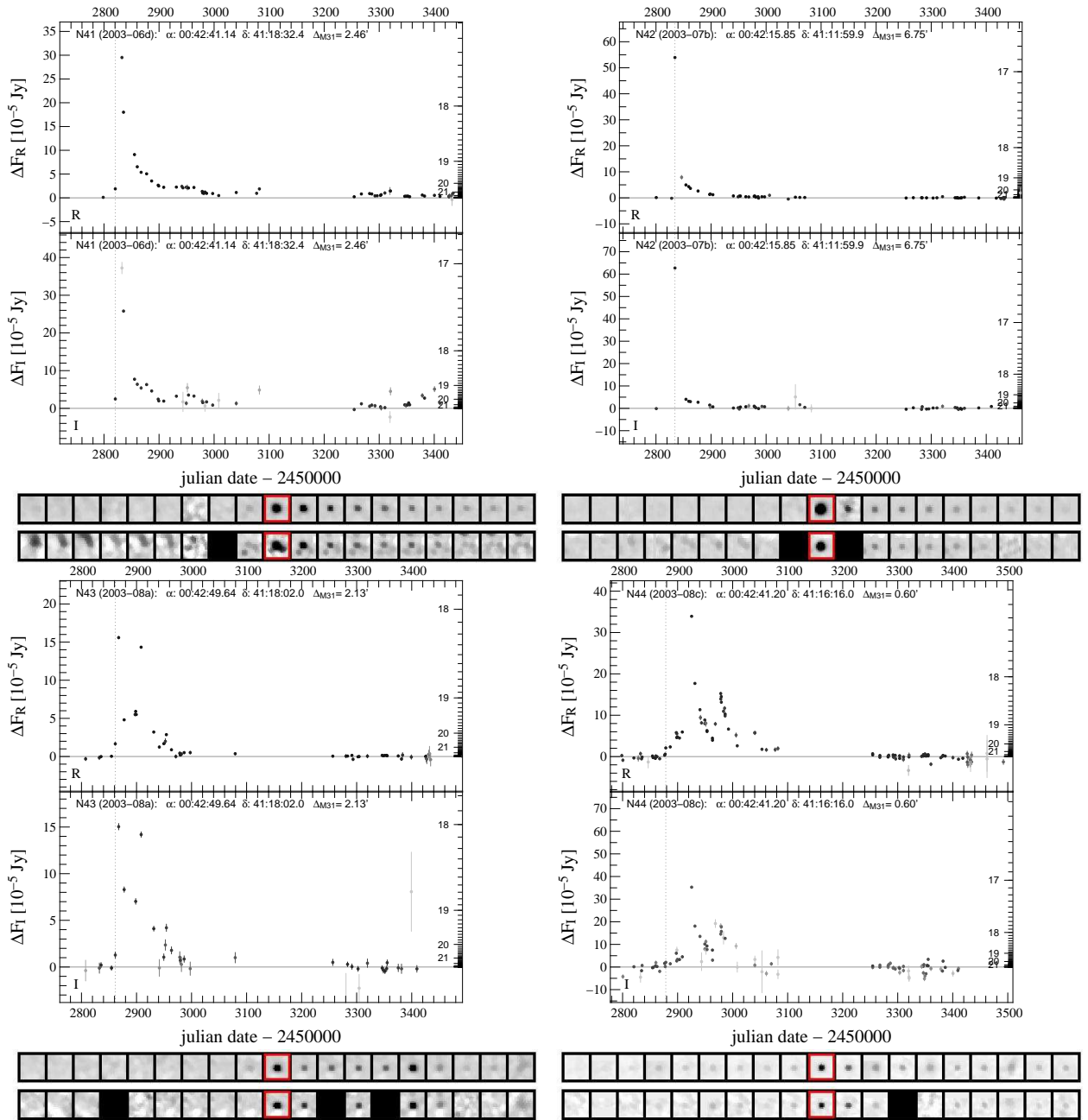


Figure 5.22: Light curves of WeCAPP nova N41-N44.

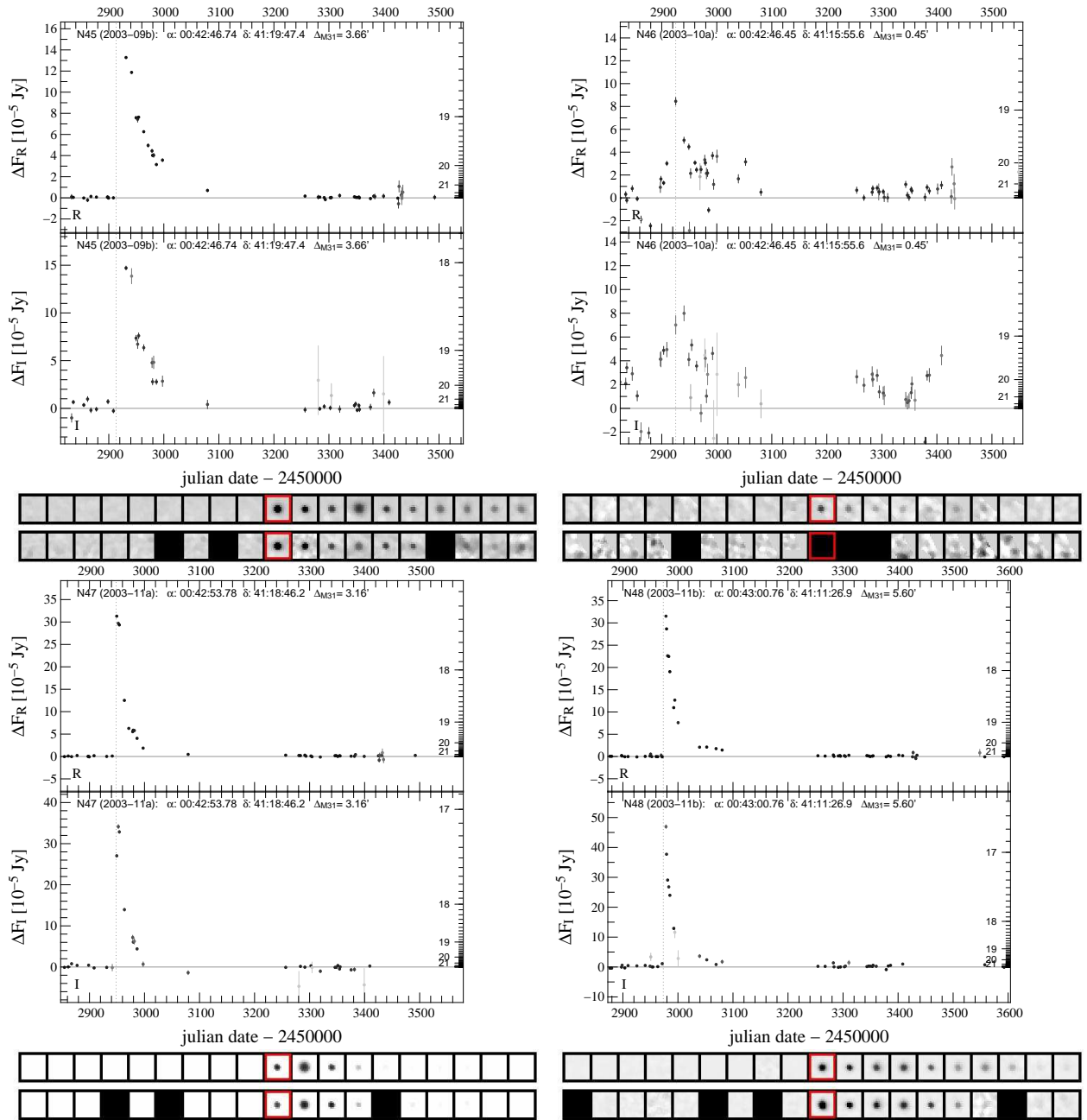


Figure 5.23: Light curves of WeCAPP nova N45-N48.

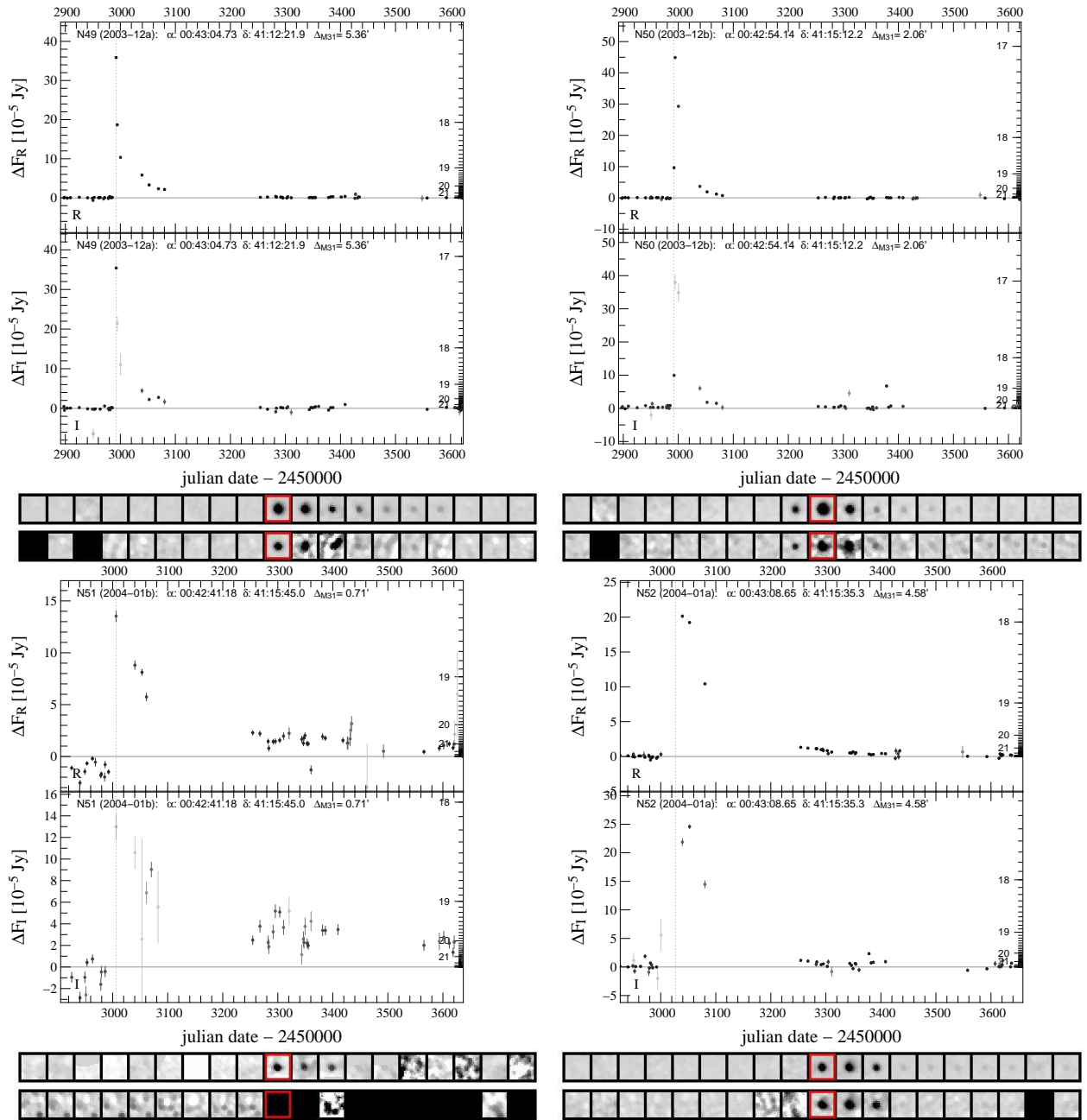


Figure 5.24: Light curves of WeCAPP nova N49-N52.

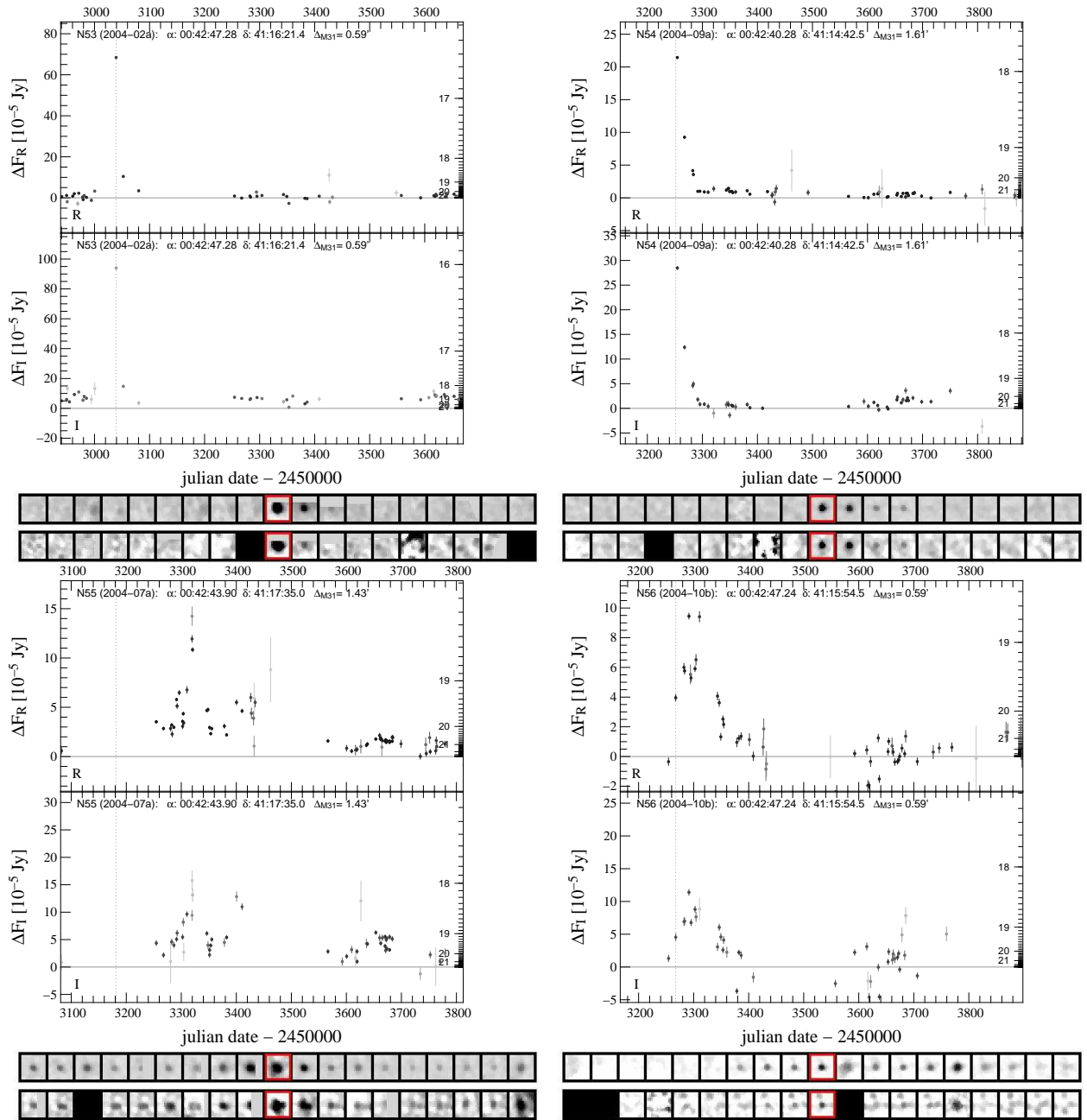


Figure 5.25: Light curves of WeCAPP nova N53-N56.

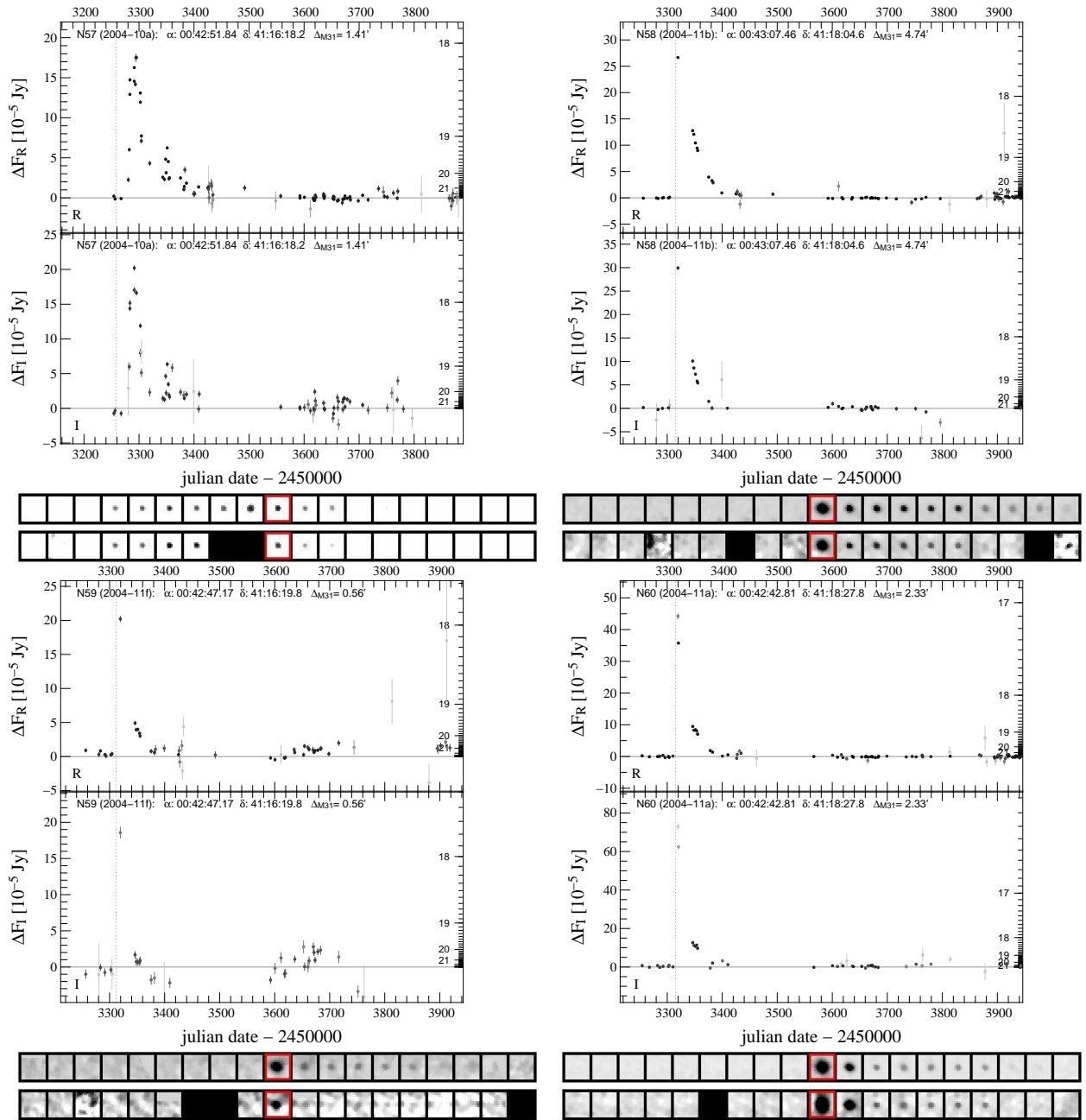


Figure 5.26: Light curves of WeCAPP nova N57-N60.

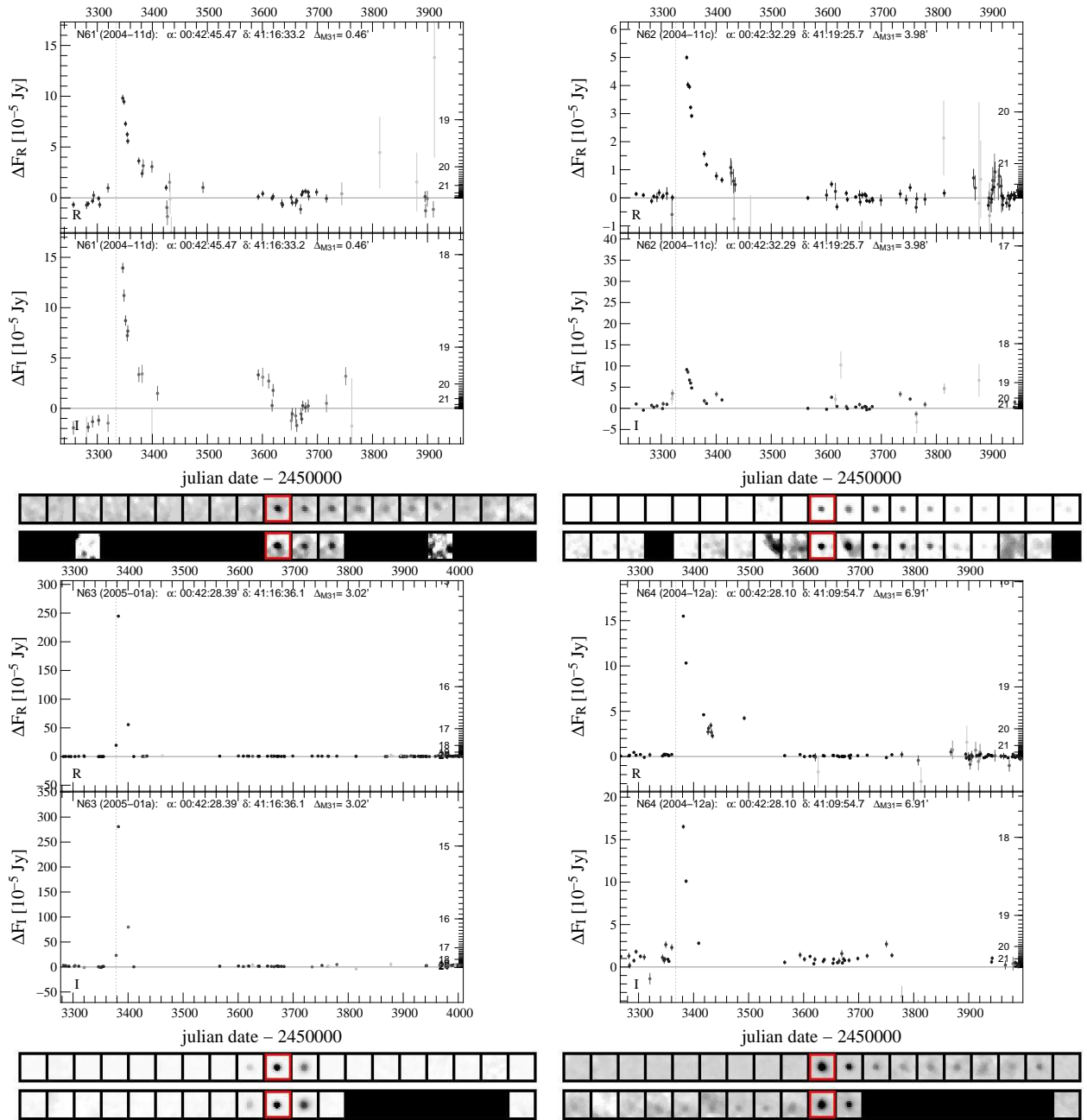


Figure 5.27: Light curves of WeCAPP nova N61-N64.

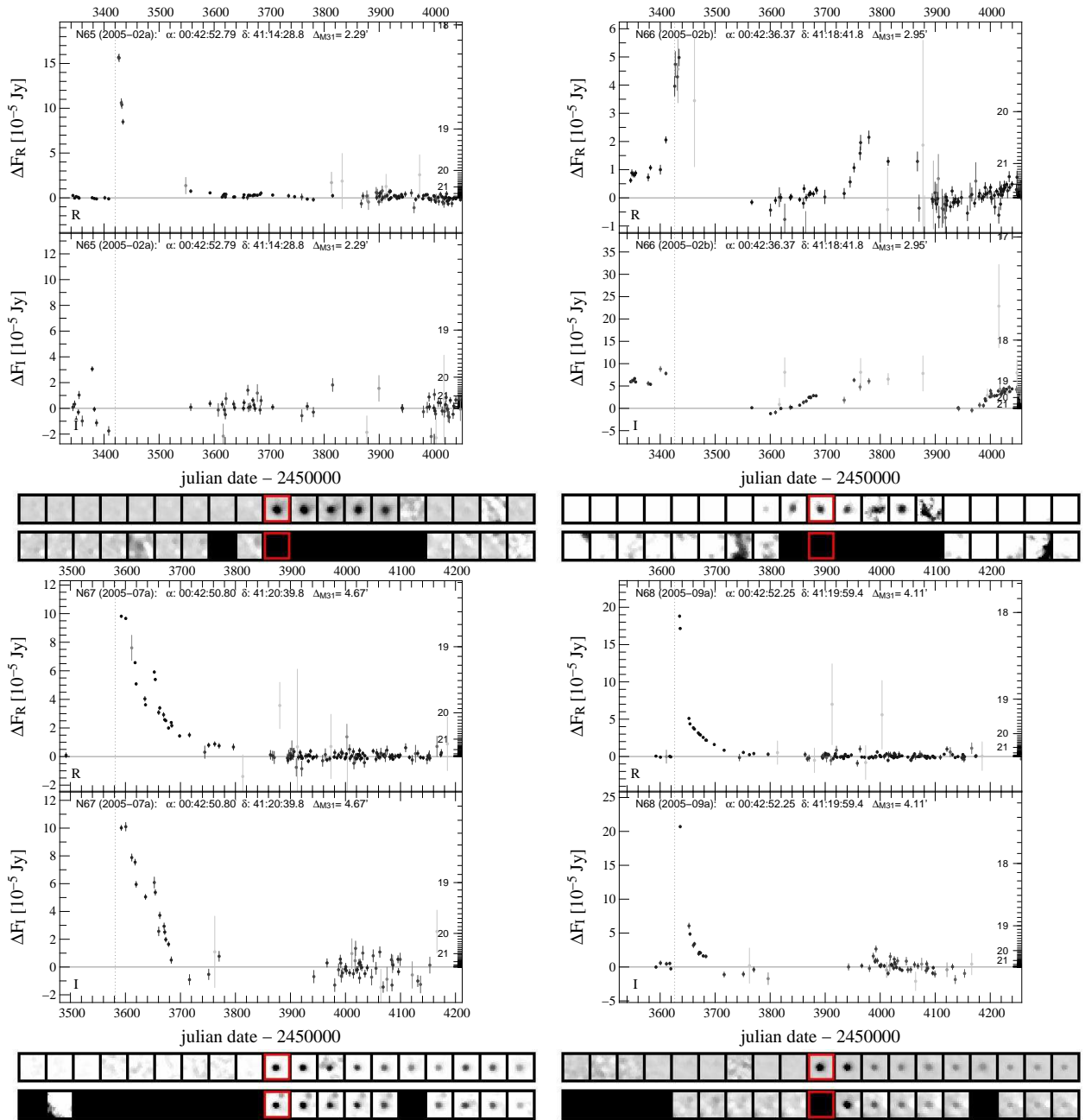


Figure 5.28: Light curves of WeCAPP nova N65-N68.

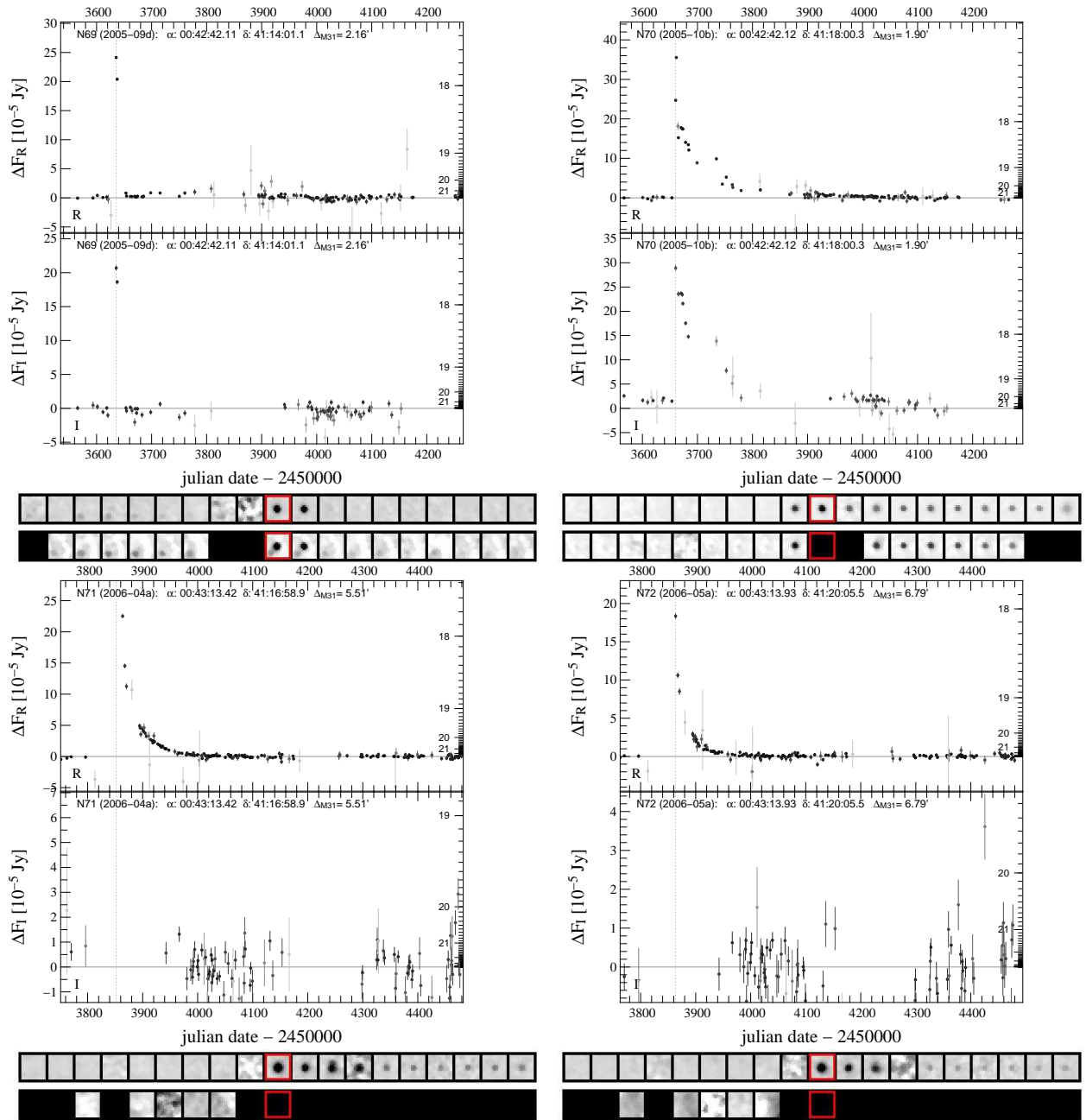


Figure 5.29: Light curves of WeCAPP nova N69-N72.

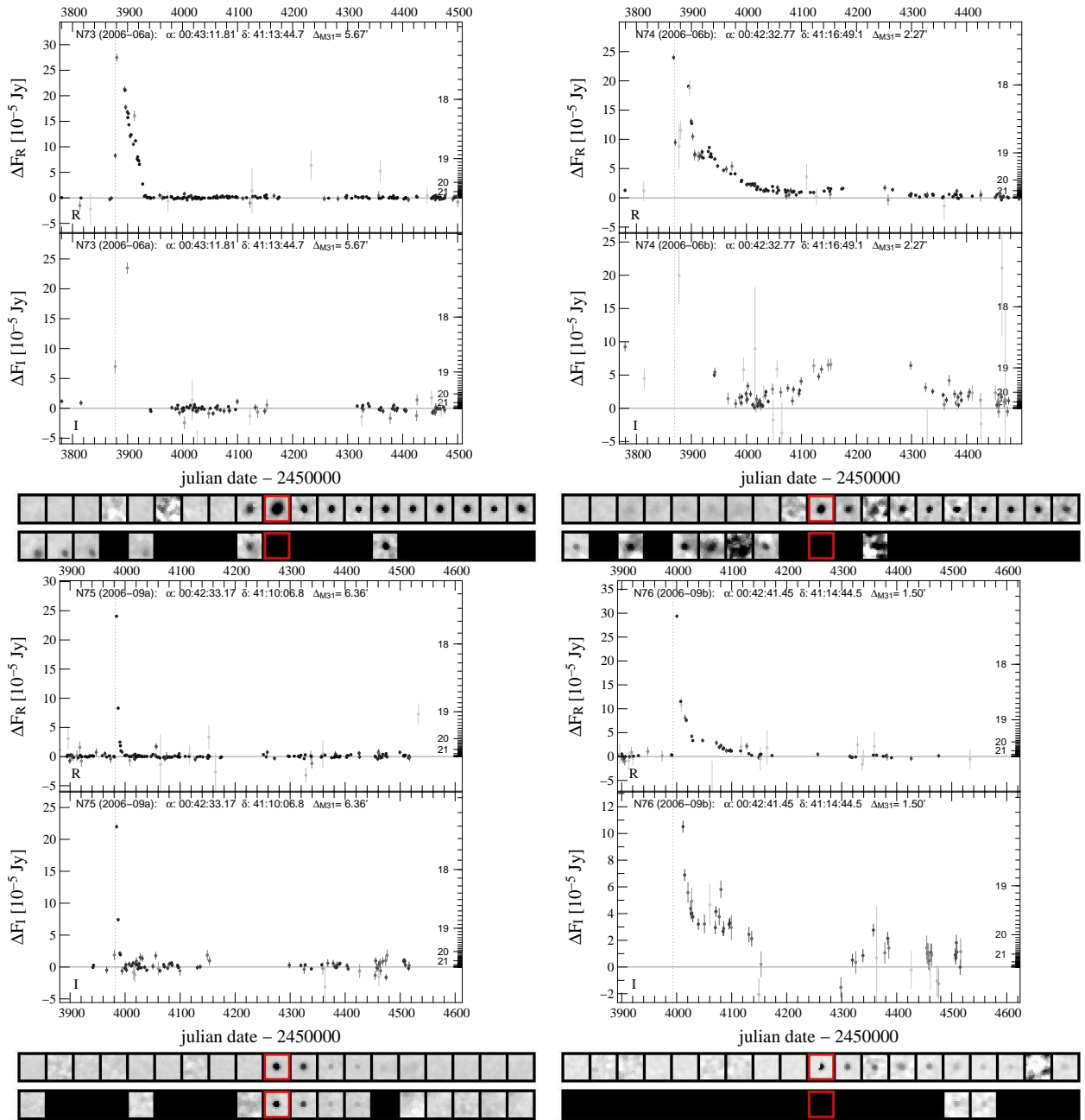


Figure 5.30: Light curves of WeCAPP nova N73-N76.

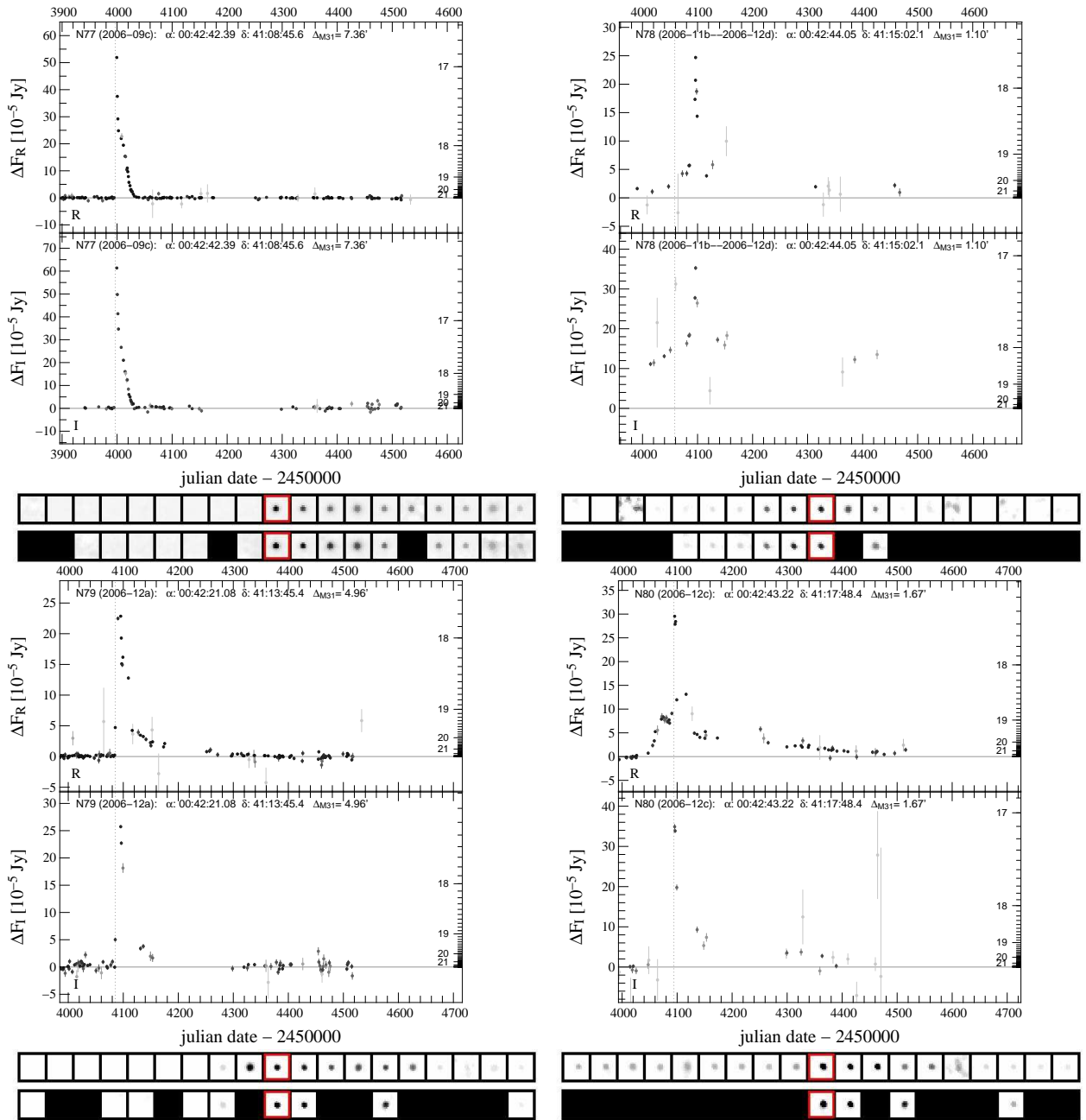


Figure 5.31: Light curves of WeCAPP nova N77-N80.

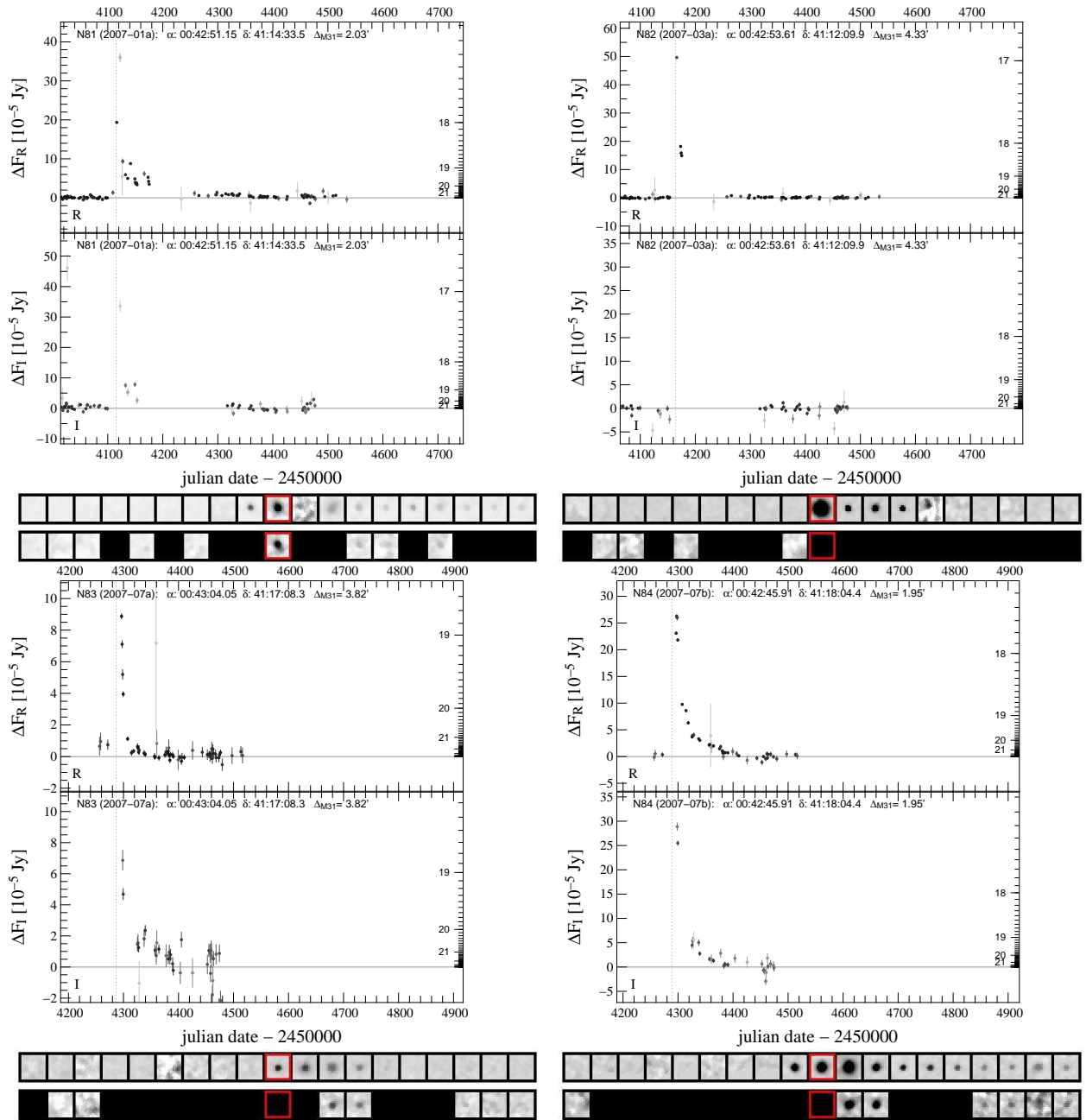


Figure 5.32: Light curves of WeCAPP nova N81-N84.

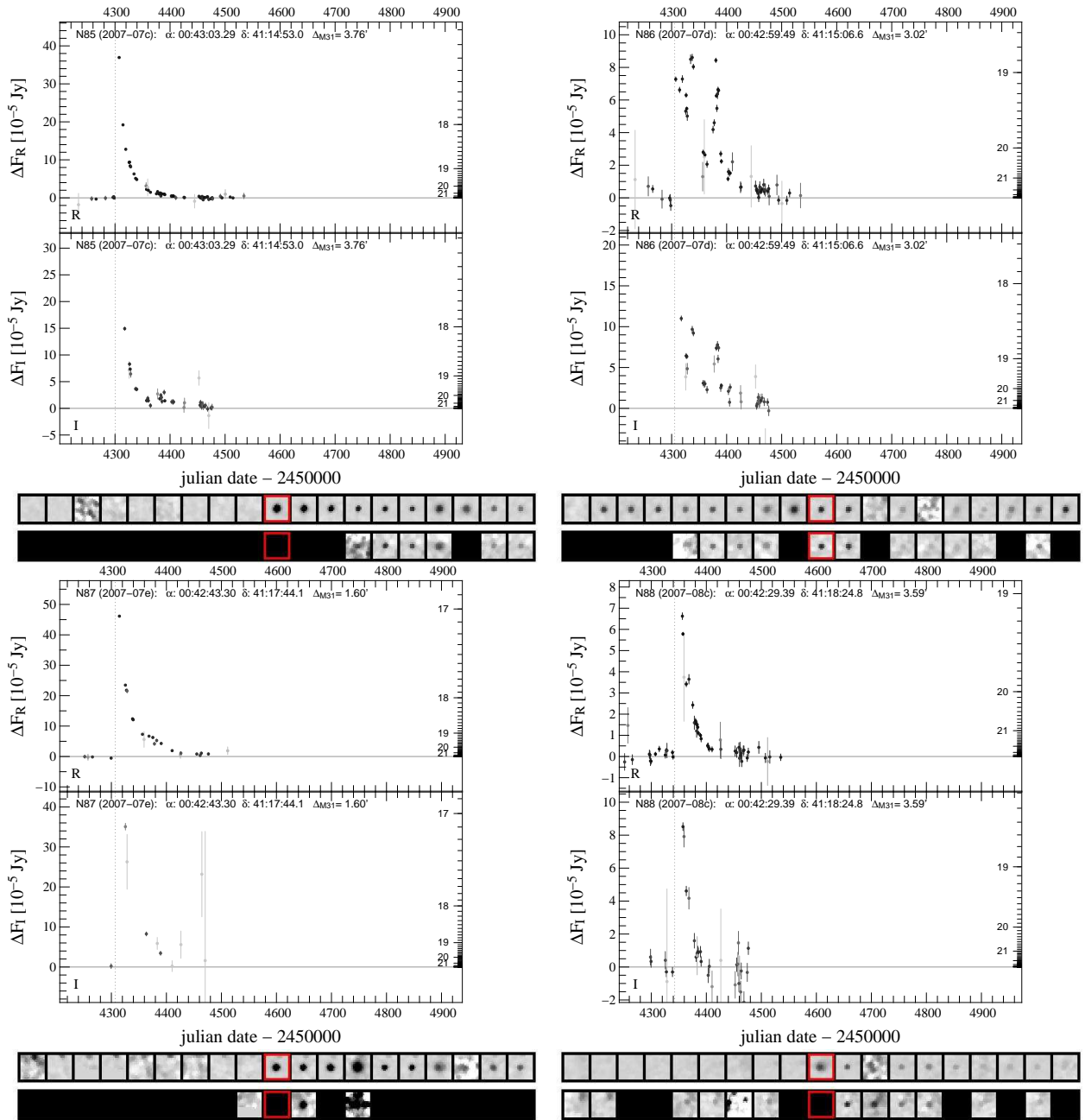


Figure 5.33: Light curves of WeCAPP nova N85-N88.

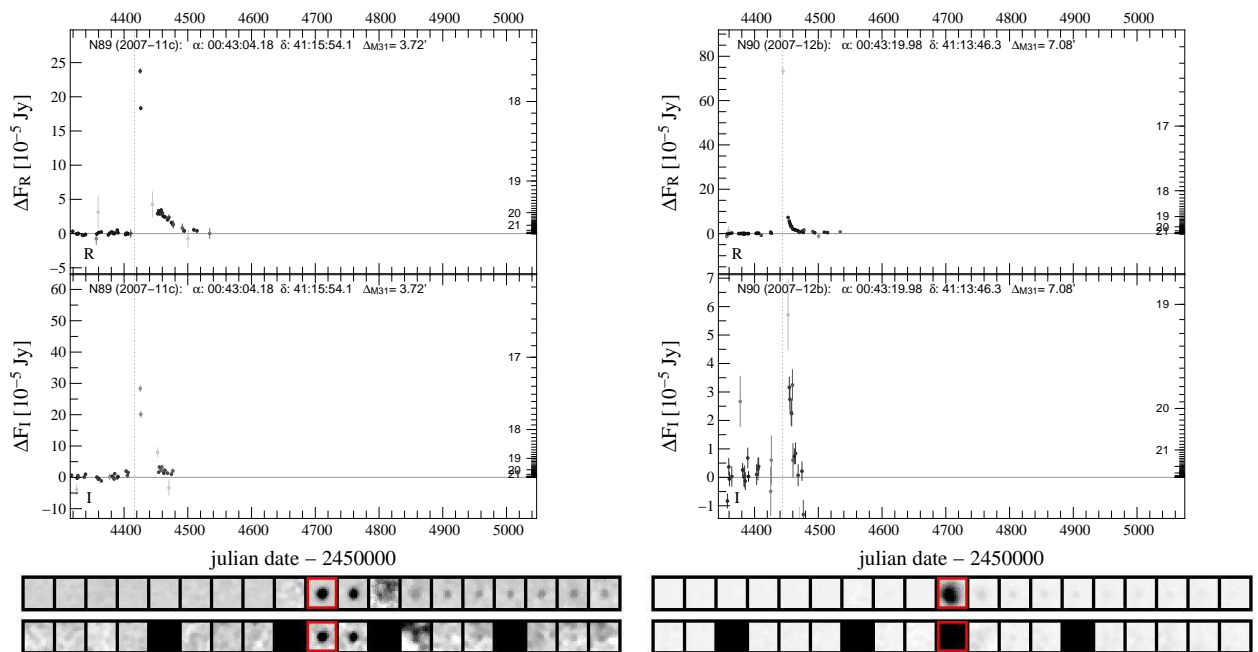
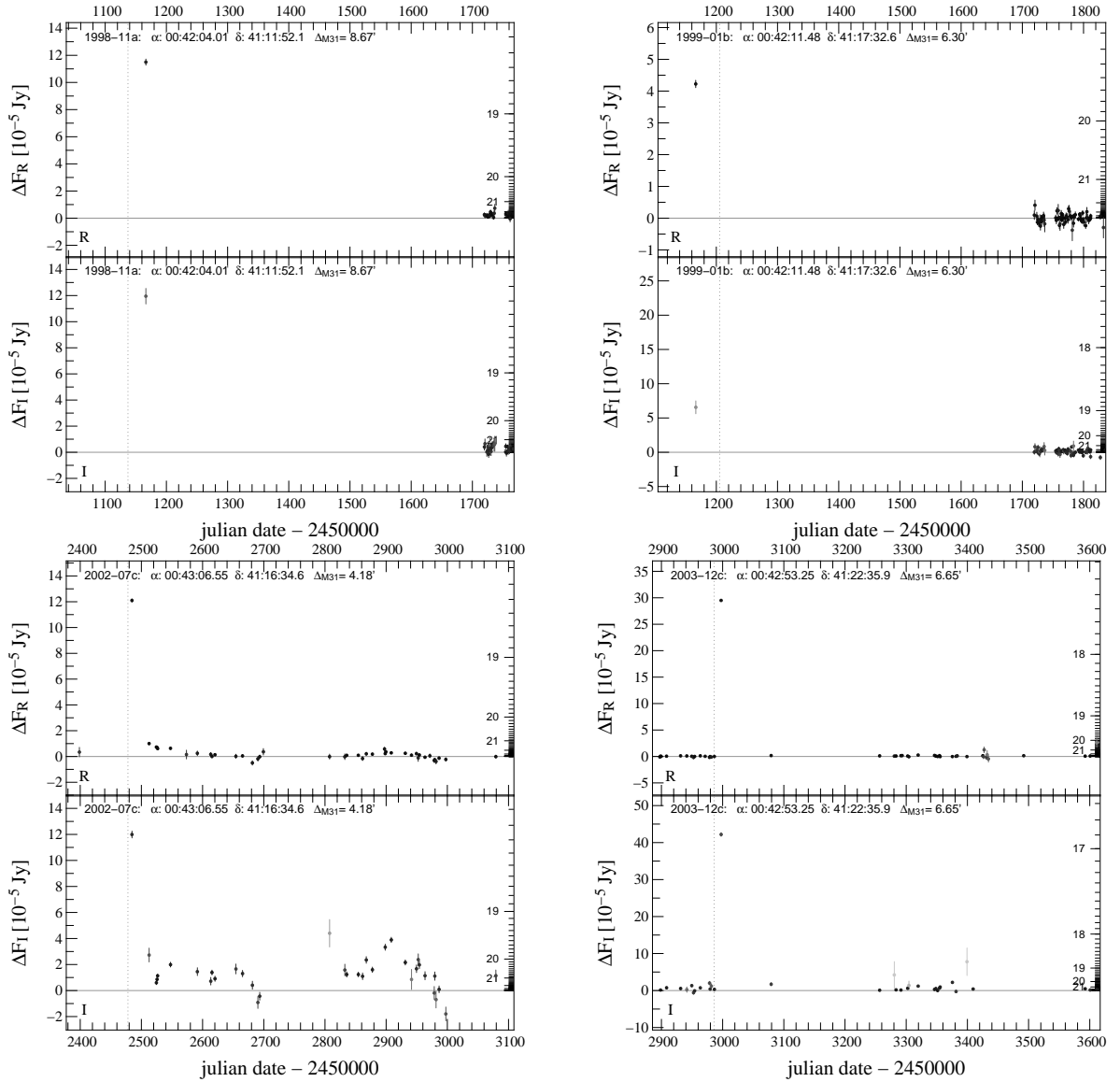


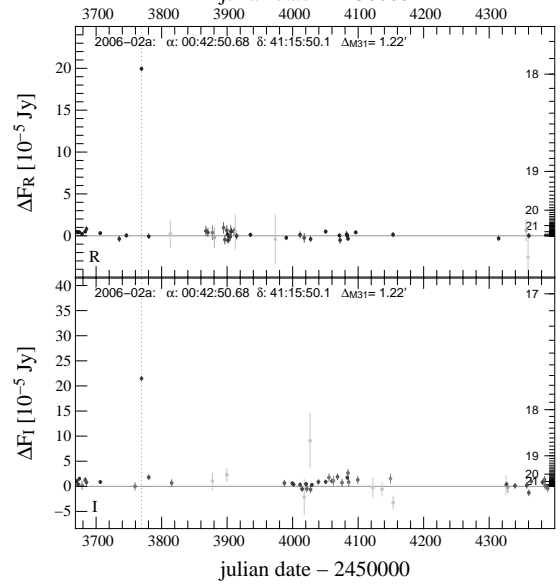
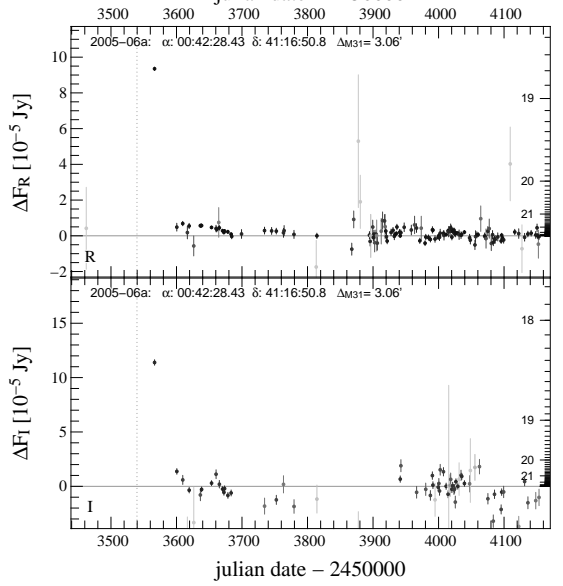
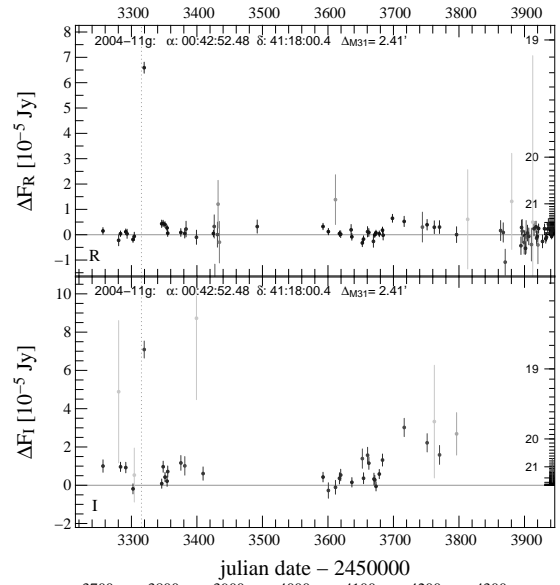
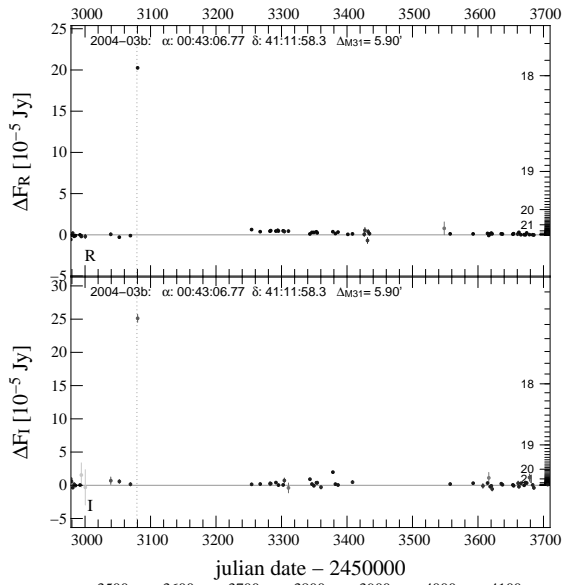
Figure 5.34: Light curves of WeCAPP nova N89 and N90.

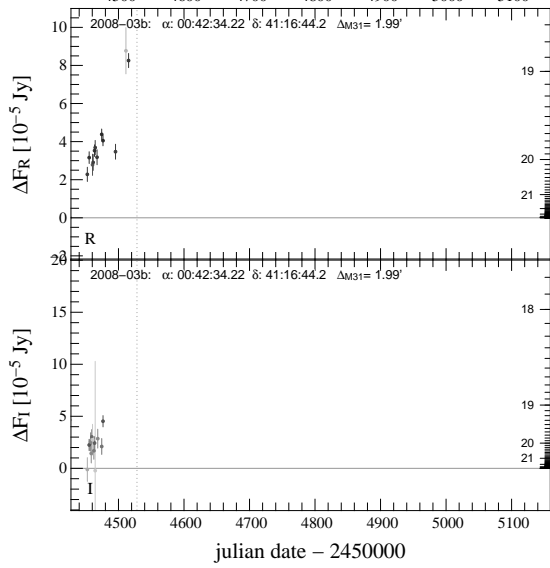
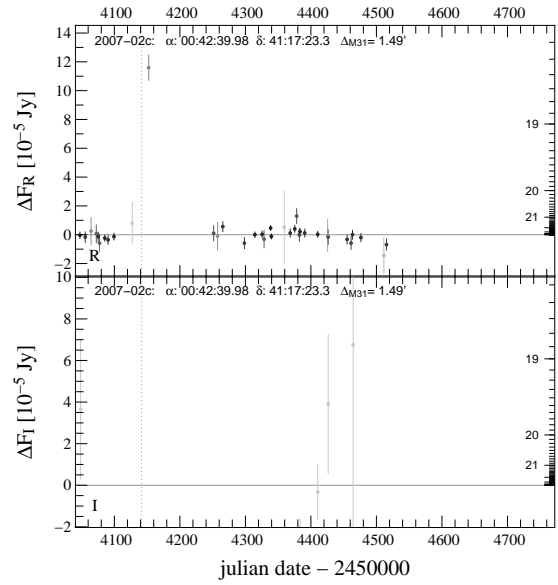
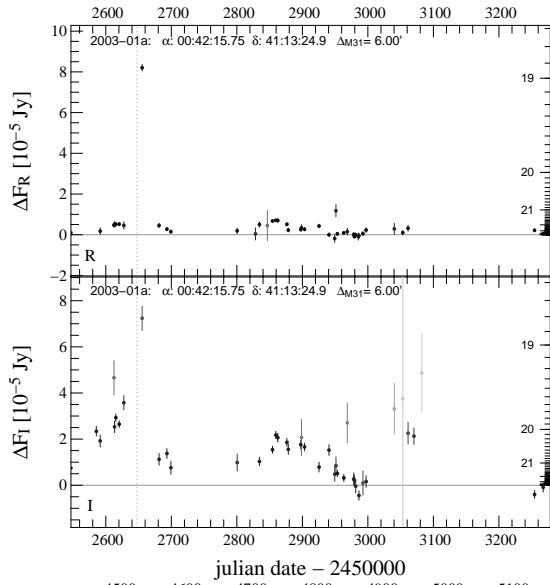
5.9 Appendix B: Light curves of nova candidates from literature

Here we present light curves for nova candidates reported by other group(s) in M31 within the field of view and time span of WeCAPP project but which do not pass our nova detection criteria. The name, position and distance to the center of M31 are shown in the figures. The time of outburst according to [Pietsch *et al.* \(2007\)](#); [Pietsch \(2010\)](#) is indicated by the vertical grey line. For every nova candidate we investigate why it did not fulfill our nova detection criteria. We group the nova candidates according to our findings and summarize these findings for each of these groups in the following.

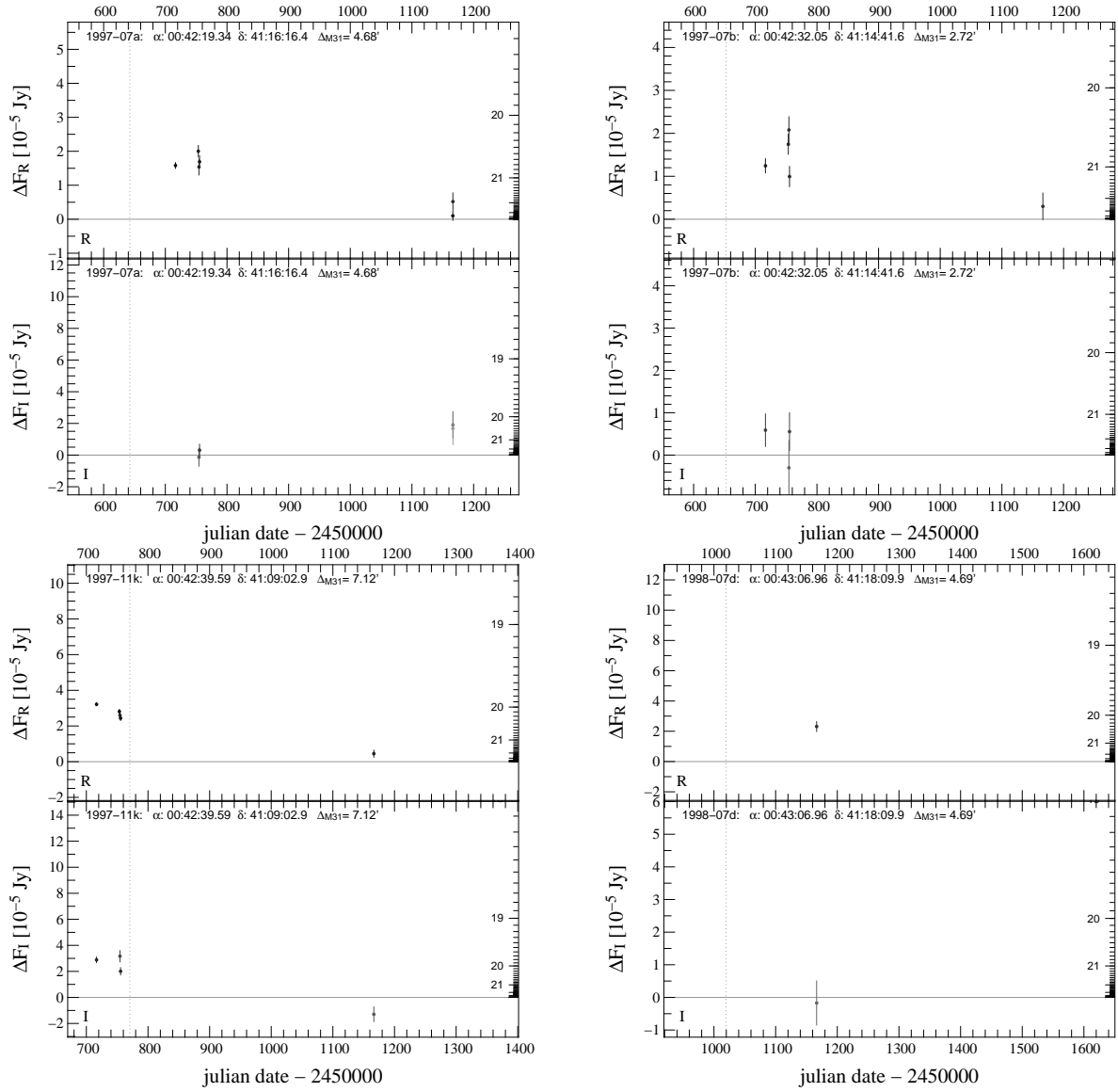
I. There are 11 nova candidates which have either a long gap of data after one single high flux excess data point or the first measurement after the peak is already below 2×10^{-5} Jy. All these candidates can in fact still be nova, but they are not well enough sampled at the peak to be positively classified as novae by us.

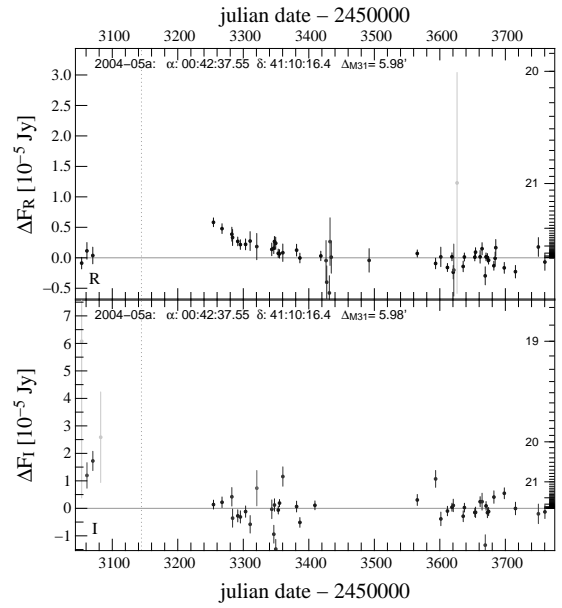
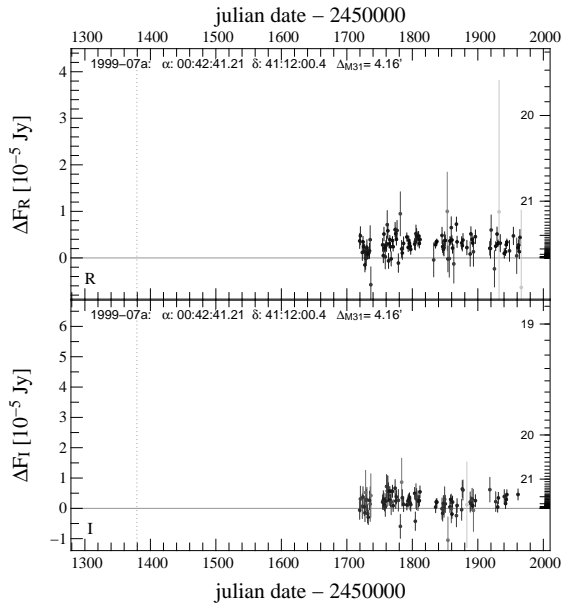
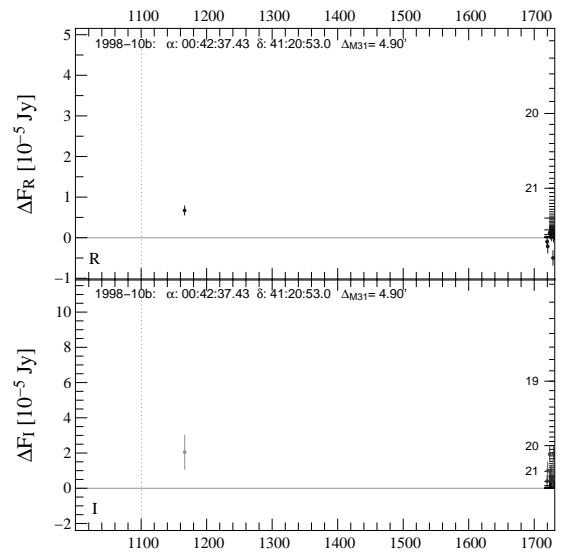
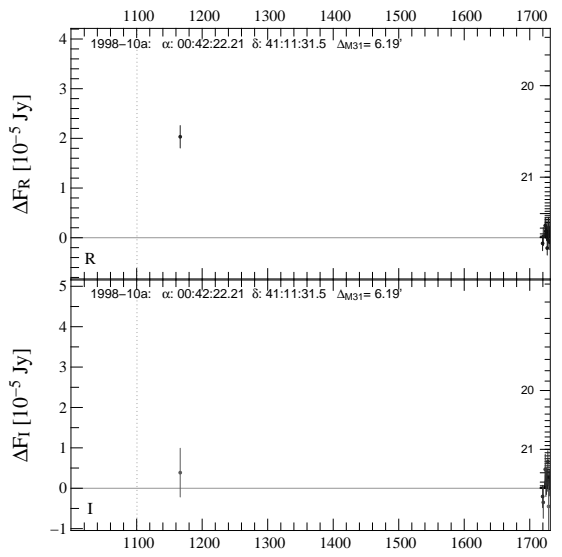


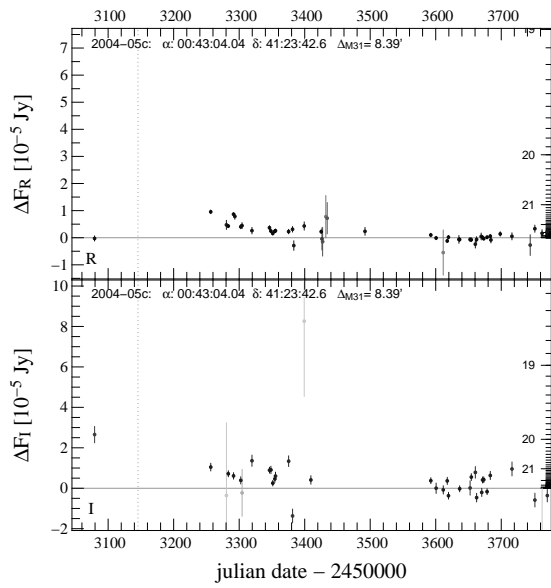




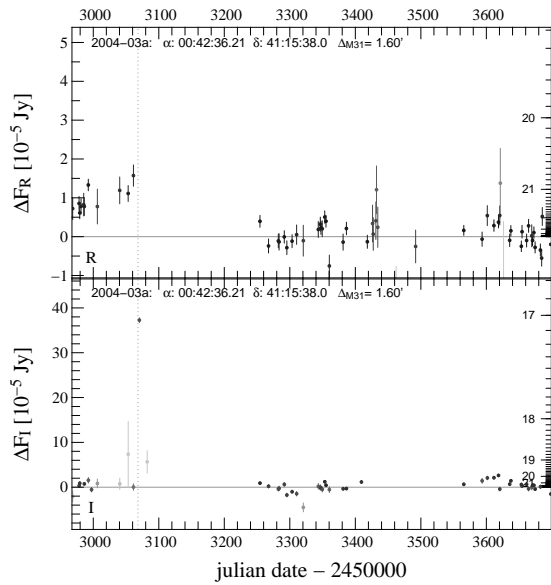
II. There are 9 nova light curve candidates for which the highest flux excess is not bright enough, peak flux $< 4 \times 10^{-5}$ Jy, to be classified as a nova candidate by us.



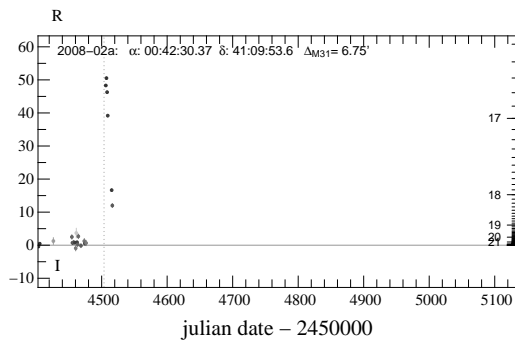




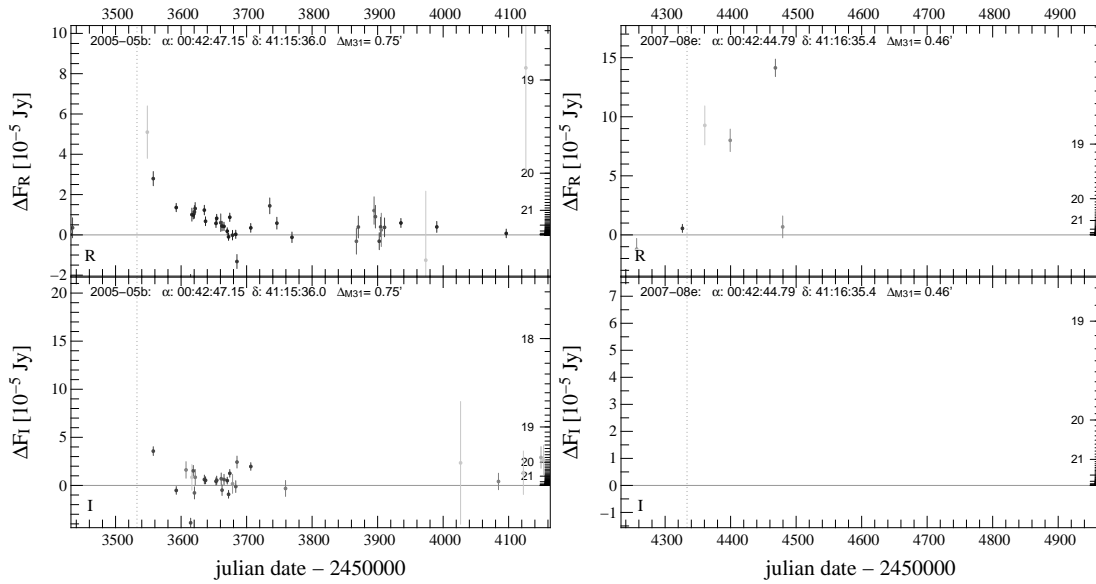
III. There are 2 nova candidates for which we miss the outburst in *R* completely. For both of them we measure the outburst in *I*, but this is not a criteria for our nova detection.



2008-02a: $\alpha: 00:42:30.37$ $\delta: 41:09:53.6$ $\Delta_{M31} = 6.75'$

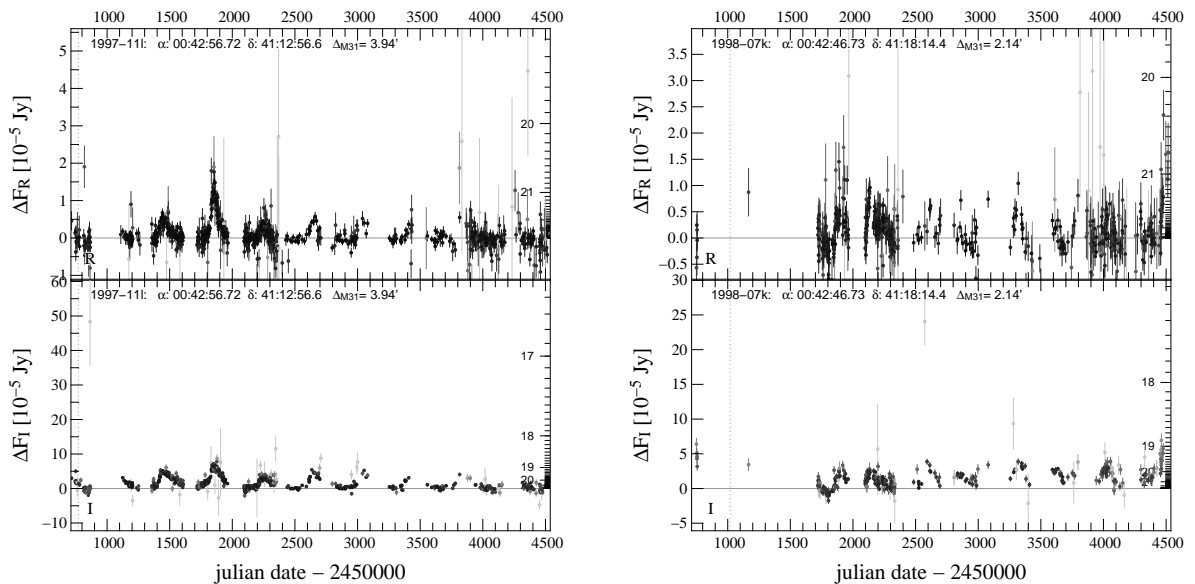


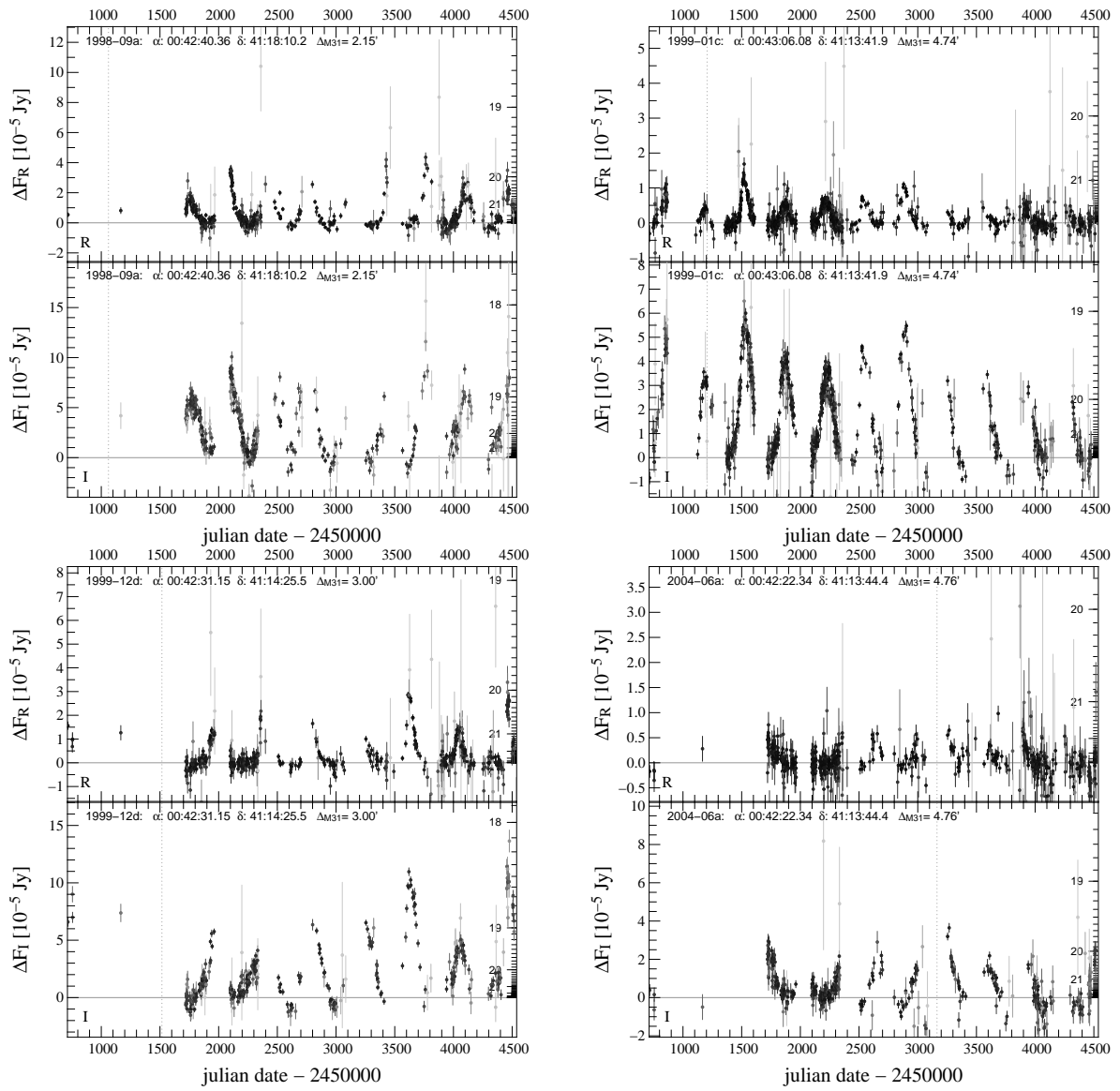
IV. There are 2 nova candidates for which the high flux excess data point has a large error and thus not fulfill our $10 \sigma_{\text{peak}}$ criterion.

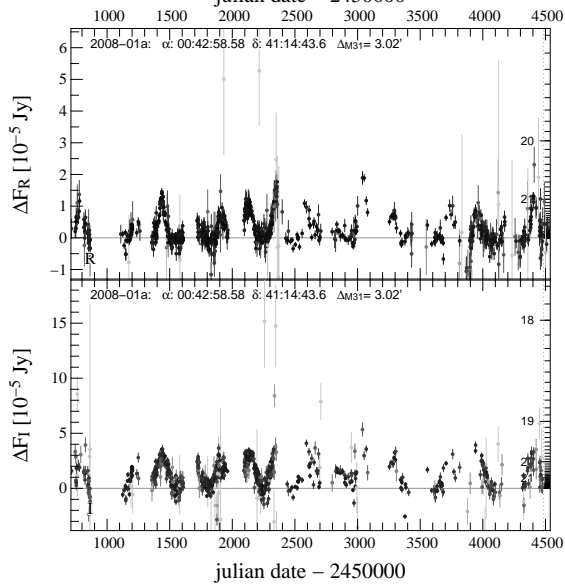
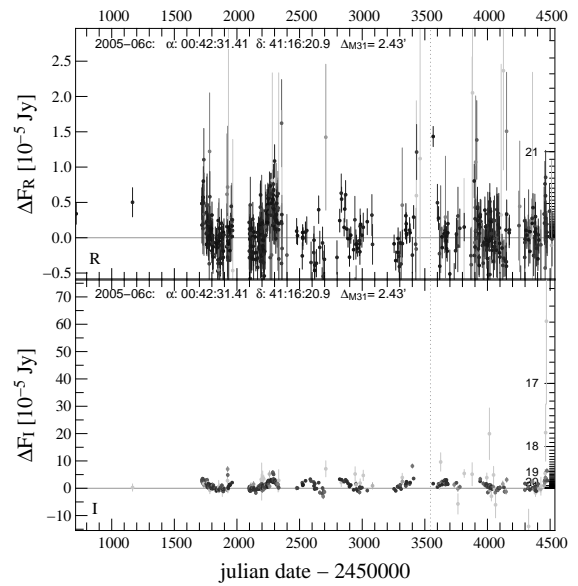
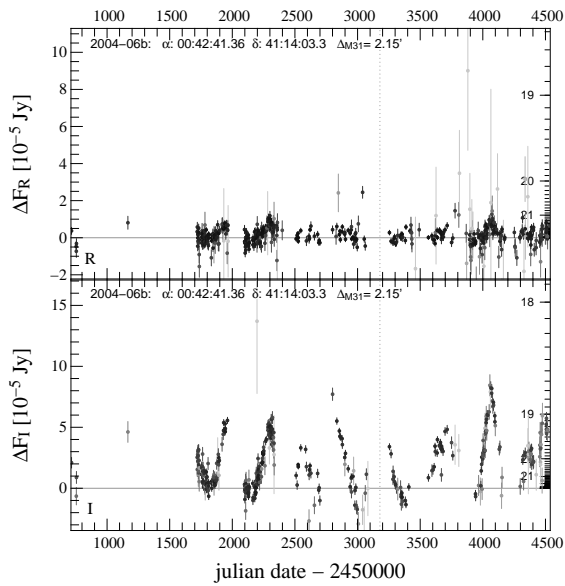


V. For 15 of previously reported nova candidates, we would doubt the nova nature.

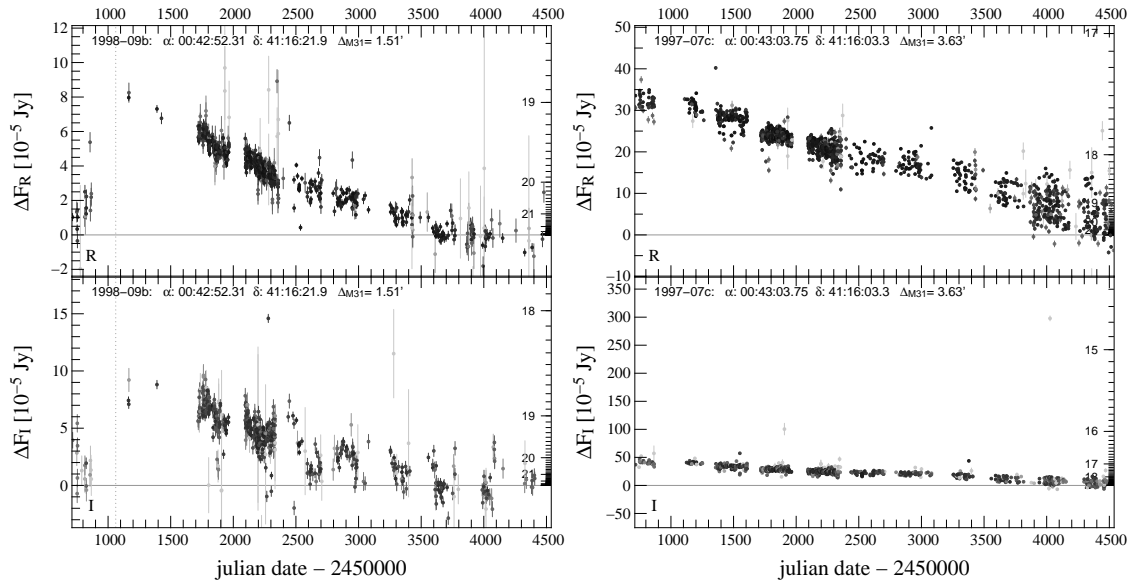
V.(a) 9 of them are very likely to be variable stars and are shown now



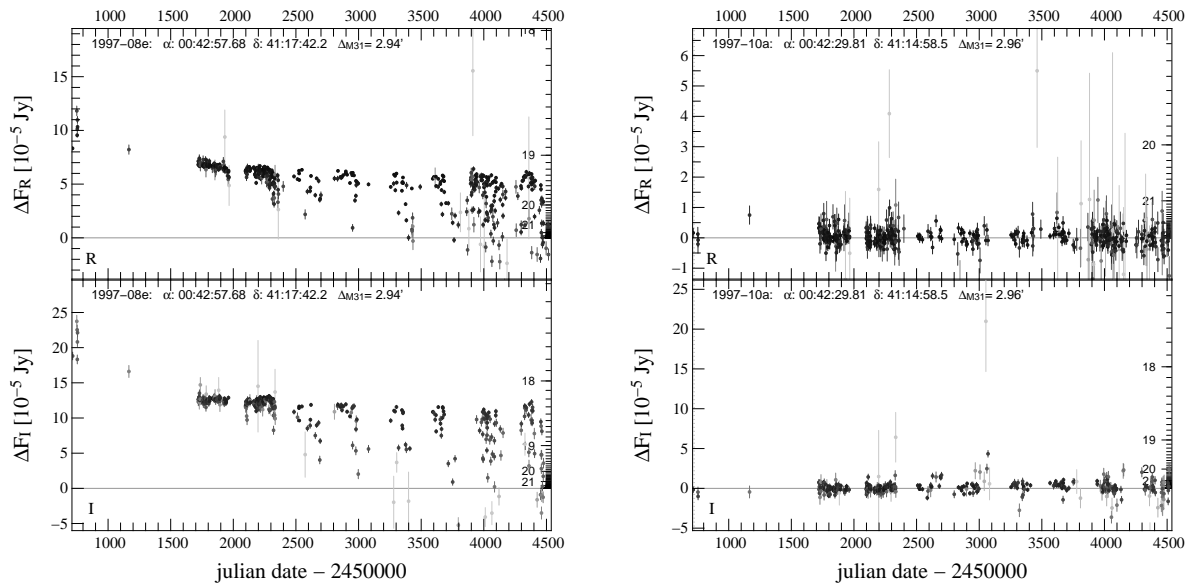


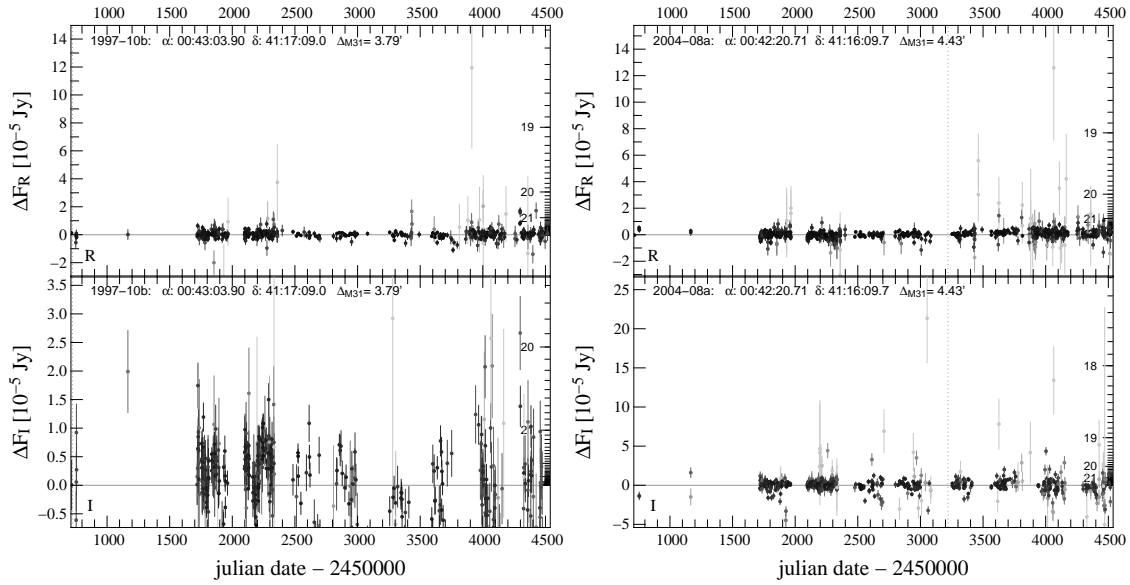


V.(b) 2 of these previous nova candidates are classified as FU variable stars by us (for FU Ori or V 1057 Cyg see (Herbig 1977))

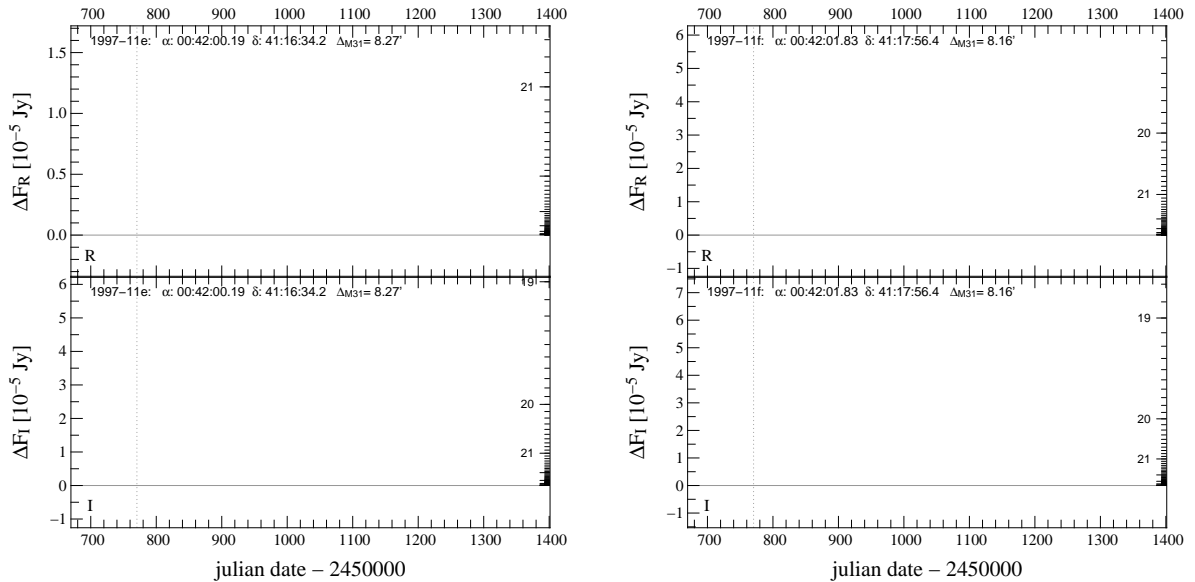


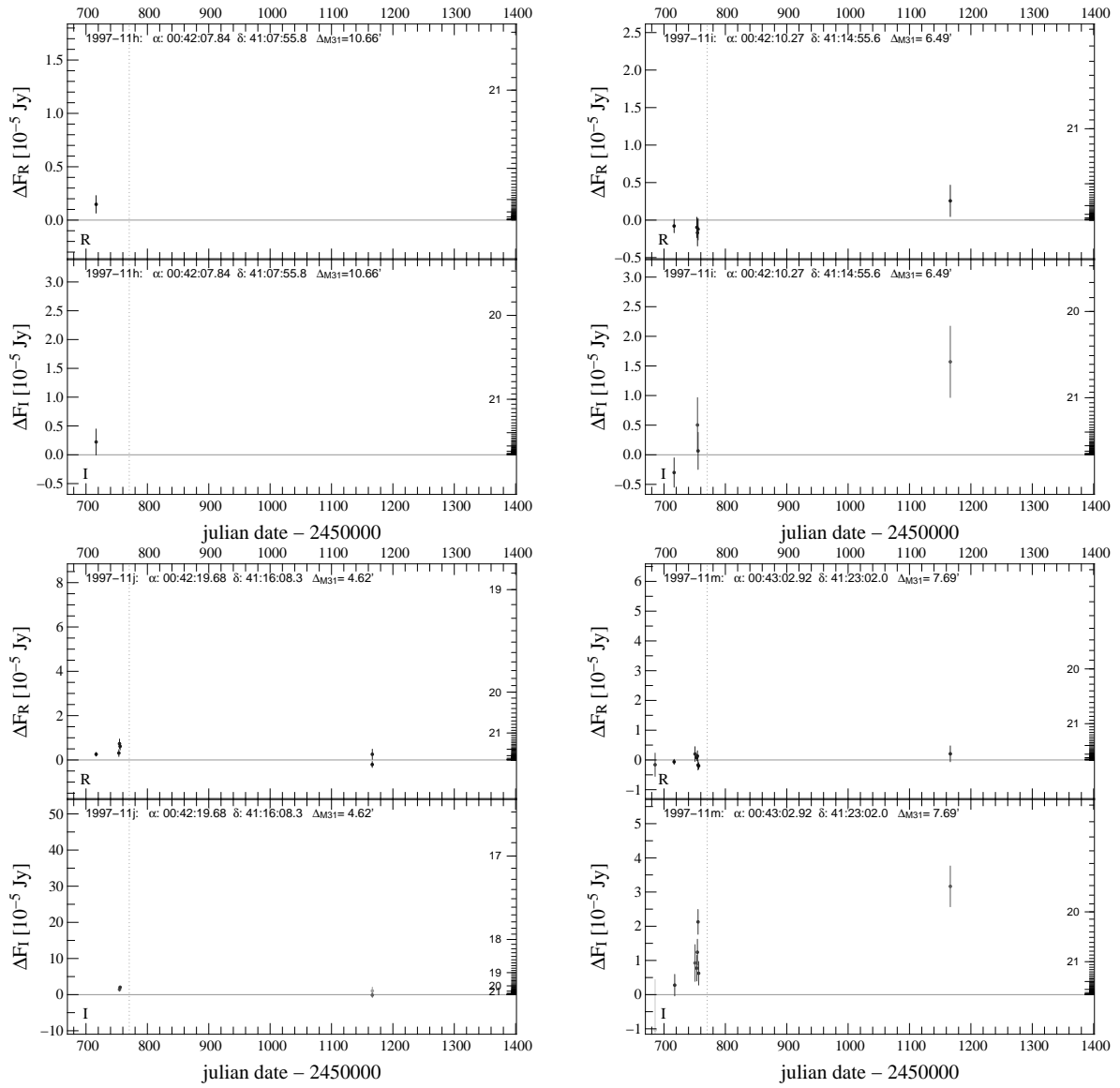
V.(c) for 4 of these previous nova candidates we see minor variability at the time of nova detection but the light curve has no nova features otherwise.

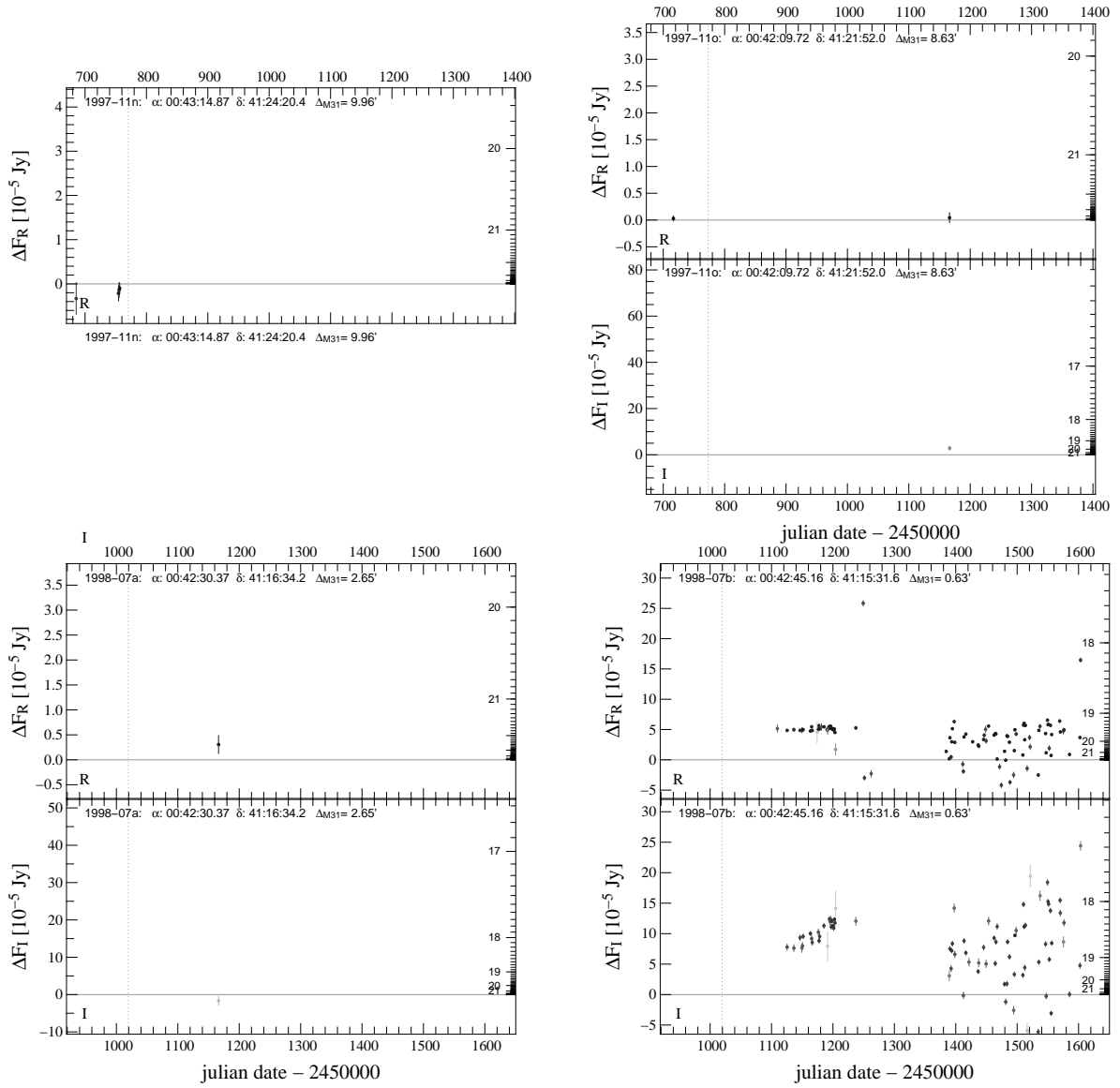


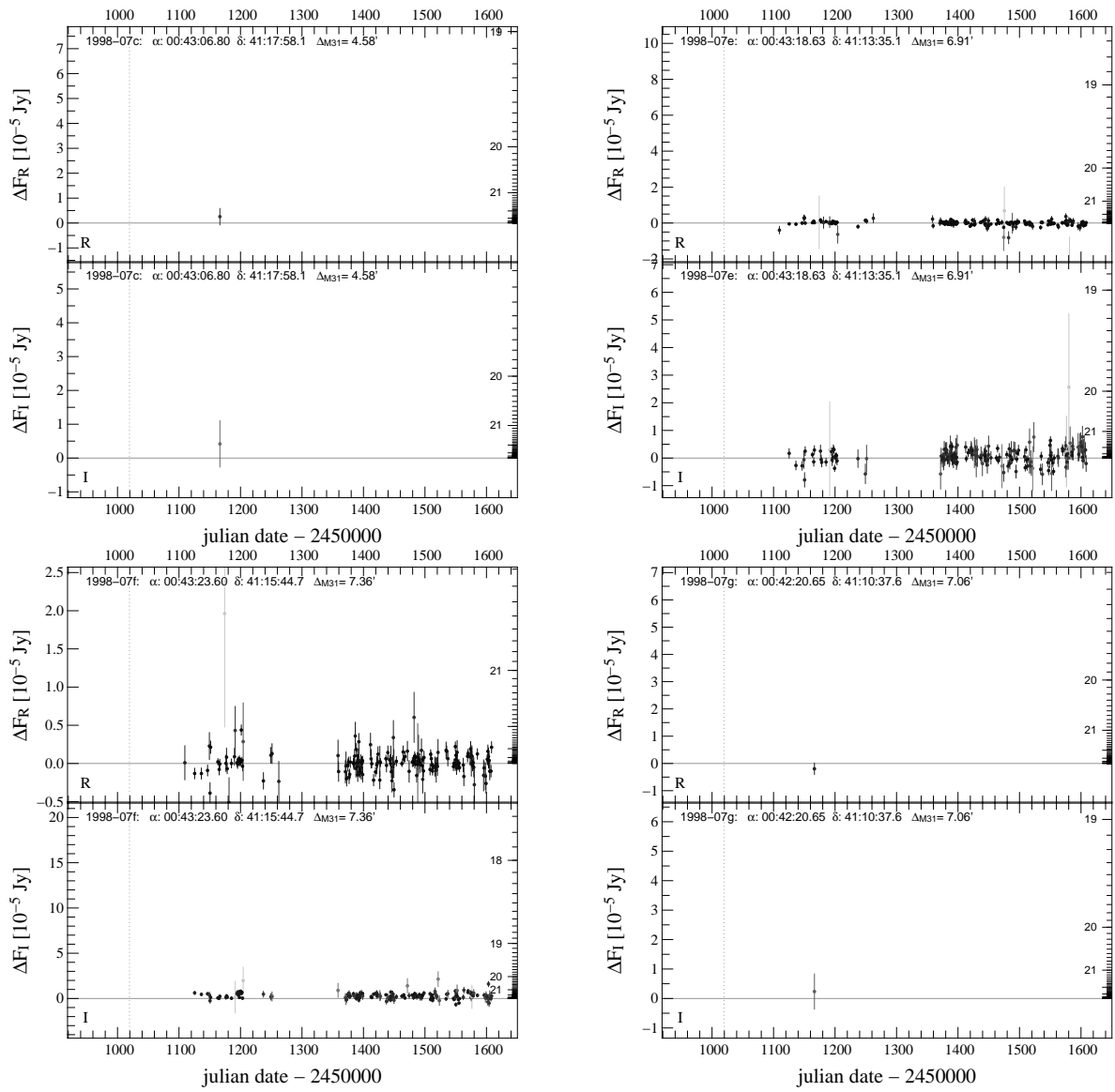


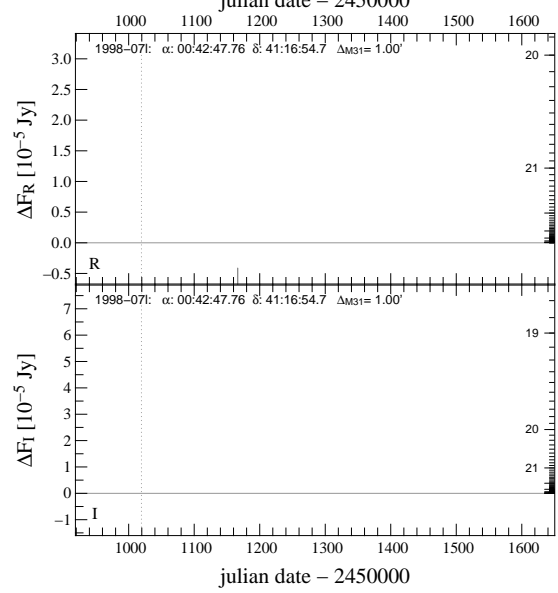
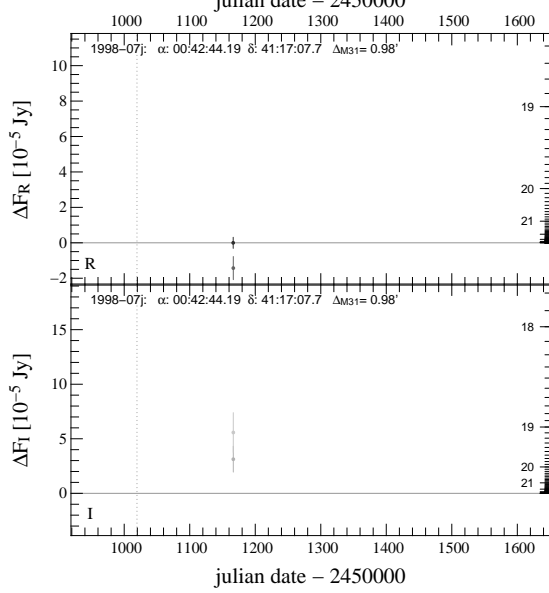
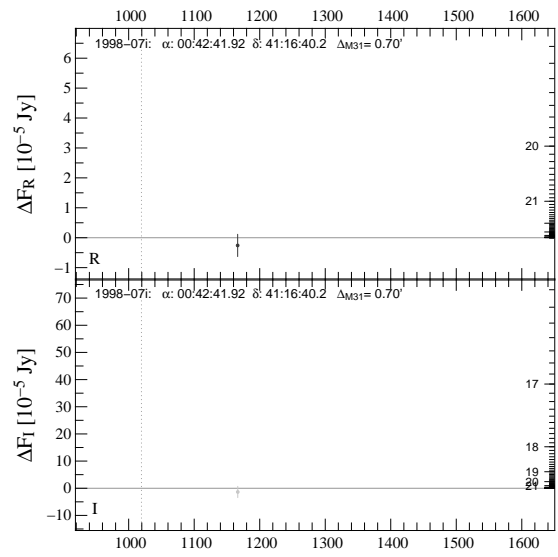
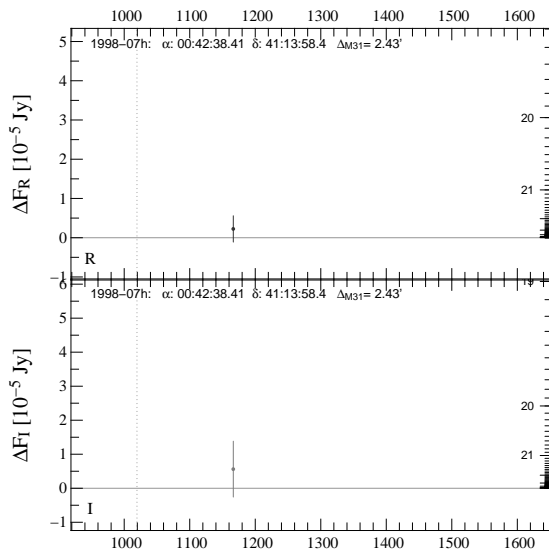
VI. For 32 nova candidates we have no data at all around the maximum brightness so we can not contribute to the classification of these objects. However, we have data at previous or later times that can be combined with those from the original nova measurements to further constrain the nova nature.

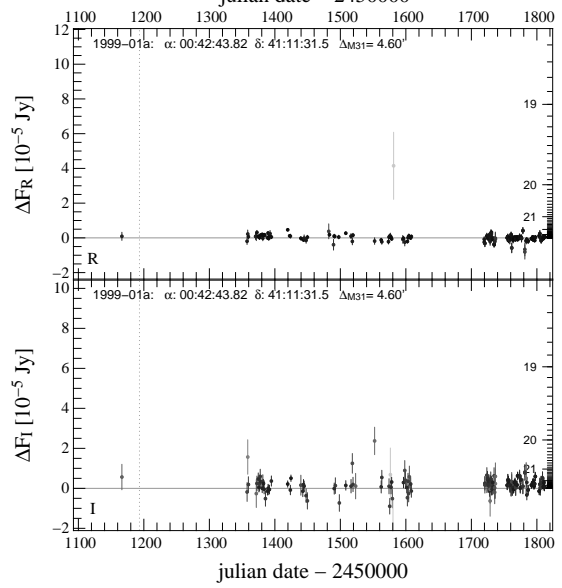
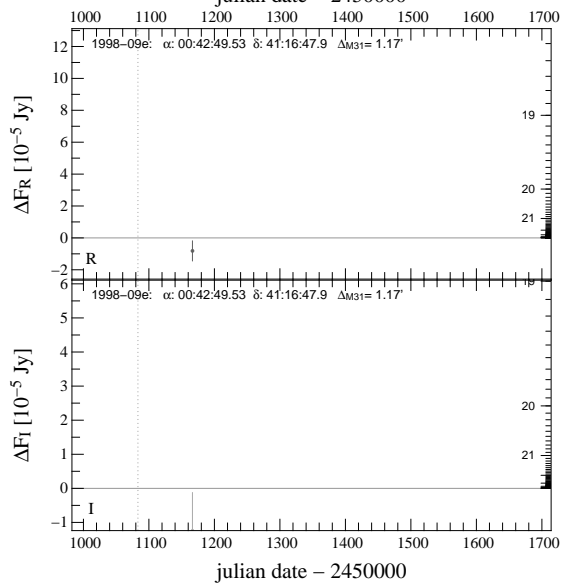
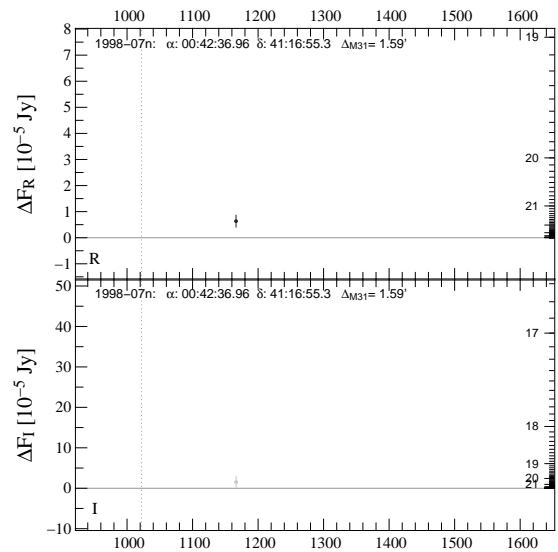
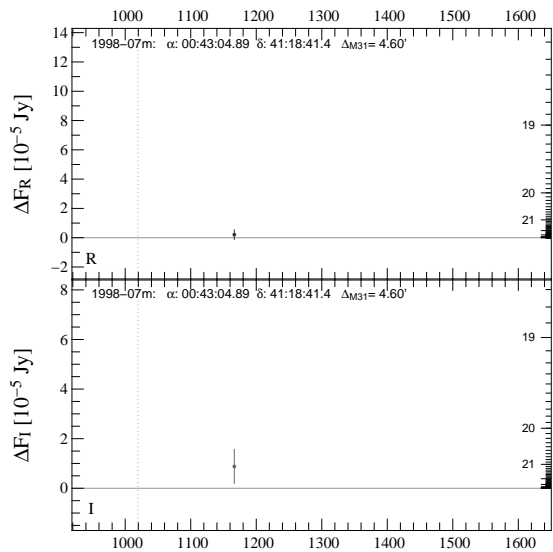


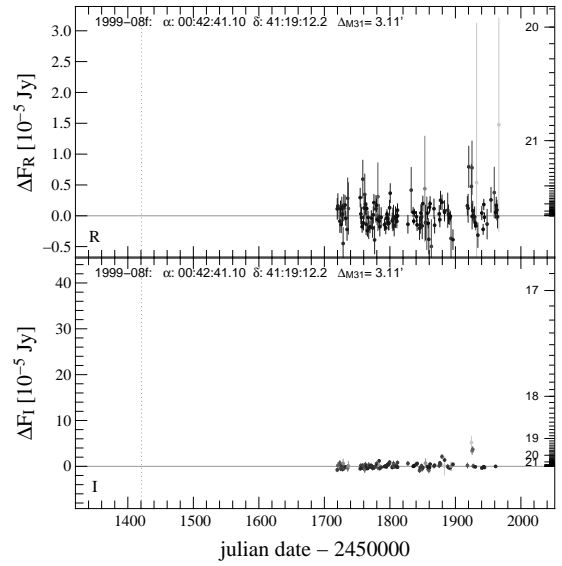
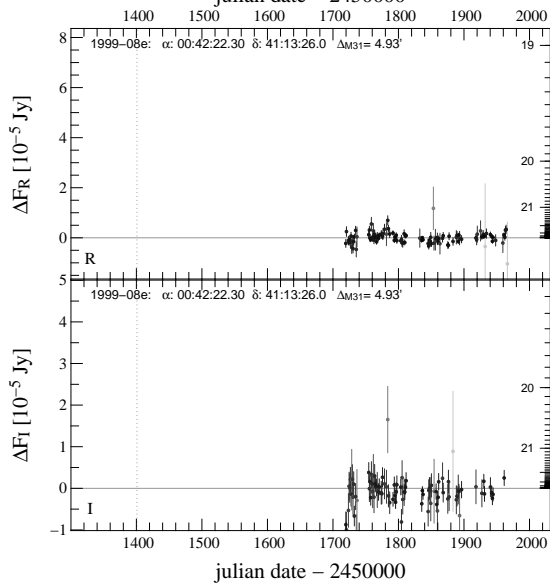
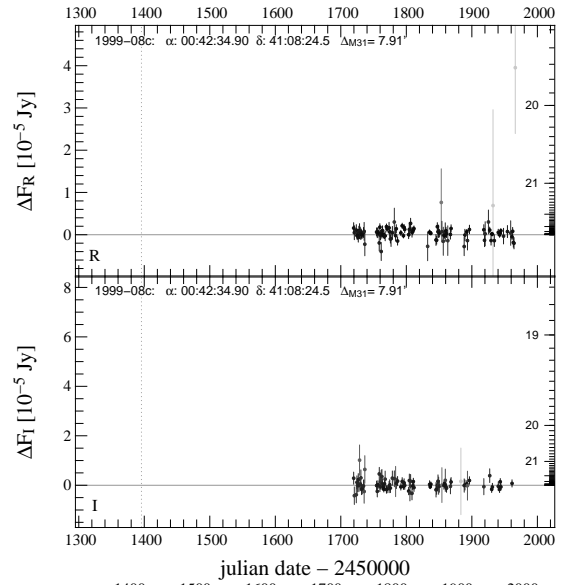
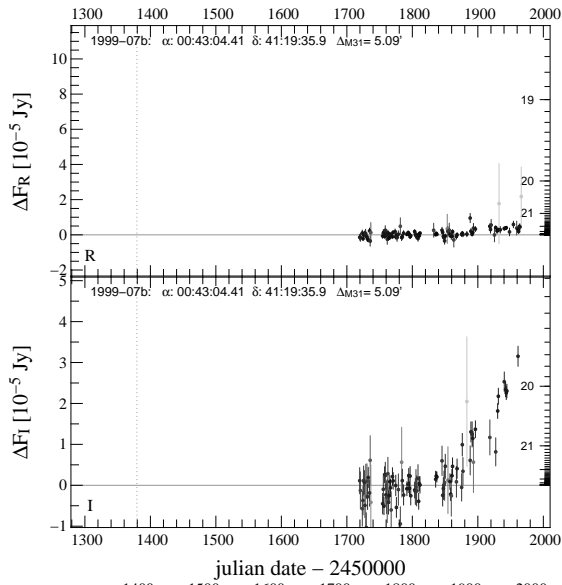


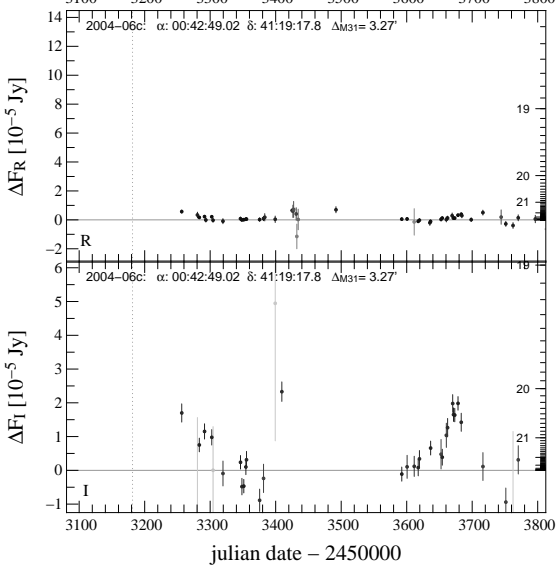
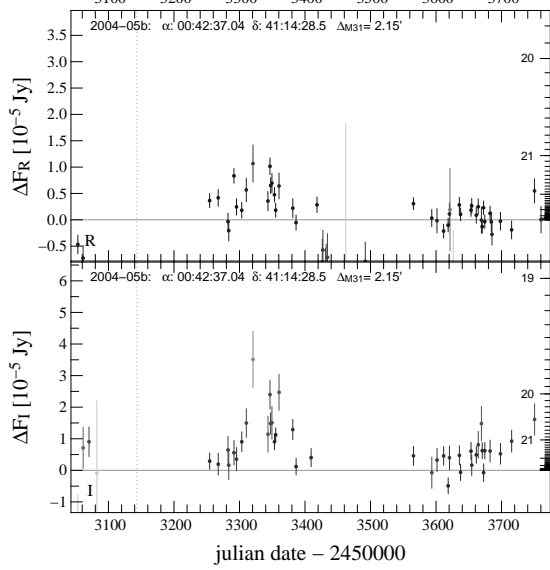
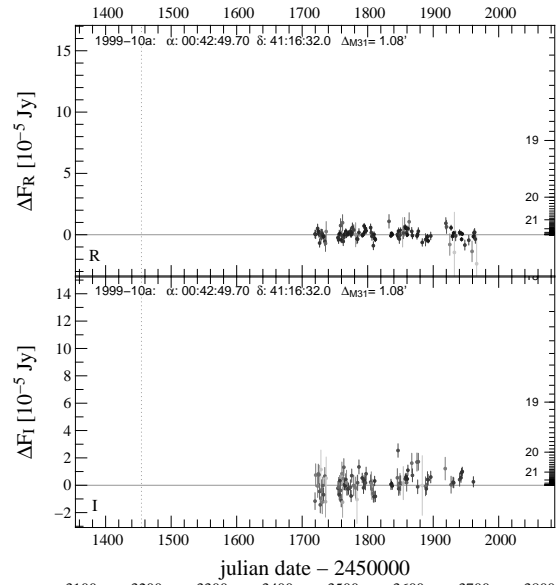
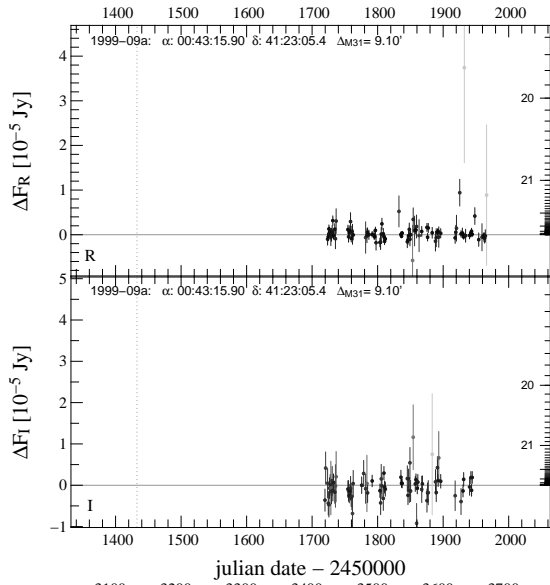


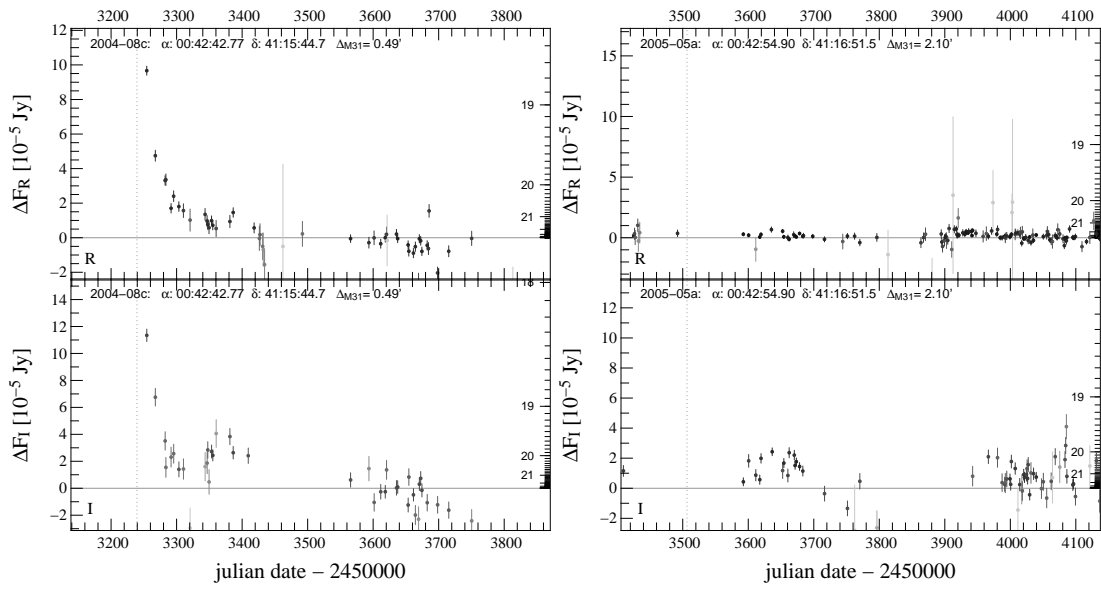












5.10 Appendix C: Separate microlensing events from variables

In this section we present the signal to noise ratio and the t_{FWHM} versus the $\chi_{\text{dof}} \equiv \sqrt{\chi_{\text{dof}}}$ for the pixel light curves from the WeCAPP data set. To better separate the microlensing events from novae, we require i) $t_{\text{FWHM}} < 100$ days, ii) $S/N > 9$ for both R and I -band light curves and iii) the χ_{dof} smaller than 1.6 for R and 1.8 for I -band. In Fig. 5.35 the upper left region encompassed by the black lines indicates the S/N and the χ_{dof} criteria to draw out the microlensing candidates from variables. In Fig. 5.36 the lower left region encompassed by the black lines indicates the t_{FWHM} and the χ_{dof} criteria to draw out the microlensing candidates from variables.

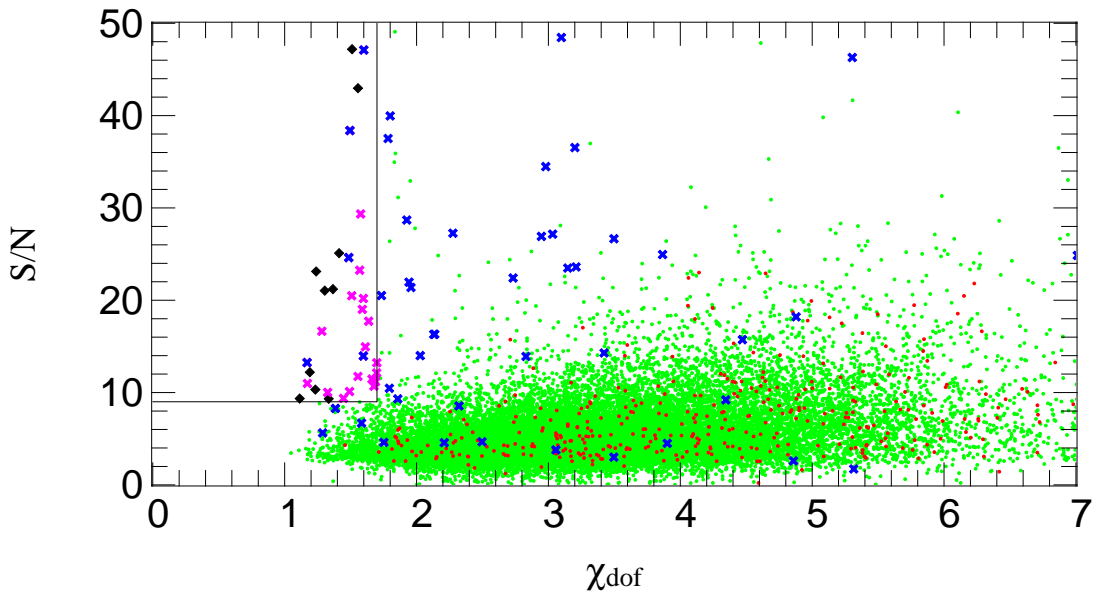


Figure 5.35: The S/N and χ used to filter out microlensing candidates (black) from the 22646 pixel light curves with good PSF fitting (green) obtained in the WeCAPP campaign. The blue points are the novae from the WeCAPP catalogue. The red points show the variables presented in Fliri *et al.* (2006). The magenta points indicate the light curves fulfilling the S/N and χ criteria mentioned in the main text. The black points are the microlensing candidates which pass further criteria.

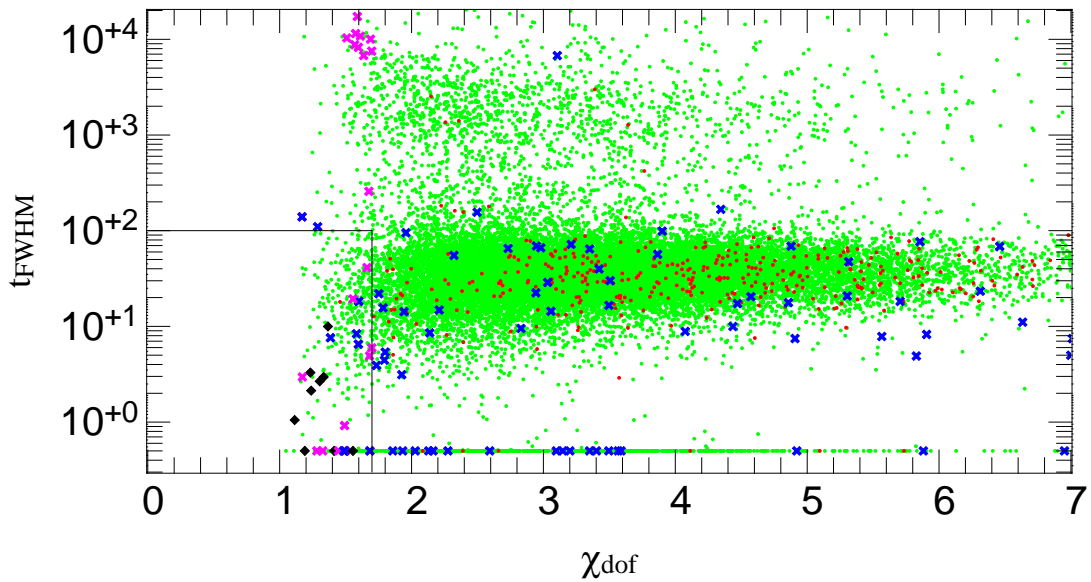


Figure 5.36: The t_{FWHM} and χ used to filter out microlensing candidates (black) from the 22646 pixel light curves with good PSF fitting (green) obtained in the WeCAPP campaign. The blue points are the novae from the WeCAPP catalogue. The red points show the variables presented in Fliri *et al.* (2006). The magenta points indicate the light curves fullfilling the t_{FWHM} and χ criteria mentioned in the main text. The black points are the microlensing candidates which pass further criteria.

Chapter 6

First results from PAndromeda - A dedicated deep survey of M31 with Pan-STARRS

6.1 The PANSTARRS survey and PAndromeda

The extragalactic group at MPE and USM is a member of the PS1 survey. PS1 observations are carried out with the 1.8m Panoramic Survey Telescope and Rapid Response System (Pan-STARRS) located at Haleakala in Hawaii. The camera used is currently the largest one in the world. It consists of 60 OTAs (orthogonal transfer arrays), which have 8×8 CCDs each, with 584×591 pixels. The total number of pixels is ~ 1.33 Gigapixels. The pixel size is 0.26 arcsec. This makes the angular size of one OTA to $\sim 30' \times 30'$, and the total FOV to about 7 degree^2 . The aims of Pan-STARRS are to map 3π of the sky with 12 epochs in $g'r'i'z'y$ within 3 years and to map several Medium-Deep Fields for longer exposure time. Within the PS1 survey we have designed and lead the M31 monitoring project PAndromeda, which is one of the 12 key projects of PS1.

PAndromeda is designed to identify microlensing events towards M31 with high cadence of observations (0.5 h per night for a time span of 5 months per year). With the large field of view of Pan-STARRS, it is possible to monitor the whole M31 with one single exposure (see Fig. 6.2). This enables us to compare the self-lensing event rate (caused by bulge and disk stars within M31) from observations to the prediction from the theoretical calculation assuming a certain detection efficiency (which is given from the set-up of PAndromeda and simulations). A discrepancy in the observed and theoretical self-lensing event rate can indicate that the assumptions in the M31 model under consideration (e.g. stellar population) might need to be improved. The microlensing event rate will help us to constrain the mass-fraction of compact objects in M31 and the Milky Way halo, as well as the mass function at the low mass end of the M31 bulge.

PAndromeda also aims to shed light on the stellar population properties of M31 based on the color profiles, SFB-fluctuations, resolved stars and variables. It will thus improve our understanding of the mix of stellar ages and metallicities in the halo, bulge, stellar streams and dwarfs of M31. It will also constrain the extinction within M31. These informations are required for an accurate interpretation of the microlensing events.

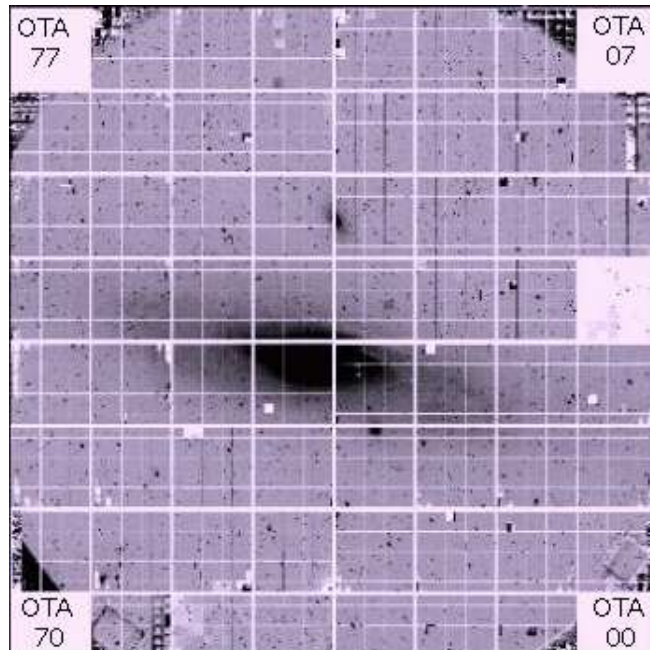


Figure 6.1: The Giga Pixel Camera (GPC) and its 60 Orthogonal Transfer Arrays (OTAs). Each OTA is composed of 8×8 CCDs and has 584×591 pixels per CCD. The field of view of GPC is $\sim 7 \text{ degree}^2$. The entire Andromeda galaxy, M32 and NGC 205 can be imaged with one pointing (as shown in the figure).

6.2 First season of PAndromeda data

Pan-STARRS started the first observation season in 2010 and observed M31 in r' and i' -band from 23/07/2010 to 27/12/2010. We use two filters to confirm the microlensing events from their achromaticity. We acquired 90 nights in r' and 66 nights in i' . The total number of images and integration time obtained in the first observation season of PAndromeda are listed in Table 6.1. The number of images accumulated in r' and i' -band as a function of time are shown in Fig. 6.3.

Table 6.1: PAndromeda integration time in r' - and i' -band.

Filter	Nights	Images	Total integration Time
r'	90	1179	70740s
i'	66	603	36180s

The 0.5 h integration time per night was divided into two observation blocks separated by 4 to 6 hours in order to trace microlensing events with time scales shorter than 1 day. The observation cadence is shown in Fig. 6.4.

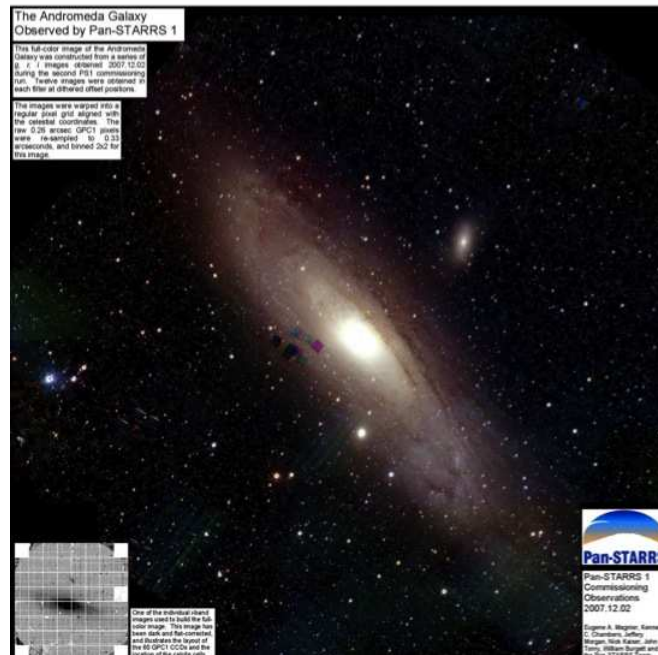


Figure 6.2: The Andromeda galaxy observed by PS1. The color image is combined by g' , r' and i' images taken during the commissioning run in 2007.

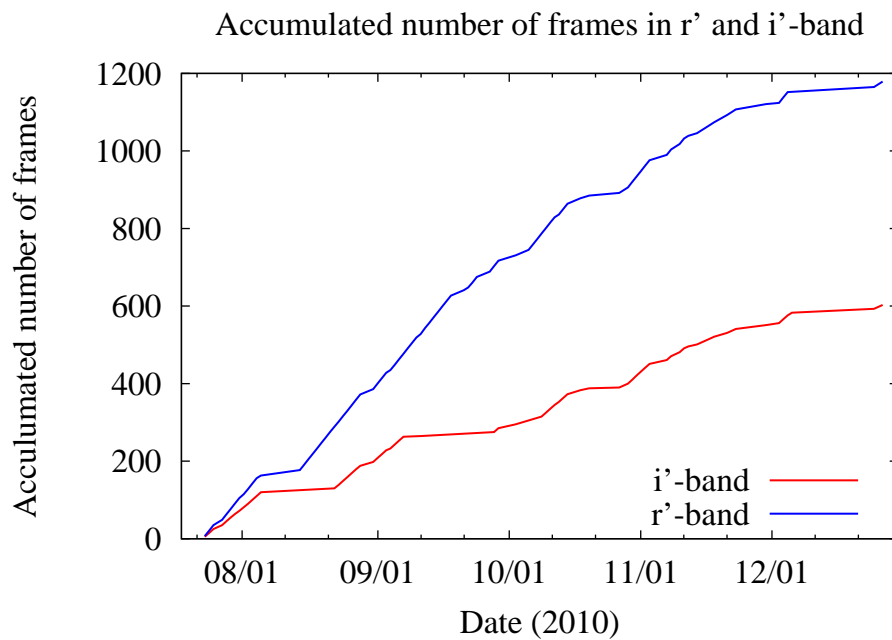


Figure 6.3: Accumulated number of images observed by PANDROMEDA in r' - and i' -band.

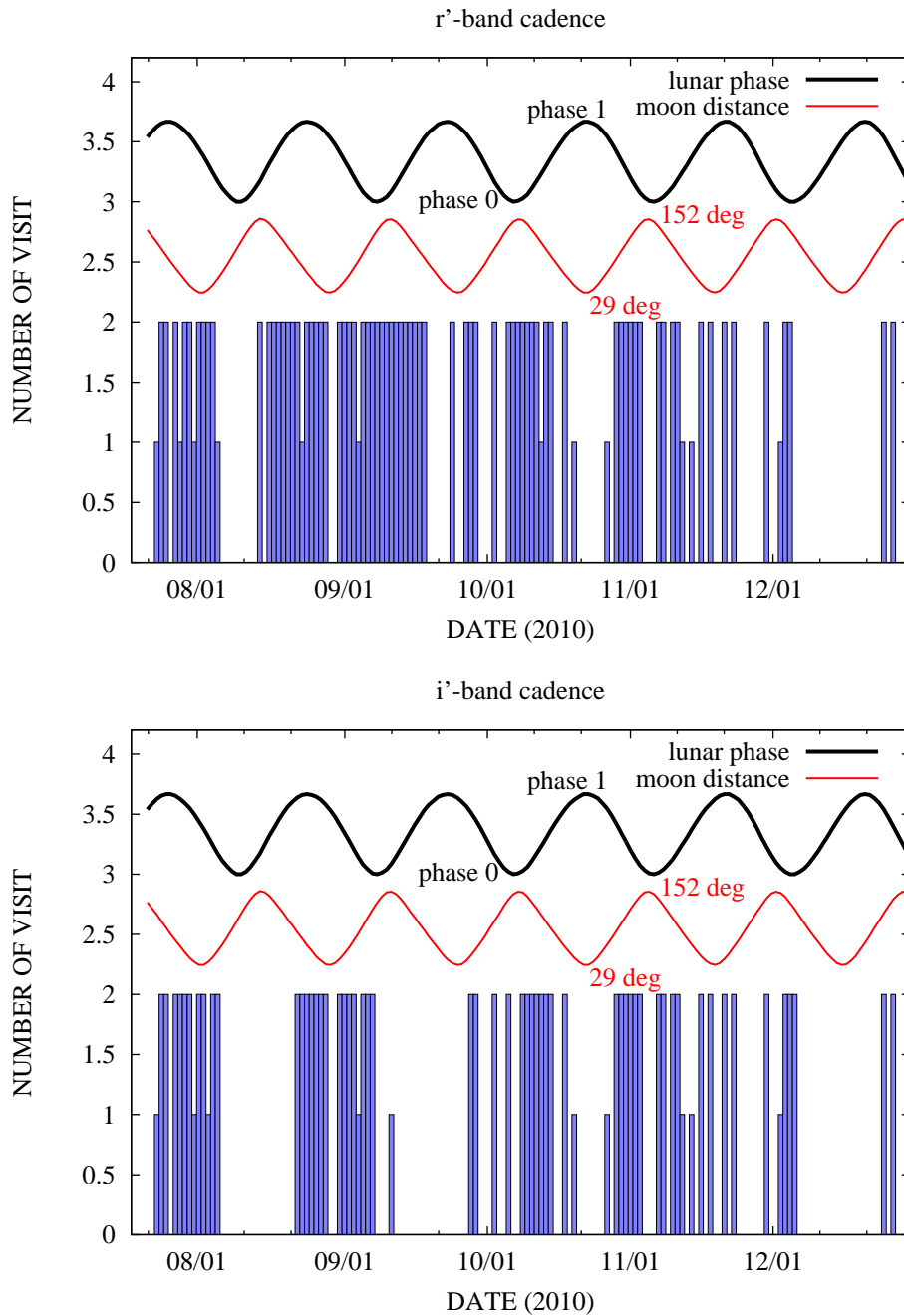


Figure 6.4: Pandromeda observation cadence. The histogram shows the number of visits (0, 1 or 2 times per night) on M31. The black line indicates the lunar phase (1 for full moon and 0 for dark night). The red line shows the distance of the M31 center from the moon as a function of observing date.

6.3 Photometric stability and study of variables from PAndromeda

To understand the data quality of PAndromeda, we first investigate two sub-fields, one in the bulge of M31 and one in the disk. We use the “Astro-wise” pipeline to obtain the point-spread function (PSF) of individual frames. A histogram of the PSF is shown in Fig. 6.5. The maximum peaks at 1 arcsec. To quantify the precision of the photometry, we perform a test on sub-fields in the bulge and disk of M31. We use Source Extractor to extract stars for every observing date in these two sub-fields and measure light curves, i.e. flux difference of these stars relative to the mean flux as a function of time. Since most of the stars are not variable, the scatter of the estimated flux difference (relative to the mean flux) is an estimate for the photometric precision as a function of the magnitude of the star. The ratio for this rms-error relative to the stellar flux is plotted for each star in Fig. 6.6. It shows that the photometric precision is 1% for stars with $r' \sim 19$ mag.

We also analyze the light curves for the periodically varying δ -Cepheid stars. Their period and their flux difference at minimum and maximum are precisely known from our previous WeCAPP survey where the central bulge field was monitored as well. We used the known periods to produce phase diagrams for their variability and compare the light curves during one pulsation at different times. The scatter among the light curves for different pulsation periods is similar to the scatter presented in the previous observations with WeCAPP. This indicates that the image quality is stable as a function of time.

During the time span of the first observing season of PAndromeda we detect one nova (M31N-2010-10a) in the central sub-field. The light curve of M31N-2010-10a is shown in Fig. 6.8.

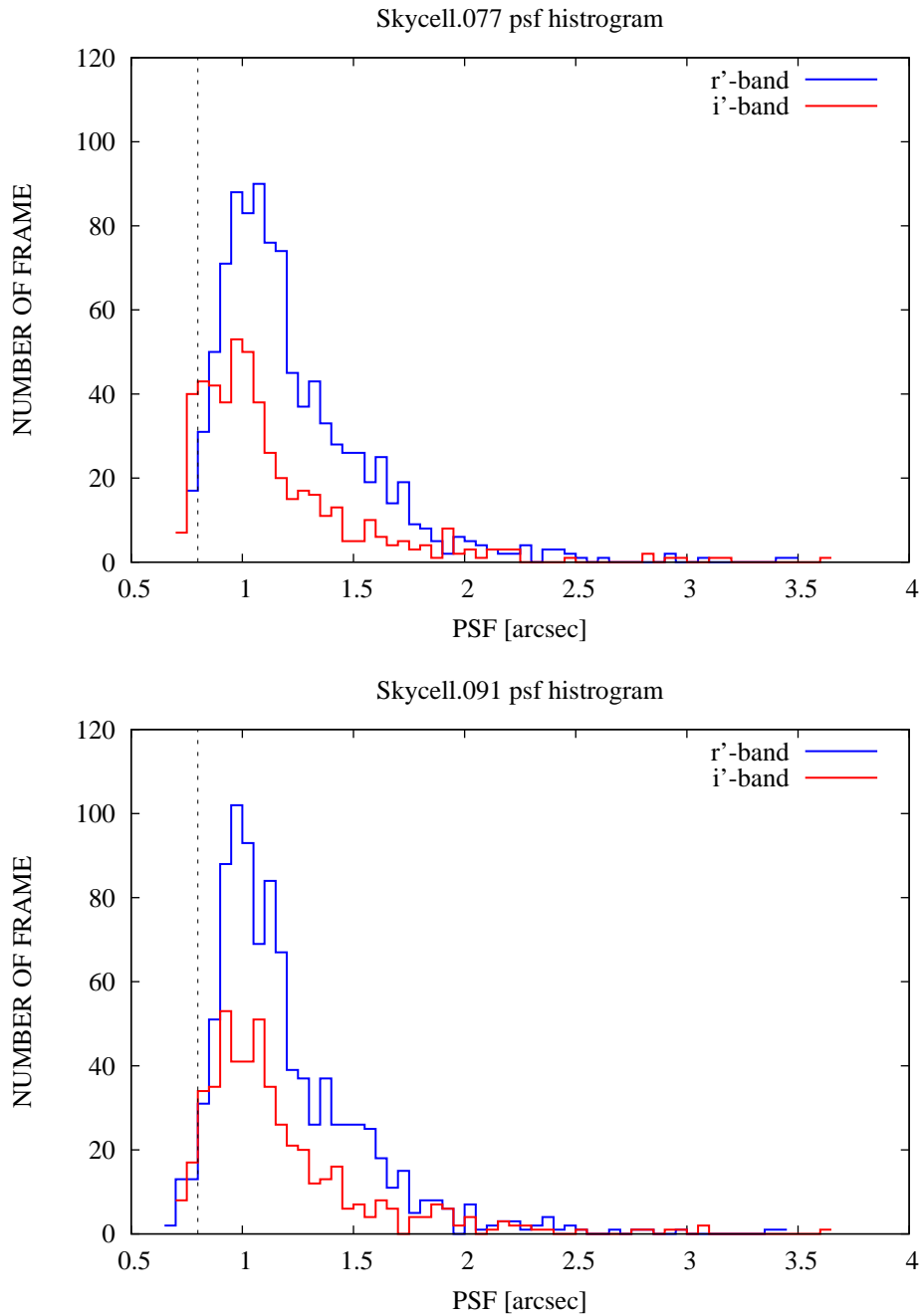


Figure 6.5: Point-Spread Function (PSF) distribution of the first season of PAndromeda in the bulge (upper panel) and disk (lower panel) field. The PSF distributions of the r' (i') data are shown in the blue (red). The dashed vertical lines indicate the promised PSF ($0''.8$) of PS1.

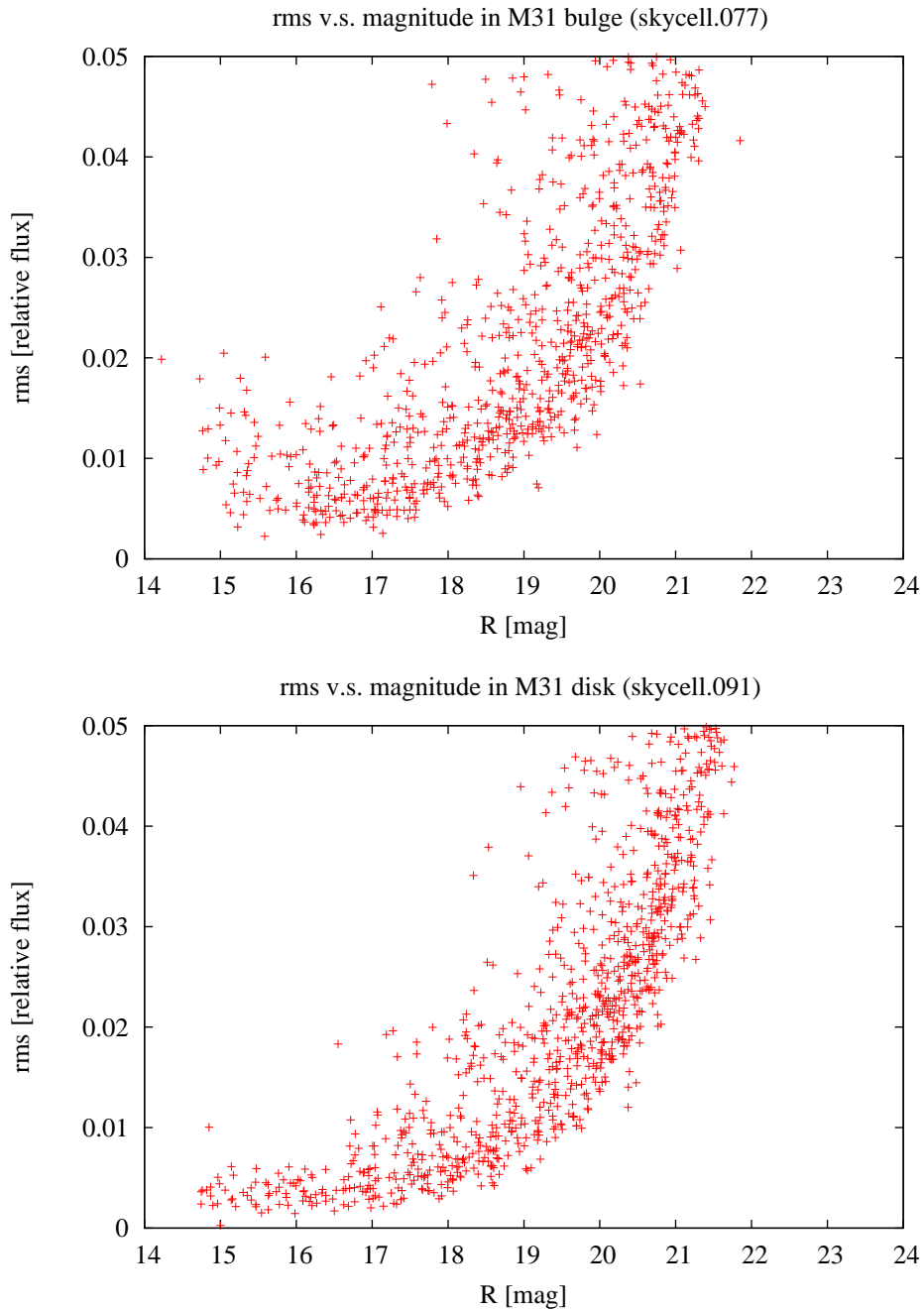


Figure 6.6: Photometric accuracy (rms) as a function of the magnitude of stars from images taken by PAndromeda. The rms is derived from the light curves of each stars. The R -band magnitude is obtained by comparing the flux of stars in the PAndromeda data to the USNO-A2 catalog (Since at that time when this figure was made the absolute flux calibration in the static sky image of the PAndromeda data was not precisely known).

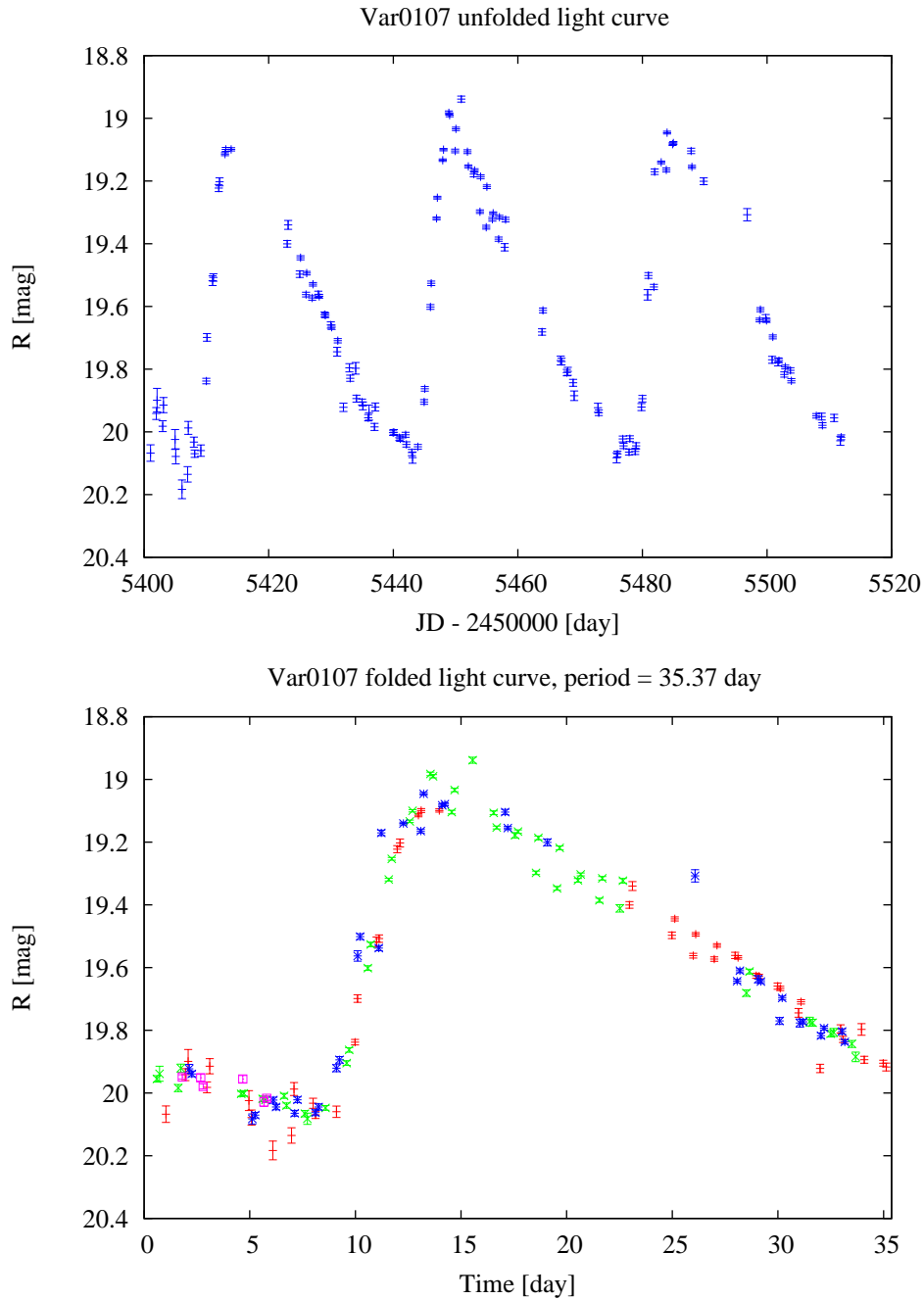


Figure 6.7: Delta Cepheid light curves from PAndromeda data. Upper panel: magnitude as a function of the PAndromeda observing date. Lower panel: magnitude as a function of the pulsation phase. The magnitude is obtained by comparing the r' -band flux from the stars in PAndromeda to the R -band catalog in USNO-A2. Here we focus on the variation in the magnitude rather than the absolute magnitude of the Delta Cepheid.

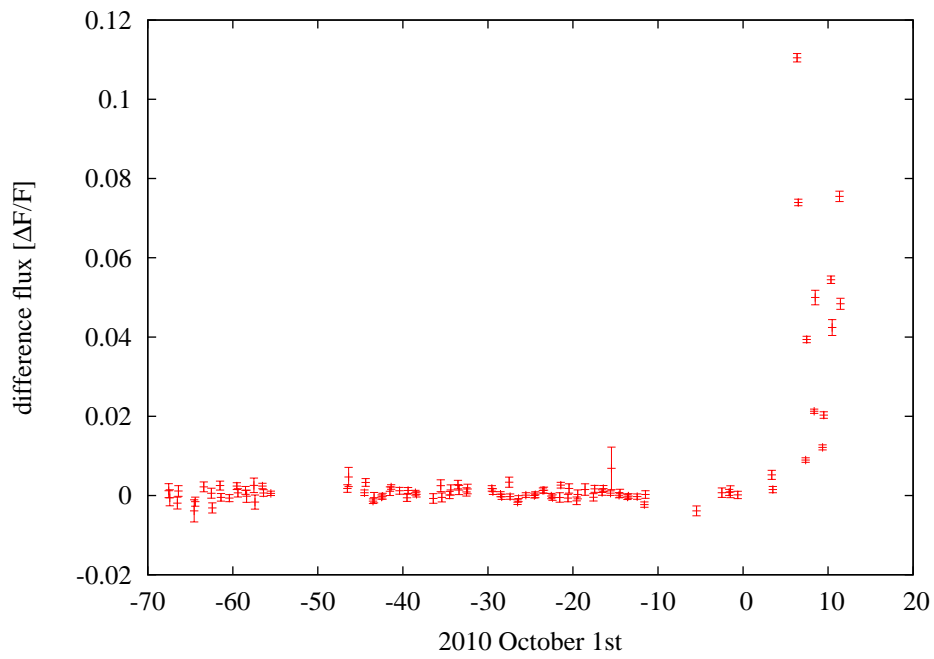


Figure 6.8: Light curve of the nova M31N-2010-10a from PAndromeda r' -band data. The vertical axis is the difference flux (relative to the mean flux of the PSF standard).

6.4 Microlensing results from PAndromeda

To compare with the WeCAPP results, we first analyzed the central region of the M31 field ($21' \times 21'$) and detect 6 candidates. The positions and light curves of these 6 candidates are shown in Fig. 6.9 and Fig. 6.10 - 6.15.

Among the 6 candidates, PAnd 5 has the shortest t_{FWHM} . Though there is only one observation before the light curve maximum, PAnd 5 is not likely to be a variable for the following reasons. First of all, let consider the case of stellar pulsation and assume the star expands from radius R_1 to R_2 without changing the temperature (this assumption must hold for variables that could mimic achromatic microlensing events. This implies, that whatever causes the variability it must not imply a change of the effective temperature of the atmosphere, because that would result in a color change). The flux (F) is proportional to the square of the stellar radius, thus we have

$$\frac{\Delta F}{F_1} = \frac{R_2^2 - R_1^2}{R_1^2} = \frac{R_2^2}{R_1^2} - 1 \quad . \quad (6.1)$$

The amount of change in the radius can not exceed the accoustic speed (at $T \approx 10,000\text{K}$) times the t_{FWHM} , which is smaller than $0.34 R_{\odot}$. The star can not be too bright because it is not resolved in the image, thus we assume it to be dimmer than 23.2th mag. The relation of flux and AB magnitude is (Oke, 1974)

$$F = 10^{(23.9 - \text{mag})/2.5} \times 10^{-6} \text{Jy} \quad . \quad (6.2)$$

The flux for a 23.2th magnitude star is $1.6 \times 10^{-6} \text{Jy}$. Recall from equation 6.1, one has

$$\Delta F = \left(\frac{R_2^2}{R_1^2} - 1 \right) \times F = 0.8 \times 1.6 \times 10^{-6} \text{Jy} \quad (6.3)$$

which is not enough for the flux excess observed in PAnd 5. Secondly, PAnd 5 can not be a nova because the nova light curve would be asymmetric and much brighter. The possibility of a dwarf nova or stellar flare can also be ruled out, since these phenomena are too faint to be observed at the distance of M31.

The preliminary analysis of the first part of data for the first season PAndromeda data demonstrates that one can indeed detect microlensing events. The data are also useful for novae detection and investigation of other variables. This is a positive surprise given the facts that a) the PSF distribution is much worse than expected, and b) artefacts by the CCD, electronics and optics are much more severe than anticipated.

We are currently analyzing the full amount of the first season PAndromeda data. A paper concerning the 6 microlensing events is in preparation.

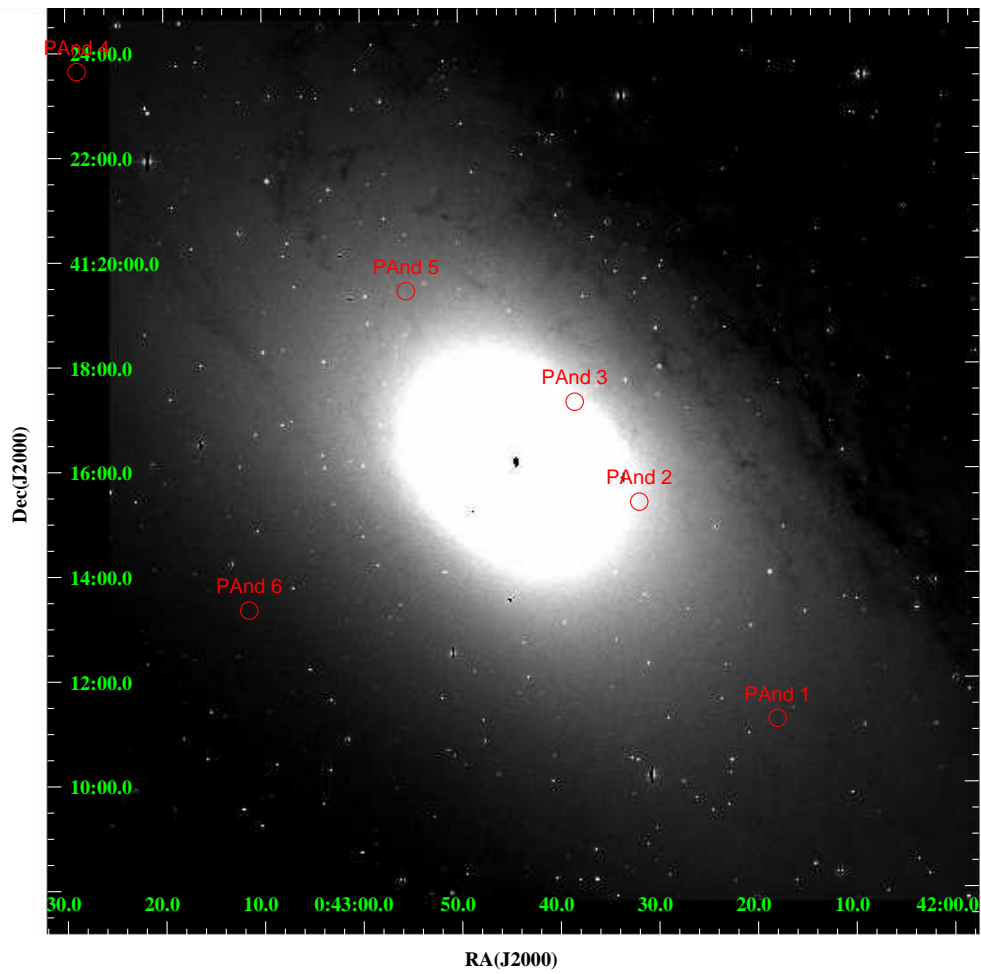


Figure 6.9: Position of the six microlensing event candidates detected in the central region of M31 from PAndromeda.

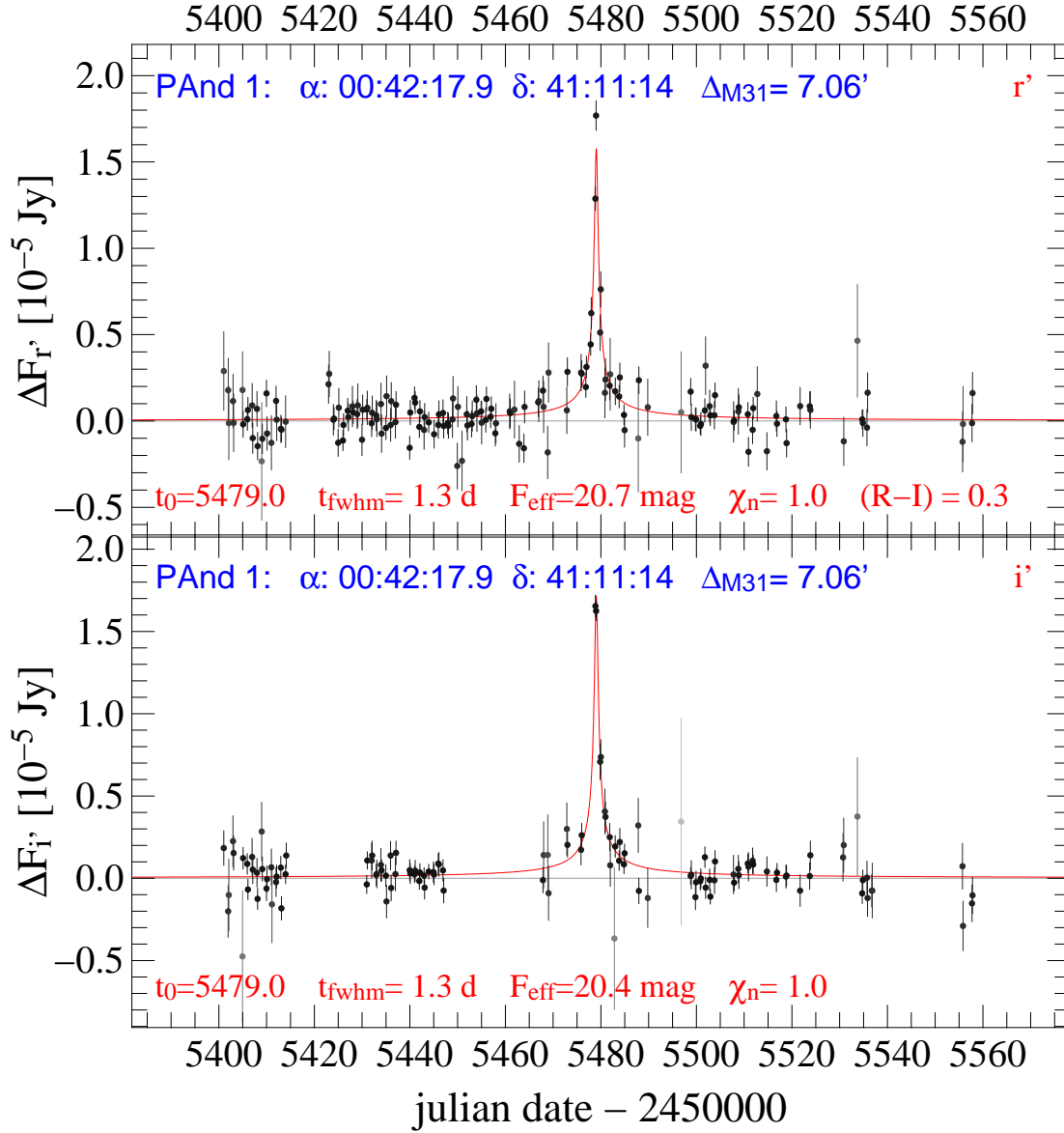


Figure 6.10: Light curves of the microlensing event PAnd 1 detected in the bulge of M31 from Pandromeda. Upper (lower) panel shows the light curve in r' (i'). In the figure there are also the name of the event (PAnd 1), the coordinates α (RA) and δ (Dec) at the epoch of J2000, the distance to the center of M31 (Δ_{M31}) in arcminutes. The best-fit light curves and parameters are shown in red, which are the time at maximum magnification (t_0), the event timescale (t_{FWHM}) in units of a day, the equivalent magnitude at maximum magnification (F_{eff}) in each filter, the normalized $\chi_n := \sqrt{\chi_n^2}$ in each filter and the color (R-I) of the event.

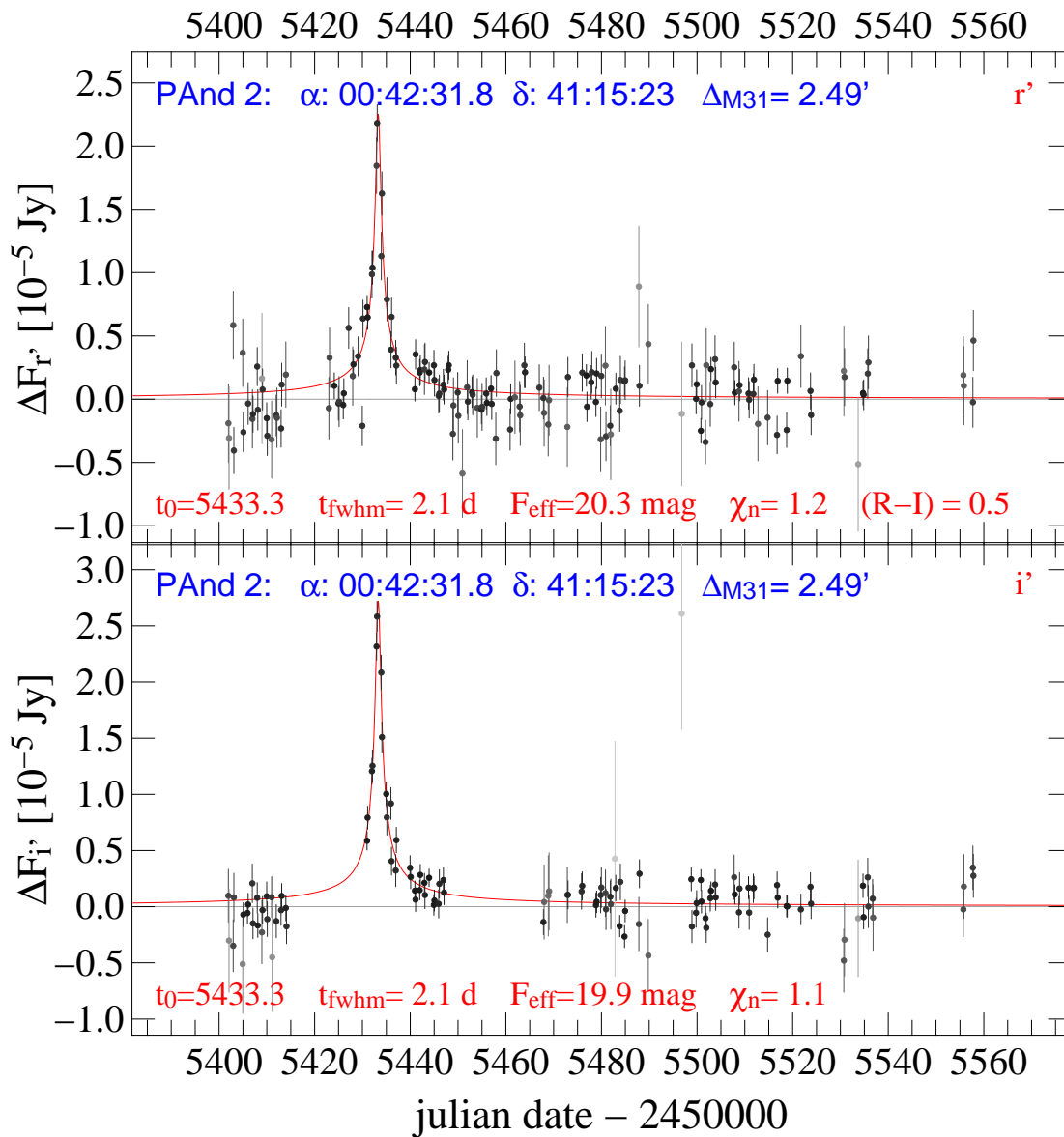


Figure 6.11: Light curves of the microlensing event PAnd 2 detected in the bulge of M31 from Pandromeda.

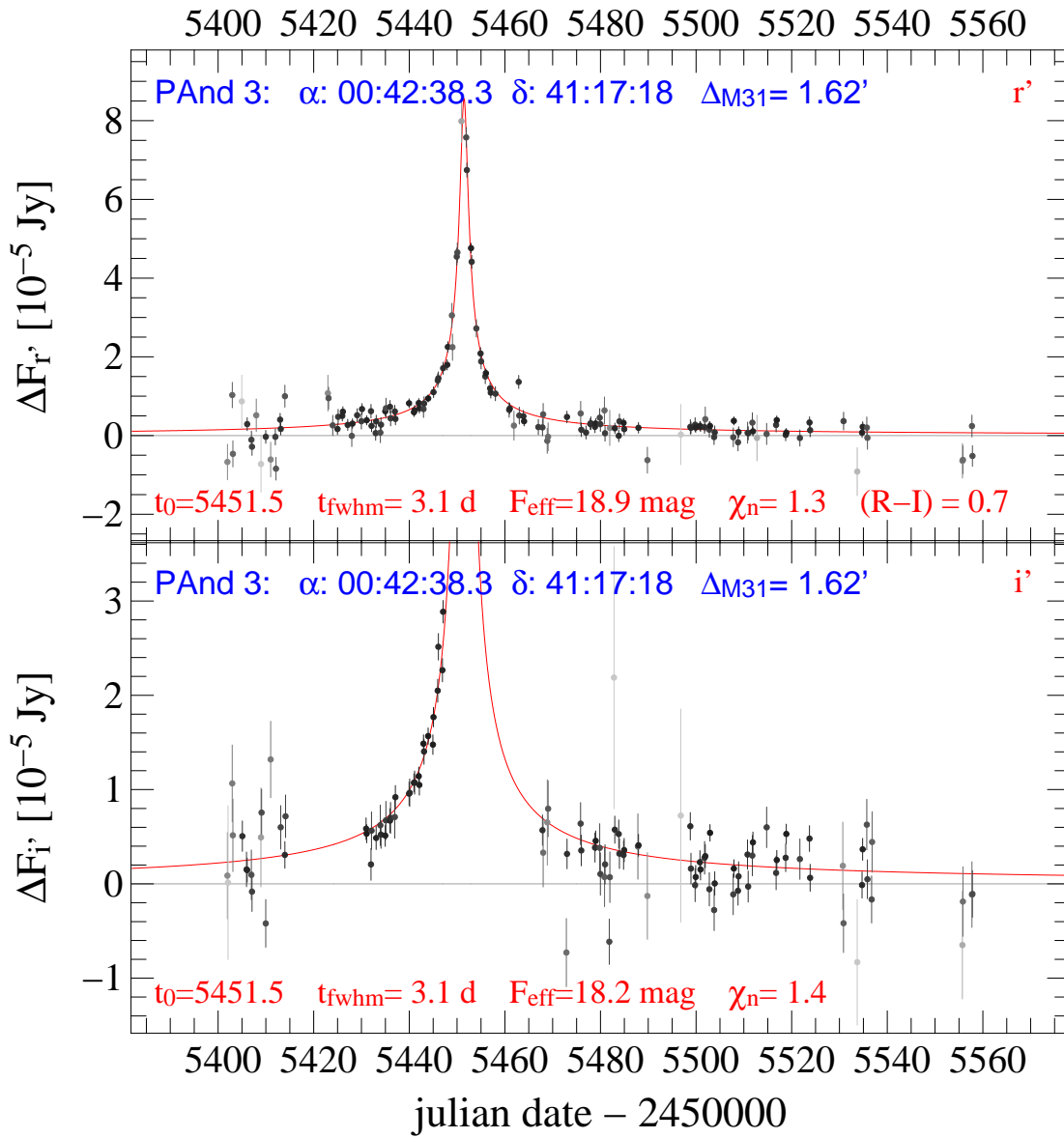


Figure 6.12: Light curves of the microlensing event PAnd 3 detected in the bulge of M31 from Pandromeda.

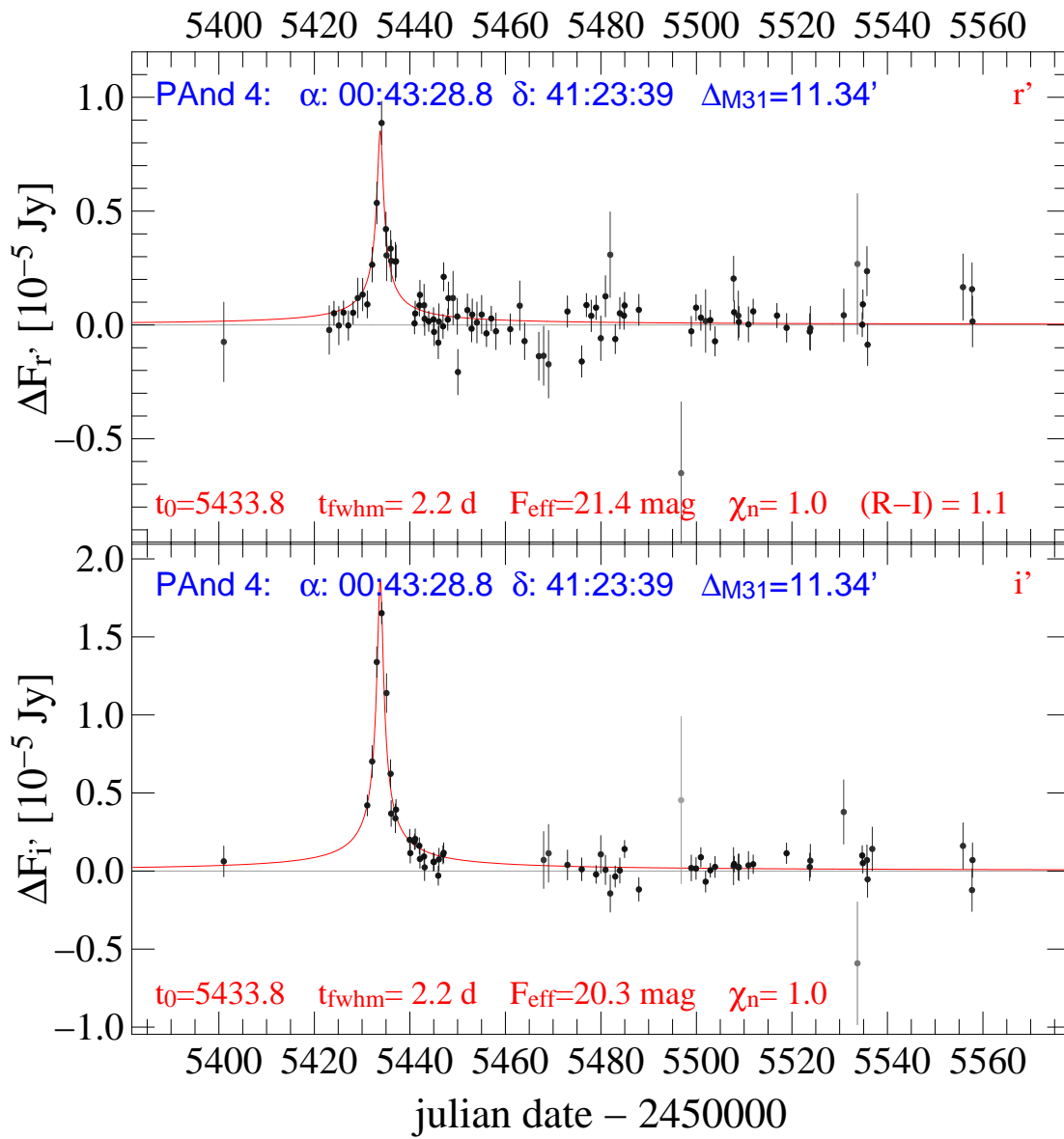


Figure 6.13: Light curves of the microlensing event PAnd 4 detected in the bulge of M31 from Pandromeda.

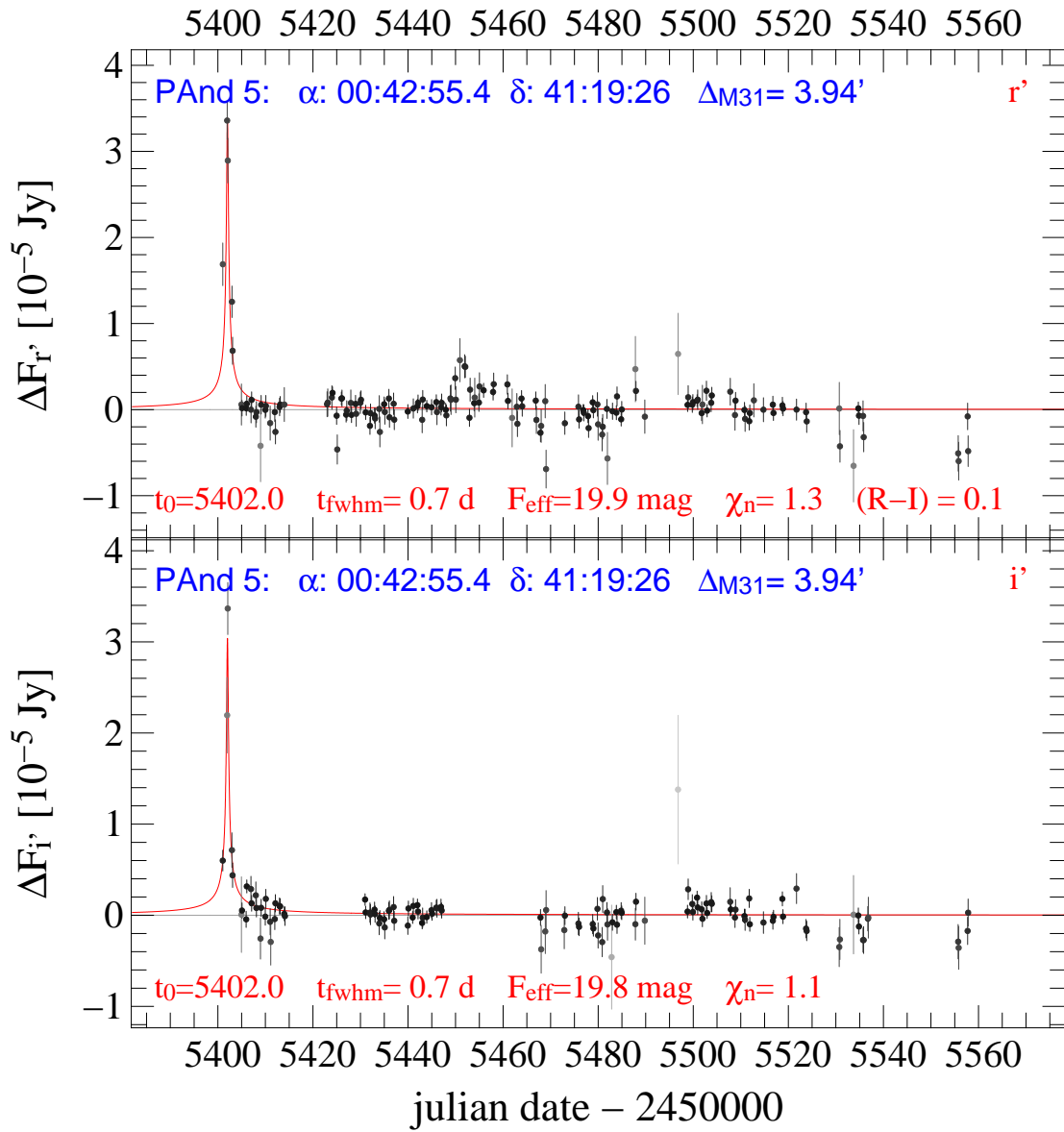


Figure 6.14: Light curves of the microlensing event PAnd 5 detected in the bulge of M31 from Pandromeda.

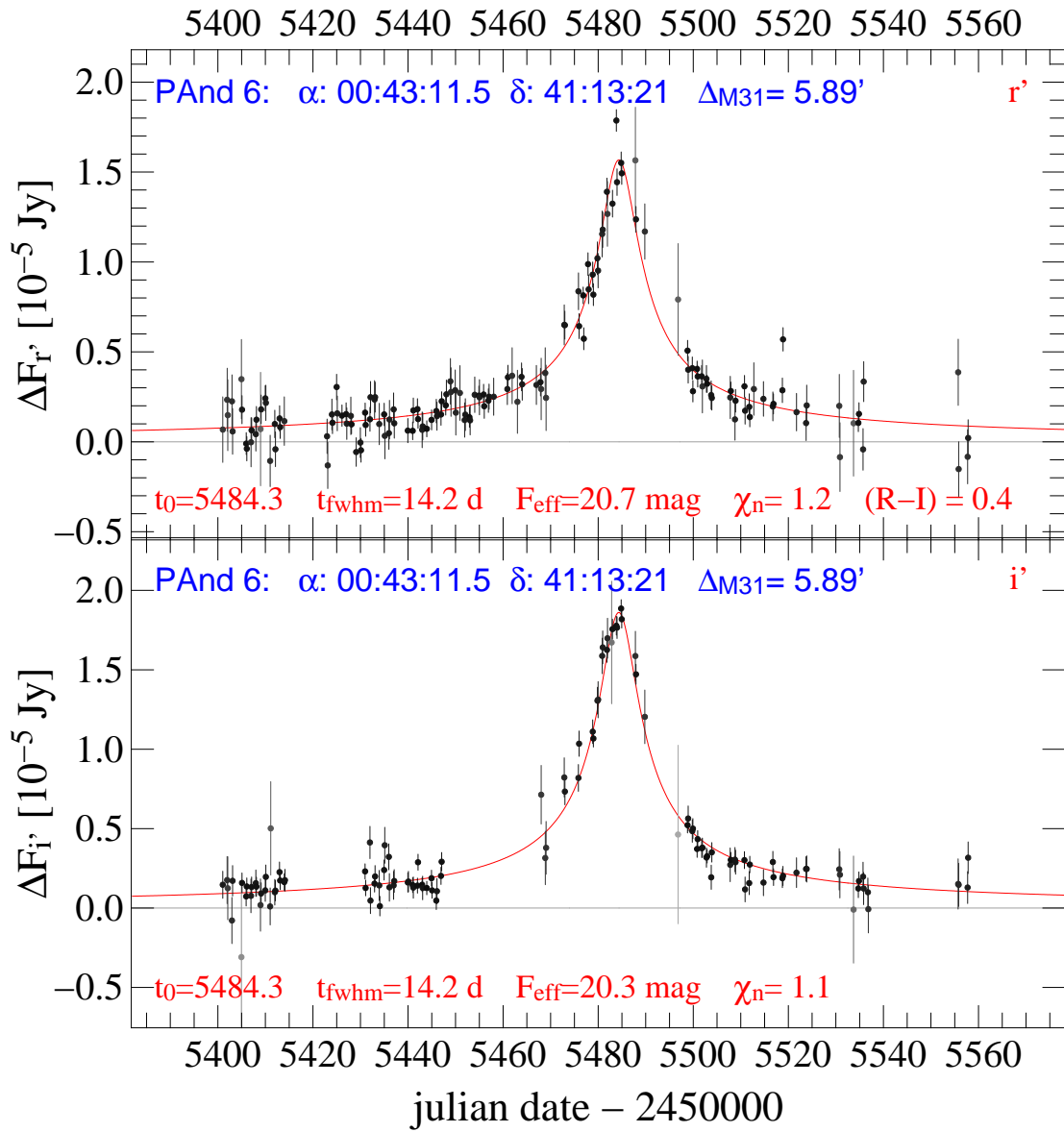


Figure 6.15: Light curves of the microlensing event PAnd 6 detected in the bulge of M31 from Pandromeda.

Chapter 7

Summary and outlook

In the context of modern cosmology more than 95% of the universe are in the form of “dark components”. Although we are able to quantify the total contribution of dark matter in our universe, we have very little understanding of its nature. Since dark matter does not interact with baryons electromagnetically, an elegant way to reveal the presence of dark matter is through gravitational lensing. Several groups have monitored the Galactic Bulge and the Magellanic Clouds to search for MACHOs as dark matter candidates since 1993. This has led to the discovery of more than 500 microlensing events (mostly self-lensing towards the Galactic Bulge) per year. However, the information of the MACHO mass, distance and velocity is degenerate in the Einstein timescale. This hinders the understanding of the properties of the dark matter. In order to break the degeneracy, we need a “standard ruler” to measure the Einstein radius to better constrain the identity of the microlensing events.

One of such standard ruler is the size of the source. If the signature of an extended source (in terms of the Einstein radius) is revealed in the light curves and if we can obtain the real size of the source by other means (e.g. from its color or spectra), we are able to derive the Einstein radius. In Chapter 2 we presented a fast and accurate algorithm to calculate the finite-source effects in the light curve. This algorithm can be implemented into light curve fitting routines and facilitate the recognition of finite-source effects in the huge amount of light-curve data.

The astrometric signal of a microlensing event can also serve as a standard ruler. For point-source point-mass microlensing, its astrometric trajectory will trace out an ellipse. The size of the ellipse projected on the sky tells us the size of the Einstein radius. It is even better than the finite-source method, because the extended nature of the source is revealed only when the lens transits the source. The astrometric trajectory, however, are present in all microlensing events. In Chapter 3 we apply the algorithm of Chapter 2 to astrometric microlensing. Benefiting from the adoption of lens-centered coordinates, we will be able to take into account both finite-source and finite-lens effects for the first time. With the launch of the *GAIA* satellite in the next years, we are able to routinely measure the astrometric signal and determine the Einstein radius for microlensing events towards the Galactic Bulge.

In addition to the Magellanic Clouds, M31 is another excellent target to search for MACHOs. In Chapter 4 I show the uniqueness of M31 as a target to search for MACHOs in the halo (of Milky Way or of M31). We shortly review how to account for the microlensing event rate in M31 and our previous works to improve our understanding of M31.

The Extragalactic group at USM has started the Wendelstein Calar Alto Pixellensing Project (WeCAPP), which monitored the M31 bulge to search for microlensing signals, for more than one decade ago. I have joined the very end phase of WeCAPP and helped in quantifying the parameters of the detected microlensing events. We found that novae can also mimic the microlensing events, so we collected all the novae in the WeCAPP data set and constrained the criteria in the light-curve fitting χ^2 and the signal-to-noise ratio to separate microlensing events from novae. This study also led to a catalogue and light curves of 90 novae, which is the hugest amount of CCD-based nova light curves nowadays. Such optical nova data, combined with X-ray observations (e.g. [Pietsch *et al.*, 2005](#)) are essential for the study of the outburst mechanism and evolution of nova.

In Chapter 6 I present the first results from PAndromeda, one of the key projects of the Pan-STARRS 1 (PS1) survey. The PS1 just started its first observing season last year. Here I show some preliminary results of PAndromeda. I have studied the data quality and photometric stability of the PAndromeda data. I obtain light curves of Delta Cepheids and detected one nova. For the microlensing experiment, we first analyzed a subfield from the center of M31 and detected 6 microlensing events. Our results demonstrate the feasibility to discover microlensing events with PAndromeda data despite the PSF is worse than expected. We are planning to publish these 6 events soon. The full amount of the first season PAndromeda data are currently under analysis.

The second observing season of PAndromeda will be starting in July this year. In addition to the r' and i' -band, we will extend the observation to include more filters. This will improve our understanding of basic properties of M31, such as the stellar mass function, density of stars, extinction and many other aspects.

Besides the PS1, a 2-meter telescope is currently under construction at the Wendelstein Observatory in the Bavarian Alps in Germany. The first light is expected to be in the summer of this year. One of its science goals is to observe M31 coordinated with PS1. This will provide a better temporal coverage and will enable us to discover microlensing events with time scales below one day.

With these instruments we are in the position to pin down the MACHO fraction in the halo of M31 and have a better understanding of the dark matter in our neighbouring galaxy.

Bibliography

- Agol, E. 2002: *Occultation and Microlensing*, ApJ, 579, 430, cited on p. [21](#), [32](#), [46](#)
- Alard, C. & Lupton, R. H. 1998: *A Method for Optimal Image Subtraction*, ApJ, 503, 325, cited on p. [5](#), [12](#), [59](#)
- Albrow, M. D., Beaulieu, J., Caldwell, J. A. R., Dominik, M., Gaudi, B. S., Gould, A., Greenhill, J., Hill, K., Kane, S., Martin, R., Menzies, J., et al. 2000: *Detection of Rotation in a Binary Microlens: PLANET Photometry of MACHO 97-BLG-41*, ApJ, 534, 894, cited on p. [10](#), [39](#)
- Alcock, C., Akerlof, C. W., Allsman, R. A., Axelrod, T. S., Bennett, D. P., Chan, S., Cook, K. H., Freeman, K. C., Griest, K., Marshall, S. L., Park, H., et al. 1993: *Possible gravitational microlensing of a star in the Large Magellanic Cloud*, Nature, 365, 621, cited on p. [ix](#), [4](#), [8](#), [9](#)
- Alcock, C., Allen, W. H., Allsman, R. A., Alves, D., Axelrod, T. S., Banks, T. S., Beaulieu, S. F., Becker, A. C., Becker, R. H., Bennett, D. P., Bond, I. A., et al. 1997a: *MACHO Alert 95-30: First Real-Time Observation of Extended Source Effects in Gravitational Microlensing*, ApJ, 491, 436, cited on p. [23](#), [32](#), [39](#)
- Alcock, C., Allsman, R. A., Alves, D., Axelrod, T. S., Becker, A. C., Bennett, D. P., Cook, K. H., Freeman, K. C., Griest, K., Keane, M. J., Lehner, M. J., et al. 1997b: *First Detection of a Gravitational Microlensing Candidate toward the Small Magellanic Cloud*, ApJL, 491, L11, cited on p. [48](#), [49](#)
- Alcock, C., Allsman, R. A., Alves, D. R., Axelrod, T. S., Becker, A. C., Bennett, D. P., Cook, K. H., Dalal, N., Drake, A. J., Freeman, K. C., Geha, M., et al. 2000: *The MACHO Project: Microlensing Results from 5.7 Years of Large Magellanic Cloud Observations*, ApJ, 542, 281, cited on p. [5](#), [49](#)
- Alcock, C., Allsman, R. A., Alves, D. R., Axelrod, T. S., Becker, A. C., Bennett, D. P., Cook, K. H., Drake, A. J., Freeman, K. C., Geha, M., Griest, K., et al. 2001: *Direct detection of a microlens in the Milky Way*, Nature, 414, 617, cited on p. [ix](#), [8](#), [9](#), [10](#), [32](#), [39](#)
- Alcock, C., Axelrod, T. S., Bennett, D. P., Cook, K. H., Park, H. S., Griest, K., Perlmutter, S., Stubbs, C. W., Freeman, K. C., & Peterson, B. A. 1992: *The search for massive compact halo objects with a (semi) robotic telescope*, in Astronomical Society of the Pacific Conference Series, Vol. 34, Robotic Telescopes in the 1990s, ed. A. V. Filippenko, 193–202, cited on p. [16](#)
- Allen, R. J., Peterson, D. M., & Shao, M. 1997: *Space Interferometry Mission: taking the measure of the universe*, in Society of Photo-Optical Instrumentation Engineers (SPIE) Conference

- Series, Vol. 2871, Society of Photo-Optical Instrumentation Engineers (SPIE) Conference Series, ed. A. L. Ardeberg, 504–515, cited on p. 12, 32
- An, J. H., Evans, N. W., Hewett, P., Baillon, P., Calchi Novati, S., Carr, B. J., Crézé, M., Giraud-Héraud, Y., Gould, A., Jetzer, P., Kaplan, J., et al. 2004: *The POINT-AGAPE Survey - I. The variable stars in M31*, MNRAS, 351, 1071, cited on p. 64, 65
- Ansari, R., Aurière, M., Baillon, P., Bouquet, A., Coupinot, G., Coutures, C., Ghesquière, C., Giraud-Héraud, Y., Gillieron, D., Gondolo, P., Hecquet, J., et al. 2004: *Variable stars towards the bulge of M 31: The AGAPE catalogue*, A&A, 421, 509, cited on p. 59
- Arp, H. C. 1956: *Novae in the Andromeda nebula.*, AJ, 61, 15, cited on p. 58, 59
- Aubourg, E., Bareyre, P., Bréhin, S., Gros, M., Lachière-Rey, M., Laurent, B., Lesquoy, E., Magneville, C., Milsztajn, A., Moscoso, L., Queinnec, F., et al. 1993: *Evidence for gravitational microlensing by dark objects in the Galactic halo*, Nature, 365, 623, cited on p. 4, 8
- Baillon, P., Bouquet, A., Giraud-Héraud, Y., & Kaplan, J. 1993: *Detection of Brown Dwarfs by the Microlensing of Unresolved Stars*, A&A, 277, 1, cited on p. 4
- Batista, V., Dong, S., Gould, A., Beaulieu, J. P., Cassan, A., Christie, G. W., Han, C., Udalski, A., Allen, W., Depoy, D. L., Gal-Yam, A., et al. 2009: *Mass measurement of a single unseen star and planetary detection efficiency for OGLE 2007-BLG-050*, A&A, 508, 467, cited on p. 32, 39
- Belokurov, V. A. & Evans, N. W. 2002: *Astrometric microlensing with the GAIA satellite*, MNRAS, 331, 649, cited on p. 32
- Bianchini, A., Friedjung, M., & Brinkmann, W. 1992: *New light on post-maximum oscillations of novae*, A&A, 257, 599, cited on p. 72
- Binney, J. & Tremaine, S. 1987, Galactic dynamics, ed. Binney, J. & Tremaine, S., cited on p. 52
- Bode, M. F., Darnley, M. J., Shafter, A. W., Page, K. L., Smirnova, O., Anupama, G. C., & Hilton, T. 2009: *Optical and X-ray Observations of M31N 2007-12b: An Extragalactic Recurrent Nova with a Detected Progenitor?*, ApJ, 705, 1056, cited on p. 67
- Boden, A. F., Shao, M., & van Buren, D. 1998: *Astrometric Observation of MACHO Gravitational Microlensing*, ApJ, 502, 538, cited on p. 42
- Calchi Novati, S., Covone, G., de Paolis, F., Dominik, M., Giraud-Héraud, Y., Ingrassio, G., Jetzer, P., Mancini, L., Nucita, A., Scarpetta, G., Strafella, F., et al. 2007: *Probing MACHOs by observation of M 31 pixel lensing with the 1.5 m Loiano telescope*, A&A, 469, 115, cited on p. 66
- Calchi Novati, S., Dall’Ora, M., Gould, A., Bozza, V., Bruni, I., De Paolis, F., Dominik, M., Gualandi, R., Ingrassio, G., Jetzer, P., Mancini, L., et al. 2010: *M31 Pixel Lensing Event OAB-N2: A Study of the Lens Proper Motion*, ApJ, 717, 987, cited on p. 59
- Cassan, A., Beaulieu, J., Fouqué, P., Brilliant, S., Dominik, M., Greenhill, J., Heyrovský, D., Horne, K., Jørgensen, U. G., Kubas, D., Stempels, H. C., et al. 2006: *OGLE 2004-BLG-254: a K3 III Galactic bulge giant spatially resolved by a single microlens*, A&A, 460, 277, cited on p. 18, 32, 39

- Ciardullo, R., Ford, H. C., Neill, J. D., Jacoby, G. H., & Shafter, A. W. 1987: *The spatial distribution and population of novae in M31*, ApJ, 318, 520, cited on p. 59
- Ciardullo, R., Shafter, A. W., Ford, H. C., Neill, J. D., Shara, M. M., & Tomaney, A. B. 1990: *The H-alpha light curves of novae in M31*, ApJ, 356, 472, cited on p. 59
- Crotts, A. P. S. 1992: *M31 - A unique laboratory for gravitational microlensing*, ApJL, 399, L43, cited on p. 4, 51
- Csák, B., Kiss, L. L., Retter, A., Jacob, A., & Kaspi, S. 2005: *Spectroscopic monitoring of the transition phase in nova V4745 Sgr*, A&A, 429, 599, cited on p. 72
- Darnley, M. J., Bode, M. F., Kerins, E., Newsam, A. M., An, J., Baillon, P., Belokurov, V., Calchi Novati, S., Carr, B. J., Crézé, M., Evans, N. W., et al. 2006: *Classical novae from the POINT-AGAPE microlensing survey of M31 - II. Rate and statistical characteristics of the nova population*, MNRAS, 369, 257, cited on p. 59
- Darnley, M. J., Bode, M. F., Kerins, E., Newsam, A. M., An, J., Baillon, P., Novati, S. C., Carr, B. J., Crézé, M., Evans, N. W., Giraud-Héraud, Y., et al. 2004: *Classical novae from the POINT-AGAPE microlensing survey of M31 - I. The nova catalogue*, MNRAS, 353, 571, cited on p. 58, 64, 65
- de Vaucouleurs, G., de Vaucouleurs, A., Corwin, Jr., H. G., Buta, R. J., Paturel, G., & Fouque, P. 1991, Third Reference Catalogue of Bright Galaxies, ed. de Vaucouleurs, G., de Vaucouleurs, A., Corwin, H. G., Jr., Buta, R. J., Paturel, G., & Fouque, P., cited on p. 51
- della Valle, M. & Livio, M. 1995: *The Calibration of Novae as Distance Indicators*, ApJ, 452, 704, cited on p. 58
- Delplancke, F. 2008: *The PRIMA facility phase-referenced imaging and micro-arcsecond astrometry*, New Astronomy Review, 52, 199, cited on p. 32, 49
- Dominik, M. & Sahu, K. C. 2000: *Astrometric Microlensing of Stars*, ApJ, 534, 213, cited on p. 32, 42
- Drake, A. J., Cook, K. H., & Keller, S. C. 2004: *Resolving the Nature of the Large Magellanic Cloud Microlensing Event MACHO-LMC-5*, ApJL, 607, L29, cited on p. 10
- Einstein, A. 1936: *Lens-Like Action of a Star by the Deviation of Light in the Gravitational Field*, Science, 84, 506, cited on p. 4
- Fliri, J., Riffeser, A., Seitz, S., & Bender, R. 2006: *The Wendelstein Calar Alto Pixellensing Project (WeCAPP): the M 31 variable star catalogue*, A&A, 445, 423, cited on p. xiv, xv, 60, 121, 122
- Fouqué, P., Heyrovský, D., Dong, S., Gould, A., Udalski, A., Albrow, M. D., Batista, V., Beaulieu, J.-P., Bennett, D. P., Bond, I. A., Bramich, D. M., et al. 2010: *OGLE 2008-BLG-290: an accurate measurement of the limb darkening of a galactic bulge K Giant spatially resolved by microlensing*, A&A, 518, A51, cited on p. ix, 10
- Frieman, J. A., Turner, M. S., & Huterer, D. 2008: *Dark Energy and the Accelerating Universe*, ARA&A, 46, 385, cited on p. 2

- Fukugita, M. & Peebles, P. J. E. 2004: *The Cosmic Energy Inventory*, ApJ, 616, 643, cited on p. xvii, 3
- Gössl, C. A. & Riffeser, A. 2002: *Image reduction pipeline for the detection of variable sources in highly crowded fields*, A&A, 381, 1095, cited on p. 59
- Gould, A. 1992: *Extending the MACHO search to about 10 exp 6 solar masses*, ApJ, 392, 442, cited on p. 8, 32
- Gould, A. 1994: *Proper motions of MACHOs*, ApJL, 421, L71, cited on p. x, 15, 16, 18, 19, 20, 39, 46
- Gould, A. 1996: *Theory of Pixel Lensing*, ApJ, 470, 201, cited on p. 5, 13, 15
- Gould, A. 2000: *A Natural Formalism for Microlensing*, ApJ, 542, 785, cited on p. 8, 31
- Gould, A. 2004: *Resolution of the MACHO-LMC-5 Puzzle: The Jerk-Parallax Microlens Degeneracy*, ApJ, 606, 319, cited on p. ix, 9, 10
- Gould, A., Bennett, D. P., & Alves, D. R. 2004: *The Mass of the MACHO-LMC-5 Lens Star*, ApJ, 614, 404, cited on p. 10
- Goullioud, R., Catanzarite, J. H., Dekens, F. G., Shao, M., & Marr, IV, J. C. 2008: *Overview of the SIM PlanetQuest Light mission concept*, in Presented at the Society of Photo-Optical Instrumentation Engineers (SPIE) Conference, Vol. 7013, Society of Photo-Optical Instrumentation Engineers (SPIE) Conference Series, cited on p. 32, 48
- Hachisu, I. & Kato, M. 2006: *A Universal Decline Law of Classical Novae*, ApJS, 167, 59, cited on p. 58, 68, 69, 75, 76
- Hachisu, I. & Kato, M. 2009: *Optical and Supersoft X-Ray Light-Curve Models of Classical Nova V2491 Cygni: A New Clue to the Secondary Maximum*, ApJL, 694, L103, cited on p. 69
- Hachisu, I., Kato, M., Kiyota, S., Kubotera, K., Maehara, H., Nakajima, K., Ishii, Y., Kamada, M., Mizoguchi, S., Nishiyama, S., Sumitomo, N., et al. 2008: *Optical Light Curves of RS Oph (2006) and Hydrogen Burning Turnoff*, in Astronomical Society of the Pacific Conference Series, Vol. 401, RS Ophiuchi (2006) and the Recurrent Nova Phenomenon, ed. A. Evans, M. F. Bode, T. J. O'Brien, & M. J. Darnley, 206, cited on p. 77
- Henze, M., Pietsch, W., Haberl, F., Hernanz, M., Sala, G., Della Valle, M., Hatzidimitriou, D., Rau, A., Hartmann, D. H., Greiner, J., Burwitz, V., et al. 2010a: *X-ray monitoring of classical novae in the central region of M 31. I. June 2006-March 2007*, A&A, 523, A89, cited on p. 67
- Henze, M., Pietsch, W., Haberl, F., Hernanz, M., Sala, G., Hatzidimitriou, D., Della Valle, M., Rau, A., Hartmann, D. H., & Burwitz, V. 2010b: *X-ray monitoring of classical novae in the central region of M 31. II. Autumn and winter 2007/2008 and 2008/2009*, ArXiv e-prints, cited on p. 67
- Henze, M., Pietsch, W., Haberl, F., Sala, G., Hernanz, M., Hatzidimitriou, D., Rau, A., Hartmann, D. H., Greiner, J., Orío, M., Stiele, H., et al. 2010c: *Recent discoveries of supersoft X-ray sources in M 31*, Astronomische Nachrichten, 331, 193, cited on p. 67

- Henze, M., Pietsch, W., Podigachoski, P., Burwitz, V., Haberl, F., Updike, A., Hartmann, D., Milne, P., Williams, G., Papamastorakis, G., Reig, P., et al. 2009: *M31N 1997-11k - a very fast recurrent nova in M31 or a foreground CV?*, The Astronomer's Telegram, 2286, 1, cited on p. 76
- Heyrovský, D. 2003: *Measuring Stellar Limb Darkening by Gravitational Microlensing*, ApJ, 594, 464, cited on p. 23
- Heyrovsky, D. & Loeb, A. 1997: *Microlensing of an Elliptical Source by a Point Mass*, ApJ, 490, 38, cited on p. 17
- Hodge, P. & Lee, M. G. 1988: *UBVR CCD photometry of stars in M31. II - Five disk fields*, ApJ, 329, 651, cited on p. 54
- Hog, E., Novikov, I. D., & Polnarev, A. G. 1995: *MACHO photometry and astrometry.*, A&A, 294, 287, cited on p. 11, 32, 33
- Hosokawa, M., Ohnishi, K., Fukushima, T., & Takeuti, M. 1993: *Parallactic variation of gravitational lensing and measurement of stellar mass*, A&A, 278, L27, cited on p. 11, 33
- Hubble, E. P. 1929: *A spiral nebula as a stellar system, Messier 31.*, ApJ, 69, 103, cited on p. 57, 58, 59
- Ibata, R., Irwin, M., Lewis, G., Ferguson, A. M. N., & Tanvir, N. 2001: *A giant stream of metal-rich stars in the halo of the galaxy M31*, Nature, 412, 49, cited on p. 5
- Jeong, Y., Han, C., & Park, S. 1999: *The Effect of Bright Lenses on the Astrometric Observations of Gravitational Microlensing Events*, ApJ, 511, 569, cited on p. 42
- Jetzer, P. 1994: *Gravitational microlensing by the halo of the Andromeda galaxy*, A&A, 286, 426, cited on p. 4
- Jiang, G., DePoy, D. L., Gal-Yam, A., Gaudi, B. S., Gould, A., Han, C., Lipkin, Y., Maoz, D., Ofek, E. O., Park, B., Pogge, R. W., et al. 2004: *OGLE-2003-BLG-238: Microlensing Mass Estimate of an Isolated Star*, ApJ, 617, 1307, cited on p. 32, 39
- José, J. & Hernanz, M. 2007: *TOPICAL REVIEW: Nucleosynthesis in classical nova explosions*, Journal of Physics G Nuclear Physics, 34, 431, cited on p. 58
- Joshi, Y. C., Pandey, A. K., Narasimha, D., Giraud-Héraud, Y., Sagar, R., & Kaplan, J. 2004: *Photometric study of two novae in M 31*, A&A, 415, 471, cited on p. 59, 65
- Kaiser, N., Aussel, H., Burke, B. E., Boesgaard, H., Chambers, K., Chun, M. R., Heasley, J. N., Hodapp, K., Hunt, B., Jedicke, R., Jewitt, D., et al. 2002: *Pan-STARRS: A Large Synoptic Survey Telescope Array*, in Presented at the Society of Photo-Optical Instrumentation Engineers (SPIE) Conference, Vol. 4836, Society of Photo-Optical Instrumentation Engineers (SPIE) Conference Series, ed. J. A. Tyson & S. Wolff, 154–164, cited on p. 78
- Kato, T., Nakajima, K., Maehara, H., & Kiyota, S. 2009: *Rebrightening Phenomenon in Classical Novae*, ArXiv e-prints, cited on p. 69
- Kent, S. M. 1989: *An improved bulge model for M31*, AJ, 97, 1614, cited on p. 54

- Kervella, P., Thévenin, F., Di Folco, E., & Ségransan, D. 2004: *The angular sizes of dwarf stars and subgiants. Surface brightness relations calibrated by interferometry*, A&A, 426, 297, cited on p. 11
- Kozłowski, S., Woźniak, P. R., Mao, S., & Wood, A. 2007: *The First Direct Detection of a Gravitational μ -Lens toward the Galactic Bulge*, ApJ, 671, 420, cited on p. 8, 32, 39
- Law, N. M., Kulkarni, S. R., Dekany, R. G., Ofek, E. O., Quimby, R. M., Nugent, P. E., Surace, J., Grillmair, C. C., Bloom, J. S., Kasliwal, M. M., Bildsten, L., et al. 2009: *The Palomar Transient Factory: System Overview, Performance, and First Results*, PASP, 121, 1395, cited on p. 78
- Lee, C., Riffeser, A., Seitz, S., & Bender, R. 2009: *Finite-Source Effects in Microlensing: A Precise, Easy to Implement, Fast, and Numerically Stable Formalism*, ApJ, 695, 200, cited on p. 15, 32, 35
- Lee, C. H., Riffeser, A., Seitz, S., Bender, R., Fliri, J., Hopp, U., Ries, C., Bärnbantner, O., & Gössl, C. 2011 submitted: *WeCAPP nova catalogue*, A&A, cited on p. 57
- Lee, C. H., Seitz, S., Riffeser, A., & Bender, R. 2010: *Finite-source and finite-lens effects in astrometric microlensing*, MNRAS, 407, 1597, cited on p. 31
- Lindgren, L., Perryman, M. A., Bastian, U., Dainty, J. C., Hog, E., van Leeuwen, F., Kovalevsky, J., Labeyrie, A., Loiseau, S., Mignard, F., Noordam, J. E., et al. 1994: *GAIA: global astrometric interferometer for astrophysics*, in Society of Photo-Optical Instrumentation Engineers (SPIE) Conference Series, Vol. 2200, Society of Photo-Optical Instrumentation Engineers (SPIE) Conference Series, ed. J. B. Breckinridge, 599–608, cited on p. 32
- Livio, M. 1992: *Classical novae and the extragalactic distance scale*, ApJ, 393, 516, cited on p. 58
- Lynch, D. K., Woodward, C. E., Gehrz, R., Helton, L. A., Rudy, R. J., Russell, R. W., Pearson, R., Venturini, C. C., Mazuk, S., Rayner, J., Ness, J., et al. 2008: *Nova V2362 Cygni (nova Cygni 2006): Spitzer, Swift, and Ground-Based Spectral Evolution*, AJ, 136, 1815, cited on p. 72
- Lynds, R. & Petrosian, V. 1986: *Giant Luminous Arcs in Galaxy Clusters*, in Bulletin of the American Astronomical Society, Vol. 18, Bulletin of the American Astronomical Society, 1014, cited on p. 4
- Madore, B. F. & Freedman, W. L. 1991: *The Cepheid distance scale*, PASP, 103, 933, cited on p. 51
- Mao, S. & Witt, H. J. 1998: *Extended source effects in astrometric gravitational microlensing*, MNRAS, 300, 1041, cited on p. 32, 34, 39
- McConnachie, A. W., Irwin, M. J., Ibata, R. A., Dubinski, J., Widrow, L. M., Martin, N. F., Côté, P., Dotter, A. L., Navarro, J. F., Ferguson, A. M. N., Puzia, T. H., et al. 2009: *The remnants of galaxy formation from a panoramic survey of the region around M31*, Nature, 461, 66, cited on p. ix, 5
- McElroy, D. B. 1983: *Dynamics of the stellar component of the bulge of M31*, ApJ, 270, 485, cited on p. 54
- McLaughlin, D. B. 1945: *The Relation between Light-Curves and Luminosities of Novae*, PASP, 57, 69, cited on p. 58

- Miyamoto, M. & Yoshii, Y. 1995: *Astrometry for Determining the MACHO Mass and Trajectory*, AJ, 110, 1427, cited on p. 11, 32, 33
- Montalto, M., Seitz, S., Riffeser, A., Hopp, U., Lee, C.-H., & Schönrich, R. 2009: *Properties of M31. I. Dust. Basic properties and a discussion about age-dependent dust heating*, A&A, 507, 283, cited on p. xiii, 54, 55
- Oke, J. B. 1974: *Absolute Spectral Energy Distributions for White Dwarfs*, ApJS, 27, 21, cited on p. 132
- Orio, M. 2006: *A Close Look at the Population of Supersoft and Quasi-soft X-Ray Sources Observed in M31 with XMM-Newton*, ApJ, 643, 844, cited on p. 67
- Paczynski, B. 1986: *Gravitational microlensing by the galactic halo*, ApJ, 304, 1, cited on p. 4, 15, 17, 18
- Paczynski, B. 1987: *Giant luminous arcs discovered in two clusters of galaxies*, Nature, 325, 572, cited on p. 4
- Payne-Gaposchkin, C. 1964, The galactic novae, ed. Gaposchkin, C. H. P., cited on p. 68
- Peebles, P. J. E. 1993, Principles of Physical Cosmology, ed. Peebles, P. J. E., cited on p. 1
- Pejcha, O. 2009: *Time-Dependent Rebrightenings in Classical Nova Outbursts: A Late-Time Episodic Fuel Burning?*, ApJL, 701, L119, cited on p. 72
- Penzias, A. A. & Wilson, R. W. 1965: *A Measurement of Excess Antenna Temperature at 4080 Mc/s.*, ApJ, 142, 419, cited on p. 1
- Perlmutter, S., Aldering, G., Goldhaber, G., Knop, R. A., Nugent, P., Castro, P. G., Deustua, S., Fabbro, S., Goobar, A., Groom, D. E., Hook, I. M., et al. 1999: *Measurements of Omega and Lambda from 42 High-Redshift Supernovae*, ApJ, 517, 565, cited on p. 2
- Pietsch, W. 2010: *X-ray emission from optical novae in M 31*, Astronomische Nachrichten, 331, 187, cited on p. 58, 61, 76, 102
- Pietsch, W., Fliri, J., Freyberg, M. J., Greiner, J., Haberl, F., Riffeser, A., & Sala, G. 2005: *Optical novae: the major class of supersoft X-ray sources in M 31*, A&A, 442, 879, cited on p. 58, 67, 78, 142
- Pietsch, W., Haberl, F., Sala, G., Stiele, H., Hornoch, K., Riffeser, A., Fliri, J., Bender, R., Bühler, S., Burwitz, V., Greiner, J., et al. 2007: *X-ray monitoring of optical novae in M 31 from July 2004 to February 2005*, A&A, 465, 375, cited on p. 61, 64, 66, 67, 76, 78, 102
- Press, W. H. 2002, Numerical recipes in C++ : the art of scientific computing, ed. Press, W. H., cited on p. 16, 18
- Quirrenbach, A., Coudé du Foresto, V., Daigne, G., Hofmann, K. H., Hofmann, R., Lattanzi, M., Osterbart, R., Le Poole, R. S., Queloz, D., & Vakili, F. 1998: *PRIMA: study for a dual-beam instrument for the VLT Interferometer*, in Society of Photo-Optical Instrumentation Engineers (SPIE) Conference Series, Vol. 3350, Society of Photo-Optical Instrumentation Engineers (SPIE) Conference Series, ed. R. D. Reasenberg, 807–817, cited on p. 32

- Rau, A., Kulkarni, S. R., Law, N. M., Bloom, J. S., Ciardi, D., Djorgovski, G. S., Fox, D. B., Gal-Yam, A., Grillmair, C. C., Kasliwal, M. M., Nugent, P. E., et al. 2009: *Exploring the Optical Transient Sky with the Palomar Transient Factory*, PASP, 121, 1334, cited on p. 78
- Rector, T. A., Jacoby, G. H., Corbett, D. L., & Denham, M. 1999a: *A search for novae in the bulge of M31.*, in Bulletin of the American Astronomical Society, Vol. 31, Bulletin of the American Astronomical Society, 1420–1421, cited on p. 64
- Rector, T. A., Jacoby, G. H., Corbett, D. L., Denham, M., & RBSE Nova Search Team. 1999b: *A Search for Novae in the Bulge of M31*, in American Astronomical Society Meeting Abstracts, Vol. 195, American Astronomical Society Meeting Abstracts, 36.08, cited on p. 59
- Renn, J., Sauer, T., & Stachel, J. 1997: *The origin of gravitational lensing: a postscript to Einstein's 1936 Science paper.*, Science, 275, 184, cited on p. 4
- Riess, A. G., Filippenko, A. V., Challis, P., Clocchiatti, A., Diercks, A., Garnavich, P. M., Gilliland, R. L., Hogan, C. J., Jha, S., Kirshner, R. P., Leibundgut, B., et al. 1998: *Observational Evidence from Supernovae for an Accelerating Universe and a Cosmological Constant*, AJ, 116, 1009, cited on p. 2
- Riffeser, A., Fliri, J., Bender, R., Seitz, S., & Gössl, C. A. 2003: *The Wendelstein Calar Alto Pixel-lensing Project (WeCAPP): First MACHO Candidates*, ApJL, 599, L17, cited on p. 59
- Riffeser, A., Fliri, J., Gössl, C. A., Bender, R., Hopp, U., Bärnbantner, O., Ries, C., Barwig, H., Seitz, S., & Mitsch, W. 2001: *WeCAPP - Wendelstein Calar Alto pixellensing project I. Tracing dark and bright matter in M 31*, A&A, 379, 362, cited on p. 59
- Riffeser, A., Fliri, J., Seitz, S., & Bender, R. 2006: *Microlensing toward Crowded Fields: Theory and Applications to M31*, ApJS, 163, 225, cited on p. xiii, 5, 13, 16, 51, 52, 54
- Riffeser, A., Seitz, S., & Bender, R. 2008: *The M31 Microlensing Event WeCAPP-GL1/POINT-AGAPE-S3: Evidence for a MACHO Component in the Dark Halo of M31?*, ApJ, 684, 1093, cited on p. 59
- Rosino, L. 1964: *Novae in Messier 31 discovered and observed at Asiago from 1955 to 1963.*, Annales d'Astrophysique, 27, 498, cited on p. 59
- Rosino, L. 1973: *Novae in M 31 discovered and observed at Asiago from 1963 to 1970*, A&AS, 9, 347, cited on p. 59
- Rosino, L., Capaccioli, M., D'Onofrio, M., & della Valle, M. 1989: *Fifty-two novae in M31 discovered and observed at Asiago from 1971 to 1986*, AJ, 97, 83, cited on p. 59
- Rubin, V. C., Ford, W. K. J., & Thonnard, N. 1980: *Rotational properties of 21 SC galaxies with a large range of luminosities and radii, from NGC 4605 /R = 4kpc/ to UGC 2885 /R = 122 kpc/*, ApJ, 238, 471, cited on p. 2
- Saglia, R. P., Fabricius, M., Bender, R., Montalto, M., Lee, C.-H., Riffeser, A., Seitz, S., Morganti, L., Gerhard, O., & Hopp, U. 2010: *The old and heavy bulge of M 31 . I. Kinematics and stellar populations*, A&A, 509, A61, cited on p. 54

- Schaefer, B. E. 2010: *Comprehensive Photometric Histories of All Known Galactic Recurrent Novae*, ApJS, 187, 275, cited on p. 58, 76
- Schneider, P., Ehlers, J., & Falco, E. E. 1992, Gravitational Lenses, ed. Schneider, P., Ehlers, J., & Falco, E. E., cited on p. 7
- Schneider, P., Kochanek, C. S., & Wambsganss, J. 2006, Gravitational Lensing: Strong, Weak and Micro, ed. Schneider, P., Kochanek, C. S., & Wambsganss, J., cited on p. 6, 7
- Shafter, A. W. 1997: *On the Nova Rate in the Galaxy*, ApJ, 487, 226, cited on p. 58
- Shafter, A. W., Bode, M. F., Darnley, M. J., Misselt, K. A., Rubin, M., & Hornoch, K. 2011a: *A Spitzer Survey of Novae in M31*, ApJ, 727, 50, cited on p. 67, 78
- Shafter, A. W., Darnley, M. J., Hornoch, K., Filippenko, A. V., Bode, M. F., Ciardullo, R., Misselt, K. A., Hounsell, R. A., Chornock, R., & Matheson, T. 2011b: *A Spectroscopic and Photometric Survey of Novae in M31*, ApJ, 734, 12, cited on p. 67
- Shafter, A. W. & Irby, B. K. 2001: *On the Spatial Distribution, Stellar Population, and Rate of Novae in M31*, ApJ, 563, 749, cited on p. 58, 59, 64
- Shara, M. M. 1981: *A theoretical explanation of the absolute magnitude-decline time $M_B - t_3$ relationship for classical novae*, ApJ, 243, 926, cited on p. 58
- Sharov, A. S. & Alksnis, A. 1991: *Novae in M31 discovered with wide field telescopes in Crimea and Latvia*, Ap&SS, 180, 273, cited on p. 59
- Sharov, A. S., Alksnis, A., Zharova, A. V., & Shokin, Y. A. 2000: *Novae in M31 in 1998*, Astronomy Letters, 26, 433, cited on p. 64
- Soucail, G., Fort, B., Mellier, Y., & Picat, J. P. 1987: *A blue ring-like structure, in the center of the A 370 cluster of galaxies*, A&A, 172, L14, cited on p. 4
- Strope, R. J., Schaefer, B. E., & Henden, A. A. 2010: *Catalog of 93 Nova Light Curves: Classification and Properties*, AJ, 140, 34, cited on p. 58, 68, 69, 72, 74, 75, 76, 78
- Takahashi, R. 2003: *Astrometric Microlensing by Finite-Size Lenses*, ApJ, 595, 418, cited on p. 31, 32, 36, 39
- Tanaka, J., Nogami, D., Fujii, M., Ayani, K., & Kato, T. 2011: *On the Rebrightenings of Classical Novae during the Early Phase*, PASJ, 63, 159, cited on p. 72
- Tempel, E., Tuvikene, T., Tamm, A., & Tenjes, P. 2011: *SDSS surface photometry of M 31 with absorption corrections*, A&A, 526, A155, cited on p. xiii, 53
- Tisserand, P., Le Guillou, L., Afonso, C., Albert, J. N., Andersen, J., Ansari, R., Aubourg, É., Bareyre, P., Beaulieu, J. P., Charlot, X., Coutures, C., et al. 2007: *Limits on the Macho content of the Galactic Halo from the EROS-2 Survey of the Magellanic Clouds*, A&A, 469, 387, cited on p. 5, 49
- Tomaney, A. B. & Shafter, A. W. 1992: *The spectroscopic and photometric evolution of novae in the bulge of M31*, ApJs, 81, 683, cited on p. 59

- Tyson, J. A. 2002: *Large Synoptic Survey Telescope: Overview*, in Presented at the Society of Photo-Optical Instrumentation Engineers (SPIE) Conference, Vol. 4836, Society of Photo-Optical Instrumentation Engineers (SPIE) Conference Series, ed. J. A. Tyson & S. Wolff, 10–20, cited on p. 78
- Udalski, A. 2003: *The Optical Gravitational Lensing Experiment. Real Time Data Analysis Systems in the OGLE-III Survey*, Acta Astronomica, 53, 291, cited on p. 19
- Udalski, A., Szymanski, M., Kaluzny, J., Kubiak, M., Krzeminski, W., Mateo, M., Preston, G. W., & Paczynski, B. 1993: *The optical gravitational lensing experiment. Discovery of the first candidate microlensing event in the direction of the Galactic Bulge*, Acta Astronomica, 43, 289, cited on p. 4, 8
- Udalski, A., Szymanski, M., Kaluzny, J., Kubiak, M., & Mateo, M. 1992: *The Optical Gravitational Lensing Experiment*, Acta Astronomica, 42, 253, cited on p. 16
- Šimon, V., Hornoch, K., Kušnirák, P., Šarounová, L., & Wolf, M. 2005: *Discovery and Photometry of 8 Novae in the M31 Galaxy in 2002 - 2004*, in Astronomical Society of the Pacific Conference Series, Vol. 330, The Astrophysics of Cataclysmic Variables and Related Objects, ed. J.-M. Hameury & J.-P. Lasota, 449, cited on p. 65, 66
- Walker, M. A. 1995: *Microlensed Image Motions*, ApJ, 453, 37, cited on p. 11, 32, 33, 34
- Walsh, D., Carswell, R. F., & Weymann, R. J. 1979: *0957 + 561 A, B - Twin quasistellar objects or gravitational lens*, Nature, 279, 381, cited on p. 4
- Walterbos, R. A. M. & Kennicutt, Jr., R. C. 1987: *Multi-color photographic surface photometry of the Andromeda galaxy*, A&AS, 69, 311, cited on p. 51
- Wambsganss, J. 1998: *Gravitational Lensing in Astronomy*, Living Reviews in Relativity, 1, 12, cited on p. 6
- Williams, R. E. 1992: *The formation of novae spectra*, AJ, 104, 725, cited on p. 68
- Witt, H. J. & Mao, S. 1994: *Can lensed stars be regarded as pointlike for microlensing by MACHOs?*, ApJ, 430, 505, cited on p. 11, 16, 18
- Wyrzykowski, Ł., Kozłowski, S., Skowron, J., Belokurov, V., Smith, M. C., Udalski, A., Szymański, M. K., Kubiak, M., Pietrzyński, G., Soszyński, I., Szewczyk, O., et al. 2009: *The OGLE view of microlensing towards the Magellanic Clouds - I. A trickle of events in the OGLE-II LMC data*, MNRAS, 397, 1228, cited on p. 49
- Xu, C. & Helou, G. 1996: *High-Resolution IRAS Maps and Infrared Emission of M31. II. Diffuse Component and Interstellar Dust*, ApJ, 456, 163, cited on p. 54
- Yee, J. C., Udalski, A., Sumi, T., Dong, S., Kozłowski, S., Bird, J. C., Cole, A., Higgins, D., McCormick, J., Monard, L. A. G., Polishook, D., et al. 2009: *Extreme Magnification Microlensing Event OGLE-2008-BLG-279: Strong Limits on Planetary Companions to the Lens Star*, ApJ, 703, 2082, cited on p. 32, 39

- Yoo, J., DePoy, D. L., Gal-Yam, A., Gaudi, B. S., Gould, A., Han, C., Lipkin, Y., Maoz, D., Ofek, E. O., Park, B., Pogge, R. W., et al. 2004: *OGLE-2003-BLG-262: Finite-Source Effects from a Point-Mass Lens*, ApJ, 603, 139, cited on p. 18, 19, 23, 32, 36, 39
- Zub, M., Cassan, A., Heyrovský, D., Fouqué, P., Stempels, H. C., Albrow, M. D., Beaulieu, J.-P., Brilliant, S., Christie, G. W., Kains, N., Kozłowski, S., et al. 2011: *Limb-darkening measurements for a cool red giant in microlensing event OGLE 2004-BLG-482*, A&A, 525, A15, cited on p. 32, 39
- Zwicky, F. 1936: *Life-Luminosity Relation for Novae*, PASP, 48, 191, cited on p. 58
- Zwicky, F. 1937: *On the Masses of Nebulae and of Clusters of Nebulae*, ApJ, 86, 217, cited on p. 2

Acknowledgments

This thesis would not have been finished without the help from many people. First of all, i would like to thank my supervisor Ralf Bender and my thesis advisor Stella Seitz. Thank you so much for giving me the opportunity for pursuing my PhD at USM. Stella is a great mentor, always guides me with insightful questions.

Many thank you go to Arno Riffeser. I have gained a lot of help from his expertise in modeling, data reduction and data analysis.

I am indebted to Johannes Koppenhöfer. Thank you for the immense efforts of helping me fighting with the Astro-WISE. I would also like to thank Jan Snigula, whom i bothered a lot for debugging with the Astro-WISE.

I would like to thank Johannes Koppenhöfer and Fabrice Brimioulle for translating my abstract into a German version.

Last but not the least, I would like to express my gratitude to my family. You are always there when needed and are confident in my ability, believing that I can accomplish anything I set up in mind. Thank you so much for your constant helping and supporting me to become an astronomer!

Curriculum Vitae

Name: Chien-Hsiu Lee
Born: Taoyuan, Taiwan
Citizenship: Taiwan
Home: Tumblingerstrasse 54, Zimmer 043, 80337 Munich, Germany
Education
2000 - 2004 B.S., Physics, National Taiwan University
2004 - 2006 M.S., Astronomy, National Central University
2007 - Ph.D. Student, Universitäts-Sternwarte, LMU Munich